

Design of functional polymeric materials for cancer-targeted drug delivery and cellular capture
and isolation

by

Esther L Radaha

B.S., Kansas State University, 2017

AN ABSTRACT OF A DISSERTATION

submitted in partial fulfillment of the requirements for the degree

DOCTOR OF PHILOSOPHY

Tim Taylor Department of Chemical Engineering
Carl R. Ice College of Engineering

KANSAS STATE UNIVERSITY
Manhattan, Kansas

2021

Abstract

Synthetic polymeric materials offer many exciting advantages with the plethora of functionalization techniques affording materials with unique properties, multiple functionalities, and elaborate architectures for a variety of applications. In the drug delivery field, the use of synthetic polymers as nano-sized drug carriers in cancer nanomedicine has gained tremendous interest as an alternative to conventional small molecule anticancer drugs to reduce drug-related toxicity and increase targetability. Like other nanocarriers, synthetic polymeric nanocarriers rely on passive-drug targeting, also known as the Enhanced Permeability and Retention (EPR) effect in leaky tumor vasculature for delivery of therapeutics. The biological complexity and barriers that exist in the body however have proven to be a huge challenge in selectively delivering therapeutics to cancer cells. Synthetic polymers also offer significant advantages for improved isolation and characterization of microbes attached to surfaces compared to conventional techniques. However, the retrieval of microbes from synthetic polymer interfaces with high spatial precision without damaging the underlying live bacterial cells remains a critical challenge for further characterization. Therefore, the goal of this dissertation is to explore and develop synthetic, functional, stimulus-responsive polymeric interfaces (polymeric micelles, photodegradable hydrogels) for targeted drug delivery to cancer cells and improved isolation of microbes for molecular characterization.

The majority of this thesis (**chapters 2, 3, and 4**) focuses on utilizing the intrinsic properties present in tumor microenvironments (TME), mainly elevated levels of reactive oxygen species (ROS) and overproduction of matrix metalloproteinase-2 (MMP-2) enzyme for the design and synthesis of stimuli-sensitive synthetic block copolymer polymeric micelles (BCPMs) by reversible addition-fragmentation chain transfer (RAFT) polymerization for targeted delivery of

therapeutics to cancer cells. The synthesized BCPMs were extensively studied and evaluated for their chemistry and biological functions in *in vitro* cancer therapy. In **chapter 2**, the conventional chemotherapeutic drug, Doxorubicin (DOX) was loaded physically into the hydrophobic core of BCPMs bearing a library of oxidation-sensitive thioether groups. Results showed that the micelles, especially micelles with intermediate ROS sensitivity, significantly increased toxicity of DOX in liver cancer cells (HepG2) but protected normal cells, human umbilical endothelial cells (HUVECs) from DOX cytotoxicity. Taking it a step further, in **chapter 3**, hydrogen sulfide (H₂S) prodrug (ADT) was chemically conjugated to the core of BCPMs bearing oxidation-sensitive thioether group and the anti-cancer effects of H₂S in colon cancer cells (HT29) were evaluated. A greater anti-proliferative effect was observed in HT29 cells with no significant toxicity in HUVEC cells. In **chapter 4**, a different approach was taken where BCPM bearing MMP-2 enzyme cleavable peptide motifs and chemically conjugated ADT was designed for site-specific delivery of H₂S to cancer cells. The greater release of H₂S from MMP-2 sensitive micelles exhibited stronger anti-proliferative activity in HT29 cells. The final portion of this thesis (**chapter 5**) focuses on the development of the polymer surface dissection (PSD) method which uses biofunctionalized, photodegradable polyethylene glycol (PEG)-based hydrogels for the isolation of microbes from polyvinylidene difluoride wastewater membrane surfaces. The flocs were extracted with high spatial precision and minimal DNA damage after exposure to spatiotemporally controlled ultraviolet (UV) light using a patterned illumination tool, allowing for follow-up characterization by 16S rRNA sequencing. The technique allows for the identification of microbes that form small flocs on membrane surfaces without requiring a culture step for enrichment, and will be used in future work to identify communities of microorganisms that initiate membrane biofilms in bio-separation processes.

Design of functional polymeric materials for cancer-targeted drug delivery and cellular capture
and isolation

by

Esther L Radaha

B.S., Kansas State University, 2017

A DISSERTATION

submitted in partial fulfillment of the requirements for the degree

DOCTOR OF PHILOSOPHY

Tim Taylor Department of Chemical Engineering
Carl R. Ice College of Engineering

KANSAS STATE UNIVERSITY
Manhattan, Kansas

2021

Approved by:

Co-Major Professor
Dr. Jennifer Anthony

Approved by:

Co-Major Professor
Dr. Ryan Hansen

Copyright

© Esther Radaha 2021.

Abstract

Synthetic polymeric materials offer many exciting advantages with the plethora of functionalization techniques affording materials with unique properties, multiple functionalities, and elaborate architectures for a variety of applications. In the drug delivery field, the use of synthetic polymers as nano-sized drug carriers in cancer nanomedicine has gained tremendous interest as an alternative to conventional small molecule anticancer drugs to reduce drug-related toxicity and increase targetability. Like other nanocarriers, synthetic polymeric nanocarriers rely on passive-drug targeting, also known as the Enhanced Permeability and Retention (EPR) effect in leaky tumor vasculature for delivery of therapeutics. The biological complexity and barriers that exist in the body however have proven to be a huge challenge in selectively delivering therapeutics to cancer cells. Synthetic polymers also offer significant advantages for improved isolation and characterization of microbes attached to surfaces compared to conventional techniques. However, the retrieval of microbes from synthetic polymer interfaces with high spatial precision without damaging the underlying live bacterial cells remains a critical challenge for further characterization. Therefore, the goal of this dissertation is to explore and develop synthetic, functional, stimulus-responsive polymeric interfaces (polymeric micelles, photodegradable hydrogels) for targeted drug delivery to cancer cells and improved isolation of microbes for molecular characterization.

The majority of this thesis (**chapters 2, 3, and 4**) focuses on utilizing the intrinsic properties present in tumor microenvironments (TME), mainly elevated levels of reactive oxygen species (ROS) and overproduction of matrix metalloproteinase-2 (MMP-2) enzyme for the design and synthesis of stimuli-sensitive synthetic block copolymer polymeric micelles (BCPMs) by reversible addition-fragmentation chain transfer (RAFT) polymerization for targeted delivery of

therapeutics to cancer cells. The synthesized BCPMs were extensively studied and evaluated for their chemistry and biological functions in *in vitro* cancer therapy. In **chapter 2**, the conventional chemotherapeutic drug, Doxorubicin (DOX) was loaded physically into the hydrophobic core of BCPMs bearing a library of oxidation-sensitive thioether groups. Results showed that the micelles, especially micelles with intermediate ROS sensitivity, significantly increased toxicity of DOX in liver cancer cells (HepG2) but protected normal cells, human umbilical endothelial cells (HUVECs) from DOX cytotoxicity. Taking it a step further, in **chapter 3**, hydrogen sulfide (H₂S) prodrug (ADT) was chemically conjugated to the core of BCPMs bearing oxidation-sensitive thioether group and the anti-cancer effects of H₂S in colon cancer cells (HT29) were evaluated. A greater anti-proliferative effect was observed in HT29 cells with no significant toxicity in HUVEC cells. In **chapter 4**, a different approach was taken where BCPM bearing MMP-2 enzyme cleavable peptide motifs and chemically conjugated ADT was designed for site-specific delivery of H₂S to cancer cells. The greater release of H₂S from MMP-2 sensitive micelles exhibited stronger anti-proliferative activity in HT29 cells. The final portion of this thesis (**chapter 5**) focuses on the development of the polymer surface dissection (PSD) method which uses biofunctionalized, photodegradable polyethylene glycol (PEG)-based hydrogels for the isolation of microbes from polyvinylidene difluoride wastewater membrane surfaces. The flocs were extracted with high spatial precision and minimal DNA damage after exposure to spatiotemporally controlled ultraviolet (UV) light using a patterned illumination tool, allowing for follow-up characterization by 16S rRNA sequencing. The technique allows for the identification of microbes that form small flocs on membrane surfaces without requiring a culture step for enrichment, and will be used in future work to identify communities of microorganisms that initiate membrane biofilms in bio-separation processes.

Table of Contents

List of Figures	xiii
List of Tables	xix
Acknowledgements	xx
Dedication	xxi
1 Introduction.....	1
1.1 Polymers in Daily Life.....	1
1.2 The concept of nanomedicine	1
1.2.1 Polymeric Nanomaterials in Therapeutics	2
1.2.2 Hydrogen Sulfide	4
1.2.3 Challenges for Clinical Translation	7
1.2.3.1 Biological Barriers	7
1.2.3.2 Complex Tumor Microenvironment	9
1.2.3.2.1 Tumor-associated cellular heterogeneity	9
1.2.3.2.2 Tumor physiology (Hypoxia and Acidosis)	11
1.3 Polymeric Interfaces for Capture and Detection of Microbes	12
1.3.1 Challenges for Capture and Detection of Microbes.....	14
1.3.1.1 Characterization of Biofilm Formation.....	14
1.4 Thesis Approach and Central Objective	16
1.4.1 Bioresponsive polymeric micelles for cancer-targeted drug delivery	16
1.4.2 Biofunctional photodegradable hydrogels for capture and isolation of microbes	17
2 Polymeric micelles with fine-tuned oxidation sensitivities for anti-cancer drug delivery	18
2.1 Introduction.....	19
2.2 Experimental Section	22
2.2.1 Materials	22
2.2.2 Instrumentation	23
2.2.3 Synthesis of PPFPA Homopolymer.....	25
2.2.4 Synthesis of PAM-PPFPA Diblock Copolymer	26
2.2.5 CTA End Group Removal from PAM-PPFPA Diblock Copolymer	26
2.2.6 Synthesis of Thioether-Containing Block Copolymers	27

2.2.7	Synthesis of Thioether/FITC-Containing Diblock Copolymers	27
2.2.8	Preparation of Micelles	28
2.2.9	Critical Micelle Concentration (CMC)	28
2.2.10	Change in Size Distribution of the micelles in the presence of H ₂ O ₂	29
2.2.11	H ₂ O ₂ Scavenging Rate of the Thioether Model Compounds by Iodide Oxidation Assay	29
2.2.12	Monitoring of Micelle Dissociation by the Fluorescence Recovery of Self-Quenched Fluorophores	30
2.2.13	Preparation of Dox-Loaded Micelles.....	30
2.2.14	Determination of the Dox concentration.....	30
2.2.15	Dox Release from the Micelles in Response to H ₂ O ₂	31
2.2.16	Cell Culture.....	31
2.2.17	Dissociation of Thioether/FITC-containing Micelles in HepG2 Cells.....	31
2.2.18	Cytotoxicity of Dox-Loaded Micelles in HepG2 and HUVECs	32
2.2.19	Intracellular Distribution of Dox in HepG2 Cells.....	32
2.2.20	Molecular Modeling.....	33
2.3	Results and Discussion	33
2.3.1	Effect of Chemical Structure on Oxidation of Thioether Compounds	33
2.3.2	Synthesis of Thioether-Bearing Diblock Copolymers	36
2.3.3	Preparation and Characterization of the Thioether-Bearing Micelles	38
2.3.4	Dissociation of Thioether-Bearing Micelles in Response to H ₂ O ₂	40
2.3.5	Dissociation of Thioether-Bearing Micelles in HepG2 cells.....	42
2.3.6	Dox-Loaded Thioether-Bearing Micelles	45
2.4	Conclusion	52
3	ROS-sensitive hydrogen sulfide donor micelles for cancer-targeted delivery	54
3.1	Introduction.....	55
3.2	Experimental Procedures	59
3.2.1	Materials	59
3.2.2	Instrumentation	60
3.2.3	Synthesis of PPFPA Homopolymer.....	62
3.2.4	Synthesis of PAM-PPFPA Diblock Copolymer	62

3.2.5	CTA End Group Removal from PAM-PPFPA Diblock Copolymer	63
3.2.6	Synthesis of ADTM and ADT-TPM Block Copolymers.	63
3.2.7	Preparation of Micelles	64
3.2.8	Critical Micelle Concentration (CMC).	64
3.2.9	Dissociation of Micelles in the presence of H ₂ O ₂	65
3.2.10	Cell Culture.....	65
3.2.11	Cell Viability Assay in HT29 cells	65
3.2.12	H ₂ S release from the micelles in HT29 lysate with the WSP-1 H ₂ S fluorescent detection probe.....	66
3.2.13	H ₂ S Release by Fluorescent dye WSP-1 in HT29 Cells.....	66
3.3	Results and Discussion	67
3.3.1	Synthesis of ROS-sensitive H ₂ S Donor Micelles (ADT-TPM and ADTM)	67
3.3.2	Preparation and Characterization of ADT-TPM and ADTM Micelles	69
3.3.3	Dissociation of micelles in the presence of H ₂ O ₂	70
3.3.4	H ₂ S Release from Micelles in the presence of H ₂ O ₂ in HT29 Cell Lysate.....	71
3.3.5	H ₂ S Release from Micelles in HT29.....	72
3.3.6	Anti-proliferative Effect of Micelles	73
3.4	Conclusion	74
4	MMP-2-sensitive hydrogen sulfide donor micelles for cancer-targeted delivery	76
4.1	Introduction.....	77
4.2	Experimental procedures	79
4.2.1	Materials	79
4.2.2	Instrumentation	81
4.2.3	Synthesis of PPFPA Homopolymer.....	82
4.2.4	Synthesis of PAM-PPFPA Diblock Copolymer	83
4.2.5	CTA End Group Removal from PAM-PPFPA Diblock Copolymer	83
4.2.6	Synthesis of ADT-GPLGL and ADT-GPLL Block Copolymers.	84
4.2.7	Preparation of Micelles	85
4.2.8	Critical Micelle Concentration (CMC).	85
4.2.9	Monitoring of Micelle Dissociation in Response to MMP-2.....	86

4.2.10	Determination of free leucine concentration in the micelle solution treated with MMP-2	86
4.2.11	Cell Culture.....	87
4.2.12	Cell Viability Assay in HT29 cells	87
4.2.13	H ₂ S release from the micelles in HT29 lysate with the WSP-1 H ₂ S fluorescent detection probe.....	87
4.2.14	H ₂ S Release by Fluorescent dye WSP-1 in HT29 Cells.....	87
4.2.15	Observation of H ₂ S Release by Fluorescent dye WSP-1 in HT29 cells.....	88
4.3	Results and Discussion	88
4.3.1	Synthesis of MMP-2 sensitive H ₂ S Donor Micelles (ADT-GPLGL and ADT-GPLL)	88
4.3.2	Preparation and Characterization of ADT-GPLGL and ADT-GPLL Micelles	91
4.3.3	Monitoring of micelle dissociation in the presence of MMP-2	92
4.3.4	H ₂ S Release from Micelles in the presence of MMP-2 enzyme in HT29 Cell Lysate	95
4.3.5	H ₂ S Release from Micelles in HT29.....	96
4.3.6	Anti-proliferative Effect of Micelles	99
4.4	Conclusion	100
5	Polymer surface dissection for isolation and identification of early colonizing bacteria on membrane surfaces	101
5.1	Introduction.....	102
5.2	Experimental Methods	105
5.2.1	Materials	105
5.2.2	Thiol Surface Functionalization.....	106
5.2.3	Preparation of Photodegradable Hydrogel.....	106
5.2.4	Functionalization of Hydrogel with Bio affinity Ligand (WGA).....	107
5.2.5	Transfer of Floccs from Membrane to Hydrogels	107
5.2.6	Degradation of Hydrogel and Extraction of Floccs.....	107
5.2.7	DNA Extraction	108
5.2.8	Identification with 16S rRNA Sequencing	109
5.3	Results and Discussion	109

5.3.1	DNA Quantification and 16S rRNA Analysis of Extracted Samples.....	109
5.4	Conclusion	115
6	Summary and Future Outlook	117
6.1	Design of stimuli-sensitive micelles for cancer-targeted drug delivery	117
6.1.1	ROS-sensitive approach.....	117
6.1.1.1	Future Work.....	118
6.1.2	MMP-2 sensitive approach	119
6.1.2.1	Future Work.....	120
6.2	Design of biofunctional and photodegradable hydrogels for isolation of microbes from membrane surfaces during early-stage biofouling.....	120
6.2.1	Future Work.....	121
References	123
Appendix A	-Supporting information from Chapter 2	142
Appendix B	-Supporting information from Chapter 3.....	154
Appendix C	-Supporting information for Chapter 4.....	158
Appendix D	-List of Abbreviation.....	163

List of Figures

Figure 2.1. Oxidation-sensitive polymers. (a) Poly(propylene sulfides) (PPS). ¹³⁷ (b) Poly (<i>N</i> -acryloylthiomorpholine). ¹³⁸ (c) Poly(1,4-phenyleneacetonedimethylene thioketal). ¹⁴² (d) Poly(esters) containing arylboronate ester moieties. ¹⁴¹	20
Figure 2.2. Oxidation of thioether to sulfoxide and sulfone	21
Figure 2.3. Polymeric micelles bearing thioether groups with fine-tuned oxidation sensitivities for site-specific drug release in cancer cells overproducing reactive oxygen species (ROS).	22
Figure 2.4. Oxidation of thioether model compounds by H ₂ O ₂ . (a) Chemical structures of TPAM, TMAM, and TPhAM. (b) Oxidation rate of the model compounds. H ₂ O ₂ consumption upon the addition of the model compounds was monitored in 100 mM PBS (pH 7.4) at 20°C by the iodide oxidation assay. Model compounds: 10 mM. H ₂ O ₂ : 1.0 mM. <i>n</i> =3.....	34
Figure 2.5. FT-IR spectra of thioether model compounds before and after H ₂ O ₂ treatment. The model compounds were incubated with 1 M H ₂ O ₂ at 20°C. FT-IR spectra were collected before (solid line) and after (dotted line) oxidation. (a) TPAM, (b) TMAM, (c) TPhAM. ..	36
Figure 2.6. Synthesis scheme of the thioether-bearing block copolymers. (a) AIBN, 1,4-dioxane, 60 °C, 24 h, (b) AIBN, 1,4-dioxane, 60 °C, 24 h, (c) AIBN, 1,4-dioxane, 70 °C, 24 h, (d) DMF, thioether amine, 50 °C, 24 h.....	37
Figure 2.7. TEM image of the micelles negatively stained with 2% uranyl acetate solution. (a) TP20, (b) TM20, (c) TPh20, (d) TP40, (e) TM40, (f) TPh40. Scale bars: 200 nm.	40
Figure 2.8. Dissociation of the thioether-bearing micelles upon oxidation. The micelles (0.9 mg/mL) were treated with H ₂ O ₂ (1 eq. to thioether groups) at 37°C. At the indicated time points, the size distribution of the micelles was measured by DLS. (a) TP20, (b) TM20, (c) TPh20, (d) TP40, (e) TM40, (f) TPh40. H ₂ O ₂ concentration: (a-c) 1mM, (d-f) 2 mM.	42
Figure 2.9. Dissociation of the thioether-bearing micelles in the presence of H ₂ O ₂ . (a) Chemical structure of the thioether/FITC-bearing micelles. (b) Dissociation of the thioether/FITC-bearing micelles upon oxidation as determined by fluorescence recovery of self-quenched FITC fluorophores. The TP/FITC (triangles), TM/FITC (diamonds) and TPh/FITC (squares) micelles (0.05 mg/mL in PBS (pH7.4, 100 mM)) were incubated with 100 mM	

H ₂ O ₂ at 37°C and the fluorescence intensity ($\lambda_{\text{ex}}=490$ nm, $\lambda_{\text{em}}=520$ nm) was measured at different time points. $n=3$	43
Figure 2.10. Dissociation of the thioether/FITC-bearing micelles in HepG2 cells. HepG2 cells were treated with (a,e) medium only, (b, f) TP/FITC, (c, g) TM/FITC, (d, h) TPh/FITC micelles for (a-d) 4 h and (e-h) 24 h in the absence/presence of the ROS scavenger <i>N</i> -acetylcysteine (NAC, 5 mM). An increase in the fluorescence intensity of the thioether/FITC micelles due to dissociation was observed by CLSFM. Left panel: Hoechst 33342 (nucleus, blue) and FITC (yellow), Right panel: DIC. Scale bars: 20 μm . (i,j) Intracellular fluorescence intensity in HepG2 cells treated with thioether/FITC-bearing micelles. The CLSFM images were analyzed to determine fluorescence intensity within HepG2 cells nontreated (NT) and treated with TP/FITC, TM/FITC, and TPh/FITC micelles for (i) 4 and (j) 24 h in the absence (open columns) or presence (filled columns) of NAC. ** $p<0.01$, *** $p<0.001$, n.s. $p>0.05$ ($n=3$).	45
Figure 2.11. Characterization of Dox-loaded thioether-bearing micelles. (a) Dox loading for the different micelle solutions. Dox was mixed with thioether-bearing micelles (Dox:micelles = 1:5 by weight) in NMP and added dropwise to water to prepare Dox-loaded micelles. Free Dox was removed from the micelles by ultrafiltration and quantified by UV-Vis spectroscopy to determine the Dox loading capacity (Dox/micelles w/w%). Gray bar: TP20, TM20 and TPh20, White bar: TP40, TM40 and TPh40. $n=3$. (b-d) Dox release in response to H ₂ O ₂ . The thioether-bearing micelles (b), TP40, (c) TM40, (d) TPh40 loaded with Dox (Dox concentration: 4 mM) were incubated in the absence (grey circles) or presence (white circles) of 5 mM H ₂ O ₂ at 37°C. $n=3$	47
Figure 2.12. Cytotoxicity of the Dox-loaded micelles in (a) HepG2 cells and (b) HUVECs. Cells were cultured in the presence of Dox and Dox-loaded micelles for 2 d. Cell viability was measured by MTT assay. $n=3$	48
Figure 2.13. Intracellular distribution of Dox in HepG2 cells. Cells were cultured in the presence of (a) Dox and the Dox-loaded micelles (b)TP40, (c) TM40 and (d) TPh40. After culturing for 4 h, cells were observed by CLSFM. Dox concentration: 0.5 μM . Left panel: Hoechst 33342 (nucleus, blue), center: panel Dox (red), Right panel : Merged. Scale bars: 20 μm ..	51
Figure 2.14. Colocalization analysis of Dox with the cell nucleus (Hoechst 33342) of HepG2 cells. Person's correlation coefficient (PCC) was calculated from the CLSFM 3D image	

slices obtained at the indicated time points. Free Dox (circles), Dox-loaded micelles. TP40 (triangles), TM40 (diamonds) and TPh40 (squares). $n=3$	52
Figure 3.1. H ₂ S donor micelles bearing oxidation-sensitive thioether group for targeted delivery of H ₂ S in cancer cells with elevated levels ROS (courtesy of Hasegawa and Radaha).....	59
Figure 3.2. Synthesis Scheme of the ADT-TPM and ADTM block copolymers. (a) AIBN, 1,4-dioxane, 60 °C, 24 h (b) AIBN, 1,4-dioxane, 60 °C, 24 h (c) AIBN, 1,4-dioxane, 70 °C, 24 h (d) DMF, ADT-NH ₂ ·TFA and TEA at 50 °C for 24 h followed by addition of TP-NH ₂ at 50 °C for 24 h.....	68
Figure 3.3. Characterization of ADT-TPM and ADTM micelles. (a-b) Size distribution by DLS, (c-d) TEM images of micelles negatively stained with 2% uranyl acetate solution. (a,c) ADT-TPM micelles, (b,d) ADTM micelles. Scale bar: 200 nm.....	69
Figure 3.4. Dissociation of ADT-TPM (squares) and ADTM (circles) micelles upon oxidation by H ₂ O ₂ . The micelles were treated with 100 mM H ₂ O ₂ at 37°C and change in the scattered light intensity of micelles was monitored by DLS (a) Change in scattered light intensity, (b) FT-IR spectra of ADT-TPM micelles before (solid line) and after (dotted line) treatment with H ₂ O ₂ . Red line indicates sulfoxide vibration. $n=3$	71
Figure 3.5. H ₂ S release in HT29 cell lysate. ADT-TPM and ADTM micelles were added to HT29 cell lysate containing WSP-1 H ₂ S detection probe in the absence/presence of 100 Mm H ₂ O ₂ . Fluorescence intensity ($\lambda_{ex}=465$ nm, $\lambda_{em}=515$ nm) was monitored at indicated time point. ADT-TPM (+) H ₂ O ₂ : circles, ADT-TPM (-) H ₂ O ₂ : triangles, ADTM (+) H ₂ O ₂ : diamonds, ADTM (-) H ₂ O ₂ : squares. $n=3$	72
Figure 3.6. H ₂ S release in HT29 cells. Cells were cultured in the presence of ADT-TPM (circles) and ADTM (squares) micelles, ADT donor (diamonds), and medium as a control (triangles) at indicated time points (ADT Concentration: 50 μ M). Cells were washed and incubated prior with WSP-1 H ₂ S detection dye for 30 min. Fluorescence intensity ($\lambda_{ex}=480$ nm, $\lambda_{em}=520$ nm) was monitored at indicated time point. $n=3$	73
Figure 3.7. Cell viability of ADT donor (triangles), ADTM (circles) and ADT-TPM (squares) micelles in (a) HT29 and (b) HUVEC cells. Cells were cultured in the presence of micelles for 5 d or 2 d. Cell viability was measured by MTT assay. $n=3$	74
Figure 4.1. Polymeric micelles bearing MMP-2 cleavable peptide motifs for targeted delivery of H ₂ S in cancer cells over-expressing MMP-2 enzyme (courtesy of Hasegawa and Radaha).	79

Figure 4.2. Synthesis Scheme of the ADT-GPLGL and ADT-GPLL block copolymers. (a) AIBN, 1,4-dioxane, 60 °C, 24 h (b) AIBN, 1,4-dioxane, 60 °C, 24 h (c) Tris(trimethylsilyl)silane, AIBN, 1,4-dioxane, 70 °C, 24 h (d) DMF, GPLGL-NH₂·TFA/GPLL-NH₂·TFA, and TEA at 50 °C for 24 h followed by addition of ADT-NH₂·TFA and TEA at 50 °C for 48 h 89

Figure 4.3. Characterization of ADT-GPLGL and ADT-GPLL micelles. (a-b) Size distribution by DLS, (c-d) TEM images of micelles negatively stained with 2% uranyl acetate solution. (a,c) ADT-GPLGL micelles, (b,d) ADT-GPLL micelles. Scale bar: 200 nm. 92

Figure 4.4. Dissociation of ADT-GPLGL (circles) and ADT-GPLL (squares) micelles upon enzymatic cleavage. The micelles were treated in the (a) presence or (b) absence of 43.6 nM MMP-2 enzyme at 37°C and change in the scattered light intensity of micelles was monitored by DLS. *n*=3. 93

Figure 4.5. Cleavage of the peptide conjugated to ADT-GPLGL (circles) and ADT-GPLL (squares) micelles in response to MMP-2 enzyme. The micelles were incubated in the (a) presence or (b) absence of 43.6 nM MMP-2 enzyme at 37°C. Fluorescamine assay was used to detect leucine amino group from the N-terminus of peptide resulting from cleavage by MMP-2 enzyme. Fluorescence intensity (λ_{ex} =390 nm, λ_{em} =475 nm) was determined at indicated time points. *n*=3..... 95

Figure 4.6. H₂S release in HT29 cell lysate. ADT-GPLGL and ADT-GPLL micelles were added to HT29 cell lysate containing WSP-1 H₂S detection probe in the absence/presence of 43.6 nM MMP-2 enzyme. Fluorescence intensity (λ_{ex} =465 nm, λ_{em} =515 nm) was monitored at indicated time point. ADT-GPLGL (+) MMP-2: circles, ADT-GPLGL (-) MMP-2: triangles, ADT-GPLL (+) MMP-2: diamonds, ADT-GPLL (-) MMP-2: squares. *n*=3 96

Figure 4.7. H₂S release in HT29 cells. Cells were cultured in the presence of ADT-GPLGL (circles) and ADT-GPLL (squares) micelles, ADT donor (diamonds), and medium as a control (triangles) at indicated time points (ADT Concentration: 50 μ M). Cells were washed and incubated prior with WSP-1 H₂S detection dye for 30 min. Fluorescence intensity (λ_{ex} =480 nm, λ_{em} =520 nm) was monitored at indicated time point. *n*=3..... 97

Figure 4.8. Observation of H₂S release from ADT-GPLGL and ADT-GPLL micelles (ADT concentration: 25 μ M) in HT29 cells. HT29 cells were pre-treated with Hoechst 33342

followed by WSP-1 H ₂ S detection dye and then cultured in the presence of micelles. After culturing for 8 h, cells were observed by CLSFM. Scale bar: 20 μm.....	98
Figure 4.9. Cell viability of ADT-GPLGL (circles), ADT-GPLL (squares) micelles, and H ₂ S donor (ADT) (triangles) in HT29 cells. Cells were cultured in the presence of micelles for 5 d. Cell viability was measured by MTT assay. <i>n</i> =3.....	99
Figure 5.1. (A) Preparation of hydrogel by thiol-acrylate addition and functionalization with bioaffinity ligand (WGA). (B) Schematic of the PSD method. (i) PVDF Membranes are contacted with wastewater solutions and cell attachment to the surface is characterized using an optical microscope. (ii) The substrate is then contacted with first layer of pre-formed hydrogel functionalized with bacteria affinity ligands for flocs transfer. (iii) The hydrogel is removed from the membrane surface followed by addition of a second pre-formed hydrogel (no bioaffinity ligand) for clean extraction (iv) Cells of interest are sectioned from hydrogel base after exposure to patterned UV light (v) Sectioned cell (s) are lifted off from the hydrogel and extracted for 16S rRNA analysis. (C) Reaction scheme for functionalization of hydrogel with bioaffinity ligand by maleimide-thiol coupling and <i>N</i> -Hydroxysuccinimide ester-amine reaction.....	105
Figure 5.2. Brightfield microscope images of hydrogels during extraction of targeted flocs at varied time points. Hydrogels were unfunctionalized or functionalized with WGA then extracted using (A) a 45 mm diameter ring pattern or a (B) 40,000 mm ² open rectangle pattern.	110
Figure 5.3. DNA yield and quality quantified by Nanodrop at varying floc sizes. (A) Flocs were extracted from control hydrogel (without affinity ligand) and DNA was isolated in the absence of carrierRNA (B) Flocs were extracted from control hydrogel (without affinity ligand) and DNA was isolated in the presence of carrierRNA. (C) Flocs were extracted from WGA-functionalized hydrogel and DNA was isolated in the presence of carrierRNA. Floc sizes were determined by ImageJ. <i>n</i> =3	112
Figure 5.4. (A) DNA yield (bar chart) and quality (line chart) quantified by the Nanodrop at varying floc sizes. Blue bars and lines: Flocs isolated from control (without affinity ligand) hydrogel. Pink bars and lines: Flocs isolated from WGA-functionalized hydrogel. Floc sizes were determined by ImageJ (<i>n</i> =3). (B) Comparison of DNA yield quantified by Nanodrop absorbance and Qubit fluorescence at varying floc sizes.	113

Figure 5.5. Heat map showing distribution of family level bacteria ($\geq 1\%$ relative bacteria abundances) at varying floc (group) sizes (arranged in increasing order) accompanied by corresponding microscopic images (B-F). (B) Group 1: 2000-15000 μm^2 (C) Group 2: 15000-30000 μm^2 (D) Group 3: 30000-40000 μm^2 (E) Group 4: 40000-50000 μm^2 (F) Group 5: 50000-60000 μm^2 114

Figure 5.6. Distribution of corresponding bacterial phyla with $\geq 1\%$ relative bacterial abundance at varying floc (group) sizes (arranged in increasing order). Group 1: 2000-15000 μm^2 , Group 2: 15000-30000 μm^2 , Group 3: 30000-40000 μm^2 , Group 4: 40000-50000 μm^2 , Group 5: 50000-60000 μm^2 115

List of Tables

Table 1.1: Common H ₂ S donors and their known release mechanisms as well as related bioactivities	6
Table 2.1. FT-IR characterization and charge analysis of thioether model compounds.....	35
Table 2.2. Characterization of the thioether-bearing block copolymers.....	38
Table 2.3. LC ₅₀ values of Dox and the Dox-loaded micelles in HepG2 cells and HUVECs as determined by MTT Assay.	49

Acknowledgements

Pursuing a doctorate degree was not an easy decision. I am deeply grateful to my former mentor, Dr. Michael Wales, who saw something in me, and motivated and encouraged me to pursue this path. Being a Ph.D. student at Kstate has been a challenging, but fun experience. Throughout the last few years, I have come across many people who have actively been a part of my journey in supporting and encouraging me.

First and foremost, I would like to express my highest gratitude to my former advisor Dr. Urara Hasegawa and current advisor, Dr. Ryan Hansen and Dr. Jennifer Anthony, all who have been a tremendous mentor to me. I am especially thankful to Dr. Jennifer Anthony, Dr. James Edgar, and Dr. Ryan Hansen for believing in me and giving me the opportunity to successfully complete my doctorate degree here at Kstate. Your guidance, advice, and support are highly appreciated, and it has helped me shaped my research trajectory and career path.

I would also like to thank my former and current colleagues, Dr. Leonardo Garro Mena, Dr. Jason Xu, Marques Jozefowicz, Mohammad Mahmoud, Amanda Bell, Clint Barb, Christian Willcutt, Bayley Witcher-Goscha, Niloy Barua, Niloufar Fattahi, Dr. Mohammadali Masigol, my friends Narges Manavi and Abdul Hafiz, faculties, and staffs at the Tim Taylor Department of Chemical Engineering. I have been blessed with amazing people around me, making my journey here at Kstate more meaningful and special.

Most importantly, I would like to express my special thanks to my family and my husband. Words are not enough to express how grateful I am to you, Mom and Dad, my brothers, and my husband, for your constant support and unconditional love in chasing the lion in the pit. You have all shaped and molded me to be the person I am today, and I am truly grateful to God for this blessing. Lastly, I would like to thank my international family (The Kelly-Kuwata's, Hai Xu, Sun and Dennis, Seon Joo) and coffee friends (Leonard, Tom and Linda, Nick, Dave, Jim and Susan, Rolley, and Kirsten) for making me feel at home and for the countless advice.

Dedication

This thesis is dedicated to my God Almighty

To my dad and mom

Radaha Krishnan M Kalimuthu and Carol Lim Nyuk Fong

To my beloved husband

Andrew Thomas Craigo

Without whom this day would never come

1 Introduction

1.1 Polymers in Daily Life

Polymers (natural, synthetic, or pseudo-synthetic) are a versatile class of advanced materials found in almost every material in our daily life and are an emerging cornerstone for a variety of applications (biomedical, water treatment, textile). Synthetic polymers particularly, first developed in the early 1960s during the Second World War offer several advantages over natural polymers as they can be designed, synthesized, and modified to afford various structures with desired physical and chemical properties.^{1,2} With the remarkable advancement and vast toolbox of polymer chemistry and post-polymerization modification techniques in the last few decades, polymer scaffolds with increasing complexity and functionality can be generated to improve material performances. In fact, functional groups can be selectively installed at predefined points within a polymer chain affording self-regulating and life-mimicking properties for a variety of applications. **Chapter 1** of this thesis reviews the use of polymeric materials as nanocarriers in the drug delivery field and as interfaces for the isolation of microbes while simultaneously highlighting the challenges associated with their successful translation.

1.2 The concept of nanomedicine

Ever since the modern era discovery of nanoscience by pioneer physicist Richard P. Feynman with the concept of manipulation of matter at atomic level³, the term “nanotechnology” famously coined by scientist Norio Taniguchi has found its way to various applications in creating new materials with improved properties at the nanometer scale, including medicine.⁴ The use of nanotechnology in medicine, often referred to as “nanomedicine”, is where materials ranging in size from 1-100 nm are investigated for possible preventive, diagnostic, and therapeutic applications.⁵ Indeed, nanomedicine offers several advantageous features including versatile

surface modifications due to large surface-to-volume ratio, the ability to incorporate payloads of both water-soluble/insoluble molecules, and the tuning of pharmacokinetic or pharmacodynamics of the active components.

The first nanomedicine approved by the United States Food and Drug Administration Agency (FDA) in 1995 called DOXIL[®], composed of polyethylene glycol (PEG) liposomal doxorubicin (DOX), a clinical anticancer drug was used for the treatment of cancer. The use of DOXIL[®], exhibited a significant decrease in DOX-related cardiotoxicity with an extended overall pharmacokinetic profile compared to free DOX.⁶ Following this, several other nanomedicines made of different materials such as protein (Abraxane[®]), crystals (Emend[®]), lipid (Abelcet[®]), inorganic materials (Feridex[®]), and polymer (Genexol[®]) made their way to successful clinical translation cite.^{7,8} To date, diverse organic (liposomes, dendrimers, lipids, carbon nanotubes, polymers) and inorganic (metals) nanomaterials have been extensively studied as nanocarriers in nanomedicine for the delivery of therapeutics. These nanocarriers have shown immense potential such as prolonging drug circulation time, improving drug bioavailability, reduced drug side effects, controlled drug release profile, and high specificity compared to conventional drugs. The use of nanocarriers drugs, therefore, facilitates the transport of conventional free drugs to intended sites with effective therapeutic concentrations by preventing degradation, avoiding unspecific interactions, and clearance from the body.⁹

1.2.1 Polymeric Nanomaterials in Therapeutics

Amongst the commonly studied nanocarriers, polymeric nanocarriers (nanocapsules, nanogels, dendrimers, micelles) have shown great potential as drug delivery vehicles due to their biocompatibility, biodegradability, and versatility.¹⁰ In particular, polymeric micelles (PMs), first developed in 1980s are distinctly advantageous as nanocarriers in cancer therapy due to their

ability to improve the aqueous solubility of a variety of hydrophobic anti-cancer drugs, facile preparation methods, biocompatibility, and tumor targetability.¹¹⁻¹⁴ By definition, PMs are nano-sized colloidal particles comprised of amphiphilic polymers that self-assemble in aqueous environment.¹⁴ The smaller and narrower size distribution (10-100 nm) of PMs has enabled its prominent accumulation in solid tumor sites by the enhanced permeability and retention (EPR) effect, a passive targeting strategy discovered by Matsumura and Maeda based on the high permeability of tumor vasculature resulting from unaligned endothelial cells, lack of smooth muscle layer, and poor lymphatic drainage.^{15,16} The hydrophilic shell of PMs provides steric stability and reduces nonspecific uptake by the reticuloendothelial systems (RES), thus prolonging circulation time in the body.¹⁷ Additionally, the hydrophilic shell allows for active targeting by conjugation of the surface with various targeting moieties (antibody, receptor ligands, cell-penetrating peptides) for targeted delivery to tumor sites.¹⁸

The first PM formulation (Genexol[®]-PM) based on the block copolymer mPEG-*b*-poly(D,L-lactic acid) loaded with paclitaxel (PTX) in the core was approved for the treatment of a variety of cancer.¹⁹⁻²¹ Genexol[®]-PM demonstrated an increase in antitumor efficacy and a threefold increase in the maximum tolerated dose compared to free PTX in pre-clinical studies. Since then, it is worth nothing that several drug-loaded PM formulations (SP1049C, NK911, NK105) are under clinical investigation.^{22,23} To improve stability during circulation and prevent the pre-mature release of drugs, a newer generation of PM-formulation (NC-6300, NK012) with the chemical coupling of the drug to the polymer chains via a reversible bond or chemical crosslinking of the core or the shell instead of physical loading of drugs has been explored as an alternative.^{22,23} Kataoka and colleagues reported a modification of the existing PM formulation (NK911, covalently and physically loaded DOX) by covalently conjugating DOX or epirubicin to the carboxylic acid

groups of the block copolymer backbone via a hydrazone bond, enabling drug release upon exposure to pH (pH <5) stimuli.²⁴ The modified PM formulation (NC-6300) showed a substantially prolonged half-life (4 h) of epirubicin while free epirubicin was cleared in 0.4 h in male Wistar rats. In mice bearing breast tumors, treatment with NC-6300 resulted in a 74 % accumulation of free epirubicin in tumor tissues, indicating the efficient release of epirubicin in tumors.²⁵

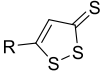
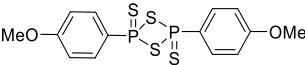
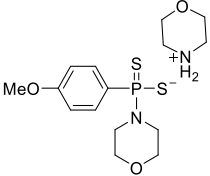
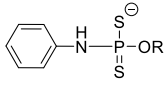
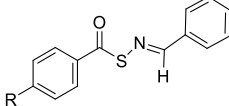
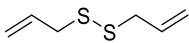
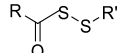
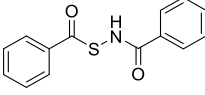
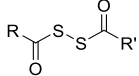
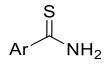
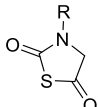
1.2.2 Hydrogen Sulfide

Hydrogen sulfide (H₂S), a poisonous gas with a characteristic rotten-egg odor also known as a gaseous signaling molecule along with other gaseous signaling molecule such as nitric oxide (NO) and carbon monoxide (CO) stands to benefit greatly from the use of polymeric nanomaterials due to its versatility of modification, ability to enhance the solubility of poorly water-soluble drugs, and the tunability of the pharmacokinetic properties to achieve targeted delivery. Over the past few years, numerous studies have revealed that H₂S plays an important role in many physiological and pathological processes in the human body. Abe and Kimura were the first to report on the possible physiological function of H₂S in 1996.²⁶ Following this, H₂S has been recognized as a gaseous signaling molecule, with its biological activities being extensively studied. The endogenous production of H₂S is ubiquitously performed by a series of enzymatic desulfhydration of cysteine, catalyzed by cystathionine γ -lyase (CSE), cystathionine β -synthase (CBS), and 3-mercaptopyruvate sulfur transferase (3-MST). H₂S can also be synthesized from methionine instead of cysteine, through the trans-sulfuration pathway.²⁷ CSE is mainly expressed in the liver and cardiovascular system²⁸ whereas CBS is heavily expressed in the brain and central nervous system.²⁹ Although its biological mechanism is not fully understood, H₂S exerts a host of

regulatory functions such as neuromodulatory,³⁰ vasodilatory,³¹ anti-apoptic,³² proangiogenic,³³ anti-oxidative,³⁴ cytoprotective,³⁵ and anti-cancer.^{36,37}

With the discovery of the diverse biological significance of H₂S, the potential for H₂S-based therapy has attracted growing attention. Due to its volatility, fast diffusion and short half-life in the body, the controlled delivery of H₂S is extremely challenging, especially with the toxic nature of H₂S. As an alternative, sulfide salts such as sodium hydrosulfide (NaHS) and sodium sulfide (Na₂S) are commonly explored and utilized in a majority of studies on H₂S biology. In aqueous solutions however, the instantaneous release of H₂S from sulfide salts results in the acute elevation of local H₂S concentration, causing side effects. To overcome this issue, a number of organosulfur compounds that release H₂S through several mechanisms such as hydrolysis or reactions with thiol-containing compounds have been developed as shown in **Table 1** with known bioactivities. These organosulfur donors include Lawessons's reagent derivatives such as GYY4137,³⁸ anethole dithiolethione (ADT) derivatives such as ADT-OH³⁹ and AP39,⁴⁰ polysulfides such as diallyl trisulfide (DATS),^{41,42} *N*-(benzoylthio)benzamides (NSHD1), arylthioamides (Thiobenzamides),⁴³ *S*-aroylthiooximes (SATO),⁴⁴ and thiocarbamates.⁴⁵ In an effort to achieve site-specific delivery and enable better spatiotemporal control of H₂S release, several enzymes,⁴⁶ light,⁴⁷ pH triggered,⁴⁸ and ROS triggered donors^{49,50} have also been reported by different groups as it enables a better spatiotemporal control of H₂S release. Zhao and Pluth reported a cell-specific stimulus-responsive H₂S donor where ROS, which is overproduced under many pathological conditions, induced the release of carbonyl sulfide (COS) that is subsequently converted to H₂S by the action of ubiquitous enzyme carbonic anhydrase.⁵⁰ This approach to delivering H₂S with ROS is the first example of a disease-specific stimulus, which could be utilized to deliver H₂S in a specific manner to diseased tissues under oxidative stress.

Table 1.1: Common H₂S donors and their known release mechanisms as well as related bioactivities

Release Mechanism	H ₂ S Donor	Structure	Bioactivity
Reduction (Enzymatic)	Dithiolethiones		Anti-inflammation, Anti-cancer
Hydrolysis	Lawesson's reagent		Anti-inflammation, Anti-cancer, Vasodilation
	GY4137		Anti-inflammation, Anti-cancer, Ion channel modulation,
	Phosphorodithiotes ²³		Anti-inflammation, Anti-oxidative
	S-Aroylthiooximes (SATO)		Anti-cancer
	Polysulfides (Diallyl Trisulfide, DATS)		-
Thiol-triggered	Acyl-protected Perthiol		Cardioprotective
	N-(Benzoylthio)benzamide (NSHD1)		Cardioprotective
	Dithioperoxyanhydrides		Vasodilation
	Arylthioamides (Thiobenzamides)		Vasodilation
Thiol-triggered+ Enzymatic	N-thiocarboxyanhydrides (NTAs)		Angiogenesis

Despite the promising results through the discovery of these small H₂S donors, there are still several issues that needs to be addressed for H₂S based therapies including poor water solubility, relatively fast H₂S release under physiological conditions, the toxicity of the donors as well as their decomposition products, and high renal clearance rates resulting in low therapeutic efficiency. As such, the use of polymeric nanomaterials for the delivery of H₂S presents an opportunity to address the issues associated with small H₂S donors and sulfide salts. In the field of H₂S delivery, the use of polymeric nanomaterials, especially PMs has enabled the controlled release of H₂S, reduced toxicity, and much higher biological activities relative to the small-molecule H₂S donors. Successful stories include a polymeric H₂S donor micelles containing an anethole dithiolethione (ADT) moiety in the micellar core reported by the Hasegawa group, capable of protecting rat cardiomyocytes from ischemic cell death, owing to the sustained release profile of H₂S compared to the donor alone (ADT-OH).⁵¹ Additionally, the group of Matson reported a *S*-aroylthoosime (SATO) functionalized block copolymer micelles (BCM) exhibiting a slower cysteine-triggered H₂S release compared to the donor SATO. Furthermore, the micelles significantly reduced the survival of HCT116 colon cancer cells compared to Na₂S, SATO, and GYY4137, but was well tolerated by immortalized fibroblasts (NIH/3T3 cells).⁵²

1.2.3 Challenges for Clinical Translation

1.2.3.1 Biological Barriers

When introduced into the blood circulation system, the fate of the bio-distribution of most nanoparticles depends heavily on the potential formation of protein corona upon contact with plasma proteins.^{53,54} The formation of protein corona often modifies the interaction of nanoparticles with cells and changes its pharmacokinetic behavior, therefore preventing its recognition and further leading to the loss of targeting ability. Additionally, it has been recognized

that the physico-chemical properties (stability, size distribution, morphology, and surface properties) of nanoparticles significantly influences the extent and constituent of protein corona formation and thereby its pharmacokinetic profile as well as uptake within the blood compartment. The loss of targeting ability causes nanoparticles to accumulate mostly in the liver and spleen due to opsonization and uptake by the mononuclear phagocytic system (MPS).⁵³ For example, Salvati et al. reported a loss in targeting specificity of a transferrin receptor targeting ligand functionalized silica nanoparticle in A549 lung cancer cells. Despite the use of polyethylene glycol (PEG), which has been shown to reduce the formation of the protein corona, the targeting ability with corresponding receptors on A549 cells were lost upon exposure to biological serum.⁵⁵

While a handful of PM formulations are being investigated in the clinical stages, the complex biological environment remains a huge challenge especially in retaining the stability of PM upon administration. The adsorption of protein onto the corona and dilution in the bloodstream disrupts the stability of the micellar structure. When the concentration is below the critical micelle forming concentration (CMC), micelles can disintegrate causing premature drug loss and compromising its blood circulation time through opsonization and deposition within the spleen and liver. In addition, the unfavorable drug distribution reduces the therapeutic efficacy of the encapsulated drugs and causes significant toxicity in off-targets sites. As an example, a significant distribution in off-target sites were observed for NC-6004, a successful clinical-stage PM formulation for cisplatin with prolonged circulation times. NC-6004 exhibited only 10 % of the injected dose is taken up in the tumor, and the rest accumulating in the liver and spleen at high levels. In another example, the micellar drug Taxotere® is removed from the blood circulation quickly once intravenously injected.⁵⁶ With BCPM formulations, it is similarly recognized that properties such as stability, size distribution, and surface properties impact their biodistribution

and pharmacokinetic profile.^{57,58} For example, the larger block copolymer micelles (BCM) (60 nm) resulting from varying block lengths of PEG and poly(caprolactone) (PEG-*b*-PCL) was less susceptible to plasma clearance with a much longer circulation half-life (29 h) compared to the smaller BCM (25 nm) (circulation half-life of 13 h). However, functionalization of the same BCM surface with epidermal growth factor (EGF) had no effect on the clearance via MPS.⁵⁹ This again highlights the unexpected consequences in a complex biological environment due to recognition by MPS on the bio-distribution and pharmacokinetic behavior of most nanoparticles.

1.2.3.2 Complex Tumor Microenvironment

1.2.3.2.1 Tumor-associated cellular heterogeneity

Effective delivery of anti-cancer agents has been hindered tremendously by the overall complexity that exists in tumors. In solid tumor masses, the tumor microenvironment (TME) is highly heterogeneous comprising of extracellular matrix (ECM), stromal cells (fibroblasts, pericytes, blood network, lymphatic network, mesenchymal stromal cells), and immune cells along with distinct physiological conditions such as hypoxia, acidosis, interstitial pressure gradients, increased production of enzymes such as matrix metalloproteinases (MMPs), and elevated levels of reactive oxygen species (ROS).⁶⁰ After being cleared from circulation, nanomedicine has to extravasate from the dense network of tumor-associated cells (fibroblasts, endothelial cells, pericytes) that provide structural support and generate neovascularization for cancer growth to reach the tumor site, hindering efficient extravasation.⁶⁰ The targeting of tumor vasculature however was successfully demonstrated by Zhang et al with the design of $\alpha v \beta 3$ integrin (found in tumor blood vessels and is associated with angiogenesis and malignant tumor growth)-targeting peptide arginine-glycine-aspartic acid (RGD)-functionalized poly(ethylene glycol)-*b*-poly(*d,l*-lactide) (PEG-PLA) PMs. In an *in vivo* model of B16-F10 melanoma-bearing mice, the micelles

loaded with chemically conjugated DOX or physically loaded combretastatin A4 showed superior destruction of the tumor vasculature and reduction of tumor cell proliferation with low side effects.⁶¹

On the other hand, tumor-associated immune cells (T-cells, B-cells, Natural Killer Cells, macrophages, dendritic cells, and neutrophils) play a diverse role in the establishment, maintenance, and progression of tumors at various stages and can either be pro- or anti-tumorigenic.⁶² The chronic exposure of the TME to inflammatory cytokines typically results in the anergy of these immune cells paired with a severe lack of anti-tumor response.^{63,64} In fact, macrophages with M1 and M2 phenotypes are associated with a large portion of immune cells known for aggressive and fast-growing tumors due to their phagocytic nature, enhanced cytotoxicity, promotion of vascularization, and role in the upregulation of pro-inflammatory cytokines, ROS, and collagen and MMPs in the ECM.^{65,66} Therefore, their macrophages are known to be a sinkhole in trapping and preventing the extravasation of nanocarriers to tumor sites, making them a unique target for cancer therapy. In this regard, R837, an FDA-approved immunostimulant that binds TLR7 overexpressed in the endosome/lysosome of macrophages and has the potential to suppress tumor growth by facilitating infiltration of cytotoxic T cells were loaded into PMs to selectively target tumor-associated macrophages in breast cancer. The combinational treatment of the tumor-macrophage targeted PM, which stimulated the maturation of tumor-associated macrophage and triggered an anti-tumor immune response together with DOX-loaded PM, which significantly induced cell death exhibited a synergistic combination of immunotherapy and chemotherapy that was promising against malignant cancer.⁶⁷

1.2.3.2.2 Tumor physiology (Hypoxia and Acidosis)

The dynamic changes in the complex TME and abnormal growth of tumor vasculature resulting in insufficient diffusion and perfusion in the proliferating tumor tissues leads to two main metabolic issues, hypoxia and acidosis. Both the overconsumption of oxygen by rapidly proliferating tumor cells and abnormal tumor vasculature causes a pathological condition called hypoxia, defined as the shortage of oxygen.⁶⁸⁻⁷⁰ Due to the larger distance from the core of the solid tumor to blood vessels ranging from 70-150 μm , the diffusion of oxygen by rapidly proliferating cells is hindered thereby causing an oxygen tension varying from <0.1 mmHg (anoxia) to 15 mmHg.^{71,72} Consequently, tumor hypoxia suppresses apoptosis and immune reactivity and promotes the release of various growth factors involved in angiogenesis by neighboring cells, hence increasing its invasiveness and metastasis which is linked to drug resistance.⁷³ On the other hand, compared to physiological pH_e of 7.2-7.4, the extracellular matrix of malignant tumors has been reported to be slightly acidic with a pH_e of 6.5-6.9 and causes tumors to be more metastatic and resistant to various anti-cancer drugs.⁷⁴ Due to the abnormal tumor vasculature and hypoxic conditions present in TME, tumor cells obtain energy from the oxygen-independent glycolysis also known as the Warburg effect where a significant increase in glucose uptake and fermentation of glucose to lactate is observed. This increase in uptake and conversion to lactate leads to an increase in production and excretion of H^+ ions.^{75,76} To maintain the intracellular pH at physiological levels, the excess protons are fluxed to the extracellular environment, resulting in a slightly acidic pH (6.5-6.9). This pH gradient limits the efficient delivery of drugs as it alters the charge of the carrier and drug, further preventing its safe journey to the tumor site.

1.3 Polymeric Interfaces for Capture and Detection of Microbes

Pathogenic microbes such as *Escherichia coli* O157:H7, *Salmonella*, *Pseudomonas aeruginosa*, *Staphylococcus aureus*, *Listeria monocytogenes*, *Legionella parisiensis* and *Campylobacter* are reported to be a serious threat to human life and health where infections occur through direct or indirect contact by air, food, medical equipment, and even drinking water.^{77,78} Bacterial-related contamination in the food industry alone accounted for roughly 47.8 million illnesses in the United States every year.⁷⁹ In industry, biofilm formation (biofouling) has been linked to degradation and corrosion of pipes and heat exchangers,⁸⁰ contamination of food products,⁸¹ medical implant infection,⁸² and reduction in membrane life in most water-treatment plants,⁸³ causing enormous financial expenditure and burden. Today, implant-related infections due to biofilm formation and contamination remain significantly high with patients, typically requiring revision surgery in the case of a severe infection.^{84,85} While antibiotics have been commonly used to treat bacterial infections, antibiotic resistance has become a serious, alarming issue.^{86,87} Upon the formation of biofilm, bacteria embedded within the biofilm are protected by self-secreted extracellular polymeric substances (EPS) and eventually become resistant to host immune responses as well as antibiotics.^{88,89} Therefore, there is an urgent need to detect pathogenic microbes in an early and precise manner to develop effective tools to combat bacterial infections and biofilm formation. The commonly used or “gold standard” method to detect and quantify bacteria is based on culturing, which includes pre-enrichment, plating, culturing, biochemical detection, and serological validations.⁹⁰ Despite providing quantitative information in a quick and cost-effective manner, culture-based methods bias the analysis on the most culturable isolates, and are time-consuming, labor intensive, and not sensitive enough, making them impractical.^{91,92} Modern molecular-based techniques (polymerase chain reaction (PCR)) and immunological

assays (enzyme-linked immunosorbent assay (ELISA)) have been developed to overcome the limitations of the culture-based methods by providing rapid results and increased detection sensitivity.⁹³⁻⁹⁵ These methods however are expensive, require significant sample preparation, and have high risk of contamination.⁹⁵ The abundance of limitations, therefore, motivates the need for culture-free and non-destructive methods to isolate and characterize microbes.

Synthetic polymeric materials whether in the micro, macro, or nano- sized range are used in a broad range of applications including biosensors/interfaces to capture, isolate, and detect microorganisms.⁹⁶⁻⁹⁹ Given the diverse palette of synthesis and fabrication techniques, synthetic polymers can be produced with a variety of functionalities with specific chemical, biological, and physical features to selectively interact or capture microorganisms by surface modification with bioaffinity molecules (antibodies, nucleic acid, peptides, enzymes, carbohydrates), or incorporation of anti-fouling and anti-bacterial properties. In particular, synthetic polymeric materials have been considered a significantly advantageous support/template for the covalent immobilization of lectins, a biomolecule/affinity probe for the capture of bacteria.^{100,101} Lectins are a group of carbohydrate-binding proteins that can interact specifically with carbohydrates through van der Waals forces, hydrophobic interactions, hydrogen bonding, or metal coordination in a highly reversible and non-covalent manner.^{102,103} Additionally, lectins show higher resistance in extreme conditions against denaturation, can be functionalized with higher densities per unit area due to their smaller molecular size, achieves rapid agglutination with bacteria, and are less expensive.¹⁰⁴⁻¹⁰⁶ Some of the commonly used lectins, each with different degrees of affinity for the capture and isolation of microbes includes *Wheat Germ Agglutinin* (WGA), *Concanavalin A* (Con A), *Peanut Agglutinin* (PNA), *Maackia Amurensis* (MAL), *Elex Europaeus Agglutinin* (UEA), and *Lens Culinaris Agglutinin* (LCA).^{107,108}

Of the numerous synthetic polymeric material platforms, hydrogels which are hydrophilic polymers with a three-dimensional (3D) network structure, have high water content, nutrient permeability, and excellent biocompatibility has emerged as a promising interface for the capture, detection, and treatment of bacterial infections.^{109–111} With the highly tunable physicochemical properties and versatile functionalization techniques, hydrogels, especially light-responsive hydrogels, have been widely modified to confer anti-microbial properties in the drug delivery and tissue engineering field to combat bacterial infection and assist in wound healing.^{97,112–117} As light offers control of wavelength, intensity, and irradiation time, it enables spatial and temporal control of materials, which is highly desirable in numerous applications.¹¹⁸ For example, Wu *et al.* reported a photothermal hydrogel synthesized by radical polymerization and composed of 3-(trimethoxysilyl)propyl methacrylate and mesoporous silica (mSiO₂) modified copper sulfide (CuS) nanoparticles for promotion of wound healing at tolerable temperatures.⁹⁷ Upon irradiation of near-infrared (NIR) light for 10 minutes, the combination of hyperthermia, production of ROS, and controlled release of copper ions from the hydrogel (*N*-isopropylacrylamide (NIPAAm) and acrylamide (AAm)) exhibited an antibacterial efficacy of 99.80% and 99.94% against *S. aureus* and *E. coli*, respectively, while simultaneously accelerating wound healing.

1.3.1 Challenges for Capture and Detection of Microbes

1.3.1.1 Characterization of Biofilm Formation

Despite the numerous efforts in combating bacterial infections in the drug delivery and tissue engineering field with the use of synthetic polymeric materials, there is a lack of tools for effectively characterizing and preventing biofilm formation in most industries. In the water-treatment industry specifically, conventional strategies to alleviate biofilm formation in industries involving scheduled cleaning, disinfecting treatments, chemical and physical treatments have not

been sufficient in effectively removing biofilm formation due to enhanced resistance.^{119,120} Instead, more effort has been focused on the modification of polymeric surfaces/coatings to prevent or weaken microbial adhesion, thus endowing anti-fouling properties.^{121–124} For example, a study using zwitterionic polyurethane polymer functionalized with carboxybetaine precursor (diethylamine ethyl acetate (DEAEA)) and DEAEA diol effectively resisted biofilm formation against two very challenging strains that form biofilm (*P. aeruginosa* PAO1 and *Staphylococcus epidermidis*) for a period of six months, demonstrating a long-term anti-fouling strategy.¹²⁵ While promising, it is still extremely difficult to find the materials with the highest repressive characteristics against the attachment of microorganisms and formation of biofilm. Therefore, there is a need to understand the exact mechanisms of biofilm formation and the spatiotemporal dynamics of interspecies interactions and communication, as it could provide detailed insights into the underlying adhesion mechanisms and bacterial community dynamics, further facilitating the design of effective methods for mitigating biofilm formation. In fact, recent findings have pointed towards early colonizers being the cornerstone of biofilm formation by expression of EPS and recruitment of other microorganisms in membrane-related processes.^{126,127} However, given the complex and heterogenous nature of EPS, the isolation and quantification of biofilm formation from membrane surfaces are limited to a number of tools, mainly membrane autopsies and laser capture microdissection (LCM).^{128,129} A major drawback with both these methods is their destructive nature to both the cells and underlying surfaces, which is not ideal for extraction of EPS as it alters its physical and chemical properties.¹³⁰ Hence, novel methods for improved isolation of cells from underlying surfaces are needed for successful characterization, allowing for the identification of communities of microorganisms that initiate biofilm formation.

1.4 Thesis Approach and Central Objective

The main objective and focus of this dissertation is to explore and develop synthetic, functional, stimulus-responsive polymeric interfaces (polymeric micelles, photodegradable hydrogels) for targeted drug delivery to cancer cells and improved isolation of microbes for molecular characterization. The proposed strategies were extensively studied and evaluated for their chemistry and biological functions in terms of cancer therapy and isolation of microbes from polyvinylidene difluoride (PVDF) wastewater membrane surfaces for molecular characterization. The new design considerations herein address the current limitations of the conventional nanocarriers for drug delivery and conventional techniques for isolation and characterization of microbes.

1.4.1 Bioresponsive polymeric micelles for cancer-targeted drug delivery

The majority of this thesis (**chapters 2, 3, and 4**) focuses on utilizing the intrinsic properties present in tumor microenvironments (TME), mainly elevated levels of reactive oxygen species (ROS) and overproduction of MMP-2 enzyme for the design and synthesis of stimuli-sensitive synthetic block copolymer polymeric micelles (BCPMs) by reversible addition-fragmentation chain transfer (RAFT) polymerization and substitution of pentafluorophenyl ester group for delivery of either physically loaded or chemically conjugated drugs selectively to cancer cells. Under the ROS-sensitive BCPM approach, the conventional chemotherapeutic drug, Doxorubicin (DOX) was loaded physically into the hydrophobic core of BCPMs bearing a library of oxidation-sensitive thioether groups (**chapter 2**). Results showed that the micelles, especially micelles with intermediate ROS sensitivity, significantly increased toxicity of DOX in liver cancer cells (HepG2) but protected normal cells, human umbilical endothelial cells (HUVECs) from DOX cytotoxicity. Taking it a step further, in **chapter 3**, hydrogen sulfide (H₂S) prodrug (ADT) was

chemically conjugated to the core of BCPMs bearing oxidation-sensitive thioether group and the anti-cancer effects of H₂S in colon cancer cells (HT29) were evaluated. A greater anti-proliferative effect was observed in HT29 cells with no significant toxicity in HUVEC cells. In **chapter 4**, a different approach was taken where BCPM bearing MMP-2 enzyme cleavable peptide motifs and chemically conjugated ADT was designed for site-specific delivery of H₂S to cancer cells. The greater release of H₂S from MMP-2 sensitive micelles exhibited stronger anti-proliferative activity in HT29 cells.

1.4.2 Biofunctional photodegradable hydrogels for capture and isolation of microbes

The final portion of this thesis (**chapter 5**) focuses on the development of the polymer surface dissection (PSD) method which uses biofunctionalized, photodegradable polyethylene glycol (PEG)-based hydrogels for the isolation of microbes from polyvinylidene difluoride (PVDF) wastewater membrane surfaces. The flocs were extracted with high spatial precision and minimal DNA damage after exposure to spatiotemporally controlled ultraviolet (UV) light using a patterned illumination tool, allowing for follow-up characterization by 16S rRNA sequencing. The technique allows for the identification of microbes that form small flocs on membrane surfaces without requiring a culture step for enrichment, and will be used in future work to identify communities of microorganisms that initiate membrane biofilms in bio-separation processes.

2 Polymeric micelles with fine-tuned oxidation sensitivities for anti-cancer drug delivery

The work in this chapter was done under the mentorship of Dr. Urara Hasegawa during her tenure at Kansas State University

Abstract

Oxidation-sensitive drug delivery systems have immense potential in treatment of cancer that overproduces reactive oxygen species (ROS) such as hydrogen peroxide (H_2O_2). Despite the development of several drug carriers that release drugs in response to ROS, the lack of selectivity towards cancer cells over healthy cells remains a challenge. Here, we report the design and characterization of thioether-bearing polymeric micelles with varying oxidation sensitivities. The oxidation experiments of different thioether model compounds as well as molecular modeling show that the rate of thioether oxidation can be modulated by both electronic and steric effects of the substituent groups bound to the sulfur atom. The micelles were prepared from amphiphilic diblock copolymers bearing different thioether groups on the hydrophobic segment, which becomes hydrophilic upon oxidation leading to micellar dissociation. The dissociation rate of the micelles in the presence of H_2O_2 was significantly affected by changing the thioether groups. The different dissociation rates of these micelles were also confirmed in human liver cancer HepG2 cells, which overproduce ROS, by observing the fluorescence recovery of the micelles containing self-quenched fluorophores. Furthermore, the micelles were loaded with doxorubicin (Dox) to evaluate their potential in drug delivery applications. Dox release from the micelles was accelerated in the presence of H_2O_2 . Encapsulating Dox in micelles having a moderate oxidation sensitivity significantly increased toxicity in HepG2 but reduced toxicity in human umbilical vein

endothelial cells (HUVECs), showing that cancer-specific drug delivery can be achieved by modulating the oxidation sensitivity of thioether groups in the micelles. Therefore, thioether-bearing micelles with fine-tuned oxidation sensitivity have potential for improving efficacy and safety of drugs in cancer treatment.

2.1 Introduction

Elevated levels of reactive oxygen species (ROS) such as hydrogen peroxide (H_2O_2), superoxide anion radical ($\text{O}_2^{\cdot-}$), singlet oxygen ($^1\text{O}_2$), and the hydroxyl radical ($\cdot\text{OH}$) are commonly observed in different types of cancer.^{131,132} These species are produced during mitochondrial electron transport in aerobic respiration or by the action of nicotinamide adenine dinucleotide phosphate oxidases, and cause oxidative cellular damage including lipid peroxidation, DNA cleavage and protein modification.¹³³ While ROS are maintained at basal levels in normal cells, many cancer cells exhibit increased rates of ROS production due to high metabolic activity and impaired antioxidant systems.^{134–136} This redox imbalance in cancer cells contributes to the characteristic tumor microenvironment, which stimulates tumor growth, invasion, and metastasis.¹³⁶

In the field of drug delivery, this oxidative tumor microenvironment has attracted attention as one of the hallmarks of cancer that provide a unique opportunity for cancer-specific drug delivery. Recently, many types of oxidation-sensitive drug carriers that release drugs in response to ROS have been developed with the goal to enhance drug accumulation in cancer tissue. These drug carriers include polymeric micelles, polymersomes, and other polymeric nanoparticles, which are composed of amphiphilic polymers containing an oxidation-sensitive building block that alters its water solubility or degrades upon oxidation by ROS. Examples of such building blocks are

polymers containing thioether,^{137–139} arylboronate ester^{140,141} and thioketal moieties^{142,143} (**Figure 2.1**).

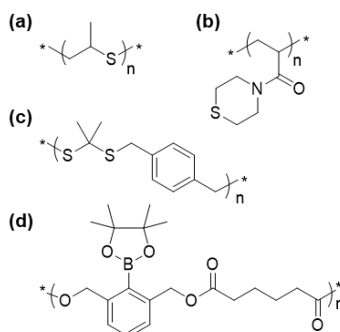


Figure 2.1. Oxidation-sensitive polymers. (a) Poly(propylene sulfides) (PPS).¹³⁷ (b) Poly(*N*-acryloylthiomorpholine).¹³⁸ (c) Poly(1,4-phenyleneacetonedimethylene thioketal).¹⁴² (d) Poly(esters) containing arylboronate ester moieties.¹⁴¹

Thioether-containing polymers are among the most widely used building blocks to confer oxidation sensitivity to drug carriers. Thioethers are known to be oxidized by ROS, analogous to the oxidation of methionine residues of proteins under oxidative stress.¹⁴⁴ Along with this oxidation reaction, thioethers, which have low dipolar moments, are converted to polar sulfoxides and, in part, sulfones (**Figure 2.2**). Therefore, thioether-containing polymers undergo a hydrophobic-hydrophilic phase transition upon oxidation. Hubbell and colleagues were the first to report oxidation-sensitive polymersomes and polymeric micelles prepared from amphiphilic block copolymers consisting of a hydrophobic poly(propylene sulfide) (PPS) block and a hydrophilic poly(ethylene glycol) (PEG) block, which dissociate in the presence of H₂O₂ under physiological conditions.^{137,139,145,146} These nanostructures improved delivery of a wide variety of drugs, such as siRNA,¹⁴⁷ cyclosporin A,¹⁴⁸ gardiquimod, and ovalbumin¹⁴⁹ to cancer and dendritic cells. Following these reports, other types of thioether-containing polymers such as poly(methionine)^{150,151} and poly(*N*-acryloyl thiomorpholine)¹³⁸ have been developed.

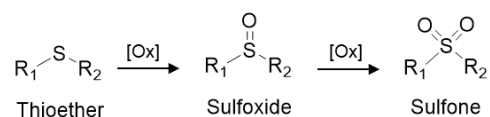


Figure 2.2. Oxidation of thioether to sulfoxide and sulfone

Despite the promising results of oxidation-sensitive drug carriers, their selectivity towards cancer remains questionable. So far, most studies have focused on improving the ROS sensitivity of the drug carrier. For example, sulfur in thioether-containing polymers is replaced with selenium or tellurium to increase their susceptibility to oxidation.^{152,153} However, considering ubiquitous ROS production in healthy tissues, drug carriers with a high ROS sensitivity may react with ROS at basal levels (< 10 nM)¹⁵⁴ leading to non-specific drug release. Indeed, according to the report by Duvall *et al.*, while drug release from PPS-based polymeric micelles was enhanced in murine macrophages that overproduce ROS in response to lipopolysaccharide activation, a significant amount of drug release was also observed for non-activated macrophages.¹⁵⁵ This indicates that PPS-based drug carriers can be destabilized in healthy tissues containing low levels of ROS. Therefore, fine-tuning of the ROS sensitivity is needed to develop drug carriers that are stable in healthy tissues, but release payloads in tumor tissues associated with elevated ROS levels (> 0.1-10 μM).¹⁵⁴

Here, we present a library of thioether-containing polymeric micelles having different oxidation sensitivities (**Figure 2.3**). The oxidation of the thioether groups is expected to be dependent on the electronic and steric effects of the substituent groups attached to the sulfur atom. Therefore, we hypothesize that the oxidation sensitivity of polymeric micelles can be controlled by designing amphiphilic block copolymers with different thioether pendant groups. Dissociation of these micelles in the presence of H_2O_2 and human liver cancer HepG2 cells was investigated.

Furthermore, these micelles were encapsulated with doxorubicin (Dox) to evaluate intracellular Dox release and cytotoxicity.

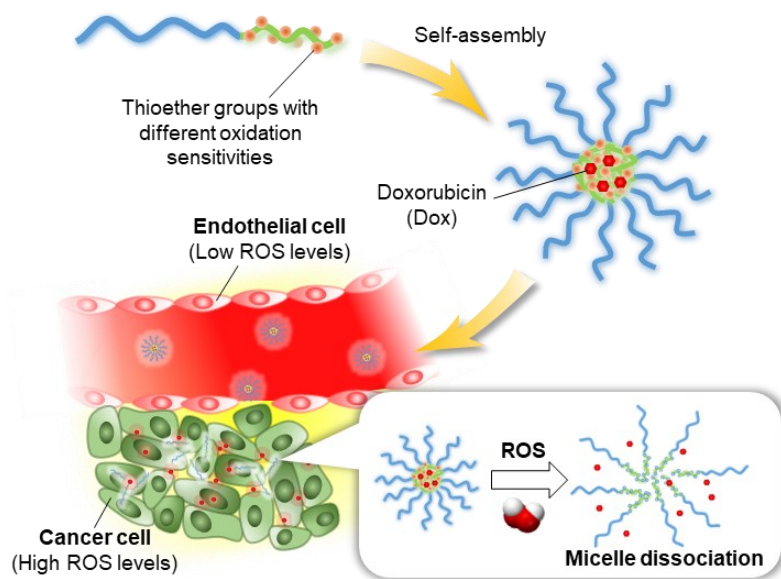


Figure 2.3. Polymeric micelles bearing thioether groups with fine-tuned oxidation sensitivities for site-specific drug release in cancer cells overproducing reactive oxygen species (ROS).

2.2 Experimental Section

2.2.1 Materials

Pentafluorophenyl acrylate (PFPA), 3-methylthiopropylamine (TP), and thiomorpholine (TM), were purchased from Tokyo Chemical Industry (USA). 4-(methylthio)benzylamine·HCl salt (TPh·HCl) was purchased from Enamine (USA). 4-acryloylmorpholine (AM), 2,2'-azobis(isobutyronitrile) (AIBN), 2-(dodecylthiocarbonothioylthio)-2-methylpropionic acid (CTA), aluminum oxide (Al_2O_3), 1-methyl-2-pyrrolidinone (NMP), 4-dimethylamiopyridine (DMAP), deuterated chloroform (CDCl_3), calcium hydride (CaH_2), trifluoroacetic acid (TFA), sodium dodecyl sulfate (SDS), phosphor pentoxide (P_4O_{10}) and 4Å molecular sieves were purchased from Sigma Aldrich (USA). 1,4-dioxane, anhydrous dimethylformamide (DMF), tetrahydrofuran (THF), acetonitrile (CH_3CN), ethyl acetate (EtOAc), diethyl ether (Et_2O), ethanol

(EtOH), triethylamine (TEA), potassium hydroxide (KOH) pellets, acetic anhydride (Ac₂O), sodium bicarbonate (NaHCO₃), hydrochloric acid (HCl), hydrogen peroxide (H₂O₂) solution (3 and 50 wt%) (H₂O₂), phosphate-buffered saline (10x, PBS), Nile red, Hoechst 33342, MEM, fetal bovine serum, penicillin-streptomycin, trypsin-EDTA, and *N*-acetyl-L-cysteine (NAC) were purchased from Fisher Scientific (USA). Fluorescein isothiocyanate isomer I was purchased from Acros Organics. Tert-butyl *N*-(2-aminoethyl) carbamate was purchased from Oakwood Products. XPell pellets were purchased from Xplosafe (USA). Regenerated cellulose dialysis tubing (MWCO 2 kDa) was purchased from Spectrum Laboratories (USA). Sephadex LH20 and G20 were purchased from GE Healthcare (USA). Doxorubicin·HCl was purchased from Cayman Chemical Company (USA). 3-(4,5-dimethylthiazol-2-yl)-2,5-diphenyltetrazolium bromide (MTT) was purchased from MP Biomedical (USA). HepG2 cells and HUVECs were purchased from ATCC (USA). Transparent and black 96 well plates and disposable 5 mL polypropylene columns were purchased from ThermoFisher Scientific (USA). The glass-bottom dishes were purchased from Matsunami Glass (USA). 200 mesh carbon-coated copper grids were purchased from Electron Microscopy Science (USA).

AIBN was recrystallized from MeOH. Pentafluorophenyl acrylate and 4-acryloylmorpholine were passed through a plug of Al₂O₃ to remove the inhibitor. 1,4-dioxane was distilled from CaH₂ and kept over molecular sieves and XPell pellets. Thioether amines (TM and TPh) and TEA were dried over KOH pellets. Other reagents were used as received without further purification.

2.2.2 Instrumentation

Proton NMR (¹H NMR) Spectroscopy. ¹H NMR spectra were measured with a Varian 400MHz NMR spectrometer. A number of 32 scans was collected and the delay time (D1) was set to 10 s

for polymers and 1 s for small compounds. The chemical shifts are referenced to the residual undeuterated NMR solvent signal at 7.26 ppm (CDCl_3),

Attenuated Total Reflection Infrared Spectroscopy (ATR-IR). Attenuated total reflection infrared (ATR-IR) spectra were obtained using a Perkin Elmer Spectrum 400 spectrometer.

Gel Permeation Chromatography (GPC). Elution profiles of the polymers were obtained using a ResiPore PL1113-6300 GPC column on an Agilent Technologies 1220 Infinity II LC GPC system equipped with a 1260 RI detector and a 1260 MCT column oven. THF was used as the eluent with a flow rate of 1.0 mL/min. The temperature of the RI detector and column oven was 40 °C. The polymers were dissolved in THF at 5 mg/ml and 10 μL of the solution was injected. The polydispersity index (M_w/M_n) was calculated from the elution profiles of a polystyrene standard (Agilent).

UV-Vis spectroscopy. The UV/Vis spectra were measured on a Thermo Scientific Nanodrop One^c spectrophotometer.

Dynamic Light Scattering (DLS). Dynamic light scattering measurements were done using a Malvern Zetasizer Nano ZS Series instrument. Freshly prepared micelle solutions were filtered using a polyethersulfone (PES) syringe filter (pore size: 0.45 μm) and placed in disposable microcuvettes (ZEN0040, Malvern). The Z-average diameter and polydispersity index (PDI) of the micelles were determined by the cumulant method. For multimodal samples, the CONTIN analysis was used to determine the size distribution.

Transmission Electron Microscopy (TEM). The morphology of the micelles was observed by transmission electron microscopy using the negative staining method. The micelle solution (1 mg/ml in water) was mixed with 2 w/v% uranyl acetate aqueous solution (volume ratio of 1:1) and added to 200 mesh carbon-coated copper grids. The grids were air-dried after removing the

solution by blotting the side of the grid with filter paper. Images were acquired on a FEI Tecnai G2 Spirit BioTWIN instrument operating at 80 kV.

UV-Vis / fluorescence spectroscopy with Plate Reader. The UV-Vis absorbance and fluorescence intensities were measured with a Tecan infinite M200 plate reader.

Confocal Laser Scanning Fluorescence Microscopy (CLSM). Fluorescence images were acquired on an Olympus Fluoview FV1000-D confocal microscope equipped with 405, 473, 559, and 632 nm lasers. Colocalization analysis of images was performed using the FV-10-ASW software. Pearson's correlation coefficients were obtained using three single slice images.

2.2.3 Synthesis of PPFPA Homopolymer

PPFPA was synthesized by RAFT polymerization using AIBN as the initiator and 2-(dodecylthiocarbonothioylthio)-2-methylpropionic acid as the chain transfer agent (CTA). For PPFPA20, 1190.6 mg (5 mmol) of PFPA, 72.9 mg (0.2 mmol) of CTA, and 3.28 mg (0.02 mmol) of AIBN were dissolved in 1,4-dioxane (Total volume: 2.5 mL). For PPFPA40, 476.2 mg (2 mmol) of PFPA, 14.6 mg (0.04 mmol) of CTA, and 0.657 mg (0.004 mmol) of AIBN were dissolved in 1,4-dioxane (Total volume: 2.0 mL). The reaction mixture was deoxygenated by five freeze-pump-thaw cycles, heated to 60 °C under argon and stirred for 24 h. The polymerization was stopped by opening the Schlenk tube to air and cooling the reaction mixture to room temperature. The reaction mixture was added dropwise to 75 mL of EtOH. The precipitate was filtered, washed with 10 mL EtOH and dried under reduced pressure to yield yellow solids (1040.8 mg (82%) for PPFPA20 and 401.2 mg (82%) for PPFPA40). The polymers were characterized by ¹H NMR, GPC, and FT-IR as shown in Supporting Information.

2.2.4 Synthesis of PAM-PPFPA Diblock Copolymer

For PAM-PPFPA20, 352.9 mg (2.5 mmol) of AM, 157.9 mg (0.031 mmol) of PPFPA20, and 0.411 mg (0.0025 mmol) of AIBN were dissolved in 1,4-dioxane (Total volume: 2.5 mL). For PAM-PPFPA40, 282.3 (2.0 mmol) of AM, 245.4 mg (0.025 mmol) of PPFPA40, and 0.328 mg (0.002 mmol) of AIBN were dissolved in 1,4-dioxane (Total volume: 2.0 mL). The reaction mixture was deoxygenated by five freeze-pump-thaw cycles, heated to 60 °C under argon and stirred for 24 h. The polymerization was stopped by opening the Schlenk tube to air and cooling the reaction mixture to room temperature. The reaction mixture was added dropwise to 75 mL of Et₂O. The precipitate was filtered, washed with 10 mL Et₂O and dried under reduced pressure to yield yellow solids (410 mg (80%) for PAM-PPFPA20 and 458 mg (87%) for PAM-PPFPA40). The polymers were characterized by ¹H NMR, GPC and FT-IR as shown in Supporting Information.

2.2.5 CTA End Group Removal from PAM-PPFPA Diblock Copolymer

The CTA end group was removed by radical-induced cleavage of the thiocarbonylthio group.¹⁵⁶ 380 mg (0.021 mmol) of PAM-PPFPA20 polymer and 123 mg (0.75 mmol) of AIBN, 440 mg (0.019 mmol) of PAM-PPFPA40 and 110 mg (0.67 mmol) of AIBN were dissolved in 3 mL of 1,4-dioxane, respectively. The solution was deoxygenated by five freeze-pump-thaw cycles, heated to 70 °C under argon, and stirred for 24 h. The reaction was stopped by opening the Schlenk tube to air and cooling the reaction mixture to room temperature. The reaction mixture was added dropwise to 90 mL of Et₂O. The precipitate was filtered, washed with 10 mL Et₂O, and dried under reduced pressure to yield white solids (320 mg (85%) for PAM-PPFPA20 and 382 mg (87%) for PAM-PPFPA40). The polymers were characterized by GPC, and FT-IR as shown in Supporting Information.

2.2.6 Synthesis of Thioether-Containing Block Copolymers

After drying at 40 °C under vacuum for 24 h in the presence of P₄O₁₀, 40 mg of PAM-PPFPA polymers (0.045 and 0.071 mmol of PFPA groups for PAM-PPFPA20 and PAM-PPFPA40, respectively) was dissolved in 2 mL anhydrous DMF, followed by the addition of thioether amines (5 eq. relative to PFPA groups). In the case of TPh·HCl, 5 eq. of TEA relative to PFPA groups was added. After three purge-evacuate cycles, the reaction mixture was heated at 50 °C under argon and stirred for 24 h. The reaction mixture was cooled to room temperature, filtered through a plug of glasswool and added dropwise to 60 mL of Et₂O. The precipitate was filtered, washed with 10 mL of Et₂O, and dried under reduced pressure to yield white solids. The polymers were dissolved in 6 mL of tetrahydrofuran and filtered through a plug of glasswool to further purify the polymers by removing the amine pentafluorophenol salts and TEA·HCl yielding 30.4 mg (83%) for PAM-PTP20, 29.8 mg (82%) for PAM-PTM20, 27.9 mg (72%) for PAM-PTPh20, 29.5 mg (87%) for PAM-PTP40, 28.2 mg (83%) for PAM-PTM40, and 26.7 mg (71%) for PAM-PTPh40. The polymers were characterized by ¹H NMR, FT-IR, and GPC as shown in Supporting Information.

2.2.7 Synthesis of Thioether/FITC-Containing Diblock Copolymers

PAM-PPFPA40 was dried at 40 °C under vacuum for 24 h in the presence of P₄O₁₀. The PAM-PPFP40 diblock copolymer (15 mg, 0.027 mmol of PFPA group) was dissolved in 1 mL anhydrous DMF, followed by the addition of FITC-NH₂·TFA (0.516 mg, 0.00092 mmol, 0.034 eq. relative to PFPA group) and TEA (0.116 mg, 0.0011 mmol). The reaction mixture was heated at 50°C under argon following three purge-evacuate cycles and stirred for 24 h. Next, thioether amines (0.056 mmol, 2 eq. relative to PFPA groups) were added to the reaction mixture under argon. In the case of TPh·HCl, TEA (0.056 mmol, 1 eq. relative to TPh·HCl) was added. The

reaction mixture was heated at 50°C under argon following three purge-evacuate cycles and stirred for another 24 h. The polymer was separated from unreacted thioether amines and pentafluorophenol by Sephadex LH-20 size exclusion column chromatography (column diameter: 13 mm, length: 250 mm) using DMF as the eluent. The absorbance at 280 nm of each fraction was measured using Nanodrop and plotted as a function of elution volume to obtain the elution profile. Fractions containing polymer were combined, diluted 2x with deionized (DI) water and dialyzed against 1 L of DI water for 2 d, with regularly replacing the water. Polymers were recovered by lyophilization.

2.2.8 Preparation of Micelles

The thioether-containing block copolymers were dissolved in NMP (25 mg/mL) and added dropwise to DI water (volume ratio 1:9) under stirring (final concentration: 2.5 mg/mL). The solutions were dialyzed (MWCO, 2kDa) against 1 L of DI water for 1 d, with regular replacing the water. To determine polymer concentration after dialysis, part of the micelle solution was lyophilized and the amount of polymer was determined gravimetrically.

2.2.9 Critical Micelle Concentration (CMC)

The CMC of the micelles was determined using the Nile red method.¹⁵⁷ To 350 μ L of the micelle solutions at different concentrations, 3.5 μ L of 0.1 mg/mL Nile red solution in DMSO was added and kept at RT for 2 h in the dark. The micelle/Nile red mixtures were transferred to a 96-well plate (100 μ L/well, $n=3$) and incubated at room temperature for 2 h in the dark. The fluorescence intensity ($\lambda_{\text{ex}}=530$ nm, $\lambda_{\text{em}}=630$ nm) was recorded and plotted against $\log(\text{concentration})$. The CMC values were determined based on the intersection between the linear fits of the low and high concentration regions as shown in Supporting Information.

2.2.10 Change in Size Distribution of the micelles in the presence of H₂O₂

To evaluate the micelle dissociation in the presence of H₂O₂, 90 μL of 1 mg/mL micelle solutions were mixed with 10 μL of H₂O₂ (Final concentration of H₂O₂: 100 mM) and incubated at 37°C. The size distribution of the micelles was measured by DLS at the indicated time points.

2.2.11 H₂O₂ Scavenging Rate of the Thioether Model Compounds by Iodide

Oxidation Assay

The thioether model compound dissolved in 2.16 mL in 10% DMF/PBS (pH7.4) in glass vials were mixed with 0.27 mL H₂O₂ in PBS (pH7.4) to give final concentrations of 10 mM of the model compound and 1.0 mM H₂O₂. At the indicated time points, 0.2 mL of the solutions was withdrawn and mixed with 0.2 mL of a 1000 mM NaI solution in 10% DMF/PBS (pH7.4) inside a glass vial. After reacting for 15 min, the samples were transferred to a quartz cuvette and the absorbance at 350 nm measured due to the I₃⁻ anion formed by oxidation of the I⁻ anion by remaining H₂O₂. The % Remaining H₂O₂ was calculated as follows:

$$\% \text{ Remaining H}_2\text{O}_2 = \frac{[\text{Abs of sample}]}{[\text{Abs of nontreated sample}]} \times 100$$

After collecting the last data points, the thioether model compound/H₂O₂ solutions (2.7 mL) were lyophilized and the residue was extracted with CHCl₃ (4 mL total). After removing solvent in a flow of air and drying under vacuum at 40°C, the residue was dissolved in deuterated chloroform to measure ¹H NMR. ¹H NMR spectra were in agreement with the product obtained by oxidation of the model compound in aqueous H₂O₂.

2.2.12 Monitoring of Micelle Dissociation by the Fluorescence Recovery of Self-Quenched Fluorophores

The thioether/FITC-containing micelle solutions (0.5 mg/mL, 10 μ L/well) were placed in a 96 well plate and mixed with 90 μ L/well of H₂O₂ in 100 mM PBS (pH 7.4) containing 10 mM EDTA (micelles: 0.05 mg/mL, H₂O₂: 90 mM). The plate was sealed with a plate sealer and incubated at 37°C in the dark. At the indicated time points, fluorescence intensities (FI) (λ_{ex} =490 nm, λ_{em} =520 nm) of H₂O₂ treated and nontreated micelles were measured using a microplate reader. The percent increase in FI of thioether/FITC-containing micelles was calculated as follows:

$$\% \text{ Fluorescence recovery} = \frac{[(\text{FI of H}_2\text{O}_2 \text{ treated}) - (\text{FI of nontreated})]}{[(\text{Max. FI of H}_2\text{O}_2 \text{ treated}) - (\text{FI of nontreated})]} \times 100$$

2.2.13 Preparation of Dox-Loaded Micelles

Dox·HCl was dissolved in DMSO at 10 mg/mL and mixed with TEA (1 eq.). This solution (20 μ L) was mixed with 100 μ L of 10 mg/mL thioether-containing polymer solution in NMP and added dropwise to 880 μ L of DI water and kept under stirring in the dark for 1 h at RT. The Dox-loaded micelles were separated from free Dox by ultrafiltration using an Amicon filter with MWCO of 3 kDa (14,000 x g, 25 min) and subsequently washed with DI water by ultrafiltration (3x) to remove the organic solvents. The absorbance at 500 nm of the first filtrate was measured using Nanodrop to quantify the Dox loading efficiency.

2.2.14 Determination of the Dox concentration

The Dox-loaded micelle solution (1 μ L) was mixed with DMSO (9 μ L) and the absorbance at 500 nm was measured to determine the Dox concentration in the micelle solution. The standard samples were prepared by dissolving Dox·HCl in water/DMSO (10/90 v/v%) and the absorbance at 500 nm was measured to prepare the standard curve.

2.2.15 Dox Release from the Micelles in Response to H₂O₂

Dox-loaded micelles (90 µL) were mixed with 10 µL of 50 mM H₂O₂ solution or PBS and incubated for 2 h at 37 °C in the dark. The Dox-loaded micelles were separated from free Dox by Sephadex G-25 size exclusion column chromatography (column diameter: 13 mm, height: 70 mm) using PBS as the eluent. The fractions containing the micelles were combined, lyophilized and dissolved in 30 µL of DMSO. The absorbance at 500 nm was measured to determine the Dox concentration in the samples (*C*). To determine the initial Dox concentration (*C*₀) in each sample, 100 µL of the Dox-loaded micelle solutions were lyophilized, dissolved in 30 µL of DMSO and the absorbance at 500 nm was measured. Percent Dox release from the micelles after the addition of water or H₂O₂ was calculated as follows:

$$\% \text{ Dox Release} = \left(\frac{C_0 - C}{C_0} \right) \times 100$$

2.2.16 Cell Culture

Human liver cancer HepG2 cells were cultured in MEM containing 10% fetal bovine serum and 1% penicillin-streptomycin (10,000 U/mL) in a 5% CO₂ incubator at 37 °C. Human umbilical vein endothelial cells (HUVECs) were cultured in a vascular basal medium containing the cell growth kit and 0.1 % Amphotericin B in a 5 % CO₂ incubator at 37 °C.

2.2.17 Dissociation of Thioether/FITC-containing Micelles in HepG2 Cells

HepG2 cells were seeded in quadruple well glass-bottom dishes at a density of 2.0 x 10⁴ cells/well and cultured for 1 d. The medium was replaced with 100 µL/well of fresh medium containing 8 nM Hoechst 33342 dye, and cells were incubated for 5 min at 37 °C. Then, the Hoechst 33342 solution was removed and 90 µL of fresh medium and 10 µL of 0.5 mg/mL thioether/FITC-containing micelle solution were added (Final micelle concentration: 0.05 mg/mL). After culturing for 4 and 24 h, cells were washed with PBS and observed by CLSFM.

For the *N*-acetylcysteine (NAC)-treated cells, the cells were pre-treated with 5 mM of NAC in the culture medium for 3 h, treated with Hoechst 33342 dye for 5 min and incubated in the medium containing 5 mM NAC and 0.05 mg/mL of thioether/FITC-containing micelles. The images were analyzed using ImageJ software to evaluate the fluorescence intensity due to dissociated micelles within cells. The mean fluorescence intensity was calculated by subtracting the mean fluorescence intensity of the background (non-cell area) from the mean fluorescence intensity of the cell area.

2.2.18 Cytotoxicity of Dox-Loaded Micelles in HepG2 and HUVECs

HepG2 cells and HUVECs were seeded in a 96-well plate at a density of 1.0×10^4 cells/well and 5.0×10^3 cells/well, respectively and cultured for 1 d. After the medium was replaced with 100 μ L/well of fresh medium containing 10 μ L of the aqueous solution of the micelles loaded with/without Dox or 1 μ L of Dox/DMSO, the cells were cultured for 2 d in a CO₂ incubator. The medium was replaced with 100 μ L of 0.5 mg/ml of MTT in a medium. The cells were cultured for 3 h and the formazan crystals formed were dissolved in 100 μ L/well of 100 mg/mL sodium dodecyl sulfate (SDS) solution in 0.01 M HCl (aq). The absorbance at 570 nm was measured using a microplate reader and cell viability was expressed as % of the absorbance of untreated cells.

2.2.19 Intracellular Distribution of Dox in HepG2 Cells

HepG2 cells were seeded in quadruple well glass-bottom dishes at a density of 2.0×10^4 cells/well and cultured for 1 d. The medium was replaced with 100 μ L of fresh medium containing 8 nM Hoescht 33342 dye, and cells were incubated for 5 min at 37 °C. The medium was then replaced with 100 μ L of fresh medium containing 10 μ L of Dox-loaded micelle solution or 0.2 μ L of Dox/DMSO (Final Dox concentration: 2 nM). After culturing for 0, 1, 4, and 24 h, cells were observed by CLSFM.

2.2.20 Molecular Modeling

Density functional theory (DFT) calculations were performed using the Vienna ab initio simulation package (VASP).¹⁵⁸ The generalized gradient approximation GGA-PBE¹⁵⁹ functional was used to account for electron exchange-correlation effects. The projector augmented wave (PAW) method¹⁶⁰ was used to represent the ionic cores. All the calculations were spin-polarized. The energy cutoff for the plane wave function was 400 eV. The break condition for self-consistent interaction is 1×10^{-6} . Ionic relaxation was stopped when the forces on all atoms were smaller than -0.02 eV/Å. The Γ k-point was employed throughout the entire DFT calculations.

TPAM, TMAM, and TPhAM and their corresponding oxidized products, sulfoxides, were placed in a large box of $25 \times 25 \times 25 \text{ \AA}^3$ for geometry optimization as shown in **Figure A.1** (Supporting Information). The vibrational frequencies were obtained based on the simple harmonic approximation of the optimized molecular structures. The S-O bond stretching modes were corroborated by FT-IR spectroscopy. Bader charge analysis¹⁶¹ of the S atom in TPAM, TMAM and TPhAM was also performed to evaluate its nucleophilicity.

2.3 Results and Discussion

2.3.1 Effect of Chemical Structure on Oxidation of Thioether Compounds

Thioethers are known to be oxidized by biologically relevant oxidants such as hydrogen peroxide (H_2O_2), which is the most abundant ROS in the human body. The proposed mechanism of thioether oxidation by H_2O_2 involves the transfer of oxygen by nucleophilic attack of the sulfur atom onto H_2O_2 .¹⁶² Therefore, it is expected that the oxidation sensitivity of thioethers depends on the nucleophilicity of the sulfur atom, which can be fine-tuned by changing the substituent groups. To test this hypothesis, we prepared three different thioether amide compounds, 3-methylthiopropylamide (TPAM), thiomorpholine amide (TMAM), and 4-

(methylthio)benzylamide (TPhAM) (**Figure 2.4a**), and investigated their oxidation by H_2O_2 . TPAM, TMAM, and TPhAM were reacted with H_2O_2 and the remaining H_2O_2 was determined by the iodide oxidation assay at the indicated time points.¹⁶³ TPAM reacted rapidly with H_2O_2 and was consumed completely within 20 h (**Figure 2.4b**). The oxidation of TPhAM was much slower and 40% of H_2O_2 remained after 48 h. This might be due to the electron-withdrawing effect of the phenyl group, which decreases electron density on the sulfur atom and lower its nucleophilicity thereby slowing down the oxidation by H_2O_2 . TMAM, on the other hand, showed intermediate reactivity with 10% of H_2O_2 remaining after 48 h. Since the chemical environment around sulfur is similar for TMAM and TPAM, the slower oxidation of TMAM seems to be related to the ring structure.

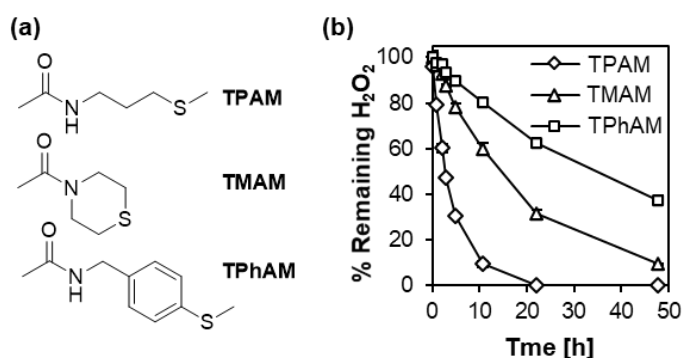


Figure 2.4. Oxidation of thioether model compounds by H_2O_2 . (a) Chemical structures of TPAM, TMAM, and TPhAM. (b) Oxidation rate of the model compounds. H_2O_2 consumption upon the addition of the model compounds was monitored in 100 mM PBS (pH 7.4) at 20°C by the iodide oxidation assay. Model compounds: 10 mM. H_2O_2 : 1.0 mM. $n=3$.

To confirm that the thioether model compounds can be oxidized to the corresponding sulfoxide, the model compounds were reacted with H_2O_2 and characterized by FT-IR. As shown in **Figure 2.5**, an absorbance at around $1000\text{-}1050\text{ cm}^{-1}$, which is attributed to the sulfoxide $\text{S}=\text{O}$ stretching vibration appeared in the IR spectra for all products, indicating that the sulfides had been oxidized to sulfoxides. According to DFT calculations, the vibrational frequencies for $\text{S}=\text{O}$

stretching in the sulfoxide species of TPAM, TMAM, and TPhAM are 1066 cm^{-1} , 1049 cm^{-1} , and 1072 cm^{-1} respectively (**Table 2.1**). These values agree rather well with values determined experimentally by FT-IR, and thus confirm the formation of sulfoxides. Furthermore, we also confirmed sulfoxide formation by ^1H NMR (see experimental details and **Figures A.2 and A.3** in Supporting Information).

Table 2.1. FT-IR characterization and charge analysis of thioether model compounds.

	$\nu(\text{S=O})^{\text{a}}$ [cm^{-1}]	$\nu(\text{S=O})^{\text{b}}$ [cm^{-1}]	Charge on S atom ^b [e]
TPAM	1015	1066	- 0.010
TMAM	1000	1049	- 0.042
TPhAM	1042	1072	+ 0.074

^a Experimental.

^b Calculated.

To evaluate the effects of the substituent groups on thioether oxidation, we performed Bader charge analysis on the sulfur atom of the thioether model compounds. As for the linear thioether compounds (TPAM and TPhAM), the thioether compound with a more negatively charged sulfur atom (TPAM) accelerates oxidation (**Figure 2.4b**), which is in agreement with the mechanism proposed for thioether oxidation, where the nucleophilic attack of the sulfur atom on an oxygen atom of H_2O_2 leads to the formation of sulfoxide.¹⁶² On the other hand, while the charge on the sulfur atom in TMAM was higher than that of TPAM, the oxidation of TMAM was slower than that of TPAM. This unexpected result may relate to its cyclic structure. It has been reported that one of the key steps of thioether oxidation is the formation of a thioether- H_2O_2 adduct, which is affected by both electronic and steric effects of the substituent groups.¹⁶⁴ Therefore, the

formation of this intermediate may not be favored due to the ring strain of TMAM, thereby slowing down its oxidation compared to TPAM.

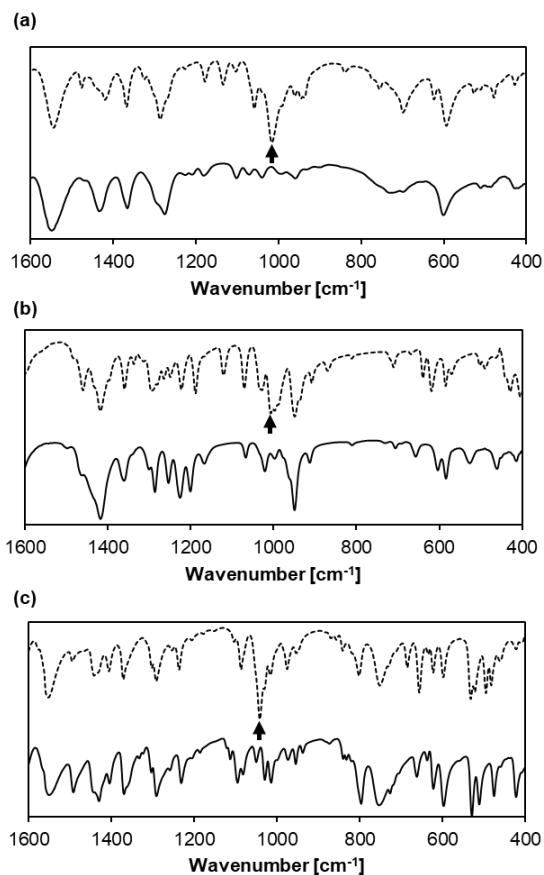


Figure 2.5. FT-IR spectra of thioether model compounds before and after H_2O_2 treatment. The model compounds were incubated with 1 M H_2O_2 at 20°C . FT-IR spectra were collected before (solid line) and after (dotted line) oxidation. (a) TPAM, (b) TMAM, (c) TPhAM.

2.3.2 Synthesis of Thioether-Bearing Diblock Copolymers

Encouraged by the model compound results, we designed amphiphilic diblock copolymers consisting of a hydrophilic poly(*N*-acryloyl morpholine) (PAM) block and a hydrophobic block bearing different thioether groups as shown in **Figure 2.6**. We first synthesized the poly(pentafluorophenyl acrylate) polymers (PPFPA) with different lengths (PPFPA20 and

PPFPA40, **Table 2.2**, **Figure A.4**, Supporting Information) by reversible addition-fragmentation chain transfer (RAFT) polymerization using 2-(dodecylthiocarbonothioylthio)-2-methylpropionic acid as the chain transfer agent (CTA). These polymers were used as macro CTAs to synthesize the PAM-PPFPA diblock copolymers with a PAM block length of 90 units. The obtained polymers had narrow size distributions with M_w/M_n below 1.15 as measured by GPC (**Table 2.2**, **Figure A.5**, Supporting Information). After removing the trithiocarbonate end group by radical-induced cleavage,¹⁵⁶ the PAM-PPFPA diblock copolymers were modified with amine-containing thioether compounds by substituting the pentafluorophenyl ester group to form amides,^{165,166} yielding the thioether-bearing diblock copolymers (TP, TM and TPh). Successful conjugation of the thioether amines was confirmed by the absence of C-F stretching vibration (1000 cm^{-1}), C=C stretching vibration of the aromatic ring (1510 cm^{-1}), and C=O stretching vibration of the activated ester group (1780 cm^{-1}) in the FT-IR spectra. (**Figures A.6** and **A.7**, Supporting Information). Furthermore, GPC showed that all the thioether-bearing block copolymers had a unimodal size distribution with a low M_w/M_n (**Table 2.2** and **Figure A.8**, Supporting Information). The presence of the thioether groups was also confirmed by ^1H NMR (**Figure A.9**, Supporting Information).

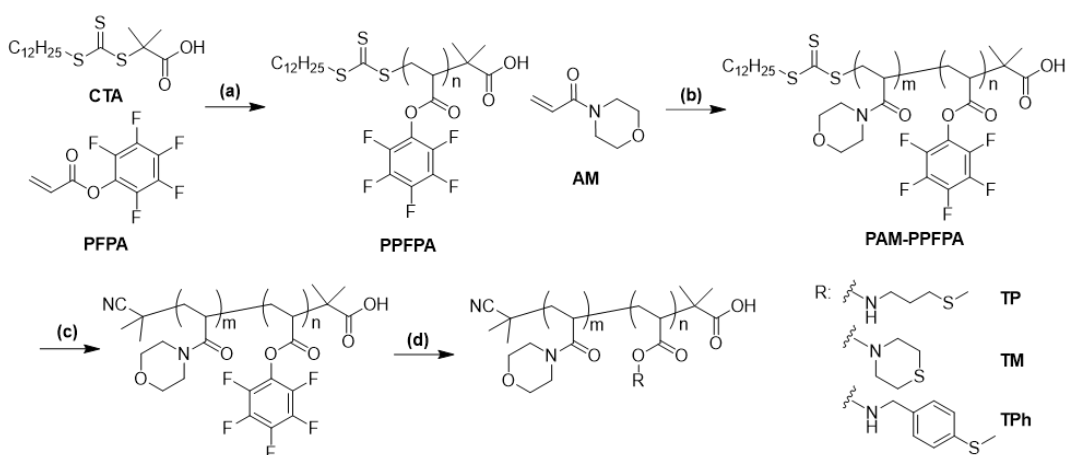


Figure 2.6. Synthesis scheme of the thioether-bearing block copolymers. (a) AIBN, 1,4-dioxane, $60\text{ }^\circ\text{C}$, 24 h, (b) AIBN, 1,4-dioxane, $60\text{ }^\circ\text{C}$, 24 h, (c) AIBN, 1,4-dioxane, $70\text{ }^\circ\text{C}$, 24 h, (d) DMF, thioether amine, $50\text{ }^\circ\text{C}$, 24 h.

Table 2.2. Characterization of the thioether-bearing block copolymers.

Polymers	n^a	m^a	M_w/M_n^b	D_h [nm] ^c	PDI ^c	CMC [μ M] ^d
PPFPA20	20		1.14	-	-	-
PPFPA40	40		1.10	-	-	-
PAM-PPFPA20	-	90	1.10	-	-	-
PAM-PPFPA40	-	90	1.10	-	-	-
TP20	-		1.22	155 \pm 6	0.53 \pm 0.06	20.9
TM20	-		1.28	30 \pm 4	0.17 \pm 0.03	12.9
TPh20	-		1.11	29 \pm 5	0.09 \pm 0.01	3.2
TP40	-		1.21	183 \pm 7	0.56 \pm 0.03	19.6
TM40	-		1.24	25 \pm 3	0.17 \pm 0.01	4.7
TPh40	-		1.19	28 \pm 4	0.08 \pm 0.01	1.7

^a Determined by ¹H NMR.

^b Weight average molecular weight (M_w) and number average molecular weight (M_n) determined by GPC using polystyrene standard.

^c Hydrodynamic diameter (D_h) and polydispersity index (PDI) of the micelles in PBS as determined by DLS using the cumulant method.

^d Critical micelle concentration (CMC) in water as determined by the Nile red fluorescence assay.

2.3.3 Preparation and Characterization of the Thioether-Bearing Micelles

The micelles were prepared by self-assembly of the TP, TM, and TPh diblock copolymers from organic solvent in water. In all cases, the thioether-bearing block was hydrophobic enough to drive micellization. The TM20, TM40, TPh20 and TPh40 polymers formed monodisperse micelles with a diameter (D_h) in the range of 25-30 nm as determined by DLS (**Table 2.2**). There was no obvious effect of the thioether-bearing block length on micelle size. In contrast, the TP20 and TP40 polymers showed a broad peak in the range of 50-200 nm. The morphology of the

micelles was confirmed by TEM using the negative staining method (**Figure 2.7**). Monodisperse spherical structures were observed for TM20, TM40, TPh20, and TPh40 micelles. While DLS did not show a notable effect of thioether block length on D_h , the TEM images of the micelles formed from the polymers with a longer thioether-bearing block (TM40 and TPh40) appeared much larger compared to those obtained for the shorter polymers (TM20 and TPh20). Since only the hydrophobic core of the micelles can be observed with the negative staining method and not the PAM corona, the TEM images indicate that the polymers with a longer thioether-bearing block form a micelle with a larger hydrophobic core. The size of TP20 and TP40 micelles were rather heterogeneous containing some large spherical structures of about 50 nm. Furthermore, the critical micelle concentrations (CMCs), the polymer concentration above which micelles form, were determined by the Nile red method to assess the thermodynamic stability of micelles. (**Figure A.10**, Supporting Information).¹⁵⁷ TPh20 micelles showed the lowest CMC indicating the highest structural stability compared to TM20 and TP20 micelles (**Table 2.2**). This may be due to the lower aqueous solubility and/or π - π stacking of the aromatic ring of TPh groups, which stabilizes the micellar structure. Furthermore, the polymers with a longer thioether-bearing block exhibited lower CMCs, showing that a longer hydrophobic polymer chain stabilizes the micellar structure.

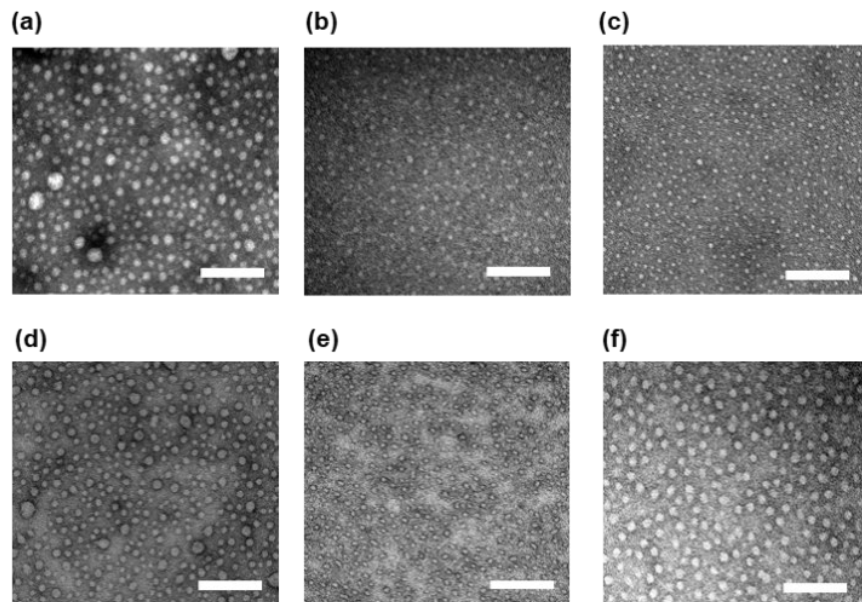


Figure 2.7. TEM image of the micelles negatively stained with 2% uranyl acetate solution. (a) TP20, (b) TM20, (c) TPh20, (d) TP40, (e) TM40, (f) TPh40. Scale bars: 200 nm.

2.3.4 Dissociation of Thioether-Bearing Micelles in Response to H_2O_2

We tested whether the thioether-bearing micelles dissociate in the presence of H_2O_2 . The size distributions of the thioether-bearing micelles (1 mg/mL) incubated with 100 mM H_2O_2 (aq) at 37°C were measured by DLS. In the case of TP20 micelles, the intensity of the scattered light decreased rapidly within 2 h, showing dissociation of the micelles in the presence of H_2O_2 (**Figure 2.8a**). The TM20 micelles also showed a significant decrease in the scattered light intensity after 2 h (**Figure 2.8b**). Although no dissociation of TPh20 micelles was observed for 8 h, the intensity of the scattered light by the micelles significantly decreased after 12 h (**Figure 2.8c**). For the micelles having a longer thioether-bearing block (TP40, TM40, TPh40), the dissociation was slower compared to the polymers with a shorter thioether-bearing block as shown in **Figure 2.8d-f**. Interestingly, while the peak due to the original TP40 micelles disappeared within 2 h, larger particles of 500-700 nm appeared, which might be due to the aggregation of the partially

oxidized/destabilized micelles. The formation of larger structures was also observed for TM40 after 8 h. Micelle dissociation after H₂O₂ treatment was also confirmed by TEM using the negative staining method. For TP20 and TM20 micelles, the micellar structures were not observed after 24 h as shown in **Figure A.11a-b** (Supporting Information). In the case of TPh20 micelles, spherical structures were still observed even after 24 h (**Figure A.11c**, Supporting Information). Similarly, no micellar structures were observed for the TP40 and TM40 micelles after 24 h as shown in **Figure A.12a-b** (Supporting Information), while spherical structures could be still observed for TPh40 micelles (**Figure A.12c**, Supporting Information). These TEM images are in agreement with the changes observed by DLS. It should be noted that the positively stained (black) spots that appear in the TEM images of TP20, TM20, TP40, and TM40 micelles treated with H₂O₂ are due to the interaction of sulfoxide and/or thioether groups of the dissociated polymers with uranyl acetate resulting in aggregation. This is supported by our observation that the H₂O₂ treated samples became turbid upon the addition of the uranyl acetate staining solution, whereas the micelle solution without H₂O₂ stayed clear. Furthermore, to show that micelle dissociation was induced by the oxidation of the thioether groups, the presence of sulfoxides was confirmed by FT-IR. As shown in **Figure A.13** in Supporting Information, we observed the sulfoxide vibration at around 1100 cm⁻¹ for TP20, TM20, and TPh20 micelles treated with H₂O₂.

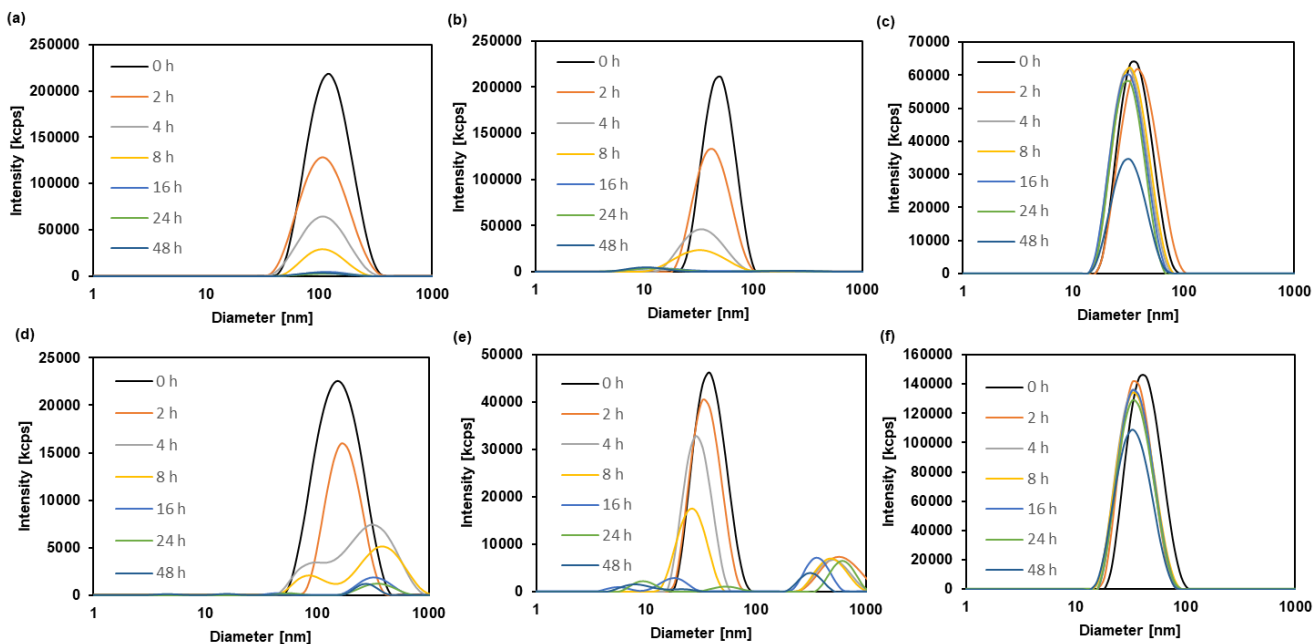


Figure 2.8. Dissociation of the thioether-bearing micelles upon oxidation. The micelles (0.9 mh/mL) were treated with H_2O_2 (1 eq. to thioether groups) at 37°C . At the indicated time points, the size distribution of the micelles was measured by DLS. (a) TP20, (b) TM20, (c) TPh20, (d) TP40, (e) TM40, (f) TPh40. H_2O_2 concentration: (a-c) 1mM, (d-f) 2 mM.

2.3.5 Dissociation of Thioether-Bearing Micelles in HepG2 cells

To monitor the dissociation of the micelles under physiologically relevant conditions, we prepared thioether-bearing micelles containing self-quenched fluorescein isothiocyanate (FITC) fluorophores in the micelle core (**Figure 2.9a**). The intact micelles are expected to be non-fluorescent due to self-quenching of FITC, whereas dissociation of the micelles will cause a recovery of fluorescence.¹⁶⁷ The micelles were incubated in 100 mM H_2O_2 (aq) at 37°C , and the fluorescence recovery of the micelles was monitored (**Figure 2.9b**). A rapid increase of fluorescence intensity was observed for the TP/FITC micelles, which reached a plateau after 2 h. The TM/FITC micelles showed a slower fluorescence increase compared to the TP/FITC micelles and complete dissociation was observed after 9 h. Furthermore, much slower fluorescence recovery was observed for the TPh/FITC micelles, which required 50 h for complete dissociation.

These results are in good agreement with the change in the size distribution of the micelles in the presence of H₂O₂ (**Figure 2.8**) and follow the reactivity trend of the thioether model compounds towards H₂O₂ oxidation (**Figure 2.4b**).

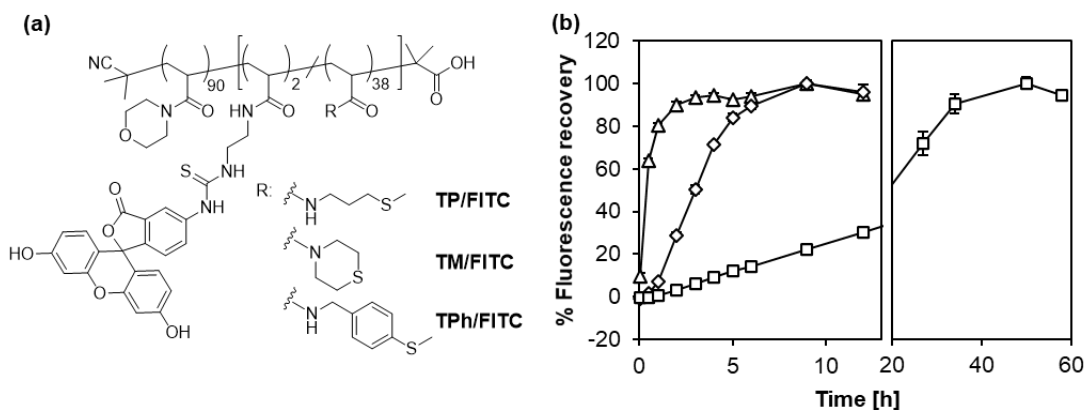


Figure 2.9. Dissociation of the thioether-bearing micelles in the presence of H₂O₂. (a) Chemical structure of the thioether/FITC-bearing micelles. (b) Dissociation of the thioether/FITC-bearing micelles upon oxidation as determined by fluorescence recovery of self-quenched FITC fluorophores. The TP/FITC (triangles), TM/FITC (diamonds) and TPh/FITC (squares) micelles (0.05 mg/mL in PBS (pH7.4, 100 mM)) were incubated with 100 mM H₂O₂ at 37°C and the fluorescence intensity ($\lambda_{\text{ex}}=490$ nm, $\lambda_{\text{em}}=520$ nm) was measured at different time points. $n=3$.

We next evaluated the dissociation of the thioether/FITC-bearing micelles in human liver cancer HepG2 cells. It is known that cancer cells produce elevated levels of ROS.^{168–171} Therefore, we hypothesized that the micelles would be oxidized by intracellular ROS after cellular uptake and subsequently dissociated. HepG2 cells were treated with the thioether/FITC-bearing micelles for 24 h and observed by CLSM after 4 and 24 h to assess micelle dissociation (**Figure 2.10a-h**). To show that the dissociation of the micelles can be inhibited by scavenging intracellular ROS, we also pretreated the cells with the ROS scavenger *N*-acetylcysteine (NAC) before treatment with the micelles. For cells without NAC treatment (NAC(-)), bright fluorescence spots (yellow color in **Figure 2.10**) appeared within cells after 4 h of incubation with TP/FITC micelles while those yellow spots in NAC-treated cells were significantly weaker. This result clearly shows that the

dissociation of TP/FITC micelles was induced by intracellular ROS. For TM/FITC micelles, the fluorescence was relatively weak after 4 h but became stronger after 24 h, which is different from TP/FITC micelles, which showed strong FITC fluorescence at the earlier time point (4 h) and exhibited minimal change after 24 h (**Figure 2.10b** and **f**). This indicates that TP/FITC micelles undergo a dissociation at an earlier time point compared to TM/FITC micelles. In addition, the fluorescence observed in the cells treated with TPh/FITC micelles was much weaker than that observed in the cells treated with TP/FITC and TM/FITC micelles, showing that TPh/FITC micelles are more stable than TP/FITC and TM/FITC micelles. These results are in line with the different dissociation rates of the micelles in the presence of H₂O₂ as shown in **Figure 2.9b**.

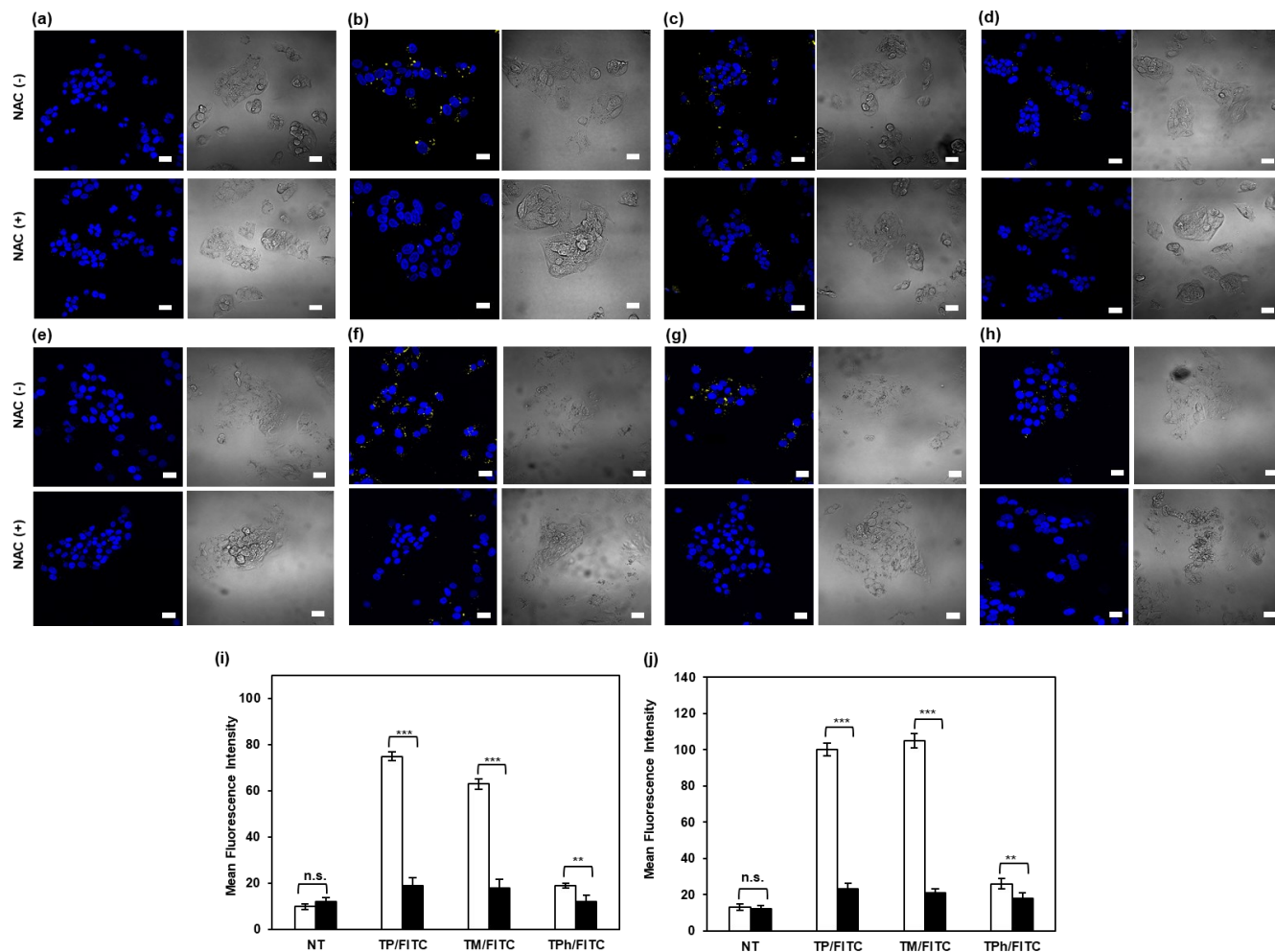


Figure 2.10. Dissociation of the thioether/FITC-bearing micelles in HepG2 cells. HepG2 cells were treated with (a,e) medium only, (b, f) TP/FITC, (c, g) TM/FITC, (d, h) TPh/FITC micelles for (a-d) 4 h and (e-h) 24 h in the absence/presence of the ROS scavenger *N*-acetylcysteine (NAC, 5 mM). An increase in the fluorescence intensity of the thioether/FITC micelles due to dissociation was observed by CLSM. Left panel: Hoechst 33342 (nucleus, blue) and FITC (yellow), Right panel: DIC. Scale bars: 20 μ m. (i,j) Intracellular fluorescence intensity in HepG2 cells treated with thioether/FITC-bearing micelles. The CLSM images were analyzed to determine fluorescence intensity within HepG2 cells nontreated (NT) and treated with TP/FITC, TM/FITC, and TPh/FITC micelles for (i) 4 and (j) 24 h in the absence (open columns) or presence (filled columns) of NAC. ** $p < 0.01$, *** $p < 0.001$, n.s. $p > 0.05$ ($n = 3$).

2.3.6 Dox-Loaded Thioether-Bearing Micelles

To explore the potential application of the thioether-bearing micelles for drug delivery applications, we encapsulated the anticancer drug doxorubicin (Dox) in the micelles to evaluate

their functions as drug carriers. Dox and the thioether-bearing polymers (1:5 by weight) were mixed in *N*-methyl pyrrolidone (NMP) and added dropwise to water to prepare Dox-loaded micelles. As shown in **Figure 2.11a**, all micelles had drug loading capacities of >15 w/w% (weight ratio of Dox/micelle). In the case of TPh20 and TPh40 micelles, nearly all Dox was encapsulated (about 20 w/w%), which may be due to the strong interaction between the aromatic ring of TPh and anthraquinone rings of Dox. Furthermore, there was no obvious effect of thioether block length on Dox loading.

Dox release from the thioether-bearing micelles was measured in the presence of 10 mM H₂O₂ at 37°C. As shown in **Figure 2.11b-d**, the amount of Dox released was significantly higher in the presence of H₂O₂ showing that the micelles release Dox in response to H₂O₂. TP40, TM40, and TPh40 micelles released approximately 3, 2.5, and 2 times higher amount of Dox after 1 h of incubation with 10 mM H₂O₂ relative to the non-treated micelles (H₂O₂ (-)). This observation agrees with the oxidation-sensitive dissociation of the micelles as shown by DLS (**Figure 2.8**) and the fluorescence recovery assay (**Figure 2.9b**) where TP40 micelles exhibited the fastest dissociation followed in order by TM40 and TPh40 micelles.

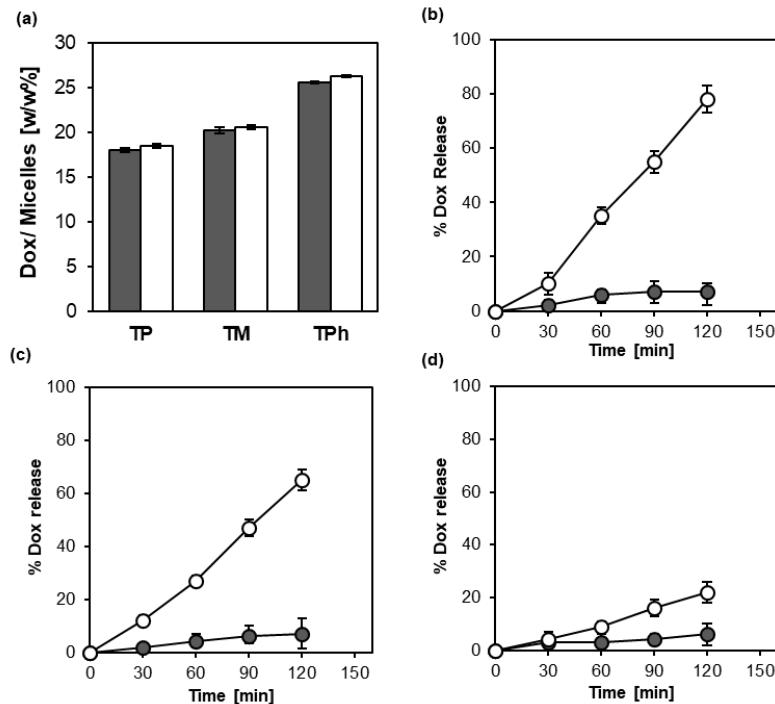


Figure 2.11. Characterization of Dox-loaded thioether-bearing micelles. (a) Dox loading for the different micelle solutions. Dox was mixed with thioether-bearing micelles (Dox:micelles = 1:5 by weight) in NMP and added dropwise to water to prepare Dox-loaded micelles. Free Dox was removed from the micelles by ultrafiltration and quantified by UV-Vis spectroscopy to determine the Dox loading capacity (Dox/micelles w/w%). Gray bar: TP20, TM20 and TPh20, White bar: TP40, TM40 and TPh40. $n=3$. (b-d) Dox release in response to H₂O₂. The thioether-bearing micelles (b), TP40, (c) TM40, (d) TPh40 loaded with Dox (Dox concentration: 4 mM) were incubated in the absence (grey circles) or presence (white circles) of 5 mM H₂O₂ at 37°C. $n=3$.

The cytotoxicity of the Dox-loaded micelles was evaluated in HepG2 cells and human umbilical endothelial cells (HUVECs) by MTT assay. As shown in **Figure 2.12a** and **Table 2.3**, encapsulating Dox in the TP40 and TM40 micelles significantly increased its cytotoxicity in HepG2 cells as shown by the lower LC₅₀ values compared to Dox alone. The LC₅₀ value for Dox-loaded TPh40 micelles was slightly higher compared to the TP40 and TM40 micelles but lower than Dox alone. These results indicate that TP40 and TM40 micelles efficiently released Dox in HepG2 cells, which are known to overproduce ROS^{168–171}, while the TPh40 micelles were not sensitive enough to release similar amounts of Dox in response to ROS produced by HepG2 cells.

In contrast to HepG2 cells, TM40 and TPh40 micelles showed significantly higher LC₅₀ (i.e., lower cytotoxicity) than Dox alone in HUVECs having basal levels of ROS (**Figure 2.12b**). This protective effect in HUVECs seems to relate to the higher stability of these micelles in the presence of ROS at basal levels, which prevents the release of Dox within HUVECs. Compared to TM40 and TPh40 micelles, Dox encapsulated in TP40 micelles showed higher toxicity, indicating TP40 micelles with a high sensitivity towards ROS can be destabilized by basal ROS levels in HUVECs resulting in Dox release. Overall, TM40 micelles, exhibiting moderate ROS sensitivity, seems to be the most promising drug carrier to increase the cytotoxicity of Dox in cancer cells (HepG2) but protect normal cells (HUVECs) from the side effects of Dox. It is important to note that all micelles without Dox were not toxic at concentrations up to 1 mg/mL (**Figure A.14**, Supporting Information), which is higher than the micelle concentrations tested in **Figure 2.12**.

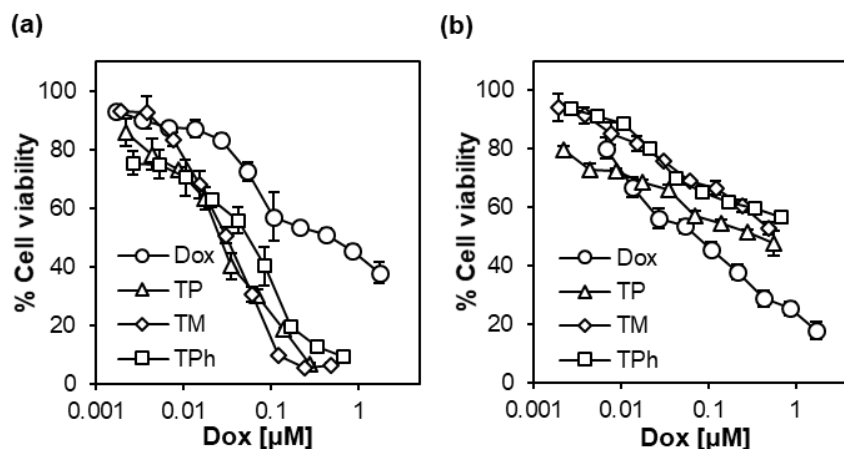


Figure 2.12. Cytotoxicity of the Dox-loaded micelles in (a) HepG2 cells and (b) HUVECs. Cells were cultured in the presence of Dox and Dox-loaded micelles for 2 d. Cell viability was measured by MTT assay. $n=3$.

Table 2.3. LC₅₀ values of Dox and the Dox-loaded micelles in HepG2 cells and HUVECs as determined by MTT Assay.

	LC ₅₀ [μ M]	
	HepG2	HUVEC
Dox	0.520	0.077
Dox-TP40	0.028	0.385
Dox-TM40	0.031	>0.480
Dox-TPh40	0.060	>0.67

To understand the reason for the enhanced cytotoxicity of the Dox-loaded micelles in HepG2, we further explored how the thioether-bearing micelles affect the intracellular distribution of Dox in HepG2 cells using its intrinsic fluorescence properties. In contrast to Dox alone, which shows immediate accumulation in the nucleus, the majority of Dox was observed in the cytoplasm along with the moderate accumulation of Dox in the nucleus after 4 h in the case of Dox-loaded micelles (**Figure 2.13**). Since the FITC-labeled micelles were observed only in the cytoplasm and not in the nucleus as shown in **Figure 2.10**, it is unlikely that Dox-loaded micelles entered the nucleus. This implies that Dox must have been released from the micelles in the cytoplasm in order to enter the nucleus. Therefore, the observed slow accumulation of Dox in the nucleus suggests a sustained release of Dox from the micelles inside the cells.

To evaluate the colocalization of Dox with the nucleus in a quantitative way, we determined the Pearson's Correlation Coefficient (PCC) from the 3D Z-stack images. PCC values close to 1 indicate that fluorescence intensities of two probes are perfectly and linearly related (i.e., colocalization), a value of zero indicates that the distributions of two probes are not correlated with one another (no colocalization), and values near -1 imply the perfect inverse colocalization of two

probes. As shown in **Figure 2.14**, the PCC values increased within 1 h for Dox showing rapid colocalization with the nucleus while the Dox-loaded micelles show intermediate PCC values (0.3-0.5) even after 4 h, indicating a moderate correlation of the Dox and Hoechst fluorescence signals. This difference between Dox and the Dox-loaded micelles seems to be due to a sustained release of Dox from the micelles. Therefore, enhanced toxicity of the Dox-loaded micelles can be attributed to the sustained release of Dox from the micelles as shown by CLSFM, enabling continuous delivery of Dox for an extended period. In addition, it has been reported that while Dox is prone to hydrolysis in physiological buffer solution, encapsulating Dox within a hydrophobic core of micelles significantly slows down its hydrolysis.¹⁷² Therefore, it is possible that the beneficial effects of the micelles is also due to the improved chemical stability of Dox under biological condition.

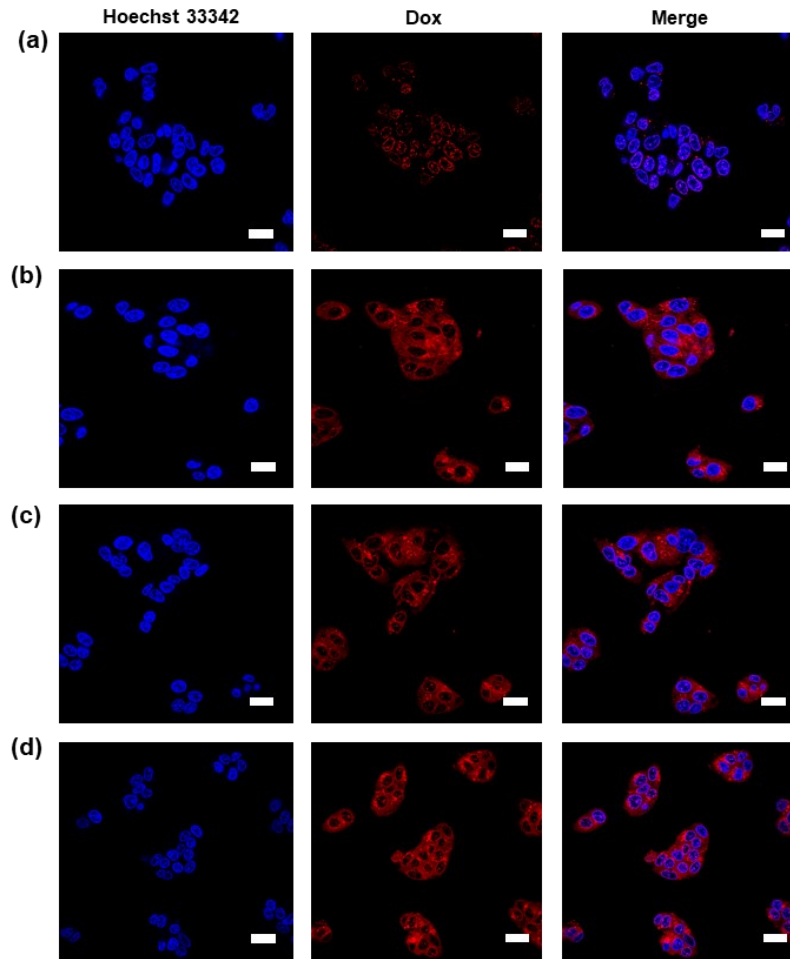


Figure 2.13. Intracellular distribution of Dox in HepG2 cells. Cells were cultured in the presence of (a) Dox and the Dox-loaded micelles (b)TP40, (c) TM40 and (d) TPh40. After culturing for 4 h, cells were observed by CLSFM. Dox concentration: 0.5 μ M. Left panel: Hoechst 33342 (nucleus, blue), center: panel Dox (red), Right panel : Merged. Scale bars: 20 μ m.

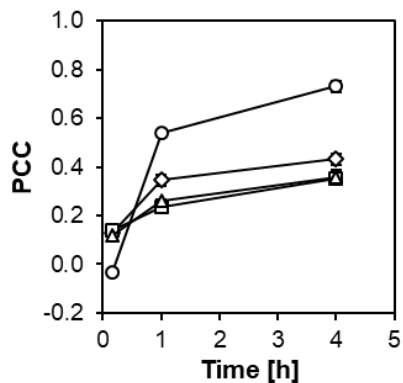


Figure 2.14. Colocalization analysis of Dox with the cell nucleus (Hoechst 33342) of HepG2 cells. Person's correlation coefficient (PCC) was calculated from the CLSFM 3D image slices obtained at the indicated time points. Free Dox (circles), Dox-loaded micelles. TP40 (triangles), TM40 (diamonds) and TPh40 (squares). $n=3$.

2.4 Conclusion

We herein report a library of thioether-bearing polymeric micelles with different oxidation sensitivities. The effects of substituent groups on the H_2O_2 oxidation of thioether were first investigated using different thioether model compounds, 3-methylthiopropylamide (TPAM), thiomorpholine amide (TMAM), and 4-(methylthio)benzylamide (TPhAM). TPAM with a more nucleophilic sulfur atom, according to Bader charge analysis, showed much faster oxidation than TPhAM. On the other hand, the cyclic thioether TMAM, which showed a higher charge density than TPAM exhibited slower oxidation than TPAM. These results indicate that both electronic and steric effects contribute to the oxidation rate of thioethers. A similar trend was observed for the polymeric micelles bearing these thioether groups (TP, TM, and TPh micelles). Micelle dissociation following the oxidation of thioether groups was confirmed both in the presence of H_2O_2 and human liver cancer HepG2 cells, which produce elevated levels of ROS. The dissociation rate was faster for TP micelles followed in order by TM and TPh micelles. Furthermore, the thioether-bearing micelles were loaded with Dox and their potential application

in cancer treatment was investigated. Among the micelles, TM micelles significantly increased the toxicity of Dox in HepG2 cells but protected normal cells (HUVECs) from Dox cytotoxicity. These results clearly show that the dissociation of thioether-bearing micelles can be modulated by designing thioether groups with different substituent groups. Therefore, fine-tuning oxidation sensitivities of the thioether groups is a promising approach for rationally designing cancer cell-specific drug delivery systems that release drugs in cancer tissues under oxidative stress but are stable in healthy tissues.

3 ROS-sensitive hydrogen sulfide donor micelles for cancer-targeted delivery

The work in this chapter was done under the mentorship of Dr. Urara Hasegawa during her tenure at Kansas State University

Abstract

Hydrogen sulfide (H_2S), an important gaseous signaling molecule in the human body has shown immense therapeutic potential such as inhibition of cancer cell proliferation. Since the anti-cancer effect of exogenous H_2S is known to be significantly affected by the concentration and duration of exposure, the development of H_2S -releasing materials with controlled release of H_2S is thereby crucial. Despite the development of several H_2S donors that exhibit controlled release of H_2S , there is a lack of site-specific delivery of H_2S especially to cancer cells. Here, reactive oxygen species (ROS)-sensitive polymeric micelles were prepared from amphiphilic block copolymers consisting of a hydrophilic poly(*N*-acryloyl morpholine) (PAM) segment and a hydrophobic segment bearing H_2S -releasing anethole dithiolthione (ADT) group and an oxidation-sensitive thioether motif (TP) for selective and controlled delivery of H_2S to cancer cells in response to elevated levels of ROS. In the presence of hydrogen peroxide (H_2O_2), a greater release of H_2S was observed in colon cancer cells from the ROS-sensitive micelles due to the faster dissociation rate compared to the non-sensitive micelles and the H_2S donor (ADT). Furthermore, the ROS-sensitive micelles exhibited greater anti-proliferative activity in colon cancer with no obvious cytotoxicity in human umbilical endothelial cells (HUVECs), which is known to produce basal levels of ROS.

3.1 Introduction

Hydrogen sulfide (H₂S) has been recognized as an important cellular signaling molecule belonging to a family known as gasotransmitters along with nitric oxide (NO) and carbon monoxide (CO). In the body, H₂S is ubiquitously produced by the action of a series of enzymes consisting of cystathionine γ -lyase (CSE), cystathionine β -synthase (CBS), and 3-mercaptopyruvate sulfur transferase (3-MST).²⁷ Accumulating evidence has shown that both endogenous production of H₂S and exogenous administration of H₂S exerts diverse regulatory functions in the body including proangiogenic,^{33,173,174} vasodilatory,¹⁷⁵ neuromodulatory,³⁰ anti-apoptotic,¹⁷⁶ anti-inflammatory,¹⁷⁷ anti-cancer,^{36,178,179} and cytoprotective effects.³⁵ Among the diverse therapeutic effects of H₂S, its dual role in cancer biology has attracted vast attention. An increase in expression of the three main H₂S producing enzymes, cystathionine γ -lyase (CSE), cystathionine β -synthase (CBS), and 3-mercaptopyruvate sulfurtransferase (3MST) has been reported in numerous types of cancer, suggesting that endogenous H₂S production is important for the growth and proliferation of cancer.^{180–183} Inhibition or silencing of CBS particularly in colon, ovarian, and breast cancer have been explored and were shown to exhibit anti-tumor activity.^{184,185} Interestingly, the anti-cancer effects by inhibition or silencing of H₂S biosynthesis is contradicted by many studies where exogeneous administration of H₂S exert anti-cancer effects *in vitro* and *in vivo*.^{178,179,186–189} To date, sulfide salts such as Na₂S and NaHS are the most widely used H₂S donors to study the biological activities of H₂S. While convenient, there is a discrepancy in the release rate along with a proper dosage of H₂S to suppress the growth of cancer cells due to the instantaneous and uncontrollable release of H₂S from these salts, which do not accurately mimic the controlled endogenous production of H₂S.

With the increasing awareness of the role of H₂S in cancer biology, which has been reported to be heavily dependent on the concentration, duration, and location of H₂S exposure, many studies have been reported with varying H₂S donors used to evaluate its potential in suppressing cancer cell growth. Synthetic H₂S donors including Lawesson's reagent derivatives such as morpholin-4-ium 4-methoxyphenyl(morpholino) phosphinodithioate (GYY4137),¹⁸⁸ anethole dithioethione (ADT) derivatives such as ADT-OH,³⁹ and naturally occurring polysulfides such as diallyl trisulfide (DATS)^{41,42} with various H₂S release mechanisms have attracted attention in studying the anti-cancer effects of H₂S due to their protective effects and ability to release H₂S over a prolonged period of time. For example, continuous exposure of the water-soluble and slow-release H₂S donor GYY4137 at high concentrations was shown to remarkably inhibit cancer cell proliferation in various cancer cell lines by induction of cell cycle arrest, apoptosis, and intracellular acidification.^{186,188} A similar effect was observed in colorectal cancer (Caco-2) where treatment with 0.5-1.0 mM GYY4137 inhibited proliferation by induction of cell cycle arrest, apoptosis, and necrosis.¹⁷⁹ More recently, a novel hybrid H₂S-releasing donor, HA-ADT with hyaluronic acid (HA) conjugated to ADT-OH demonstrated superior ability in releasing greater amounts of H₂S and significantly inhibiting proliferation through suppression of angiogenesis in human breast cancer cells compared to other donors (NaHS and GYY4137).¹⁹⁰ Despite the promising results of these donors in exhibiting anti-cancer effect, there is a lack of site-specificity as most of these H₂S donors utilize molecular triggers that are ubiquitously present in the body, thus inducing H₂S release in any part of the body. Hence, these donors are less viable in studying the anti-cancer effects of H₂S in specific target cells or tissues.

To achieve site-specific delivery of H₂S, donors that release H₂S in response to stimuli such as reactive oxygen species (ROS),⁵⁰ enzyme activation,⁴⁶ light,¹⁹¹ and pH⁴⁸ modulation have

emerged as a promising approach and demonstrated superior protective effects. Of particular interest is the ROS-activated carbonyl sulfide (COS) donors reported by Pluth and co-workers, where COS release is triggered by hydrogen peroxide (H_2O_2) commonly overproduced in many pathological conditions, followed by hydrolysis to produce hydrogen sulfide by ubiquitous enzyme carbonic anhydrase.⁵⁰ This was the first example of H_2S donor triggered by disease-specific cellular species and was capable of exhibiting cytoprotective effects against oxidative stress in cervical cancer cell (HeLa). Despite the promising potential of these diverse arrays of H_2S donors, several challenges still remain in regards to the delivery of H_2S to cancer cells. First, a majority of H_2S donors still show relatively fast H_2S release under physiological conditions which is not desirable for therapeutic in suppressing cancer cell growth requiring sustained release of H_2S . Secondly, the biological effects of these low molecular weight organic compounds are often blurred due to their decomposition products. In addition, these small donors are rapidly removed from the blood circulation by renal clearance, resulting in low therapeutic efficiency.

Macromolecule-based donors such as polymer-drug conjugates as well as polymeric nanoparticles have been known to significantly prolong the blood circulation time of drugs, enhance their accumulation in the target tissues and alleviate side effects. In the field of H_2S delivery, there have been several reports of macromolecule-based systems for H_2S delivery.^{52,192} Previously, a polymeric H_2S donor micelle containing ADT moiety in the micellar core capable of protecting rat cardiomyocytes from ischemic cell death, owing to the sustained release profile of H_2S compared to the donor alone (ADT-OH) was reported.¹⁹³ Foster and colleagues reported a S-arylothiooxime (SATO) functionalized amphiphilic block copolymer micelles, which showed a substantially slower cysteine-triggered H_2S release compared to the donor (SATO) alone and demonstrated anti-cancer activity.⁵² The micelles significantly reduced the survival of HCT116

colon cancer cells compared to Na₂S, SATO, and GYY4137 donors, but was well tolerated by immortalized fibroblasts (NIH/3T3 cells). Interestingly, this was one of the first studies that demonstrated the ability of H₂S macromolecule-based systems to selectively suppress cancer cell growth, which the authors attributed to the sustained release of H₂S. Although the H₂S donor micelles show sustained H₂S release compared to their respective small H₂S donors, the lack of cell-type specificity may be a drawback in understanding the exact role of H₂S, especially in cancer biology.

Here, we designed and synthesized H₂S donor micelles containing H₂S-donating ADT groups as previously reported^{51,174} with the addition of an oxidation-sensitive thioether group in the hydrophobic micellar core for site-specific delivery of H₂S in response to elevated levels of reactive oxygen species (ROS) in cancer cells (**Figure 3.1**). Thioether-containing polymers are among the most widely used building blocks to confer oxidation sensitivity to drug carriers. Thioethers that have low dipolar moments are known to be oxidized by ROS to polar sulfoxides and, in part, sulfones. We envisioned that the H₂S release profile from the micelles will be modulated by controlling the micellar association/dissociation in response to elevated levels of ROS at diseased sites such as cancer cells, where the thioether groups will be converted to hydrophilic groups and thereby destabilize the micellar structure. Dissociation of these micelles in the presence of H₂O₂ and human colon cancer HT29 cells was investigated. Furthermore, the cytotoxicity of these micelles in HT29 and human umbilical vein endothelial cells (HUVECs) were evaluated.

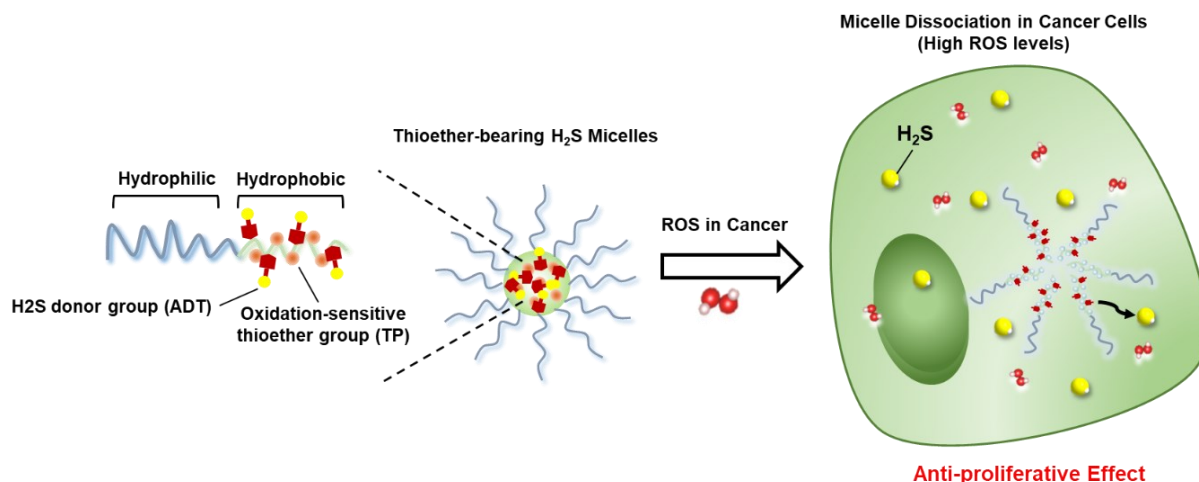


Figure 3.1. H₂S donor micelles bearing oxidation-sensitive thioether group for targeted delivery of H₂S in cancer cells with elevated levels ROS (courtesy of Hasegawa and Radaha).

3.2 Experimental Procedures

3.2.1 Materials

Pentafluorophenyl acrylate (PFPA) was purchased from Tokyo Chemical Industry (USA). 4-acryloylmorpholine (AM), 2,2'-azobis(isobutyronitrile) (AIBN), 2-(dodecylthiocarbonothioylthio)-2-methylpropionic acid (CTA), aluminum oxide (Al₂O₃), 1-methyl-2-pyrrolidinone (NMP), deuterated chloroform (CDCl₃) deuterated dimethyl sulfoxide ((CD₃)₂SO), calcium hydride (CaH₂), trifluoroacetic acid (TFA), sodium dodecyl sulfate (SDS), phosphor pentoxide (P₄O₁₀) and 4Å molecular sieves were purchased from Sigma Aldrich (USA). Tris(trimethylsilyl)silane, 1,4-dioxane, anhydrous dimethylformamide (DMF), tetrahydrofuran (THF), diethyl ether (Et₂O), ethanol (EtOH), hexane (HA) triethylamine (TEA), potassium hydroxide (KOH) pellets, hydrogen peroxide (H₂O₂) solution (50 wt%), hydrochloric acid (HCl), Tricine, Sodium Chloride (NaCl), calcium chloride (CaCl₂), Leucine, Nile red, Hoechst 33342, McCoy's 5A, fetal bovine serum, penicillin-streptomycin, and trypsin-EDTA were purchased from Fisher Scientific (USA). Fluorescamine was purchased from

Acros Organics. XPell pellets were purchased from Xplosafe (USA). Regenerated cellulose dialysis tubing (MWCO 2 kDa) was purchased from Spectrum Laboratories (USA). ADT-NH₂ was synthesized as reported previously.¹⁹⁴ Sephadex LH20 and G20 were purchased from GE Healthcare (USA). WSP-1 fluorescent probe was purchased from Cayman Chemical Company (USA). HT29 cells were purchased from ATCC (USA). Amicon[®] Ultra 4 mL Centrifugal Filters, transparent and black 96 well plates and disposable 5 mL polypropylene columns were purchased from Thermo Fisher Scientific (USA). The glass-bottom dishes were purchased from Matsunami Glass (USA). 200 mesh carbon-coated copper grids were purchased from Electron Microscopy Science (USA).

Pentafluorophenyl acrylate and 4-acryloylmorpholine were passed through a plug of Al₂O₃ to remove the inhibitor. AIBN was recrystallized from MeOH. 2-(dodecylthiocarbonothioylthio)-2-methylpropionic acid was recrystallized from HA. 1,4-dioxane was distilled from CaH₂ and kept over molecular sieves and XPell pellets. TEA was dried over KOH pellets. Other reagents were used as received without further purification.

3.2.2 Instrumentation

Proton NMR (¹H NMR) Spectroscopy. ¹H NMR spectra were measured with a Varian 400MHz NMR spectrometer. A number of 32 scans was collected and the delay time (D1) was set to 10 s for polymers and 1 s for small compounds. The chemical shifts are referenced to the residual undeuterated NMR solvent signal at 7.26 ppm (CDCl₃) and 2.50 ((CD₃)₂SO),

Attenuated Total Reflection Infrared Spectroscopy (ATR-IR). Attenuated total reflection infrared (ATR-IR) spectra were obtained using a Perkin Elmer Spectrum 400 spectrometer.

Gel Permeation Chromatography (GPC). Elution profiles of the polymers were obtained using a ResiPore PL1113-6300 GPC column on an Agilent Technologies 1220 Infinity II LC GPC

system equipped with a 1260 RI detector and a 1260 MCT column oven. THF was used as the eluent with a flow rate of 1.0 mL/min. The temperature of the RI detector and column oven was 40 °C. The polymers were dissolved in THF at 5 mg/ml and 10 µL of the solution was injected. The polydispersity index (M_w/M_n) was calculated from the elution profiles of a polystyrene standard (Agilent).

UV-Vis spectroscopy. The UV/Vis spectra were measured on a Thermo Scientific Nanodrop One^c spectrophotometer.

Dynamic Light Scattering (DLS). Dynamic light scattering measurements were done using a Malvern Zetasizer Nano ZS Series instrument. Freshly prepared micelle solutions were filtered using a polyethersulfone (PES) syringe filter (pore size: 0.45 µm) and placed in disposable micro cuvettes (ZEN0040, Malvern). The Z-average diameter and polydispersity index (PDI) of the micelles were determined by the cumulant method.

Transmission Electron Microscopy (TEM). The morphology of the micelles was observed by transmission electron microscopy using the negative staining method. The micelle solution (1 mg/ml in water) was mixed with 2 w/v% uranyl acetate aqueous solution (volume ratio of 1:1) and added to 200 mesh carbon-coated copper grids. The grids were air-dried after removing the solution by blotting the side of the grid with filter paper. Images were acquired on a FEI Tecnai G2 Spirit BioTWIN instrument operating at 80 kV.

UV-Vis/fluorescence spectroscopy with Plate Reader. The UV-Vis absorbance and fluorescence intensities were measured with a Tecan infinite M200 plate reader.

Confocal Laser Scanning Fluorescence Microscopy (CLSM). Fluorescence images were acquired on an Olympus Fluoview FV1000-D confocal microscope equipped with 405, 473, 559, and 632 nm lasers.

3.2.3 Synthesis of PPFPA Homopolymer

PPFPA was synthesized by RAFT polymerization using AIBN as the initiator and 2-(dodecylthiocarbonothioylthio)-2-methylpropionic acid as the chain transfer agent (CTA). For PPFPA26, 595.3 mg (2.5 mmol) of PFPA, 36.5 mg (0.1 mmol) of CTA, and 1.64 mg (0.01 mmol) of AIBN were dissolved in 1,4-dioxane (Total volume: 2.5 mL). The reaction mixture was deoxygenated by six freeze-pump-thaw cycles, heated to 60 °C under argon and stirred for 24 h. The polymerization was stopped by quenching the reaction with liquid nitrogen and opening the Schlenk tube to air. After thawing to room temperature, the reaction mixture was added dropwise to 75 mL of EtOH. The precipitate was filtered, washed with EtOH (3x10 mL) and dried under reduced pressure to yield 485.3 mg of yellow solids. The filter was then washed with CH₂Cl₂ (3x4 mL) and evaporated at room temperature. After drying under reduced pressure, 20.8 mg of yellow solids were recovered with a total yield of 506.1 mg (80%). The polymers were characterized by ¹H NMR, GPC, and FT-IR as shown in Supporting Information.

3.2.4 Synthesis of PAM-PPFPA Diblock Copolymer

PAM-PPFPA diblock copolymer was synthesized by dissolving 352.9 mg (2.50 mmol) of AM, 157.9 mg (0.031 mmol) of PPFPA, and 0.3411 mg (0.0025 mmol) of AIBN in 1,4-dioxane (Total volume: 2.50 mL). The reaction mixture was deoxygenated by five freeze-pump-thaw cycles, heated to 60 °C under argon, and stirred for 24 h. The polymerization was stopped quenching the reaction with liquid nitrogen and opening the Schlenk tube to air. After cooling to room temperature, the reaction mixture was added dropwise to 75 mL of Et₂O. The precipitate was filtered, washed with 10 mL Et₂O (3x10 mL), and dried under reduced pressure to yield 433.3 mg yellow solids. The filter was then washed with CH₂Cl₂ (4x4 mL) and evaporated at room temperature. After drying under reduced pressure, 24.6 mg of yellow solids were recovered with

a total yield of 457.9 mg (89%). The polymers were characterized by ^1H NMR, GPC, and FT-IR as shown in the supporting information.

3.2.5 CTA End Group Removal from PAM-PPFPA Diblock Copolymer

The CTA end group was removed by radical-induced cleavage of the thiocarbonylthio group.¹⁹⁵ PAM-PPFPA polymer (400 mg, 0.017 mmol) and AIBN (109 mg, 0.67 mmol) were dissolved in 3 mL of 1,4-dioxane. The solution was deoxygenated by five freeze-pump-thaw cycles, heated to 70 °C under argon, and stirred for 24 h. The slightly purple reaction mixture was placed in liquid nitrogen and opening the Schlenk tube to air. After warming to room temperature, the reaction mixture was added dropwise to 80 mL of Et₂O. The precipitate was filtered, washed with Et₂O (2x10 mL), and dried under reduced pressure to yield 366.4 mg (92%) of white solids. The polymers were characterized by GPC and FT-IR as shown in Supporting Information.

3.2.6 Synthesis of ADTM and ADT-TPM Block Copolymers.

PAM-PPFPA polymer (30.3 mg, 0.034 mmol of PFPFA groups) was dried at 40 °C under vacuum for 24 h in the presence of P₄O₁₀. The polymer was dissolved in 0.80 mL anhydrous DMF followed by the addition of ADT-NH₂·TFA (6.52 mg, 0.017 mmol, 0.5 eq. relative to PFPFA₂₃ groups or 13.05 mg, 0.034 mmol, 1 eq. relative to PFPFA₂₆ groups) and TEA (0.034 mmol, 2 eq. relative to ADT-NH₂·TFA or 0.068 mmol, 2 eq. relative to ADT-NH₂·TFA). After three purge-evacuate cycles, the reaction mixture was heated at 50 °C under argon and stirred for 24 h. Next, TP-NH₂ (7.17 mg, 0.068 mmol, 4 eq. relative to remaining PFPFA₂₆ groups) was added to the reaction mixture under argon. The reaction mixture was heated at 50 °C under argon following three purge-evacuate cycles and stirred for another 24 h. The polymer was separated from unreacted ADT-NH₂ and pentafluorophenol by Sephadex LH-20 size exclusion column chromatography (column diameter: 13 mm, length: 250 mm) using DMF as the eluent. The absorbance at 436 nm of each

fraction (1 mL) was measured using Nanodrop and plotted as a function of elution volume to obtain the elution profile (**Figure B.4**, Supporting Information). Then, fractions containing the polymers were combined, diluted 2x with deionized (DI) water, and dialyzed against 4 L of DI water for 2 d, with regular replacement of the water. Polymers were recovered by lyophilization.

3.2.7 Preparation of Micelles

The ADTM and ADT-TPM block copolymers were dissolved in NMP (100 mg/mL) and added dropwise to DI water (volume ratio 1:9) under stirring (Final concentration:10 mg/mL). The solutions were dialyzed (MWCO, 2kDa) against 4 L of DI water for 3 d, with regular replacement of water. To determine polymer concentration after dialysis, part of the micelle solution was lyophilized and the amount of polymer was determined gravimetrically. The remaining micelle solution was concentrated and further purified using an Amicon Ultra-4 centrifugal filter followed by absorbance measurement at 436 nm using Nanodrop. ADT concentration was determined from a standard curve of ADT-NH₂ measured at 436 nm using Nanodrop.

3.2.8 Critical Micelle Concentration (CMC).

The CMC of the micelles was determined using the Nile red method.¹⁹⁶ To 350 μ L of the micelle solutions at different concentrations, 3.5 μ L of 0.1 mg/mL Nile red solution in DMSO was added. The micelle/Nile red mixtures were transferred to a 96-well plate (100 μ L/well, n=3) and incubated at room temperature for 2 h in the dark. The fluorescence intensity (λ_{ex} =530 nm, λ_{em} =630 nm) was recorded and plotted against log(concentration). The CMC values were determined based on the intersection between the linear fits of the low and high concentration regions as shown in **Figure B.5**, Supporting Information.

3.2.9 Dissociation of Micelles in the presence of H₂O₂

The-micelle solutions (2.5 mg/mL, 90 μL) in PBS (pH 7.4) were incubated with/without 10 μL H₂O₂ (Final concentration of H₂O₂: 100 mM) at 37 °C. The size distribution of the micelles was measured by DLS at indicated time points. The dissociation rate of micelles was determined as followed:

$$\% \text{ Intensity} = \frac{\text{Scattered light intensity at indicated time point [kcps]}}{\text{Scattered light intensity at time zero [kcps]}} \times 100$$

3.2.10 Cell Culture

HT-29 human colon cancer cells were cultured in McCoy's 5A medium containing 10% fetal bovine serum and 1% penicillin-streptomycin (10,000 U/mL) in a 5% CO₂ incubator at 37 °C. Human umbilical vein endothelial cells (HUVECs) were cultured in a vascular basal medium containing the endothelial cell growth kit-VEGF and Amphotericin B in a 5 % CO₂ incubator at 37 °C.

3.2.11 Cell Viability Assay in HT29 cells

HT29 cells and HUVECs were seeded in a 96-well plate at a density of 3.0 x 10³ cells/well and 5.0 x 10³ cells/well and cultured for 1 d. The medium was replaced with 100 μL/well of fresh medium containing ADTM and ADT-TPM micelles and the cells were cultured for 5 d for HT29 cells and 2 d for HUVEC cells in a CO₂ incubator. The medium was then replaced with 100 μL of 0.5 mg/ml of MTT in medium and the cells were cultured for 2 h. The formazan crystals formed

were dissolved in 100 μL /well of 100 mg/mL sodium dodecyl sulfate (SDS) solution in 0.01 M HCl (aq). The absorbance at 570 nm was measured using a microplate reader.

3.2.12 H₂S release from the micelles in HT29 lysate with the WSP-1 H₂S fluorescent detection probe

HT29 cell lysate was diluted with PBS at a volume ratio of 1 : 5 and mixed with WSP-1 (final concentration: 25 μM for WSP-1). This mixture was then mixed with the micelle solutions followed by H₂O₂ in a 96 well plate (final concentrations: 50 μM for ADT groups and 10 mM H₂O₂). The fluorescence intensity was measured as a function of time on the plate reader ($\lambda_{\text{ex}} = 465 \text{ nm}$, $\lambda_{\text{em}} = 515 \text{ nm}$).

3.2.13 H₂S Release by Fluorescent dye WSP-1 in HT29 Cells

Measurement of H₂S release in HT29 cell was performed as reported previously.¹⁹⁷ Briefly, HT29 cells were seeded in a 96-well plate (5×10^4 cells/well) and cultured for 1 d. The medium was replaced with 100 μL /well of WSP-1/DMSO in PBS (Final concentration of WSP-1 in DMSO: 25 μM) and incubated for 30 mins at 37 °C. Then, the WSP-1/DMSO in PBS solution was removed and 100 μL /well of fresh medium containing ADTM and ADT-TPM micelles were added (Final concentration of ADT: 50 μM). Fluorescence intensity ($\lambda_{\text{excitation}} = 480 \text{ nm}$, $\lambda_{\text{emission}} = 520 \text{ nm}$) was measured at indicated time points using a microplate reader. As a control, the cells were replaced with 100 μL /well of fresh medium.

3.3 Results and Discussion

3.3.1 Synthesis of ROS-sensitive H₂S Donor Micelles (ADT-TPM and ADTM)

In previous reports, polymeric micelles consisting of amphiphilic block copolymers composed of a hydrophilic PEG segment and hydrophobic segment bearing ADT moieties were prepared by reversible addition-fragmentation chain transfer (RAFT) polymerization. The micelles were shown to release H₂S significantly slower compared to the donor, ADT-OH as well as protect rat cardiomyocytes from ischemic damages in an in vitro ischemic model. Here, ROS sensitivity is conferred to the existing design of H₂S donor micelles to deliver H₂S site-specifically to diseased sites such as cancer cells, where elevated levels of ROS have been reported. The ROS-sensitive H₂S donor micelles were prepared with an amphiphilic diblock copolymer consisting of a hydrophilic poly(N-acryloyl morpholine) (PAM) block and a hydrophobic block bearing ROS-sensitive thioether and H₂S-releasing dithiolthione group (ADT) as shown in **Figure 3.2**. It is expected that the release of H₂S from the micelles would be modulated by the destabilization of the micellar structure in response to oxidation of thioether groups to sulfoxides or sulfones by ROS.

The block copolymer PAM-b-poly(pentafluorophenyl acrylate) block copolymer was first synthesized by reversible addition-fragmentation chain transfer (RAFT) polymerization followed by the CTA group removal via the radical-induced cleavage of thiocarbonylthio group¹⁹⁵ as shown in **Figure 3.2**. The polymers were successfully synthesized with narrow size distribution (Mw/Mn) of 1.15 and below as measured by GPC (**Figure B.1**, Supporting Information) with a block length of 23 for the first hydrophobic block followed by a block length of 97 for the diblock copolymer determined by ¹H NMR. After removal of the CTA end group, the diblock copolymer was modified by substituting the pentafluorophenyl ester group to form amides sequentially with ADT-

NH₂ at a ratio of 0.5 relative to PPFPA groups followed by TP-NH₂ in two times excess relative to the remaining PPFPA group. As a control, the diblock copolymer was modified with ADT-NH₂ only in two times excess relative to PPFPA groups. Then, the polymers were isolated from unconjugated ADT-NH₂ and TP-NH₂ by Sephadex LH-20 size exclusion column chromatography. The absorbance due to ADT group at 436 nm was measured to obtain elution profiles of the ADT-conjugated polymers and ADT-NH₂ (**Figure B.4**, Supporting Information). Based on the area under the peaks for ADT-conjugated polymer and free ADT-NH₂ group, a 98 % and 99% conjugation was determined for the ROS-sensitive H₂S donor micelles (ADT-TPM) and control (ADTM) respectively, thus confirming the successful conjugation of both ADT- NH₂ and TP-NH₂. The successful conjugation of TP-NH₂ and ADT-NH₂ motifs were further confirmed by ¹H NMR (**Figure B.2**, Supporting Information). In addition, FT-IR measurements showed the absence of pentafluorophenyl ester group by the absence of C=O stretching vibration of the activated ester group (1780 cm⁻¹), C=C stretching vibration of the aromatic ring (1510 cm⁻¹), and C-F stretching vibration (1000 cm⁻¹) in the FT-IR spectra (**Figure B.3**, Supporting Information).

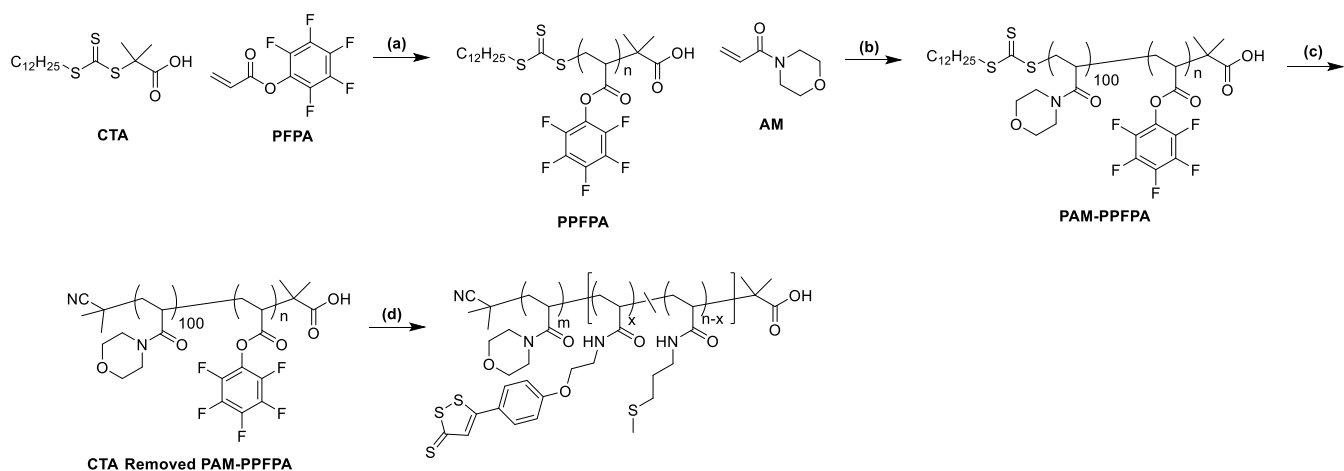


Figure 3.2. Synthesis Scheme of the ADT-TPM and ADTM block copolymers. (a) AIBN, 1,4-dioxane, 60 °C, 24 h (b) AIBN, 1,4-dioxane, 60 °C, 24 h (c) AIBN, 1,4-dioxane, 70 °C, 24 h (d) DMF, ADT-NH₂·TFA and TEA at 50 °C for 24 h followed by addition of TP-NH₂ at 50 °C for 24 h

3.3.2 Preparation and Characterization of ADT-TPM and ADTM Micelles

The micelles were prepared by self-assembly of the ADT-TPM and ADTM diblock copolymers in PBS. As shown in **Figure 3.3**, both ADT-TPM and ADTM polymers formed monodisperse micelles with a Z-average diameter (D_h) of 36 ± 4 nm and 30 ± 3 nm, respectively as determined by dynamic light scattering (DLS). TEM measurements by the negative staining method further confirmed the presence of spherical micelles as observed in **Figure 3.2**. To evaluate the thermodynamic stability of the micelles, the critical micelle concentration (CMC), the polymer concentration above which micelles form, was determined by the Nile red method¹⁵⁷ (**Figure B.5**, Supporting Information). In the case of ADT-TPM micelles, a CMC value of $29.6 \mu\text{M}$ was determined whereas ADTM micelles exhibited a lower CMC value of 8.2 nM . This shows that the ADTM micelles are slightly more stable thermodynamically compared to ADT-TPM micelles.

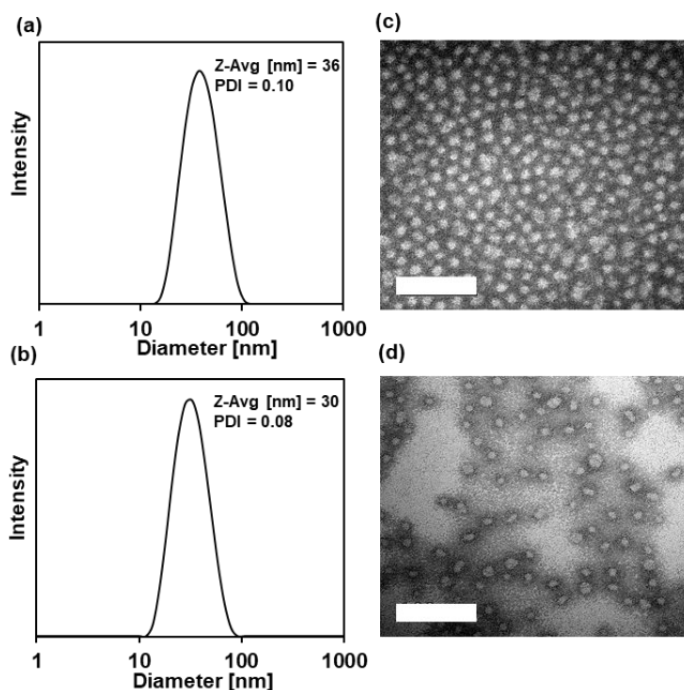


Figure 3.3. Characterization of ADT-TPM and ADTM micelles. (a-b) Size distribution by DLS, (c-d) TEM images of micelles negatively stained with 2% uranyl acetate solution. (a,c) ADT-TPM micelles, (b,d) ADTM micelles. Scale bar: 200 nm.

3.3.3 Dissociation of micelles in the presence of H₂O₂

Next, the dissociation of ADT-TPM and ADTM micelles in the presence of H₂O₂ was evaluated. The micelles (1 mg/mL) were incubated in the presence/absence of 100 mM H₂O₂ at 37 °C and the size distribution was monitored by changes in the light intensity scattered determined by DLS. Within the first 2 h of treatment, the ROS-sensitive micelles, ADT-TPM exhibited a 35 % decrease in the intensity of light scattered, showing dissociation of the micelle (**Figure 3.4a**). Over a period of 24 h, a 50 % decrease in intensity of light scattered was observed. On the other hand, only a slight decrease of about 5 % in the intensity of light scattered was observed for the control micelles, ADTM in the first 2 h (**Figure 3.4a**). Even after treatment for 24 h, ADTM micelles displayed only a 10 % decrease in intensity of light scattered compared to 50% decrease in intensity of light scattered for ADT-TPM micelles. To show that the dissociation of ADT-TPM micelles was induced by oxidation of the thioether group by H₂O₂, the presence of sulfoxide vibration at around 1100 cm⁻¹ was confirmed by FT-IR (**Figure 3.4b**). The dissociation of ADT-TPM micelles bearing ROS-sensitive thioether group upon oxidation by H₂O₂ indeed confirms the ROS-sensitivity of ADT-TPM micelles.

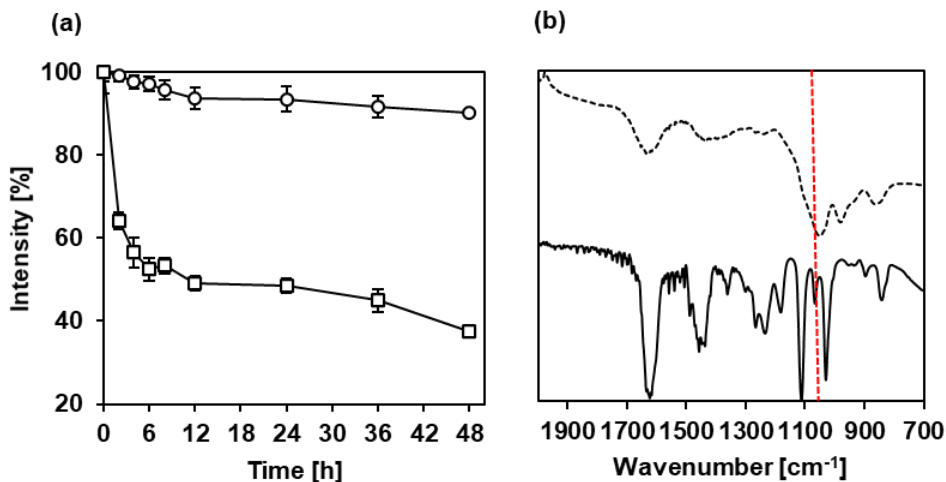


Figure 3.4. Dissociation of ADT-TPM (squares) and ADTM (circles) micelles upon oxidation by H_2O_2 . The micelles were treated with 100 mM H_2O_2 at $37^\circ C$ and change in the scattered light intensity of micelles was monitored by DLS (a) Change in scattered light intensity, (b) FT-IR spectra of ADT-TPM micelles before (solid line) and after (dotted line) treatment with H_2O_2 . Red line indicates sulfoxide vibration. $n=3$.

3.3.4 H_2S Release from Micelles in the presence of H_2O_2 in HT29 Cell Lysate

The H_2S release profiles from ADT-TPM and ADTM micelles in the absence/presence of H_2O_2 were investigated in cell lysate using the WSP-1 H_2S detection probe. In previous reports, it was shown that H_2S release is induced by intracellular components, presumably enzymes as ADT-based H_2S donors released H_2S in cell lysate but not in fetal bovine serum or glutathione-containing PBS.¹⁹⁴ Hence, it is expected that the oxidation of thioether groups by H_2O_2 would induce the dissociation of micelles and subsequent release of H_2S . In the presence of H_2O_2 , a greater release of H_2S was observed from the ROS-sensitive micelle, ADT-TPM compared to ADTM micelles as shown in **Figure 3.5**. In the absence of H_2O_2 , minimal release of H_2S was observed for both micelles. These results indicate that ADT-TPM micelles undergo a greater degree of dissociation in the presence of H_2O_2 , thus releasing more H_2S compared to ADTM micelles.

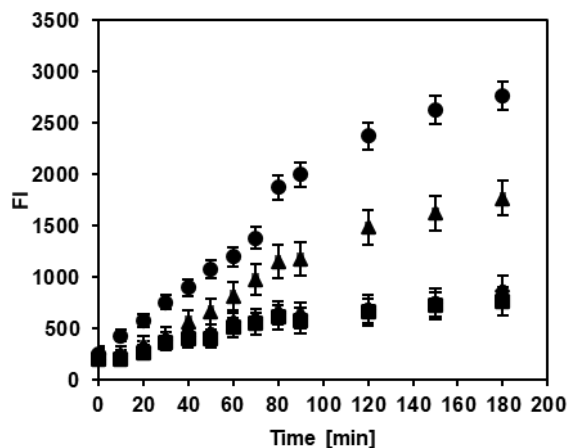


Figure 3.5. H₂S release in HT29 cell lysate. ADT-TPM and ADTM micelles were added to HT29 cell lysate containing WSP-1 H₂S detection probe in the absence/presence of 100 Mm H₂O₂. Fluorescence intensity ($\lambda_{ex}=465$ nm, $\lambda_{em}=515$ nm) was monitored at indicated time point. ADT-TPM (+) H₂O₂: circles, ADT-TPM (-) H₂O₂: triangles, ADTM (+) H₂O₂: diamonds, ADTM (-) H₂O₂: squares. n=3

3.3.5 H₂S Release from Micelles in HT29

It is widely known that cancer cells produce elevated levels of ROS.¹⁶⁸⁻¹⁷¹ So, we next investigated the release of H₂S from the micelles in human colon cancer HT29 cells. HT29 cells were cultured in the presence of both micelles (ADT-TPM and ADTM) and the small H₂S donor, ADT and the H₂S release in comparison to the non-treated cells (medium only) were determined using the fluorescent H₂S-detection dye, WSP-1. An increase in fluorescence intensity for cells treated with medium only is expected as HT29 cells are known to produce H₂S endogenously. As shown in **Figure 3.6**, ADT-TPM micelles exhibited greater release of H₂S overall compared to ADTM micelles, small H₂S donor, ADT, and non-treated cells. When comparing both micelles, ADT-TPM micelles released approximately 2 times more H₂S after 6 h of incubation compared to ADTM micelles. On the other hand, ADT and non-treated cells released a similar amount of H₂S. This observation is consistent with the ROS-sensitivity of the micelles (**Figure 3.4**) and H₂S

release in HT29 cell lysate (**Figure 3.5**) where ADT-TPM micelles exhibited greater dissociation in response to H_2O_2 , thus resulting in a higher release of H_2S .

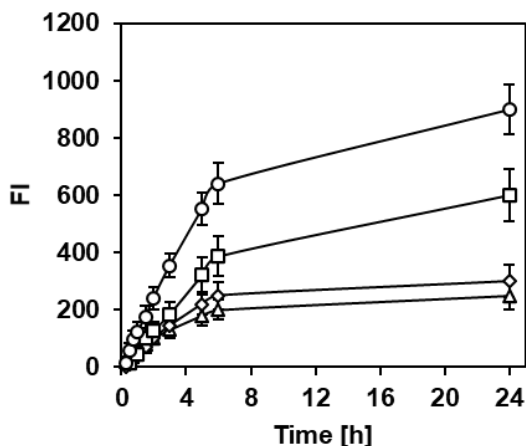


Figure 3.6. H_2S release in HT29 cells. Cells were cultured in the presence of ADT-TPM (circles) and ADTM (squares) micelles, ADT donor (diamonds), and medium as a control (triangles) at indicated time points (ADT Concentration: $50 \mu M$). Cells were washed and incubated prior with WSP-1 H_2S detection dye for 30 min. Fluorescence intensity ($\lambda_{ex}=480 \text{ nm}$, $\lambda_{em}=520 \text{ nm}$) was monitored at indicated time point. $n=3$

3.3.6 Anti-proliferative Effect of Micelles

As H_2S has been reported to play an important role in the inhibition of cancer cell proliferation,^{36,52,179,198} the anti-proliferative effect of ADT-TPM and ADTM micelles in HT29 cells and human umbilical endothelial (HUVEC) cells were evaluated by MTT assay. As shown in **Figure 3.7a**, ADT-TPM micelles exhibited a greater anti-proliferative effect compared to ADTM micelles and ADT in HT29 cells, which are known to produce elevated levels of ROS. At an ADT concentration of $100 \mu M$, ADT-TPM micelles showed a cell viability of 60 % compared to 70 % and 78% for ADTM micelles and ADT respectively. This enhanced anti-proliferative effect of ADT-TPM micelles is attributed to the greater release of H_2S in response to elevated levels of H_2O_2 as observed in **Figure 3.5-3.6**. In contrast to HT29 cells, no significant decrease in

cell viability was observed in HUVEC cells with basal levels of ROS for both ADT-TPM and ADTM micelles (**Figure 3.7b**). However, the donor ADT exhibited greater cytotoxicity with cell viability of about 50% at an ADT concentration of 100 μM compared to both micelles (82 % for ADTM micelles and 90% for ADT-TPM micelles) which have been previously shown to exhibit similar effects in RAW blue macrophages.⁵¹

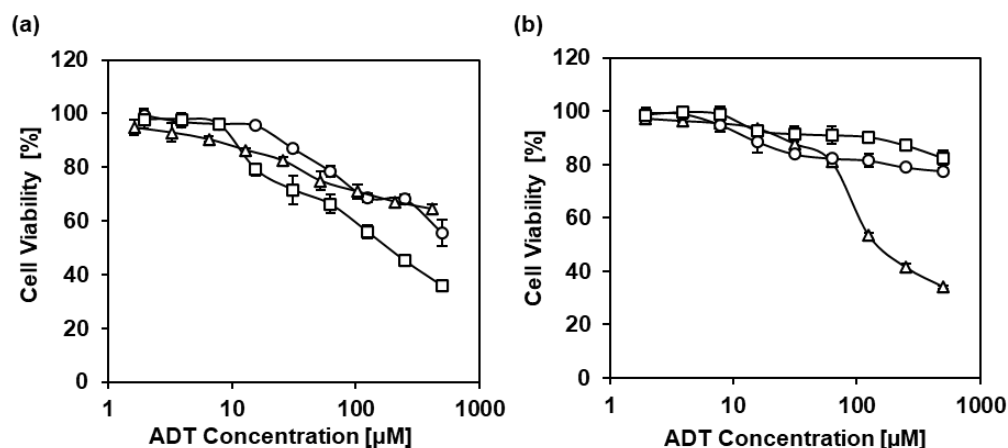


Figure 3.7. Cell viability of ADT donor (triangles), ADTM (circles) and ADT-TPM (squares) micelles in (a) HT29 and (b) HUVEC cells. Cells were cultured in the presence of micelles for 5 d or 2 d. Cell viability was measured by MTT assay. $n=3$.

3.4 Conclusion

In summary, H_2S donor micelles bearing ADT group and oxidation-sensitive thioether group (TP) were successfully synthesized. Remarkably, a much greater release profile of H_2S was observed from the oxidation-sensitive H_2S donor micelles compared to the control micelle and H_2S donor (ADT) in HT29 colon cancer cells with elevated levels of ROS. The greater release of H_2S subsequently showed enhanced anti-proliferative effects in colon cancer cells. Promisingly, the oxidation-sensitive H_2S donor micelles were well tolerated in HUVEC cells while the H_2S donor (ADT) showed significant cytotoxicity. This result is significant as it may be a valuable

tool to clarify the exact role of H₂S in terms of duration and concentration required to exert anti-proliferative activity in a targeted and controlled manner.

4 MMP-2-sensitive hydrogen sulfide donor micelles for cancer-targeted delivery

The work in this chapter was done under the mentorship of Dr. Urara Hasegawa during her tenure at Kansas State University

Abstract

Hydrogen sulfide (H₂S) has been shown to be involved in many physiological and pathophysiological functions as a gaseous signaling molecule in the body such as anti-cancer effects. With the anti-cancer effect of H₂S being largely attributed to the concentration and duration of exposure in a localized manner, the need for H₂S donors that can trigger H₂S release selectively to cancer cells is important. Here, MMP-2 enzyme sensitive polymeric micelles were prepared from amphiphilic block copolymers consisting of a hydrophilic poly(*N*-acryloyl morpholine) (PAM) segment and a hydrophobic segment bearing H₂S-releasing anethole dithiolthione (ADT) group and MMP-2 cleavable peptide motif for site-specific and controlled delivery of H₂S to cancer cells in response to upregulation of MMP-2 enzyme. The dissociation of MMP-2-sensitive micelles was significantly affected in the presence of MMP-2 enzyme, hence releasing more H₂S in colon cancer cells compared to the control and the H₂S donor (ADT). In addition, the MMP-2 sensitive micelles exhibited a more potent anti-proliferative activity in colon cancer. Hence, the design of MMP-2-sensitive H₂S donor micelles which releases H₂S in cancer cells in response to overproduction of MMP-2 enzyme could potentially provide a more detailed insight into the anti-cancer effects of H₂S.

4.1 Introduction

H₂S as a signaling molecule have shown immense therapeutic potential such as vasodilatory,¹⁷⁵ proangiogenic,^{33,173} anti-inflammatory,¹⁹⁹ neuromodulatory,³⁰ cytoprotective,²⁰⁰ and anti-cancer effects.^{36,178,179} ever since its discovery by Abe and Kimura in 1996 on its possible physiological function in the nervous system. Of particular interests is the increasing awareness of the role of H₂S in exerting anti-cancer effects where inhibition or silencing of H₂S producing enzyme cystathionine β-synthase (CBS) specifically in the colon and ovarian cancer has been shown to suppress cancer cell growth in preclinical studies.^{180,182} In a different approach, exposure of H₂S from various H₂S donors exogenously at higher concentrations or lower concentrations for a sustained period selectively inhibits cancer cell proliferation and induces apoptosis.^{37,178,186} For example, a recent report by Cai and colleagues showed that ADT-OH, inhibited the growth of melanoma and induced apoptosis by enhancing the activation of caspase-3 and significantly increasing the levels of Fas-associated protein with death domain (FADD) protein.³⁶ While convenient, a lot of these donors lack the ability to mimic the endogenous production of H₂S through enzymatic activation, which could be key to understanding the precise and detailed mechanistic understanding of the role of H₂S in selectively inhibiting cancer cell growth.

As enzymes are innate to living organisms and possess substrate specificity, it makes them unique and promising targets for diagnosis and specific drug targeting due to elevated levels in many diseases.^{201,202} In the field of H₂S delivery, only a few enzyme-triggered H₂S donors have been reported in the field of H₂S delivery. Wang and coworkers were the first to report an enzyme-triggered H₂S donor where a series of esterase-triggered H₂S donors containing the thioester group was developed by variation of the phenolic moiety, which releases H₂S upon esterase-mediated cleavage of the ester group followed by lactonization.²⁰³ Promisingly, the donors exhibit anti-

inflammatory effects by inhibiting TNF- α secretion in RAW 264.7 macrophages with no obvious cytotoxicity up to a concentration of 200 μ M, which the authors attributed to the controlled release rate of H₂S from the esterase-triggered donors. However, H₂S release could occur non-specifically throughout the body as esterase enzymes are ubiquitously present in the body. More recently, Matson and coworkers reported an elastase-triggered H₂S-releasing hydrogel bearing human neutrophil elastase (HNE) degradable peptide as the elastase sensitive moiety and H₂S-releasing S-arylothiooxime (SATO) for targeted delivery of H₂S to diseases with recurring inflammation.¹⁹⁸ Remarkably, the hydrogel showed greater release of H₂S in the presence of elastase enzyme and exhibited cytoprotective effects against doxorubicin (Dox) in HC29 rat embryonic cardiomyocytes, thus presenting a promising approach to selectively deliver H₂S to inflammation sites.

The significant upregulation of Matrix metalloproteinases (MMPs), especially MMP-2 enzyme has been reported in numerous types of cancer^{204–208} and further explored as a unique target for tumor-targeted drug delivery via an enzyme-triggered mechanism. Matrix metalloproteinases (MMPs), especially MMP-2, are known to be involved in cancer invasion, progression, and metastasis.²⁰⁹ The majority of studies utilize synthetic MMP-2 cleavable peptide sequences or crosslinkers to confer MMP-2 sensitivity to nanocarriers such as polymeric micelles and hydrogels.^{210–214} These MMP-responsive nanocarriers typically remain biologically inert and stable in normal tissues, but release payloads of drugs from the nanocarriers in tumors with increased levels of MMP-2.

Here, we report the design and synthesis of MMP-2 enzyme sensitive H₂S donor polymeric micelles containing H₂S donating ADT group and enzymatically cleavable hydrophobic peptide motif for site-specific delivery of H₂S in response to upregulation of MMP-2 in cancer cells

(**Figure 4.1**). Previously, a polymer- H₂S donor conjugate and polymeric H₂S donor micelles bearing dithiolthione moiety (ADT) that released H₂S in a slow and sustained manner compared to the small donor itself (ADT-OH) while minimizing the toxic side effects of the small ADT donor.^{192,215} In addition, the micelles were shown to further enhance the pro-inflammatory effect of gardiquimod (GDQ) in murine macrophages and protected cardiomyocytes from ischemic cell death. By adding MMP-2 cleavable peptide motifs to the existing design of H₂S-donor micelles previously reported, we expect that the release of H₂S from the micelles would be accelerated by the destabilization of micellar structure in response to upregulation of MMP-2 enzymes. In this respect, the design of MMP-2 sensitive H₂S polymeric micelles could potentially provide a platform in understanding the detailed mechanism of H₂S actions in inhibiting cancer cell growth in various types of cancer.

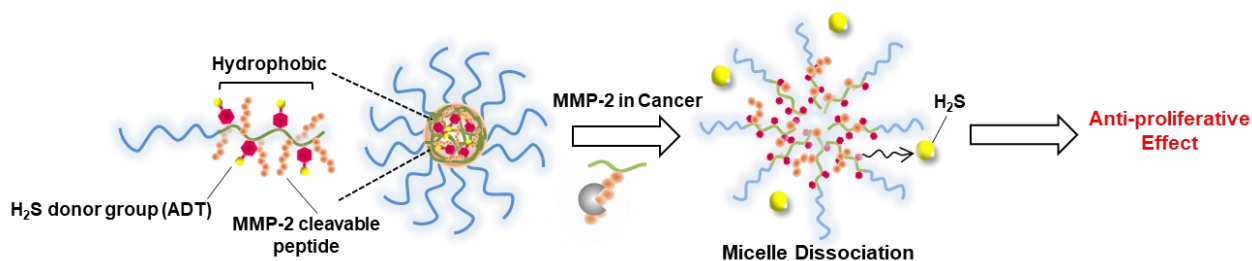


Figure 4.1. Polymeric micelles bearing MMP-2 cleavable peptide motifs for targeted delivery of H₂S in cancer cells over-expressing MMP-2 enzyme (courtesy of Hasegawa and Radaha).

4.2 Experimental procedures

4.2.1 Materials

Pentafluorophenyl acrylate (PFPA) were purchased from Tokyo Chemical Industry (USA). 4-acryloylmorpholine (AM), 2,2'-azobis(isobutyronitrile) (AIBN), 2-(dodecylthiocarbonothioylthio)-2-methylpropionic acid (CTA), aluminum oxide (Al₂O₃), 1-

methyl-2-pyrrolidinone (NMP), deuterated chloroform (CDCl_3) deuterated dimethyl sulfoxide ($(\text{CD}_3)_2\text{SO}$), calcium hydride (CaH_2), trifluoroacetic acid (TFA), sodium dodecyl sulfate (SDS), phosphor pentoxide (P_4O_{10}) and 4Å molecular sieves were purchased from Sigma Aldrich (USA). Tris(trimethylsilyl)silane, 1,4-dioxane, anhydrous dimethylformamide (DMF), tetrahydrofuran (THF), diethyl ether (Et_2O), ethanol (EtOH), triethylamine (TEA), potassium hydroxide (KOH) pellets, hydrochloric acid (HCl), Tricine, Sodium Chloride (NaCl), calcium chloride (CaCl_2), Leucine, Nile red, Hoechst 33342, McCoy's 5A, fetal bovine serum, penicillin-streptomycin, and trypsin-EDTA were purchased from Fisher Scientific (USA). Fluorescamine was purchased from Acros Organics. XPell pellets were purchased from Xplosafe (USA). Regenerated cellulose dialysis tubing (MWCO 2 kDa) was purchased from Spectrum Laboratories (USA). ADT-NH₂ was synthesized as reported previously.¹⁹⁴ The MMP-2 cleavable and non-cleavable peptides, GPLGL-NH₂·TFA and GPLL-NH₂·TFA, were synthesized at the Center for Molecular Analysis of Disease Pathways, University of Kansas. Sephadex LH20 and G20 were purchased from GE Healthcare (USA). WSP-1 fluorescent probe was purchased from Cayman Chemical Company (USA). Matrix metalloproteinase (MMP-2) was purchased from RD-SYSTEMS. 3-(4,5-dimethylthiazol-2-yl)-2,5-diphenyltetrazolium bromide (MTT) was purchased from MP Biomedical (USA). HT29 cells were purchased from ATCC (USA). Amicon[®] Ultra 4 mL Centrifugal Filters, transparent and black 96 well plates and disposable 5 mL polypropylene columns were purchased from Thermo Fisher Scientific (USA). The glass-bottom dishes were purchased from Matsunami Glass (USA). 200 mesh carbon-coated copper grids were purchased from Electron Microscopy Science (USA).

Pentafluorophenyl acrylate and 4-acryloylmorpholine were passed through a plug of Al_2O_3 to remove inhibitor. AIBN was recrystallized from MeOH. 2-(dodecylthiocarbonothioylthio)-2-

methylpropionic acid was recrystallized from HA. 1,4-dioxane was distilled from CaH₂ and kept over molecular sieves and XPell pellets. TEA was dried over KOH pellets. Other reagents were used as received without further purification.

4.2.2 Instrumentation

Proton NMR (¹H NMR) Spectroscopy. ¹H NMR spectra was measured with a Varian 400MHz NMR spectrometer. A number of 32 scans was collected and the delay time (D1) was set to 10 s for polymers and 1 s for small compounds. The chemical shifts are referenced to the residual undeuterated NMR solvent signal at 7.26 ppm (CDCl₃) and 2.50 ((CD₃)₂SO),

Attenuated Total Reflection Infrared Spectroscopy (ATR-IR). Attenuated total reflection infrared (ATR-IR) spectra were obtained using a Perkin Elmer Spectrum 400 spectrometer.

Gel Permeation Chromatography (GPC). Elution profiles of the polymers were obtained using a ResiPore PL1113-6300 GPC column on an Agilent Technologies 1220 Infinity II LC GPC system equipped with a 1260 RI detector and a 1260 MCT column oven. THF was used as the eluent with a flow rate of 1.0 mL/min. The temperature of the RI detector and column oven was 40 °C. The polymers were dissolved in THF at 5 mg/ml and 10 μL of the solution was injected. The polydispersity index (M_w/M_n) was calculated from the elution profiles of a polystyrene standard (Agilent).

UV-Vis spectroscopy. The UV/Vis spectra were measured on a Thermo Scientific Nanodrop One^c spectrophotometer.

Dynamic Light Scattering (DLS). Dynamic light scattering measurements were done using a Malvern Zetasizer Nano ZS Series instrument. Freshly prepared micelle solutions were filtered using a polyethersulfone (PES) syringe filter (pore size: 0.45 μm) and placed in disposable micro

cuvettes (ZEN0040, Malvern). The Z-average diameter and polydispersity index (PDI) of the micelles were determined by the cumulant method.

Transmission Electron Microscopy (TEM). The morphology of the micelles was observed by transmission electron microscopy using the negative staining method. The micelle solution (1 mg/ml in water) was mixed with 2 w/v% uranyl acetate aqueous solution (volume ratio of 1:1) and added onto 200 mesh carbon-coated copper grids. The grids were air-dried after removing the solution by blotting the side of the grid with filter paper. Images were acquired on a FEI Tecnai G2 Spirit BioTWIN instrument operating at 80 kV.

UV-Vis/fluorescence spectroscopy with Plate Reader. The UV-Vis absorbance and fluorescence intensities were measured with a Tecan infinite M200 plate reader.

Confocal Laser Scanning Fluorescence Microscopy (CLSM). Fluorescence images were acquired on an Olympus Fluoview FV1000-D confocal microscope equipped with 405, 473, 559, and 632 nm lasers.

4.2.3 Synthesis of PPFPA Homopolymer

PPFPA was synthesized by RAFT polymerization using AIBN as the initiator and 2-(dodecylthiocarbonothioylthio)-2-methylpropionic acid as the chain transfer agent (CTA). For PPFPA26, 535.8 mg (2.25 mmol) of PFP, 32.8 mg (0.09 mmol) of CTA, and 1.48 mg (0.009 mmol) of AIBN were dissolved in 1,4-dioxane (Total volume: 567 μ L). The reaction mixture was deoxygenated by six freeze-pump-thaw cycles, heated to 60 °C under argon and stirred for 19 h. The polymerization was stopped by quenching the reaction with liquid nitrogen and opening the Schlenk tube to air. After thawing to room temperature, the reaction mixture was diluted with 1.5 mL dioxane and added dropwise to 50 mL of EtOH. The precipitate was filtered, washed with

EtOH (2x10 mL) and dried under reduced pressure to yield 387.6 mg of yellow solids. The filter was then washed with CH₂Cl₂ (3x4 mL) and evaporated at room temperature. After drying under reduced pressure, 55.4 mg of yellow solids was recovered with a total yield of 443 mg (77%). The polymers were characterized by ¹H NMR, GPC, and FT-IR as shown in Supporting Information.

4.2.4 Synthesis of PAM-PPFPA Diblock Copolymer

AM (344.2 mg, 2.44 mmol), PPFPA26 (159.3 mg, 0.024 mmol), and AIBN (0.399 mg, 0.0024 mmol) were dissolved in 1,4-dioxane (Total volume: 2.43 mL). The reaction mixture was deoxygenated by five freeze-pump-thaw cycles, heated to 60 °C under argon and stirred for 22 h. The polymerization was stopped quenching the reaction with liquid nitrogen and opening the Schlenk tube to air. After cooling to room temperature, the reaction mixture was added dropwise to 60 mL of Et₂O. The precipitate was filtered, washed with 10 mL Et₂O (2x10 mL), and dried under reduced pressure to yield 424.4 mg yellow solids. The filter was then washed with CH₂Cl₂ (4x4 mL) and evaporated at room temperature. After drying under reduced pressure, 29.5 mg of yellow solids was recovered with a total yield of 453.9 mg (90%). The polymers were characterized by ¹H NMR, GPC, and FT-IR as shown in Supporting Information.

4.2.5 CTA End Group Removal from PAM-PPFPA Diblock Copolymer

The CTA end group was removed by radical-induced reduction of the thiocarbonylthio group.¹⁹⁵ PAM-PPFPA polymer (380 mg, 0.019 mmol), tris(trimethylsilyl)silane (28.2 μL, 0.10 mmol), and AIBN (6.0 mg, 0.037 mmol) were dissolved in 1.8 mL of 1,4-dioxane. The solution was deoxygenated by five freeze-pump-thaw cycles, heated to 70 °C under argon and stirred for 23 h. The slightly purple reaction mixture was placed in liquid nitrogen and opening the Schlenk tube to air. After warming to room temperature, the reaction mixture was added dropwise to 80 mL of Et₂O. The precipitate was filtered, washed with Et₂O (2x10 mL), and dried under reduced pressure

to yield 360.2 mg (95%) of white solids. The polymers were characterized by GPC and FT-IR as shown in Supporting Information.

4.2.6 Synthesis of ADT-GPLGL and ADT-GPLL Block Copolymers.

PAM99-PPFPA26 polymer (30 mg, 0.038 mmol of PFPFA26 groups) was dried at 40 °C under vacuum for 24 h in the presence of P₄O₁₀. The polymer was dissolved in 0.80 mL anhydrous DMF followed by the addition of MMP-2 cleavable peptide(GPLGL-NH₂·TFA) (10.80 mg, 0.019 mmol, 0.5 eq relative to PFPFA26 groups) or non-cleavable peptide (GPLL- NH₂·TFA)(9.70 mg, 0.019 mmol, 0.5 eq relative to PFPFA26 groups) and TEA (0.038 mmol, 2 eq. relative to GPLGL·TFA or GPLL·TFA). After three purge-evacuate cycles, the reaction mixture was heated at 50 °C under argon and stirred for 24 h. Next, ADT-NH₂·TFA (14.65 mg, 0.038 mmol, 1 eq. relative to PFPFA26 groups) and TEA (0.076 mmol, 2 eq. relative to ADT-NH₂·TFA) was added to the reaction mixture under argon. The reaction mixture was heated at 50 °C under argon following three purge-evacuate cycles and stirred for another 48 h. The polymer was separated from unreacted ADT-NH₂ and pentafluorophenol by Sephadex LH-20 size exclusion column chromatography (column diameter: 13 mm, length: 250 mm) using DMF as the eluent. The absorbance at 436 nm of each fraction (1 mL) was measured using Nanodrop and plotted as a function of elution volume to obtain the elution profile. To verify the successful conjugation of MMP-2 cleavable or non-cleavable peptide motif to polymer, fluorescamine assay in DMF of all fractions were performed.^{216,217} Briefly, 100 μL/well of Tricine buffer (50 mM Tricine, 150 mM NaCl, 10 mM CaCl₂, pH 7.5), 50 μL/well of peptide solution in DMF, and 50 μL/well of fluorescamine solution in acetone (Final concentration of fluorescamine: 2 mM) were added to a black 96 well plate. The plate was sealed with a plate sealer and incubated at 25 °C for 15 min. Fluorescence intensity ($\lambda_{\text{excitation}} = 387 \text{ nm}$ and $\lambda_{\text{emission}} = 480 \text{ nm}$) of each fraction was measured

using a microplate reader. Then, fractions containing polymer were combined, diluted 2x with deionized (DI) water, and dialyzed against 4 L of DI water for 3 d, with regular replacement of the water. Polymers were recovered by lyophilization.

4.2.7 Preparation of Micelles

The ADT-GPLGL and ADT-GPLL block copolymers were dissolved in NMP (100 mg/mL) and added dropwise to DI water (volume ratio 1:9) under stirring (Final concentration: 10 mg/mL). The solutions were dialyzed (MWCO, 2kDa) against 4 L of DI water for 3 d, with regular replacement of water. To determine polymer concentration after dialysis, part of the micelle solution was lyophilized and the amount of polymer determined gravimetrically. The remaining micelle solution was concentrated and further purified using an Amicon Ultra-4 centrifugal filter followed by absorbance measurement at 436 nm using Nanodrop. ADT concentration was determined from a standard curve of ADT-NH₂ measured at 436 nm using Nanodrop.

4.2.8 Critical Micelle Concentration (CMC).

The CMC of the micelles was determined using the Nile red method.¹⁹⁶ To 350 μ L of the micelle solutions at different concentrations, 3.5 μ L of 0.1 mg/mL Nile red solution in DMSO was added. The micelle/Nile red mixtures were transferred to a 96-well plate (100 μ L/well, n=3) and incubated at room temperature for 2 h in the dark. The fluorescence intensity (λ_{ex} =530 nm, λ_{em} =630 nm) was recorded and plotted against log(concentration). The CMC values were determined based on the intersection between the linear fits of the low and high concentration regions as shown in **Figure C.1**, Supporting Information.

4.2.9 Monitoring of Micelle Dissociation in Response to MMP-2

The-micelle solutions (0.5 mg/mL, 396 μ L) in Tricine buffer (50 mM Tricine, 150 mM NaCl, 10 mM CaCl₂, pH 7.5) were incubated with/without 4 μ L MMP-2 (Final concentration of MMP-2 enzyme: 43.6 nM) at 37 °C. The size distribution of the micelles was measured by DLS followed by collection of fractions (30 μ L) at indicated time points. The dissociation rate of micelles was determined as followed:

$$\% \text{ Intensity} = \frac{\text{Scattered light intensity at indicated time point [kcps]}}{\text{Scattered light intensity at time zero [kcps]}} \times 100$$

4.2.10 Determination of free leucine concentration in the micelle solution treated with MMP-2

The micelle solutions (0.5 mg/mL, 396 μ L) in Tricine buffer (50 mM Tricine, 150 mM NaCl, 10 mM CaCl₂, pH 7.5) were incubated with/without 4 μ L MMP-2 (Final concentration of MMP-2: 43.6 nM) at 37 °C. At the indicated time points, 30 μ L of the micelle solutions were collected and stored at -20 °C. The amount of free leucine in the sample was measured by fluorescamine assay.^{216,217} The sample (10 μ L/well) was placed in a 96 well black plate and mixed with 10 μ L/well of 3.6 mM fluorescamine solution in acetone and 30 μ L/well tricine buffer. The plate was sealed with a plate sealer and incubated at 25 °C for 15 min. Fluorescence intensity ($\lambda_{\text{excitation}} = 387$ nm and $\lambda_{\text{emission}} = 480$ nm) was measured using a microplate reader. The concentrations of free leucine in the samples were determined using the standard curve (**Figure C.2**, Supporting Information) and % cleaved peptide was calculated as follows:

$$\% \text{ Cleaved Peptide} = \frac{\text{Concentration of free leucine in the sample [mmol]}}{\text{Concentration of peptide in the intact micelles [mmol]}} \times 100$$

4.2.11 Cell Culture

HT-29 human colon cancer cells were cultured in McCoy's 5A medium containing 10% fetal bovine serum and 1% penicillin-streptomycin (10,000 U/mL) in a 5% CO₂ incubator at 37 °C.

4.2.12 Cell Viability Assay in HT29 cells

HT29 cells were seeded in a 96-well plate at a density of 3.0×10^3 cells/well and cultured for 1 d. The medium was replaced with 100 μ L/well of fresh medium containing ADT-GPLGL and ADT-GPLL micelles and the cells were cultured for 5 d in a CO₂ incubator. The medium was then replaced with 100 μ L of 0.5 mg/ml of MTT in medium and the cells were cultured for 3 h. The formazan crystals formed were dissolved in 100 μ L/well of 100 mg/mL sodium dodecyl sulfate (SDS) solution in 0.01 M HCl (aq). The absorbance at 570 nm was measured using a microplate reader.

4.2.13 H₂S release from the micelles in HT29 lysate with the WSP-1 H₂S fluorescent detection probe

HT29 cell lysate was diluted with PBS at a volume ratio of 1:5 and mixed with WSP-1 (final concentration: 25 μ M for WSP-1). This mixture was then mixed with the micelle solutions followed by MMP-2 enzyme in a 96 well plate (final concentrations: 50 μ M for ADT groups and 43.6 nM MMP-2 enzyme). The fluorescence intensity was measured as function of time on the plate reader ($\lambda_{ex} = 465$ nm, $\lambda_{em} = 515$ nm).

4.2.14 H₂S Release by Fluorescent dye WSP-1 in HT29 Cells

Measurement of H₂S release in HT29 cell were performed as reported previously.¹⁹⁷ Briefly, HT29 cells were seeded in a 96-well plate (5×10^4 cells/well) and cultured for 1 d. The medium was replaced with 100 μ L/well of WSP-1/DMSO in PBS (Final concentration of WSP-1 in DMSO: 25

μM) and incubated for 30 mins at 37 °C. Then, the WSP-1/DMSO in PBS solution was removed and 100 μL /well of fresh medium containing ADT-GPLGL and ADT-GPLL micelles were added (Final concentration of ADT: 50 μM). Fluorescence intensity ($\lambda_{\text{excitation}} = 480 \text{ nm}$, $\lambda_{\text{emission}} = 520 \text{ nm}$) was measured at indicated time points using a microplate reader. As a control, the cells were replaced with 100 μL /well of fresh medium.

4.2.15 Observation of H₂S Release by Fluorescent dye WSP-1 in HT29 cells

HT-29 cells were seeded in a quadruple well glass-bottom dish at 2.0×10^4 cells/well with 100 μL /well medium for 1 d. the medium was replaced with 100 μL /well of fresh medium containing 8 nM Hoescht 33342 dye, and cells were incubated for 5 min at 37 °C. Thereafter, the medium was replaced with 100 μL /well of WSP-1/DMSO in PBS (Final concentration of WSP-1 in DMSO: 2.5 μM) and incubated for 30 mins at 37 °C. Then, the solution was replaced with 100 μL /well of fresh medium containing ADT-GPLGL and ADT-GPLL micelles (Final concentration of ADT: 25 μM). After culturing for 8 h, cells were observed by CLSFM.

4.3 Results and Discussion

4.3.1 Synthesis of MMP-2 sensitive H₂S Donor Micelles (ADT-GPLGL and ADT-GPLL)

To prepare the MMP-2 sensitive H₂S donor micelles, we designed an amphiphilic diblock copolymer consisting of a hydrophilic poly(N-acryloyl morpholine) (PAM) block and a hydrophobic block bearing MMP-2 cleavable peptide and H₂S-releasing dithiolthione group (ADT) (**Figure 4.2**). Previously, polymeric micelles based on amphiphilic block copolymers composed of a hydrophilic PEG segment and hydrophobic segment bearing ADT moieties were synthesized by reversible addition-fragmentation chain transfer (RAFT) polymerization. The

micelles were shown to release H₂S significantly slower compared to the donor alone, ADT-OH. In addition, the micelles protected rat cardiomyocytes from ischemic damages in an in vitro ischemic model.

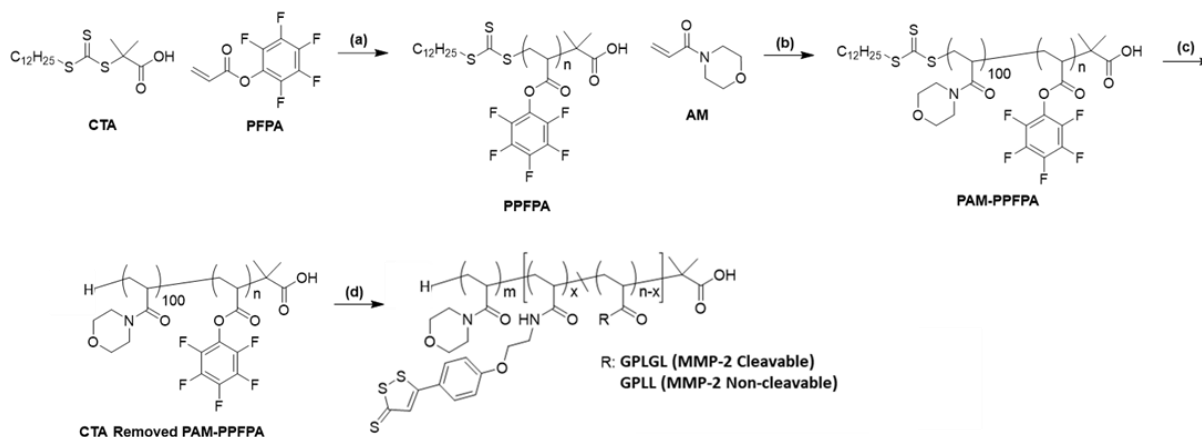


Figure 4.2. Synthesis Scheme of the ADT-GPLGL and ADT-GPLL block copolymers. (a) AIBN, 1,4-dioxane, 60 °C, 24 h (b) AIBN, 1,4-dioxane, 60 °C, 24 h (c) Tris(trimethylsilyl)silane, AIBN, 1,4-dioxane, 70 °C, 24 h (d) DMF, GPLGL-NH₂·TFA/GPLL-NH₂·TFA, and TEA at 50 °C for 24 h followed by addition of ADT-NH₂·TFA and TEA at 50 °C for 48 h

As upregulation of MMP-2 enzyme is observed in numerous cancer cells,^{204,205,207} we sought to confer enzyme sensitivity to the existing design of polymeric micelle containing H₂S donating ADT group in the hydrophobic core by addition of hydrophobic peptides containing MMP-2 cleavable peptide motif (GPLGL) for site-specific delivery of H₂S to cancer cells. The addition of MMP-2 cleavable peptide motifs to polymeric micelles have been proven to successfully enhance tumor targeting and cellular penetration.^{212,213,218} A recent work with polymeric micelles carrying MMP-2 cleavable octapeptides for tumor-specific co-delivery of siRNA and paclitaxel drug displayed enhanced tumor targeting triggered by upregulation of MMP-2.²¹² This strategy indeed

shows great potential for cancer-specific delivery of H₂S. The MMP-2-specific peptide sequence (PLGL) was used based on previous studies on the cleavage specificities of peptide sequences of nine human matrix metalloproteinases (MMPs) by high throughput Proteomic Identification of protease Cleavage Sites (PICS) method.²¹⁹ An additional glycine unit (GPLGL) was added to the sequence for improved conjugation degree with a primary amine. A scrambled MMP-2 peptide sequence (GPLL) was also chosen as a control. We hypothesize that the release of H₂S from the micelles would be modulated by the destabilization of the micellar structure in response to cleavage of peptide motifs by MMP-2 enzyme.

We first synthesized PAM-b-poly(pentafluorophenyl acrylate) block copolymer (PAM-PPFPA) by reversible addition-fragmentation chain transfer (RAFT) polymerization followed by the CTA group removal via the radical-induced reduction¹⁹⁵ as shown in **Figure 4.2**. Well-defined polymers were successfully synthesized with narrow size distribution (M_w/M_n) of 1.10 and below as measured by GPC (**Figure C.3**, Supporting Information) and a block length of 26 for the first hydrophobic block (PPFPA) followed by a block length of 99 for the diblock copolymer (PAM) determined by ¹H NMR (**Figure C.4**, Supporting Information). The diblock copolymer (PAM-PPFPA) was modified sequentially with GPLGL or GPLL peptide sequences at a ratio of 0.5 relative to PPFPA groups followed by ADT-NH₂ in two times excess relative to the remaining PPFPA group by substitution of pentafluorophenol group.^{166,220} The polymer was isolated from unconjugated ADT-NH₂ and the peptide by Sephadex LH-20 size exclusion column chromatography. The elution profiles of the ADT conjugated polymers and ADT-NH₂ were obtained by measuring the absorbance at 436 nm due to ADT group (**Figure C.5a-b**, Supporting Information). A 99 % conjugation was determined based on the area under the peaks for ADT-conjugated polymer and free ADT- NH₂ group, showing a successful conjugation of both peptide

followed by ADT-NH₂. We also determined the amount of unreacted peptide by the fluorescamine assay (**Figure C.5a-b**, Supporting Information).^{211,217} While the primary amine of ADT-NH₂ could also react with fluorescamine, the dithiolthione group typically quenches fluorescamine resulting in little to no fluorescence as observed in **Figure C.5a-b**.

Based on the unreacted peptide determined by fluorescamine assay, a 98 % conjugation was observed for both peptide sequences. The successful conjugation of GPLGL or GPLL peptide motifs and ADT group was further confirmed by the absence of C=O stretching vibration of activated ester group (1780 cm⁻¹), C=C stretching vibration of the aromatic ring (1510 cm⁻¹), and C-F stretching vibration (1000 cm⁻¹) in the FT-IR spectra (**Figure C.6**, Supporting Information). In addition, the presence of GPLGL or GPLL peptides and ADT groups was confirmed by FT-IR (**Figure C.7**) and ¹H NMR (**Figure C.4**, Supporting Information) with the characteristic peak of leucine-and ADT group.

4.3.2 Preparation and Characterization of ADT-GPLGL and ADT-GPLL Micelles

The micelles were prepared by self-assembly of the ADT-GPLGL and ADT-GPLL diblock copolymers in PBS. Both ADT-GPLGL and ADT-GPLL polymers formed monodisperse micelles with a Z-average diameter (D_h) of 37±3 nm and 39±4 nm, respectively as determined by dynamic light scattering (DLS) (**Figure 4.3**). The presence of spherical micelles were further confirmed by TEM by the negative staining method as observed in **Figure 4.3**.

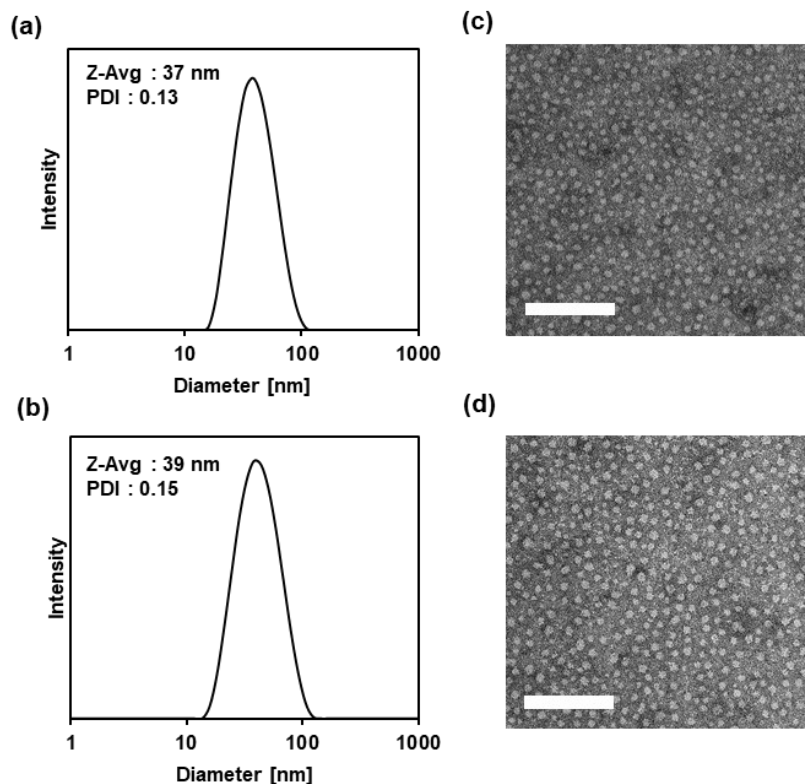


Figure 4.3. Characterization of ADT-GPLGL and ADT-GPLL micelles. (a-b) Size distribution by DLS, (c-d) TEM images of micelles negatively stained with 2% uranyl acetate solution. (a,c) ADT-GPLGL micelles, (b,d) ADT-GPLL micelles. Scale bar: 200 nm.

Furthermore, the critical micelle concentration (CMC), the polymer concentration above which micelles form, was determined by the Nile red method¹⁵⁷ to evaluate thermodynamic stability of micelles (**Figure C.1**, Supporting Information). Both micelles showed similar CMC values of 3.86 μM and 3.98 μM for ADT-GPLGL and ADT-GPLL respectively, indicating similar thermodynamic stabilities of these micelles.

4.3.3 Monitoring of micelle dissociation in the presence of MMP-2

To evaluate the MMP-2 sensitivity of ADT-GPLGL and ADT-GPLL micelles, the micelles were incubated in the absence/presence of 43.6 nM MMP-2 enzyme at 37 °C and the dissociation of micelles by MMP-2 enzyme was monitored by changes in the light intensity scattered determined

by DLS. In the case of ADT-GPLGL micelles with the MMP-2 cleavable peptide motif (GPLGL), a 60% decrease in the intensity of light scattered was observed within 24 h in the presence of MMP-2 enzyme (**Figure 4.4a**), showing dissociation of micelles due to enzymatic cleavage of MMP-2 enzyme. On the contrary, minimal dissociation was observed for ADT-GPLL micelles with MMP-2 non-cleavable peptide motif (GPLL) due to the minimal decrease in intensity of the scattered light as shown in **Figure 4.4a**.

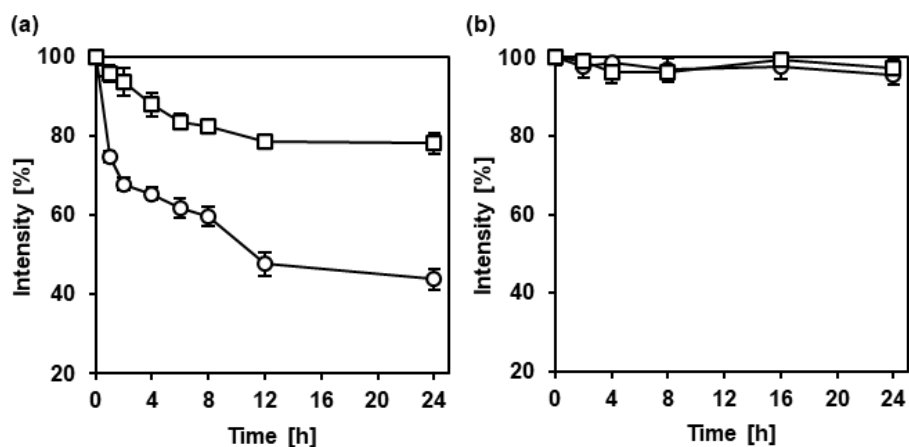


Figure 4.4. Dissociation of ADT-GPLGL (circles) and ADT-GPLL (squares) micelles upon enzymatic cleavage. The micelles were treated in the (a) presence or (b) absence of 43.6 nM MMP-2 enzyme at 37°C and change in the scattered light intensity of micelles was monitored by DLS. $n=3$.

After treatment with MMP-2 enzyme for 24 h, ADT-GPLL micelles displayed only a 20% decrease in light intensity compared to a 60% decrease in light intensity for ADT-GPLGL micelles (**Figure 4.4a**). Furthermore, no obvious dissociation was observed in the absence of MMP-2 enzyme for both micelles (**Figure 4.4b**). These results clearly indicate that ADT-GPLGL micelles bearing MMP-2 cleavable peptide motif can indeed undergo dissociation due to cleavage by MMP-2 enzymes whereas ADT-GPLL micelles bearing the non-cleavable peptide motif is less susceptible to MMP-2 cleavage. The MMP-2 sensitivity of ADT-GPLGL and ADT-GPLL

micelles following dissociation were further confirmed by monitoring the cleavage of peptide by MMP-2 enzyme with fluorescamine assay. Since MMP-2 enzyme is known to cleave peptide sequences at the site between glycine (G) and leucine (L),²²¹ fluorescamine assay was again utilized to detect the resulting leucine fraction from the N-terminus peptide sequence. Leucine concentration was determined from a calibration curve measured by fluorescamine assay (**Figure C.2**, Supporting Information).

For ADT-GPLGL micelles, 40 % of cleaved peptide (leucine) relative to the initial concentration of GPLGL was observed over a period of 24 h (**Figure 4.5a**) which is consistent with the dissociation of micelles shown in **Figure 4.4**. In contrast, ADT-GPLL micelles did not show any increase in the amount of cleaved peptide over 24 h (**Figure 4.5a**), thus confirming the minimal dissociation displayed in Figure 4. In addition, only 0.5 % of cleaved peptide was observed in 24 h for both micelles in the absence of MMP-2 enzyme (**Figure 4.5b**) Based on these results, the dissociation of ADT-GPLGL micelles (**Figure 4.3**) can be attributed to the cleavage of peptide by MMP-2 enzyme. Interestingly, ADT-GPLGL micelles did not show complete dissociation even after 24 h of treatment with MMP-2 enzyme, which is also accompanied by only a 40% increase in cleaved peptide. This could be due to the reduced accessibility of MMP-2 enzyme to the peptide motifs with the stable hydrophobic nature of the micellar core.

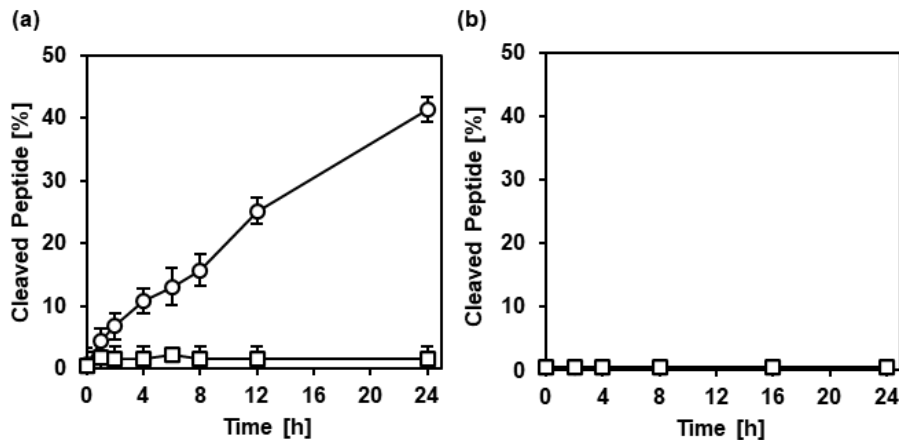


Figure 4.5. Cleavage of the peptide conjugated to ADT-GPLGL (circles) and ADT-GPLL (squares) micelles in response to MMP-2 enzyme. The micelles were incubated in the (a) presence or (b) absence of 43.6 nM MMP-2 enzyme at 37°C. Fluorescamine assay was used to detect leucine amino group from the N-terminus of peptide resulting from cleavage by MMP-2 enzyme. Fluorescence intensity ($\lambda_{\text{ex}}=390$ nm, $\lambda_{\text{em}}=475$ nm) was determined at indicated time points. $n=3$.

4.3.4 H₂S Release from Micelles in the presence of MMP-2 enzyme in HT29 Cell

Lysate

The H₂S release profiles from ADT-GPLGL and ADT-GPLL micelles in the absence/presence of MMP-2 enzyme was investigated in the presence of cell lysate using the WSP-1 H₂S detection probe.¹⁹⁷ Previously, it was showed that ADT-based H₂S donors released H₂S in cell lysate but not fetal bovine serum or glutathione-containing PBS, implying that H₂S release is induced by intracellular components, presumably enzymes.¹⁹⁴ Therefore, we hypothesize that the peptide motifs within micelles would be cleaved by MMP-2 enzyme resulting in micelle dissociation and subsequent release of H₂S. As shown in **Figure 4.6**, ADT-GPLGL micelles released two times greater H₂S in the presence of MMP-2 enzyme in HT29 cell lysate. ADT-GPLL micelles on the other hand showed minimal H₂S release both in the presence and absence of MMP-2 enzyme. This

shows that ADT-GPLGL micelles are more susceptible to dissociation in the presence of MMP-2 enzyme compared to ADT-GPLL micelles.

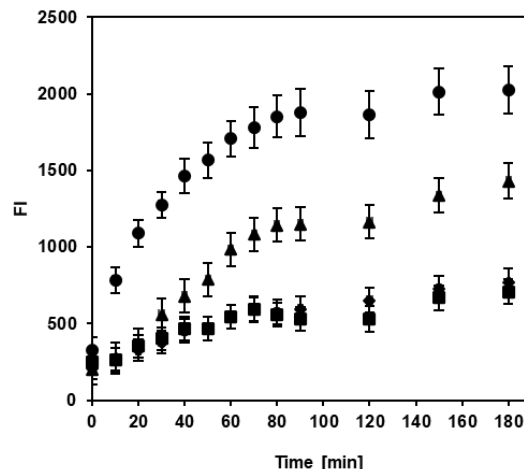


Figure 4.6. H₂S release in HT29 cell lysate. ADT-GPLGL and ADT-GPLL micelles were added to HT29 cell lysate containing WSP-1 H₂S detection probe in the absence/presence of 43.6 nM MMP-2 enzyme. Fluorescence intensity ($\lambda_{\text{ex}}=465$ nm, $\lambda_{\text{em}}=515$ nm) was monitored at indicated time point. ADT-GPLGL (+) MMP-2: circles, ADT-GPLGL (-) MMP-2: triangles, ADT-GPLL (+) MMP-2: diamonds, ADT-GPLL (-) MMP-2: squares. n=3

4.3.5 H₂S Release from Micelles in HT29

We next evaluated H₂S release from the micelles in human colon cancer HT29 cells. It is widely known that colon cancer cells produce elevated levels of MMP-2.^{205,206} HT29 cells were cultured in the presence of ADT-GPLGL micelles, ADT-GPLL micelles, and ADT donor at 50 μ M and the H₂S release in comparison to the non-treated cells (medium only) were measured using the fluorescent H₂S-detection dye, WSP-1. As HT29 cells produce H₂S endogenously,¹⁸⁴ a slight increase in fluorescence intensity for cells treated with medium only is expected. As shown in **Figure 4.7**, a similar trend of H₂S release for both micelles were observed in cell lysate in the presence of MMP-2 enzyme (**Figure 4.6**). The fluorescence intensity gradually increased up to 24 h for both ADT-GPLGL and ADT-GPLL micelles. However, ADT-GPLGL micelles released 2

times higher amount of H₂S after 10 h of incubation compared to ADT-GPLL micelles and the non-treated cells. The ADT donor itself released similar amount of H₂S in comparison to the non-treated cells. This observation is consistent with the MMP-2 sensitivity of the micelles as shown by intensity of light scattered (**Figure 4.4**) and fluorescamine assay (**Figure 4.5**), where ADT-GPLGL micelles exhibited greater dissociation in response to MMP-2, thus resulting in a higher release of H₂S.

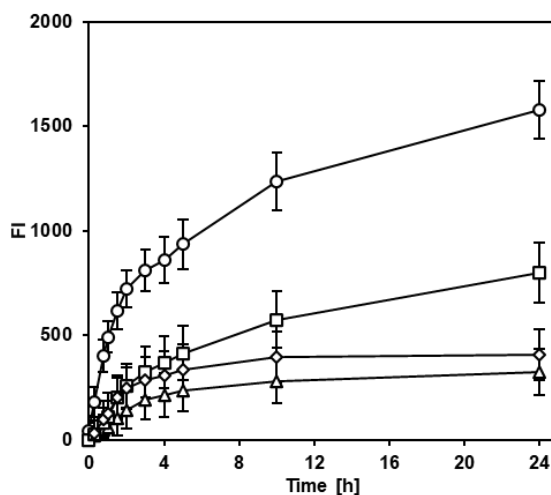


Figure 4.7. H₂S release in HT29 cells. Cells were cultured in the presence of ADT-GPLGL (circles) and ADT-GPLL (squares) micelles, ADT donor (diamonds), and medium as a control (triangles) at indicated time points (ADT Concentration: 50 μ M). Cells were washed and incubated prior with WSP-1 H₂S detection dye for 30 min. Fluorescence intensity ($\lambda_{\text{ex}}=480$ nm, $\lambda_{\text{em}}=520$ nm) was monitored at indicated time point. $n=3$

To confirm the release of H₂S from ADT-GPLGL and ADT-GPLL micelles in HT29 cells, HT29 cells were cultured in the presence of both ADT-GPLGL and ADT-GPLL micelles (25 μ M) and the H₂S release in comparison to the non-treated cells (medium only) were visualized by CLSFM using the fluorescent H₂S-detection dye, WSP-1. At 8 h, a significantly brighter fluorescence intensity was observed for ADT-GPLGL micelles in comparison to ADT-GPLL micelles and cells treated with medium only (**Figure 4.8**). ADT-GPLL micelles on the other hand displayed minimal

increase in fluorescence similar to the non-treated cells, consistent with the H₂S release profile as shown in **Figure 4.7**. Therefore, the enhanced anti-proliferative effect of ADT-GPLGL micelles can be attributed to the greater release of H₂S in response to the elevated levels of MMP-2 enzyme as shown by CLSFM.

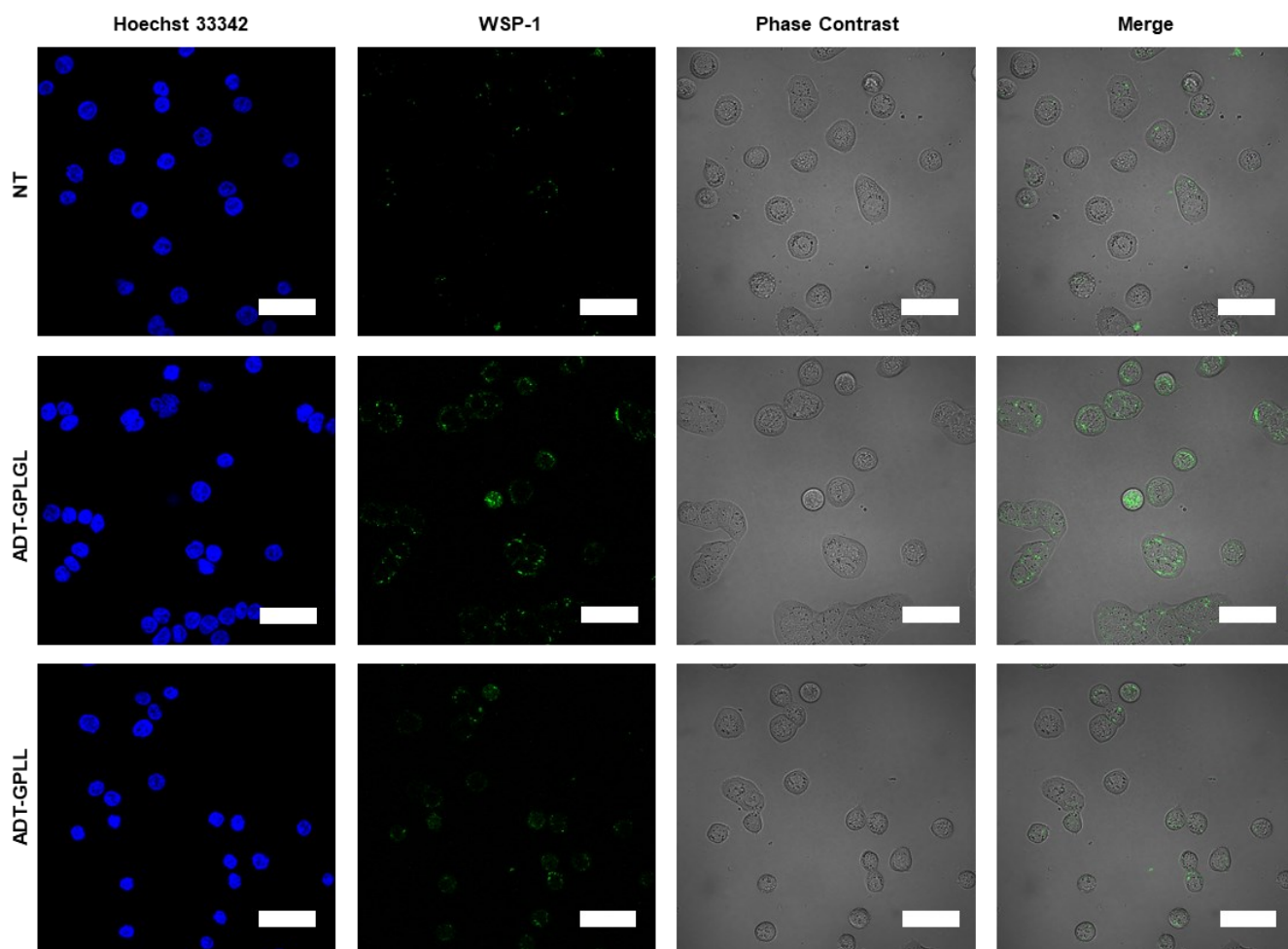


Figure 4.8. Observation of H₂S release from ADT-GPLGL and ADT-GPLL micelles (ADT concentration: 25 μ M) in HT29 cells. HT29 cells were pre-treated with Hoechst 33342 followed by WSP-1 H₂S detection dye and then cultured in the presence of micelles. After culturing for 8 h, cells were observed by CLSFM. Scale bar: 20 μ m.

4.3.6 Anti-proliferative Effect of Micelles

The antiproliferative effect of ADT-GPLGL and ADT-GPLL micelles as well as the H₂S donor (ADT) in HT29 cells was evaluated by MTT assay. H₂S has been reported to play a significant role in the inhibition of cancer cell proliferation, especially in colon cancer cells^{52,178,179,186}. Hence, we hypothesize that the release of H₂S from ADT-GPLGL micelles would exhibit the anti-proliferative effect in HT29 cells. As shown in **Figure 4.9**, ADT-GPLGL micelles exhibited a higher anti-proliferative effect compared to ADT-GPLL micelles. At an ADT concentration of 100 μM, ADT-GPLGL micelles displayed cell viability of 47 % compared to 70 % for ADT-GPLL micelles. The enhanced anti-proliferative effect of ADT-GPLGL micelles is attributed to the greater release of H₂S in response to elevated levels of MMP-2 enzyme as observed in **Figure 4.6 and 4.7**.

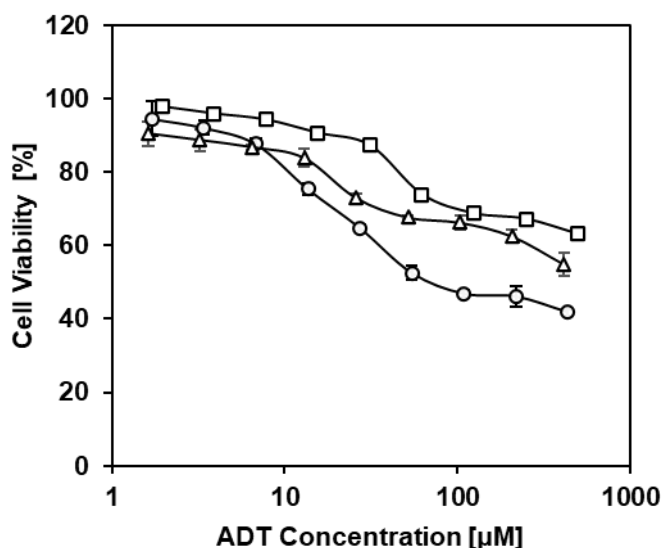


Figure 4.9. Cell viability of ADT-GPLGL (circles), ADT-GPLL (squares) micelles, and H₂S donor (ADT) (triangles) in HT29 cells. Cells were cultured in the presence of micelles for 5 d. Cell viability was measured by MTT assay. *n*=3.

4.4 Conclusion

In conclusion, H₂S donor micelles bearing MMP-2 cleavable peptide were successfully prepared and reported. The micelles bearing MMP-2 cleavable peptide sequence showed superior sensitivity to MMP-2 compared to the control micelles bearing MMP-2 scrambled peptide sequence (control). A greater release of H₂S was observed in colon cancer cells with MMP-2 sensitive micelles compared to the control and the H₂S donor (ADT). In addition, the greater release of H₂S from MMP-2 sensitive micelles exhibited stronger anti-proliferative activity in colon cancer. Hence, the design of MMP-2-sensitive H₂S donor micelles, which releases H₂S in cancer cells in response to the overproduction of MMP-2 could potentially provide an insight into the anti-cancer effects of H₂S.

5 Polymer surface dissection for isolation and identification of early colonizing bacteria on membrane surfaces

Abstract

Biofilm formation (biofouling) remains an inevitable phenomenon and constant issue in bio-separation equipment. For example, in water treatment facilities, biofouling often causes membrane surface deterioration and decreased separation performance. While there has been significant progress in understanding the factors that influence biofilm formation in membrane bioreactors, there exists a limited set of tools for characterizing the complex, spatial and temporal mechanisms of biofouling processes over membrane surfaces. Current methods of characterizing biofouling rely on membrane autopsies after membrane failure occurs, providing a bulk analysis across entire membrane segments, which gives only limited end-point information on the mechanisms that initiate and drive fouling. In an effort to improve our understanding of the spatial and temporal mechanisms of the biofouling process, a novel method of separating and isolating small, colonizing microbial aggregates from fouled membrane surfaces at discrete time points is developed. This polymer surface dissection (PSD) method utilizes photodegradable polyethylene glycol (PEG)-based hydrogels functionalized with affinity ligands to first detach microbes from the surface of a fouled membrane. Subsequent exposure of targeted flocs ($2000 \mu\text{m}^2 - 60000 \mu\text{m}^2$) to patterned ultraviolet (UV) light with high spatial precision allowed for successful extraction and isolation of flocs from the hydrogel for follow-up characterization using 16S rRNA sequencing without requiring a culture step for microbial enrichment. The approach is designed to be non-destructive to both the flocs and the membrane surface and is demonstrated here for isolation and identification of microbes that form flocs as small as $2000 \mu\text{m}^2$ on PVDF membrane surfaces.

With these capabilities, PSD approach can be used to identify sub-communities of microorganisms that initiate and drive membrane biofilm formation in a variety of bio-separation processes.

5.1 Introduction

Biofouling refers to the complex multi-step process of biofilm formation involving multiple bacterial species embedded in a matrix of extracellular polymeric substances (EPS) composed mainly of polysaccharides, proteins, lipids, and a variety of nucleic acid.^{222,223} Biofouling is driven by irreversible attachment of early colonizing microbes to a surface, followed by EPS expression, growth, and recruitment of additional microbes into a maturing biofilm.²²⁴ The EPS matrix often serves as platform for surface attachment and sequestration of nutrients and oxygen. The matrix also acts as a defense mechanism against harsh environmental conditions and impedes the transport of antibiotics, thus enabling the biofilm to continuously thrive.²²⁵⁻²²⁸ Despite the significant effort to mitigate biofilm formation, it remains an inevitable phenomenon and a constant challenge in a number of applications including the healthcare industry,⁸² food industry,⁸¹ marine systems,²²⁹ and industrial water systems.⁸³ For instance, implant-related infections due to biofilm formation and contamination remain significantly high with patients typically requiring revision surgery in the case of a severe infection.^{84,85} Biofilm formation in in the marine industry such as biofouling in ship hulls has also shown adverse effects such as increased fuel consumption due to frictional resistance, corrosion, and high maintenance cost.^{230,231}

In the water treatment industry, biofouling represents the “Achilles heel” of membrane-related fouling, accounting for the majority of membrane foulant which also consisting of inorganic, organic, and colloidal material.¹¹⁹ Membrane biofouling in wastewater bioreactors causes deterioration in membrane permeability and a significant decrease in trans-membrane

pressure, treated water flux, and separation efficiency.²³² This demands frequent chemical cleaning protocols and operational shutdown periods that are typically time-consuming, labor-intensive, costly, and ultimately shortens membrane lifetimes.^{119,120} Conventional methods such as periodic backwashing or adjustment of membrane operational conditions are not sufficient to control biofouling due to the rapid spatial and temporal growth of microorganisms on the surface of membranes.¹²⁰ Instead, biological-based anti-fouling strategies such as quorum quenching, where communication between cells is inhibited through inactivation of autoinducers have been shown to be more effective in mitigating biofilm formation.²³³⁻²³⁵ More recently, the prevention of undesired adhesion interactions between the membrane and microorganism by modification of membrane properties with anti-microbial and anti-fouling properties utilizing polymeric interfaces or nanomaterials seems to be a promising approach.¹²¹⁻¹²⁴ While much effort has focused on developing biological, chemical, and physical treatment methods to alleviate the early stages of biofouling, there is a lack of fundamental understanding of the central mechanisms that drive biofilm formation over these membrane surfaces. An improved, mechanistic understanding of this complex process may facilitate the design of effective biofouling mitigation strategies.^{126,236,237}

Recent findings point towards early colonizers - the first microbes to attach to a clean membrane surface - as the primary driver of biofilm formation in membrane bioreactors.^{126,238} The isolation and characterization methods of these early-stage colonizers however are limited to only a number of tools that are unable to provide an accurate mechanistic and spatiotemporal understanding of early-stage biofouling. Current methods of isolating and characterizing microbes rely heavily on membrane autopsies paired with a combination of molecular and microscopic methods. Membrane autopsies can provide a bulk analysis across the entire membrane segment, thus giving only limited endpoint information on the mechanisms that initiate and drive

fouling.^{128,239,240} In addition, the destructive nature of membrane autopsies is not ideal for extraction of EPS since it causes cell lysis and alters its physical and chemical membrane characteristics.¹³⁰ Another possible approach to extracting microbes is laser capture microdissection (LCM). LCM uses an optical microscope to identify cells of interest, then places them in contact with an adhesive transfer film, where a focused IR laser is used to melt the film, adhering them to the cells of interest. Targeted cells are lifted off the substrate and then lysed for downstream molecular analysis.¹²⁹ Although there have been a few reports investigating spatial heterogeneity in biofilm using LCM,^{241–243} it remains uncommon in microbiology as it is destructive to either the sectioned cells or to the underlying surface.

Here, we report the development of a polymer surface dissection (PSD) approach to target and isolate microbes that initiate biofouling spatiotemporally from wastewater membranes without destroying the microbes or the underlying polyvinylidene difluoride (PVDF) membrane surface (**Figure 5.1**). The PSD approach utilizes polyethylene glycol (PEG)-based photo-responsive hydrogels. Photodegradable hydrogels are formed using PEG-acrylate macromers modified with photocleavable *o*-NB chromophores and crosslinked with a four-armed PEG tetrathiol macromers through Michael-type addition reactions. The photodegradable hydrogels were also functionalized with affinity ligands (poly-L-lysine and *Wheat Germ Agglutinin* (WGA)) to facilitate non-destructive detachment of microbes from membrane surfaces. Upon exposure with patterned light (365 nm), bond photocleavage causes rapid degradation of hydrogel, enabling sectioning capabilities of targeted flocs at varying floc sizes at high resolution. The DNA of extracted flocs were then immediately isolated and characterized by 16S rRNA sequencing.

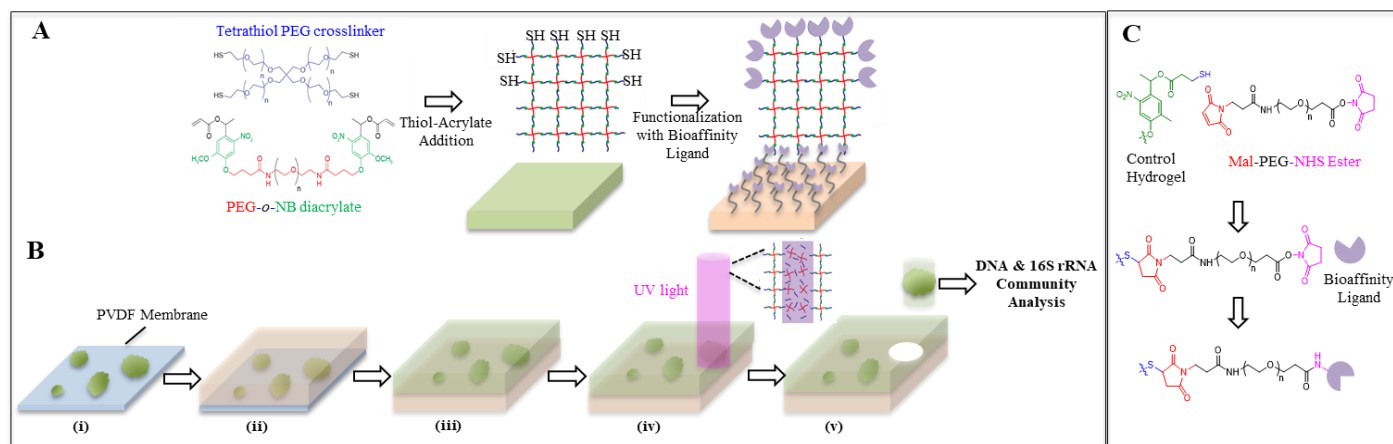


Figure 5.1. (A) Preparation of hydrogel by thiol-acrylate addition and functionalization with bioaffinity ligand (WGA). (B) Schematic of the PSD method. (i) PVDF Membranes are contacted with wastewater solutions and cell attachment to the surface is characterized using an optical microscope. (ii) The substrate is then contacted with first layer of pre-formed hydrogel functionalized with bacteria affinity ligands for flocs transfer. (iii) The hydrogel is removed from the membrane surface followed by addition of a second pre-formed hydrogel (no bioaffinity ligand) for clean extraction (iv) Cells of interest are sectioned from hydrogel base after exposure to patterned UV light (v) Sectioned cell (s) are lifted off from the hydrogel and extracted for 16S rRNA analysis. (C) Reaction scheme for functionalization of hydrogel with bioaffinity ligand by maleimide-thiol coupling and *N*-Hydroxysuccinimide ester-amine reaction

5.2 Experimental Methods

5.2.1 Materials

Triticum vulgare lectin (wheat germ agglutinin, WGA) was purchased from Sigma-Aldrich and diluted to specific concentrations in buffer and stored at -20°C . PVDF membranes were purchased from Novavem. PEG-diacrylate (PEGDA, MW 3400) was purchased from Laysan Bio. Pentaerythritol tetra (mercaptoethyl) polyoxyethylene (4 arm PEG, $((\text{CH}_2)_2\text{-SH})_4$) was purchased from NOF America Corporation. Ethanol (EtOH), methanol (MeOH), and hydrochloric acid (HCl) were purchased from Fisher. Anhydrous toluene (TL), Maleimide-PEG-NHS-ester, and 3-mercaptopropyl) trimethoxysilane (MPTS) was purchased from Sigma-Aldrich. QIAamp DNA Micro Kit was purchased from QIAGEN. All chemicals were used as received unless stated otherwise.

5.2.2 Thiol Surface Functionalization

Thiol functionalization onto coverslip surface is used here to provide covalent attachment of the hydrogel and made as previously reported with slight modification.⁹⁸ Briefly, five glass coverslips (1.8 x 1.8 cm) were cleaned with oxygen plasma for 3 min using PDC-001-HCP Plasma Cleaner (Harrick Plasma) and further hydroxylated in a mixture of 1:1 of MeOH:HCl (37 N) at RT for 1 h. The coverslips were then rinsed in ultrapure water (3x20 mL) and dried under N₂. For functionalization with thiol groups, the coverslips were immersed in (3-mercaptopropyl) trimethoxysilane (MPTS) (269 mM) solution in anhydrous TL (5 v/v) at RT for 4 h, followed by washing with TL, EtOH/TL (1:1), and EtOH, 3 times each. The thiol-functionalized coverslips were then dried under N₂ and stored in ethanol at 4 °C for further use.

5.2.3 Preparation of Photodegradable Hydrogel

The photodegradable hydrogels were synthesized by Michael-type addition reaction as previously reported.^{98,244,245} The hydrogel precursor solution was prepared by adding 5.6 μL (M_n 3400 Da, 49 mM) of photodegradable PEGDA in water to 12 μL of PBS (pH 8.0), followed by the addition of 6.9 μL of PEG-tetrathiol (M_n 10,000 Da, 20 mM) in water, resulting in an equimolar ratio of acrylate to thiol. The precursor solution was mixed thoroughly and 7 μL was quickly transferred onto a perfluoroalkylated glass slide prepared as previously reported.²⁴⁴ The slides were then contacted with the thiolated coverslip (taped (40.0 μm thickness) on both edges), enabling stable covalent attachment of the hydrogel to the surface by thiol-acrylate coupling. The gelation was complete after 25 min and the perfluoroalkylated slide was peeled off gently to prevent rupturing of the hydrogel.

5.2.4 Functionalization of Hydrogel with Bio affinity Ligand (WGA)

The pre-formed photodegradable hydrogels were functionalized with WGA by maleimide-thiol coupling and NHS ester-amine reaction. 300 μL of Maleimide-PEG-NHS-ester in PBS (1 mg/mL, pH 6.7) was first added to the hydrogels and incubated in the dark at RT for 2 h. After 2 h, the solution was removed, and the hydrogels were washed with PBS (pH 6.7) (3x300 μL). The NHS-functionalized hydrogels were then immobilized by the addition of 300 μL of WGA in PBS (0.1 mg/mL, pH 7.4) at RT for 2 h, followed by washing with PBS (pH 7.4) (3x300 μL) to remove physisorbed molecules.

5.2.5 Transfer of Floccs from Membrane to Hydrogels

Activated sludge wastewater solutions were collected from Manhattan Wastewater Treatment Plant (Manhattan, KS) into 50 mL falcon tubes. The solutions were washed/resuspended in PBS (pH 7.4) and kept upright on the bench for 10 min for complete sludge precipitation. Then, 3 mL of the wastewater solution was harvested from the interphase and added to a scintillation vial containing 0.8 x 0.8 cm membrane filters (Novamem, PVDF20, 0.02 μm) attached to a glass slide (1.0 x 1.0 cm) at the bottom of the vial. The vials were loosely capped and placed in a shaker (200 rpm) at 25 °C. After 48 h, the membranes attached to the glass slide were gently removed from the bottom of the scintillation vial in an upright position and placed in contact with the hydrogel for 30 min. Uniform pressure was applied with the use of a 10 g weight for increased contact between the membrane and hydrogel. The membranes were detached gently to prevent rupturing of both the membrane and hydrogels.

5.2.6 Degradation of Hydrogel and Extraction of Floccs

Following the transfer of floccs from the membrane to the hydrogel, the second layer of hydrogel was added to allow for a clean extraction. As before, 7 μL of the precursor solution was quickly

transferred onto a perfluoroalkylated glass slide, placed gently upside down onto the first layer of hydrogel containing flocs, and allowed to react for 22 min. After gelation of the second hydrogel layer, the perfluoroalkylated slide was peeled off gently. Flocs with desired dimensions were then identified with a BX51 upright microscope and selectively extracted by exposing the hydrogel to patterned UV light (365 nm) using the Polygon400 patterning device configured to an upright microscope (BX51, Olympus). The size of the flocs was measured prior to UV exposure using Image J software. The patterning device allows for micron-scale spatiotemporal control and the ability to tune the wavelength, intensity, irradiation time, as well as type of exposure patterns. Here, multiple patterns including solid rectangles, open rectangles, and ring patterns were used for extraction of desired flocs. Degraded parts of the hydrogel containing targeted flocs were then extracted into 200 μL solution (PBS, pH 7.4) by suctioning followed by two washes with a total liquid volume of 600 μL . The flocs were then stored at $-80\text{ }^{\circ}\text{C}$.

5.2.7 DNA Extraction

Before proceeding to DNA extraction, most of the liquid volume of each individual flocs was evaporated off leaving approximately 50 μL to keep the flocs hydrated. DNA extraction was then performed using the Qiagen QIAamp DNA Micro Kit per the manufacturer's protocol with slight modification. Briefly, the 50 μL floc samples were lysed overnight (20 h) at $56\text{ }^{\circ}\text{C}$ with 130 μL Buffer ATL and 20 μL Proteinase K. A mixture of 1 μL carrier RNA (1 $\mu\text{g}/\mu\text{L}$) in 200 μL buffer AL followed by 200 μL ethanol was then added to the sample, loaded onto the QIAamp MinElute spin column, washed, and eluted in 50 μL elution buffer. Elution was repeated a second time to increase DNA yield with a total volume of 100 μL . The samples were stored at $-20\text{ }^{\circ}\text{C}$ before sequencing analysis. Nanodrop absorbance and Qubit Fluorescence were used to quantify DNA yield and quality.

5.2.8 Identification with 16S rRNA Sequencing

The Integrated Genomics Facility (IGF) at Kansas State University provided the sequenced data as paired end demultiplexed fastq.gz files which were then imported into QIIME2 software for processing.²⁴⁶ Each sample had two fastq.gz files representing the forward and reverse reads for that sample. The forward and reverse reads were merged using the join-pairs method in the q2-vsearch plugin within QIIME2. The joined reads were then denoised with qiime deblur denoise-16S to obtain error free representative sequences.²⁴⁷ After denoising, the resulting high-quality sequence variant data was further used to determine the taxonomic composition in each sample. This was done by assigning taxonomy to the sequences using a pre-trained Naïve Bayes classifier trained on the Greengenes 13_8 99 % OTUs for the V4 region (515F/806R) of the 16s rRNA gene. The resulting QIIME2 visual artifact was visualized in “view.qiime2.org” website as taxonomic bar plots and the corresponding family/phylum level table was exported to Microsoft Excel as .CSV file for further processing. The taxonomic table at the family/level was normalized against the total number of bacterial sequences per sample to calculate the relative bacterial abundance (%) in Microsoft Excel. Taxonomically unassigned reads were excluded from the relative abundance calculation and only taxa representing $\geq 1\%$ of relative abundance in at least one of the samples were used to generate the family level taxonomic heatmaps and phylum level bar plots.

5.3 Results and Discussion

5.3.1 DNA Quantification and 16S rRNA Analysis of Extracted Samples

Here, the major goal was to assess the DNA quality and quantity of flocs extracted from the control (PEG only) and WGA-functionalized hydrogel before proceeding to 16S rRNA amplicon sequencing. Since WGA-functionalized hydrogel was previously shown to extract

higher numbers of cells without significantly decreasing cell viability compared to poly-L-lysine-functionalized hydrogel, it was used here to extract flocs for further studies on DNA quality and quantity. Functionalization of the hydrogel with WGA was achieved by maleimide-thiol group coupling followed by NHS ester-amine reaction as shown in **Figure 5.1**. Extraction of flocs from both the control and WGA-functionalized hydrogels were then carried out in a ring or open rectangle pattern to reduce DNA damage due to UV exposure (**Figure 5.2**). For larger flocs, the ring pattern was not sufficient for liftoff of the floc from the hydrogel upon first exposure. This necessitated the use of an open rectangle instead to avoid repeated exposure to UV light, which is known to be cytotoxic to bacteria through the generation of reactive oxygen species.²⁴⁸ In addition, areas of the hydrogel with no flocs present were exposed to UV light under the same conditions and extracted as a negative control.

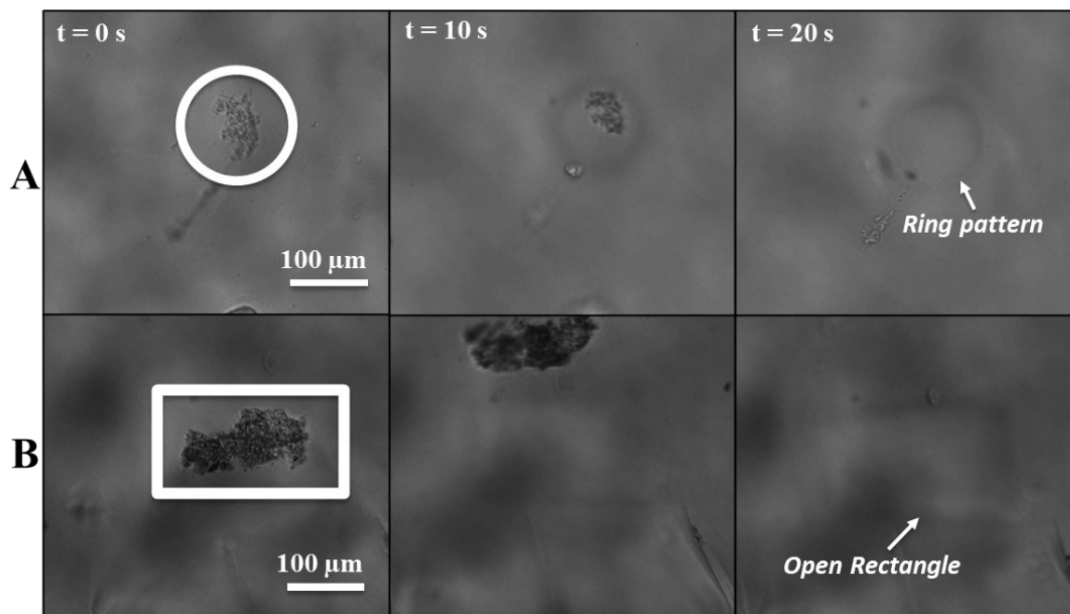


Figure 5.2. Brightfield microscope images of hydrogels during extraction of targeted flocs at varied time points. Hydrogels were unfunctionalized or functionalized with WGA then extracted using (A) a 45 mm diameter ring pattern or a (B) 40,000 mm² open rectangle pattern.

After extraction, DNA from both the flocs and the negative control were isolated using a Qiagen QIAamp DNA Micro Kit. Low concentrations of DNA from extracted flocs were expected as isolation was performed without culturing for enrichment, and necessitated the use of carrierRNA to retain as much DNA as possible.^{249,250} Extraction was followed by evaluation of DNA yield and quality by Nanodrop absorbance measurements. As shown in **Figure 5.3A**, flocs extracted from the control hydrogel in the absence of carrier RNA resulted in a much lower DNA yield (< 5 ng/ μ L) compared to flocs of similar sizes isolated in the presence of carrierRNA (>10 ng/ μ L) (**Figure 5.3B-C**). In the presence of carrierRNA, a trend of increasing DNA yield with increasing floc size was observed for both the control and WGA-functionalized hydrogels (**Figure 5.3B-C**). Furthermore, fairly similar DNA yields for each floc size were observed for the control and WGA-functionalized hydrogels.

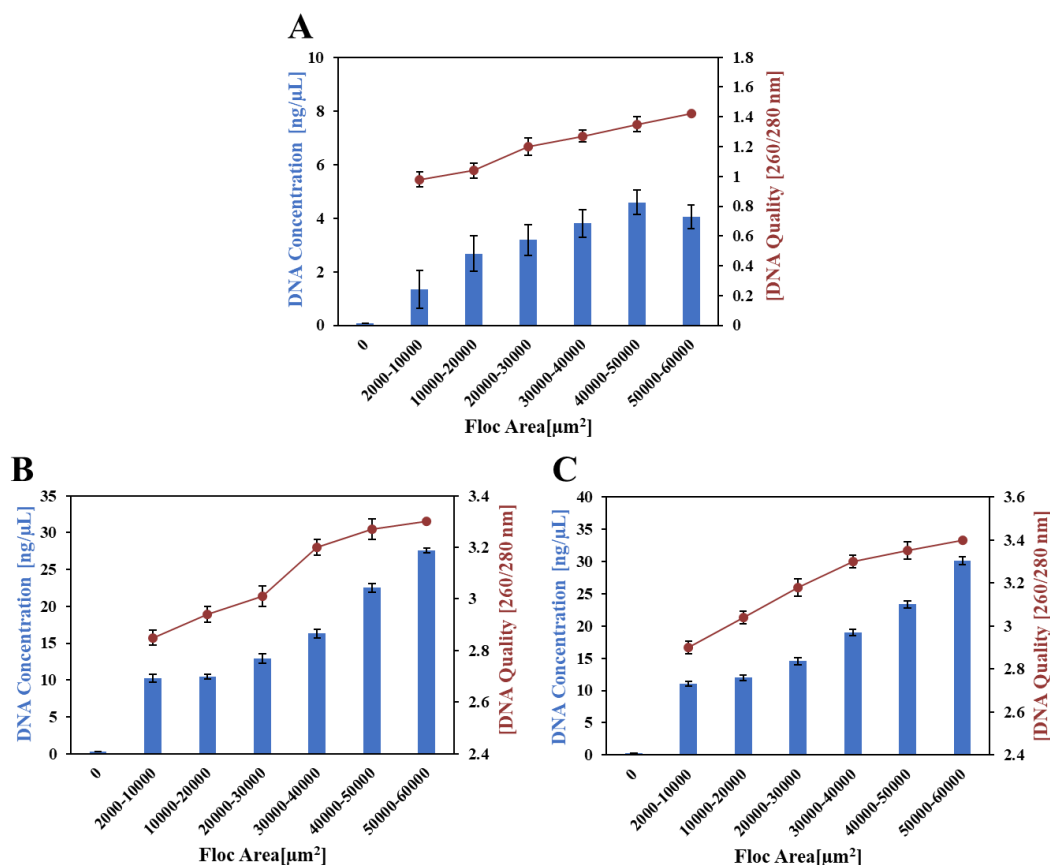


Figure 5.3. DNA yield and quality quantified by Nanodrop at varying floc sizes. (A) Flocs were extracted from control hydrogel (without affinity ligand) and DNA was isolated in the absence of carrierRNA (B) Flocs were extracted from control hydrogel (without affinity ligand) and DNA was isolated in the presence of carrierRNA. (C) Flocs were extracted from WGA-functionalized hydrogel and DNA was isolated in the presence of carrierRNA. Floc sizes were determined by ImageJ. $n=3$

The DNA quality on the other hand, determined by the ratio of absorbance (260/280nm) were much higher than the ideal quality range (1.8-2.0) due to the presence of carrierRNA that absorbs at 260 nm as well (**Figure 5.3B-C**).²⁵¹⁻²⁵³ To accommodate for this, a control sample containing blank hydrogel and the same amount of carrierRNA were ran through the silica column and quantified. The resulting DNA yield and corresponding absorbance at 260 nm were then used to re-evaluate the initial DNA yield and quality results. As observed in **Figure 5.4A**, the overall

DNA yield decreased slightly while the DNA quality fell within the ideal range (1.8-2.0) for flocs $>30,000 \mu\text{m}^2$. Similar to the DNA yield, DNA quality increased with increasing floc size. At the larger floc sizes ($50,000\text{-}60,000 \mu\text{m}^2$), DNA quality peaked at around 1.80 for both the control and WGA-functionalized hydrogel. In addition, Qubit fluorescence measurements were also performed since Nanodrop absorbance measurements are known to have lower detection limits and a tendency to overestimate DNA yield, especially in the presence of carrierRNA.²⁵¹ As expected, Nanodrop absorbance measurement exhibited a threefold higher DNA yield compared to Qubit Fluorescence measurement, further proving the tendency of Nanodrop to overestimate DNA yield (**Figure 5.4B**).

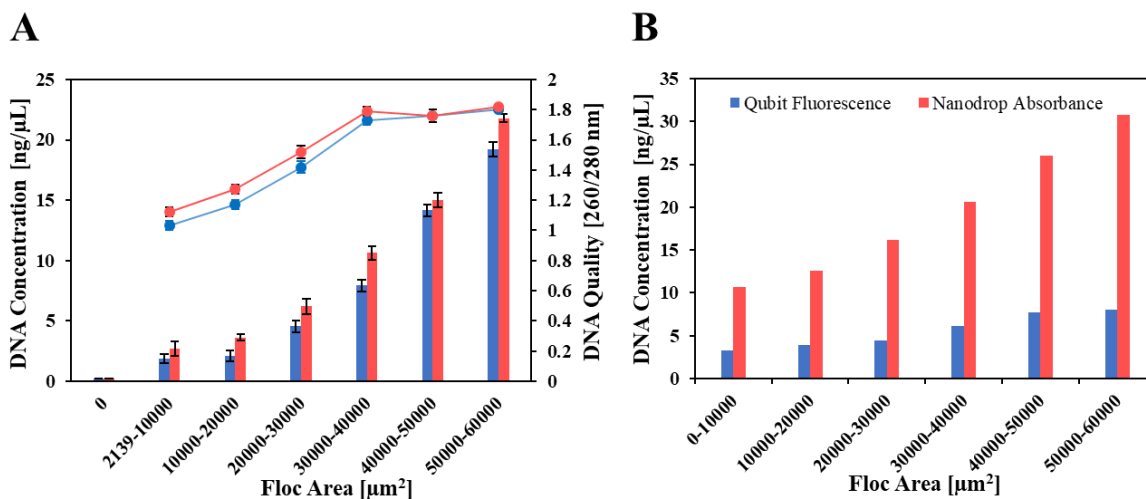


Figure 5.4. (A) DNA yield (bar chart) and quality (line chart) quantified by the Nanodrop at varying floc sizes. Blue bars and lines: Flocs isolated from control (without affinity ligand) hydrogel. Pink bars and lines: Flocs isolated from WGA-functionalized hydrogel. Floc sizes were determined by ImageJ ($n=3$). (B) Comparison of DNA yield quantified by Nanodrop absorbance and Qubit fluorescence at varying floc sizes.

After quantification of the DNA yield and quality, phylogenetic analysis of the extracted flocs and control wastewater sample was performed based on 16S rRNA sequencing to characterize the composition of each floc removed from the membrane surface. Analysis of five

flocs at varying floc sizes (**Figure 5.5B-F**) at the family level revealed an abundance of Flavobacteriaceae (~20%) and Weeksellaceae (~10 %) at the smaller floc sizes (2000-40000 μm^2) compared to an abundance of Moraxellaceae (~12%), Bradyrhizobiaceae (~12%), Brucellaceae (15-25%), and Aeromonadaceae (20-35%) at the larger floc sizes (40000-60000 μm^2) (**Figure 5.5A**). Interestingly, a shift in composition of the dominant bacterial family was observed as the floc sizes varied.

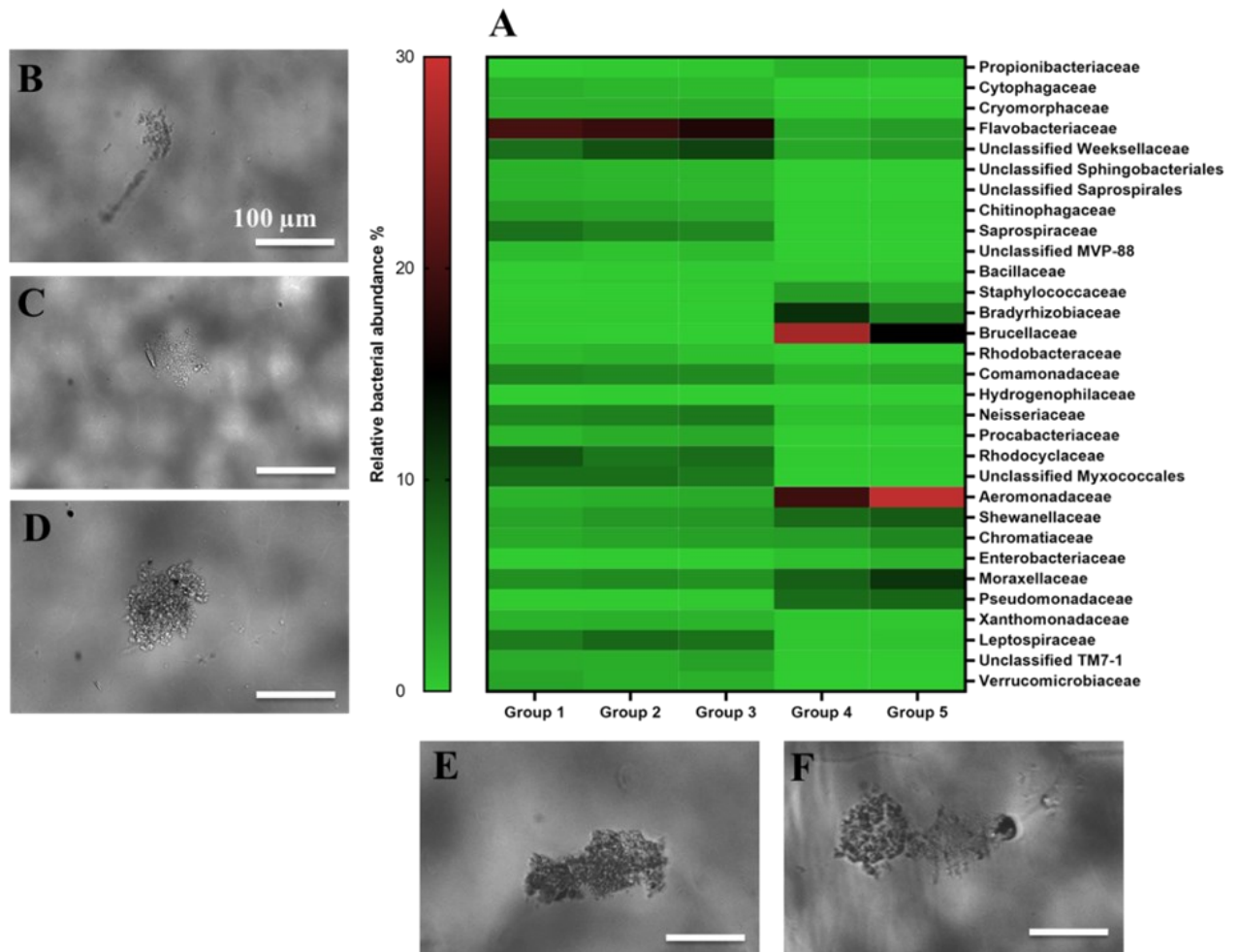


Figure 5.5. Heat map showing distribution of family level bacteria ($\geq 1\%$ relative bacteria abundances) at varying floc (group) sizes (arranged in increasing order) accompanied by corresponding microscopic images (B-F). (B) Group 1: 2000-15000 μm^2 (C) Group 2: 15000-30000 μm^2 (D) Group 3: 30000-40000 μm^2 (E) Group 4: 40000-50000 μm^2 (F) Group 5: 50000-60000 μm^2 .

At the phyla level, this corresponded to an abundance of Bacteroidetes and Proteobacteria at the smaller floc sizes and Proteobacteria at the larger floc sizes (**Figure 5.6**). This is consistent with previous studies on microbial communities in aerobic wastewater treatment systems, where Proteobacteria and Bacteroidetes were found to be the dominant bacterial phyla.²⁵⁴⁻²⁵⁶ It is important to note that these studies were conducted at different stages and conditions of reactor operations, thus presenting a more accurate depiction of the overall distribution of dominant bacterial communities. However, the PSD method used here for the extraction of microbes that form small flocs on membrane surfaces successfully demonstrates the capability for follow-up characterization of bacterial compositions by 16S rRNA sequencing without requiring a culture step for enrichment.

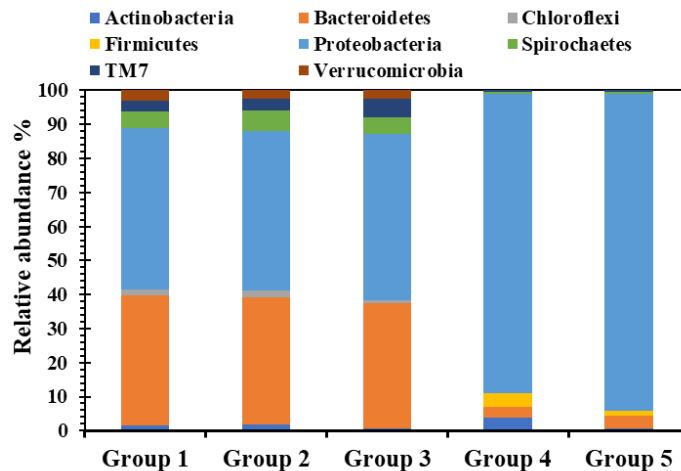


Figure 5.6. Distribution of corresponding bacterial phyla with $\geq 1\%$ relative bacterial abundance at varying floc (group) sizes (arranged in increasing order). Group 1: 2000-15000 μm^2 , Group 2: 15000-30000 μm^2 , Group 3: 30000-40000 μm^2 , Group 4: 40000-50000 μm^2 , Group 5: 50000-60000 μm^2 .

5.4 Conclusion

The PSD technique is capable isolation of individual flocs adhered to the PVDF membranes for genomic analysis. The method uses a hydrogel-based lift-off processes followed

by exposure of the hydrogel to a spatiotemporally controlled UV light from a patterned illumination tool. The process does not damage the flocs or the underlying membrane surface. Here, WGA-functionalized hydrogels were used for capture and isolation of targeted microbes after initial biofilm formation for follow-up DNA and molecular analysis. DNA analysis of the extracted flocs in terms of DNA yield and quality showed that the PSD approach was sufficient for 16S community analysis of the extracted flocs, allowing for accurate identification of microbes within the floc. Importantly, the method does not require a culture step for microbial enrichment, which would bias the sequencing in favor of highly-culturable isolates. Sequencing revealed a diverse composition of bacterial communities at the phylum and family level with varying floc sizes.

Based on these findings, it can be concluded that the PSD technique allows for genomic analysis and identification of microbes that form small flocs on membrane surfaces. The PSD approach offers significant benefits compared to bulk compositional analysis of membrane biofilms obtained from standard membrane autopsies, which will enable researchers to understand membrane biofouling in a spatiotemporal manner. Ultimately, the ability to connect microscopic information (i.e. floc area) with composition (16S rRNA sequencing) at floc sizes as low as 2000 μm^2 as demonstrated here, opens the door to a variety of additional genotype-to-phenotype determinations such as identification of membrane colonizers that produce high amounts of EPS. Future work is aimed at using the fully-developed PSD method to identify communities of microorganisms that initiate membrane biofilms in AnMBR wastewater treatment systems, where efforts to alleviate membrane fouling currently account for as much as 50% of total energy costs.²⁵⁷

Acknowledgment:

This work was supported by the National Science Foundation (Award #1805631)

6 Summary and Future Outlook

6.1 Design of stimuli-sensitive micelles for cancer-targeted drug delivery

The vast majority of this dissertation (**chapters 2, 3, and 4**) focuses on utilizing the intrinsic properties present in tumor microenvironments (TME), mainly elevated levels of reactive oxygen species (ROS) and overproduction of MMP-2 enzyme for the design and synthesis of stimuli-sensitive synthetic block copolymer polymeric micelles (BCPMs) for targeted delivery of therapeutics to cancer cells with minimized toxic side effects.

6.1.1 ROS-sensitive approach

Under the ROS-sensitive approach, micelles with fine-tuned oxidation sensitivities were designed so that they are stable in healthy tissues, but release payloads in cancer cells associated with elevated ROS levels (**Chapter 2**). As previously reported, thioether-containing drug carriers have shown promising ability to improve delivery of a variety of drugs in response to elevated levels of ROS in cancer cells. However, they often suffer from immature release of drugs due to destabilization of the drug carriers in healthy tissues with low levels of ROS, hence significantly reducing their selectivity towards cancer cells. In this study, the micelles with fine-tuned oxidation sensitivities significantly increased toxicity of Dox, a typical chemotherapy drug in liver cancer cells (HepG2) but protected normal cells (HUVECs) from Dox cytotoxicity, especially in the case of the intermediate ROS sensitive micelles, TM. Indeed, the fine-tuning of thioether oxidation sensitivities is a promising approach for rationally designing cancer cell-specific drug delivery systems that selectively release drugs in cancer tissues under oxidative stress, but are stable in healthy tissues. As a step forward, hydrogen sulfide (H₂S) prodrug (ADT) was chemically conjugated to the core of BCPMs bearing the same oxidation-sensitive thioether group as previously reported and the anti-cancer effects of H₂S in colon cancer cells (HT29) were evaluated

(Chapter 3). While numerous macromolecule-based donors for delivery of H₂S has been developed to release H₂S in a sustained manner and prevent toxic side effects caused by the donors, targeted delivery of H₂S via macromolecular approaches remains relatively new and under-explored. Typically, a slower release of H₂S from polymeric micelles is expected compared to the small H₂S donor due to the ability of the micellar structure to limit access of molecular triggers to the H₂S donating moiety located in the hydrophobic core. Remarkably, a much greater release profile of H₂S was observed from the oxidation-sensitive H₂S donor micelles compared to the control and H₂S donor in colon cancer cells with elevated levels of ROS. The greater release of H₂S subsequently showed enhanced anti-proliferative effects in colon cancer cells with minimal toxicity in normal cells (HUVECs) with low levels of ROS. This result is significant as it could clarify the amount and duration of H₂S required to exert anti-proliferative activity, whose role has been largely controversial.

6.1.1.1 Future Work

For future work, I would recommend further engineering the thioether-bearing polymeric micelle (TM) by adding a ROS generating moiety such as cinnamaldehyde and benzoyloxycinnamaldehyde to amplify the generation of ROS in cancer cells also known as ‘oxidation therapy’ while simultaneously delivering Dox in response to elevated levels of ROS. It has been reported that cancer cells are known to adapt to the oxidative stress by enhancing antioxidant defense systems to compensate for the cellular damage induced by ROS and therefore causing drug resistance. The increased ROS generation may therefore speed up ROS-induced apoptosis in cancer cell with heightened oxidative stress while simultaneously enhancing selectivity and toxicity of Dox in cancer cells in response to elevated levels of ROS. This would also minimize the toxicity in normal cells with low levels of ROS. Similarly, the use of antioxidant

suppressing compounds could also reduce the ability of cancer cells to adapt under oxidative stress, thus reducing drug resistance and increasing the toxicity of drugs.²⁵⁸ Zinc protoporphyrin is widely used as an antioxidant suppressing compound to inhibit antioxidant heme oxygenase-1 (HO-1), which is known to be overexpressed in cancer cells and protect them from oxidative stress. Adding an antioxidant suppressing compound to the existing thioether-bearing micelles could potentially enhance the selectivity of thioether-bearing micelles towards cancer cells and further increase the toxicity of Dox while simultaneously minimizing toxicity in normal cells. In addition, the *in vivo* therapeutic effectiveness of these polymeric micelle formulations need to be investigated as they are known to undergo premature release of drugs during circulation in the body.

6.1.2 MMP-2 sensitive approach

Under the MMP-2 approach, BCPM bearing MMP-2 enzyme cleavable peptide motifs and chemically conjugated H₂S prodrug (ADT) was designed for site-specific delivery of H₂S to cancer cells (**Chapter 4**). Here, H₂S donor micelles bearing MMP-2 cleavable peptides were designed to achieve site-specific delivery of H₂S in cancer cells, which overproduces MMP-2. The micelles bearing MMP-2 cleavable peptide sequence showed superior sensitivity to MMP-2 compared to the control micelles bearing MMP-2 scrambled peptide sequence. A greater release of H₂S was observed in colon cancer cells with MMP-2 sensitive micelles compared to the control and the small H₂S donor. In addition, the greater release of H₂S from MMP-2 sensitive micelles exhibited stronger anti-proliferative activity in colon cancer. Hence, the design of MMP-2-sensitive H₂S donor micelles which releases H₂S in cancer cells in response to overproduction of MMP-2 could potentially provide an insight into the anti-cancer effects of H₂S.

6.1.2.1 Future Work

While the H₂S donor micelles bearing MMP-2 cleavable peptide motif were shown to be sensitive to MMP-2 and underwent dissociation (**Figure 4.3**) due to cleavage of peptides by MMP-2, only 40 % of peptide was cleaved over a period of 24 h (**Figure 4.4**). This may be due to the reduced accessibility of MMP-2 to the peptide motif located in the hydrophobic core of the micelles. However, the majority of studies utilizing MMP-2-cleavable peptide motifs or linkers for delivery of anticancer drugs have not reported issues with the accessibility of MMP-2 to the peptide motifs or linkers. Hence, the stability of H₂S donor micelles bearing MMP-2 cleavable peptide motifs as well as cleavage studies should be further investigated to evaluate the MMP-2 mediated cleavage of peptide motif. This could potentially lead to the fine-tuning of micelle stability (varying hydrophilic and hydrophobic block lengths) to facilitate the cleavage of peptide motifs in the micellar core by MMP-2 and further modulate the release of H₂S in an effort to enhance its anti-proliferative effects. If accessibility to MMP-2 indeed is an issue, Cathepsin B, another enzyme that is overexpressed in cancer cells can be used as a target enzyme as they are typically smaller in size compared to MMP-2 enzyme. This would enable better access to the peptide motifs located in the micellar core, and possibly release more H₂S. Furthermore, the *in vivo* therapeutic effectiveness of these polymeric micelle formulations needs to be investigated to confirm their stability and specificity towards cancer cells.

6.2 Design of biofunctional and photodegradable hydrogels for isolation of microbes from membrane surfaces during early-stage biofouling

The last portion of this thesis investigates the development of the polymer surface dissection (PSD) method which uses biofunctionalized, photodegradable polyethylene glycol

(PEG)-based hydrogels for isolation of microbes from polyvinylidene difluoride (PVDF) wastewater membrane surfaces during early-stage biofouling (**Chapter 5**). Conventional techniques in characterizing the complex, spatial and temporal mechanisms of biofouling processes over membrane surfaces rely heavily on the use of membrane autopsies and laser capture microdissection (LCM), which are both destructive to the underlying live bacterial cells and surface. In addition, standard membrane autopsies only provide bulk analysis, making it difficult to understand the mechanisms that initiate and drive biofouling. Here, the PSD approach demonstrated the ability to isolate targeted flocs with sizes as low as $2,000 \mu\text{m}^2$ by a spatiotemporally controlled UV light from a patterned illumination tool without damaging the flocs or underlying membrane surface. More importantly, the PSD technique allowed for genomic analysis and identification of microbes within isolated flocs without requiring a culture step for enrichment. This result is significant as culturing typically favors highly-culturable isolates, therefore creating a biased sequencing result. Hence, the PSD approach is a promising tool that pairs microscopic information with composition, allowing for identification of early membrane colonizers in a spatiotemporal manner.

6.2.1 Future Work

With the use of municipal wastewater sludge in this study, preliminary results based on sequencing at the phylum level showed an abundance of Bacteroidetes and Proteobacteria at the smaller floc sizes compared to Proteobacteria at the larger floc sizes. This suggests that Bacteroidetes may play a role in the early stages of biofilm formation while Proteobacteria may play a role in the later stages of biofilm formation. While these results are not conclusive, it demonstrates the ability of the PSD method to accurately identify early membrane colonizers in a spatiotemporal manner. Based on this promising result, future work will focus on identifying

communities of microorganisms that initiate membrane biofouling in anaerobic membrane bioreactors (AnMBRs) using the PSD method. Instead of floc areas, other microscopic information such as extracellular polymeric substances (EPS) expression, which has been linked to attachment of early colonizing microbes can be used to identify communities of microorganisms that initiate membrane biofouling.

References

- (1) Hecht, G. Polyvinylpyrrolidon, von W. Reppe. Monographie Nr. 66 Zu „Angewandte Chemie” Und „Chemie-Ingenieur-Technik”. Verlag Chemie, GmbH., Weinheim/Bergstr. 1954, 72 S., Abb., Kart. DM 9.80. *Angew. Chemie* **1954**.
<https://doi.org/10.1002/ange.19540662115>.
- (2) Akelah, A.; Sherrington, D. C. Application of Functionalized Polymers in Organic Synthesis. *Chem. Rev.* **1981**. <https://doi.org/10.1021/cr00046a003>.
- (3) Feynman R. There’s Plenty of Room at the Bottom (Reprint from the Speech given at the Annual Meeting of the West Coast Section of the American Physical Society. *Eng Sci.* 1960.
- (4) Taniguchi, N. On the Basic Concept of “Nano-Technology.” In *the basic concept of “Nano-Technology”, Proceedings of the International Conference on Production Engineering Tokyo, Part II, Japan Society of Precision Engineering, Tokyo*; 1974.
- (5) Wagner, V.; Dullaart, A.; Bock, A. K.; Zweck, A. The Emerging Nanomedicine Landscape. *Nature Biotechnology*. 2006. <https://doi.org/10.1038/nbt1006-1211>.
- (6) Ventola, C. L. Progress in Nanomedicine: Approved and Investigational Nanodrugs. *P T* **2017**.
- (7) Bobo, D.; Robinson, K. J.; Islam, J.; Thurecht, K. J.; Corrie, S. R. Nanoparticle-Based Medicines: A Review of FDA-Approved Materials and Clinical Trials to Date. *Pharmaceutical Research*. 2016. <https://doi.org/10.1007/s11095-016-1958-5>.
- (8) Anselmo, A. C.; Mitragotri, S. Nanoparticles in the Clinic: An Update. *Bioeng. Transl. Med.* **2019**. <https://doi.org/10.1002/btm2.10143>.
- (9) Patra, J. K.; Das, G.; Fraceto, L. F.; Campos, E. V. R.; Rodriguez-Torres, M. del P.; Acosta-Torres, L. S.; Diaz-Torres, L. A.; Grillo, R.; Swamy, M. K.; Sharma, S.; et al. Nano Based Drug Delivery Systems: Recent Developments and Future Prospects. *J. Nanobiotechnology* **2018**. <https://doi.org/10.1186/s12951-018-0392-8>.
- (10) Park, J. H.; Lee, S.; Kim, J.-H.; Park, K.; Kim, K.; Kwon, I. C. Polymeric Nanomedicine for Cancer Therapy. *Prog. Polym. Sci.* **2008**, 33 (1), 113–137.
<https://doi.org/https://doi.org/10.1016/j.progpolymsci.2007.09.003>.
- (11) Jones, M. C.; Leroux, J. C. Polymeric Micelles - A New Generation of Colloidal Drug Carriers. *Eur. J. Pharm. Biopharm.* **1999**. [https://doi.org/10.1016/S0939-6411\(99\)00039-9](https://doi.org/10.1016/S0939-6411(99)00039-9).
- (12) Kwon, G. S.; Okano, T. Polymeric Micelles as New Drug Carriers. *Advanced Drug Delivery Reviews*. 1996. [https://doi.org/10.1016/S0169-409X\(96\)00401-2](https://doi.org/10.1016/S0169-409X(96)00401-2).
- (13) Kedar, U.; Phutane, P.; Shidhaye, S.; Kadam, V. Advances in Polymeric Micelles for Drug Delivery and Tumor Targeting. *Nanomedicine* **2010**, 6 (6), 714–730.
<https://doi.org/10.1016/j.nano.2010.05.005> [doi].
- (14) Croy, S.; Kwon, G. Polymeric Micelles for Drug Delivery. *Curr. Pharm. Des.* **2006**.
<https://doi.org/10.2174/138161206779026245>.
- (15) Matsumura, Y.; Maeda, H. A New Concept for Macromolecular Therapeutics in Cancer Chemotherapy: Mechanism of Tumor-tropic Accumulation of Proteins and the Antitumor Agent Smancs. *Cancer Res.* **1986**, 46 (12 Part 1), 6387 LP – 6392.
- (16) Fang, J.; Nakamura, H.; Maeda, H. The EPR Effect: Unique Features of Tumor Blood Vessels for Drug Delivery, Factors Involved, and Limitations and Augmentation of the Effect. *Adv. Drug Deliv. Rev.* **2011**, 63 (3), 136–151.

- <https://doi.org/https://doi.org/10.1016/j.addr.2010.04.009>.
- (17) Adams, M. L.; Lavasanifar, A.; Kwon, G. S. Amphiphilic Block Copolymers for Drug Delivery. *Journal of Pharmaceutical Sciences*. 2003. <https://doi.org/10.1002/jps.10397>.
 - (18) Oerlemans, C.; Bult, W.; Bos, M.; Storm, G.; Nijssen, J. F. W.; Hennink, W. E. Polymeric Micelles in Anticancer Therapy: Targeting, Imaging and Triggered Release. *Pharmaceutical Research*. 2010. <https://doi.org/10.1007/s11095-010-0233-4>.
 - (19) Kim, D. W.; Kim, S. Y.; Kim, H. K.; Kim, S. W.; Shin, S. W.; Kim, J. S.; Park, K.; Lee, M. Y.; Heo, D. S. Multicenter Phase II Trial of Genexol-PM, a Novel Cremophor-Free, Polymeric Micelle Formulation of Paclitaxel, with Cisplatin in Patients with Advanced Non-Small-Cell Lung Cancer. *Ann. Oncol.* **2007**. <https://doi.org/10.1093/annonc/mdm374>.
 - (20) Kim, T. Y.; Kim, D. W.; Chung, J. Y.; Shin, S. G.; Kim, S. C.; Heo, D. S.; Kim, N. K.; Bang, Y. J. Phase I and Pharmacokinetic Study of Genexol-PM, a Cremophor-Free, Polymeric Micelle-Formulated Paclitaxel, in Patients with Advanced Malignancies. *Clin. Cancer Res.* **2004**. <https://doi.org/10.1158/1078-0432.CCR-03-0655>.
 - (21) Lee, K. S.; Chung, H. C.; Im, S. A.; Park, Y. H.; Kim, C. S.; Kim, S. B.; Rha, S. Y.; Lee, M. Y.; Ro, J. Multicenter Phase II Trial of Genexol-PM, a Cremophor-Free, Polymeric Micelle Formulation of Paclitaxel, in Patients with Metastatic Breast Cancer. *Breast Cancer Res. Treat.* **2008**. <https://doi.org/10.1007/s10549-007-9591-y>.
 - (22) Varela-Moreira, A.; Shi, Y.; Fens, M. H. A. M.; Lammers, T.; Hennink, W. E.; Schiffelers, R. M. Clinical Application of Polymeric Micelles for the Treatment of Cancer. *Mater. Chem. Front.* **2017**, *1* (8), 1485–1501. <https://doi.org/10.1039/C6QM00289G>.
 - (23) Cabral, H.; Kataoka, K. Progress of Drug-Loaded Polymeric Micelles into Clinical Studies. *Journal of Controlled Release*. 2014. <https://doi.org/10.1016/j.jconrel.2014.06.042>.
 - (24) Nakanishi, T.; Fukushima, S.; Okamoto, K.; Suzuki, M.; Matsumura, Y.; Yokoyama, M.; Okano, T.; Sakurai, Y.; Kataoka, K. Development of the Polymer Micelle Carrier System for Doxorubicin. In *Journal of Controlled Release*; 2001. [https://doi.org/10.1016/S0168-3659\(01\)00341-8](https://doi.org/10.1016/S0168-3659(01)00341-8).
 - (25) Harada, M.; Bobe, I.; Saito, H.; Shibata, N.; Tanaka, R.; Hayashi, T.; Kato, Y. Improved Anti-Tumor Activity of Stabilized Anthracycline Polymeric Micelle Formulation, NC-6300. *Cancer Sci.* **2011**. <https://doi.org/10.1111/j.1349-7006.2010.01745.x>.
 - (26) Abe, K.; Kimura, H. The Possible Role of Hydrogen Sulfide as an Endogenous Neuromodulator. *J. Neurosci.* **1996**, *16* (3), 1066–1072.
 - (27) Stipanuk, M. H.; Beck, P. W. Characterization of the Enzymic Capacity for Cysteine Desulphhydration in Liver and Kidney of the Rat. *Biochem. J.* **1982**, *206* (2), 267–278.
 - (28) Pan, L. L.; Liu, X. H.; Gong, Q. H.; Yang, H. B.; Zhu, Y. Z. Role of Cystathionine γ -Lyase/Hydrogen Sulfide Pathway in Cardiovascular Disease: A Novel Therapeutic Strategy? *Antioxidants and Redox Signaling*. 2012. <https://doi.org/10.1089/ars.2011.4349>.
 - (29) Miles, E. W.; Kraus, J. P. Cystathionine Beta-Synthase: Structure, Function, Regulation, and Location of Homocystinuria-Causing Mutations. *J. Biol. Chem.* **2004**, *279* (29), 29871–29875. <https://doi.org/10.1074/jbc.R400005200>.
 - (30) Nagai, Y.; Tsugane, M.; Oka, J.; Kimura, H. Hydrogen Sulfide Induces Calcium Waves in Astrocytes. *FASEB J.* **2004**, *18* (3), 557–560. <https://doi.org/10.1096/fj.03-1052fje> [doi].
 - (31) Jackson-Weaver, O.; Osmond, J. M.; Riddle, M. A.; Naik, J. S.; Gonzalez Bosc, L. V.; Walker, B. R.; Kanagy, N. L. Hydrogen Sulfide Dilates Rat Mesenteric Arteries by Activating Endothelial Large-Conductance Ca(2)(+)-Activated K(+) Channels and

- Smooth Muscle Ca²⁺(+) Sparks. *Am. J. Physiol. Circ. Physiol.* **2013**, *304* (11), 1446–1455. <https://doi.org/10.1152/ajpheart.00506.2012> [doi].
- (32) Sen, N.; Paul, B. D.; Gadalla, M. M.; Mustafa, A. K.; Sen, T.; Xu, R.; Kim, S.; Snyder, S. H. Hydrogen Sulfide-Linked Sulfhydration of NF- κ B Mediates Its Antiapoptotic Actions. *Mol. Cell* **2012**, *45* (1), 13–24. <https://doi.org/10.1016/j.molcel.2011.10.021>.
- (33) Zhou, Y.; Li, X. H.; Zhang, C. C.; Wang, M. J.; Xue, W. L.; Wu, D. D.; Ma, F. F.; Li, W. W.; Tao, B. B.; Zhu, Y. C. Hydrogen Sulfide Promotes Angiogenesis by Downregulating MiR-640 via the VEGFR2/MTOR Pathway. *Am. J. Physiol. - Cell Physiol.* **2016**, *310* (4), C305–C317. <https://doi.org/10.1152/ajpcell.00230.2015>.
- (34) Sun, W. H.; Liu, F.; Chen, Y.; Zhu, Y. C. Hydrogen Sulfide Decreases the Levels of ROS by Inhibiting Mitochondrial Complex IV and Increasing SOD Activities in Cardiomyocytes under Ischemia/Reperfusion. *Biochem. Biophys. Res. Commun.* **2012**, *421* (2), 164–170. <https://doi.org/10.1016/j.bbrc.2012.03.121> [doi].
- (35) Zayachkivska, O.; Havryluk, O.; Hrycevych, N.; Bula, N.; Grushka, O.; Wallace, J. L. Cytoprotective Effects of Hydrogen Sulfide in Novel Rat Models of Non-Erosive Esophagitis. *PLoS One* **2014**, *9* (10). <https://doi.org/10.1371/journal.pone.0110688> [doi].
- (36) Cai, F.; Xu, H.; Cao, N.; Zhang, X.; Liu, J.; Lu, Y.; Chen, J.; Yang, Y.; Cheng, J.; Hua, Z. C.; et al. ADT-OH, a Hydrogen Sulfide-Releasing Donor, Induces Apoptosis and Inhibits the Development of Melanoma in Vivo by Upregulating FADD. *Cell Death Dis.* **2020**, *11* (1). <https://doi.org/10.1038/s41419-020-2222-9>.
- (37) Sun, X.; Wang, W.; Dai, J.; Jin, S.; Huang, J.; Guo, C.; Wang, C.; Pang, L.; Wang, Y. A Long-Term and Slow-Releasing Hydrogen Sulfide Donor Protects against Myocardial Ischemia/Reperfusion Injury. *Sci. Rep.* **2017**, *7* (1). <https://doi.org/10.1038/s41598-017-03941-0> [doi].
- (38) Li, L.; Whiteman, M.; Guan, Y. Y.; Neo, K. L.; Cheng, Y.; Lee, S. W.; Zhao, Y.; Baskar, R.; Tan, C. H.; Moore, P. K. Characterization of a Novel, Water-Soluble Hydrogen Sulfide-Releasing Molecule (GYY4137): New Insights into the Biology of Hydrogen Sulfide. *Circulation* **2008**, *117* (18), 2351–2361. <https://doi.org/10.1161/CIRCULATIONAHA.107.753467> [doi].
- (39) Caliendo, G.; Cirino, G.; Santagada, V.; Wallace, J. L. Synthesis and Biological Effects of Hydrogen Sulfide (H₂S): Development of H₂S-Releasing Drugs as Pharmaceuticals. *J. Med. Chem.* **2010**, *53* (17), 6275–6287. <https://doi.org/10.1021/jm901638j>.
- (40) Zhao, F. L.; Fang, F.; Qiao, P. F.; Yan, N.; Gao, D.; Yan, Y. AP39, a Mitochondria-Targeted Hydrogen Sulfide Donor, Supports Cellular Bioenergetics and Protects against Alzheimer’s Disease by Preserving Mitochondrial Function in APP/PS1 Mice and Neurons. *Oxid. Med. Cell. Longev.* **2016**, *2016*, 8360738. <https://doi.org/10.1155/2016/8360738> [doi].
- (41) Predmore, B. L.; Kondo, K.; Bhushan, S.; Zlatopolsky, M. A.; King, A. L.; Aragon, J. P.; Grinsfelder, D. B.; Condit, M. E.; Lefer, D. J. The Polysulfide Diallyl Trisulfide Protects the Ischemic Myocardium by Preservation of Endogenous Hydrogen Sulfide and Increasing Nitric Oxide Bioavailability. *Am. J. Physiol. Circ. Physiol.* **2012**, *302* (11), 2410–2419. <https://doi.org/10.1152/ajpheart.00044.2012> [doi].
- (42) Benavides, G. A.; Squadrito, G. L.; Mills, R. W.; Patel, H. D.; Isbell, T. S.; Patel, R. P.; Darley-Usmar, V. M.; Doeller, J. E.; Kraus, D. W. Hydrogen Sulfide Mediates the Vasoactivity of Garlic. *Proc. Natl. Acad. Sci. U. S. A.* **2007**, *104* (46), 17977–17983. <https://doi.org/0705710104> [pii].

- (43) Martelli, A.; Testai, L.; Citi, V.; Marino, A.; Pugliesi, I.; Barresi, E.; Nesi, G.; Rapposelli, S.; Taliani, S.; Da Settimo, F.; et al. Arylthioamides as H₂S Donors: L-Cysteine-Activated Releasing Properties and Vascular Effects in Vitro and in Vivo. *ACS Med. Chem. Lett.* **2013**, *4* (10), 904–909. <https://doi.org/10.1021/ml400239a> [doi].
- (44) Foster, J. C.; Powell, C. R.; Radzinski, S. C.; Matson, J. B. S-Aroylthiooximes: A Facile Route to Hydrogen Sulfide Releasing Compounds with Structure-Dependent Release Kinetics. *Org. Lett.* **2014**, *16* (6), 1558–1562. <https://doi.org/10.1021/ol500385a>.
- (45) Powell, C. R.; Foster, J. C.; Okyere, B.; Theus, M. H.; Matson, J. B. Therapeutic Delivery of H₂S via COS: Small Molecule and Polymeric Donors with Benign Byproducts. *J. Am. Chem. Soc.* **2016**, *138* (41), 13477–13481. <https://doi.org/10.1021/jacs.6b07204>.
- (46) Chauhan, P.; Bora, P.; Ravikumar, G.; Jos, S.; Chakrapani, H. Esterase Activated Carbonyl Sulfide/Hydrogen Sulfide (H₂S) Donors. *Org. Lett.* **2017**, *19* (1), 62–65. <https://doi.org/10.1021/acs.orglett.6b03336>.
- (47) Sharma, A. K.; Nair, M.; Chauhan, P.; Gupta, K.; Saini, D. K.; Chakrapani, H. Visible-Light-Triggered Uncaging of Carbonyl Sulfide for Hydrogen Sulfide (H₂S) Release. *Org. Lett.* **2017**, *19* (18), 4822–4826. <https://doi.org/10.1021/acs.orglett.7b02259> [doi].
- (48) Kang, J.; Li, Z.; Organ, C. L.; Park, C. M.; Yang, C. T.; Pacheco, A.; Wang, D.; Lefer, D. J.; Xian, M. PH-Controlled Hydrogen Sulfide Release for Myocardial Ischemia-Reperfusion Injury. *J. Am. Chem. Soc.* **2016**, *138* (20), 6336–6340. <https://doi.org/10.1021/jacs.6b01373> [doi].
- (49) Zhang, N.; Hu, P.; Wang, Y.; Tang, Q.; Zheng, Q.; Wang, Z.; He, Y. A Reactive Oxygen Species (ROS) Activated Hydrogen Sulfide (H₂S) Donor with Self-Reporting Fluorescence. *ACS Sensors* **2020**, *5* (2), 319–326. <https://doi.org/10.1021/acssensors.9b01093>.
- (50) Zhao, Y.; Pluth, M. D. Hydrogen Sulfide Donors Activated by Reactive Oxygen Species. *Angew. Chemie (International ed. in English)* **2016**, *55* (47), 14638–14643. <https://doi.org/10.1002/anie.201608052> [doi].
- (51) Hasegawa, U.; van, der V. Polymeric Micelles for Hydrogen Sulfide Delivery. *Medchemcomm* **2015**, *6* (2), 273–277. <https://doi.org/10.1039/C4MD00373J>.
- (52) Foster, J. C.; Radzinski, S. C.; Zou, X.; Finkielstein, C. V.; Matson, J. B. H₂S-Releasing Polymer Micelles for Studying Selective Cell Toxicity. *Mol. Pharm.* **2017**, *14* (4), 1300–1307. <https://doi.org/10.1021/acs.molpharmaceut.6b01117>.
- (53) Blanco, E.; Shen, H.; Ferrari, M. Principles of Nanoparticle Design for Overcoming Biological Barriers to Drug Delivery. *Nature Biotechnology*. 2015. <https://doi.org/10.1038/nbt.3330>.
- (54) Pino, P. Del; Pelaz, B.; Zhang, Q.; Maffre, P.; Nienhaus, G. U.; Parak, W. J. Protein Corona Formation around Nanoparticles - From the Past to the Future. *Materials Horizons*. 2014. <https://doi.org/10.1039/c3mh00106g>.
- (55) Salvati, A.; Pitek, A. S.; Monopoli, M. P.; Prapainop, K.; Bombelli, F. B.; Hristov, D. R.; Kelly, P. M.; Åberg, C.; Mahon, E.; Dawson, K. A. Transferrin-Functionalized Nanoparticles Lose Their Targeting Capabilities When a Biomolecule Corona Adsorbs on the Surface. *Nat. Nanotechnol.* **2013**. <https://doi.org/10.1038/nnano.2012.237>.
- (56) Gao, Y.; Chen, L.; Gu, W.; Xi, Y.; Lin, L.; Li, Y. Targeted Nanoassembly Loaded with Docetaxel Improves Intracellular Drug Delivery and Efficacy in Murine Breast Cancer Model. *Mol. Pharm.* **2008**. <https://doi.org/10.1021/mp800072e>.
- (57) Kwon, G. S.; Kataoka, K. Block Copolymer Micelles as Long-Circulating Drug Vehicles.

- Advanced Drug Delivery Reviews*. 1995. [https://doi.org/10.1016/0169-409X\(95\)00031-2](https://doi.org/10.1016/0169-409X(95)00031-2).
- (58) Allen, C.; Maysinger, D.; Eisenberg, A. Nano-Engineering Block Copolymer Aggregates for Drug Delivery. *Colloids Surfaces B Biointerfaces* **1999**. [https://doi.org/10.1016/S0927-7765\(99\)00058-2](https://doi.org/10.1016/S0927-7765(99)00058-2).
- (59) Lee, H.; Fonge, H.; Hoang, B.; Reilly, R. M.; Allen, C. The Effects of Particle Size and Molecular Targeting on the Intratumoral and Subcellular Distribution of Polymeric Nanoparticles. *Mol. Pharm.* **2010**. <https://doi.org/10.1021/mp100038h>.
- (60) Fukumura, D.; Jain, R. K. Tumor Microenvironment Abnormalities: Causes, Consequences, and Strategies to Normalize. *Journal of Cellular Biochemistry*. 2007. <https://doi.org/10.1002/jcb.21187>.
- (61) Wang, Y.; Yang, T.; Wang, X.; Dai, W.; Wang, J.; Zhang, X.; Li, Z.; Zhang, Q. Materializing Sequential Killing of Tumor Vasculature and Tumor Cells via Targeted Polymeric Micelle System. *J. Control. Release* **2011**. <https://doi.org/10.1016/j.jconrel.2010.10.027>.
- (62) Gonzalez, H.; Hagerling, C.; Werb, Z. Roles of the Immune System in Cancer: From Tumor Initiation to Metastatic Progression. *Genes and Development*. 2018. <https://doi.org/10.1101/GAD.314617.118>.
- (63) Nishikawa, H.; Sakaguchi, S. Regulatory T Cells in Tumor Immunity. *International Journal of Cancer*. 2010. <https://doi.org/10.1002/ijc.25429>.
- (64) Umansky, V.; Sevko, A. Tumor Microenvironment and Myeloid-Derived Suppressor Cells. *Cancer Microenviron.* **2013**. <https://doi.org/10.1007/s12307-012-0126-7>.
- (65) Eyileten, C.; Majchrzak, K.; Pilch, Z.; Tonecka, K.; Mucha, J.; Taciak, B.; Ulewicz, K.; Witt, K.; Boffi, A.; Krol, M.; et al. Immune Cells in Cancer Therapy and Drug Delivery. *Mediators of Inflammation*. 2016. <https://doi.org/10.1155/2016/5230219>.
- (66) Riabov, V.; Gudima, A.; Wang, N.; Mickley, A.; Orekhov, A.; Kzhyshkowska, J. Role of Tumor Associated Macrophages in Tumor Angiogenesis and Lymphangiogenesis. *Frontiers in Physiology*. 2014. <https://doi.org/10.3389/fphys.2014.00075>.
- (67) Wei, X.; Liu, L.; Li, X.; Wang, Y.; Guo, X.; Zhao, J.; Zhou, S. Selectively Targeting Tumor-Associated Macrophages and Tumor Cells with Polymeric Micelles for Enhanced Cancer Chemo-Immunotherapy. *J. Control. Release* **2019**. <https://doi.org/10.1016/j.jconrel.2019.09.021>.
- (68) Brown, J. M.; Giaccia, A. J. The Unique Physiology of Solid Tumors: Opportunities (and Problems) for Cancer Therapy. *Cancer Res.* **1998**.
- (69) Brown, J. M.; Wilson, W. R. Exploiting Tumour Hypoxia in Cancer Treatment. *Nature Reviews Cancer*. 2004. <https://doi.org/10.1038/nrc1367>.
- (70) Harris, A. L. Hypoxia - A Key Regulatory Factor in Tumour Growth. *Nature Reviews Cancer*. 2002. <https://doi.org/10.1038/nrc704>.
- (71) Dewhirst, M. W.; Cao, Y.; Moeller, B. Cycling Hypoxia and Free Radicals Regulate Angiogenesis and Radiotherapy Response. *Nature Reviews Cancer*. 2008. <https://doi.org/10.1038/nrc2397>.
- (72) Casazza, A.; Di Conza, G.; Wenes, M.; Finisguerra, V.; Deschoemaeker, S.; Mazzone, M. Tumor Stroma: A Complexity Dictated by the Hypoxic Tumor Microenvironment. *Oncogene*. 2014. <https://doi.org/10.1038/onc.2013.121>.
- (73) Muz, B.; de la Puente, P.; Azab, F.; Azab, A. K. The Role of Hypoxia in Cancer Progression, Angiogenesis, Metastasis, and Resistance to Therapy. *Hypoxia* **2015**. <https://doi.org/10.2147/hp.s93413>.

- (74) Cairns, R.; Papandreou, I.; Denko, N. Overcoming Physiologic Barriers to Cancer Treatment by Molecularly Targeting the Tumor Microenvironment. *Molecular Cancer Research*. 2006. <https://doi.org/10.1158/1541-7786.MCR-06-0002>.
- (75) Estrella, V.; Chen, T.; Lloyd, M.; Wojtkowiak, J.; Cornnell, H. H.; Ibrahim-Hashim, A.; Bailey, K.; Balagurunathan, Y.; Rothberg, J. M.; Sloane, B. F.; et al. Acidity Generated by the Tumor Microenvironment Drives Local Invasion. *Cancer Res*. **2013**. <https://doi.org/10.1158/0008-5472.CAN-12-2796>.
- (76) Heiden, M. G. V.; Cantley, L. C.; Thompson, C. B. Understanding the Warburg Effect: The Metabolic Requirements of Cell Proliferation. *Science*. 2009. <https://doi.org/10.1126/science.1160809>.
- (77) Wolfe, N. D.; Dunavan, C. P.; Diamond, J. Origins of Major Human Infectious Diseases. *Nature*. 2007. <https://doi.org/10.1038/nature05775>.
- (78) Hill-Cawthorne, G.; Sorrell, T. Future Directions for Public Health Research in Emerging Infectious Diseases. *Public Heal. Res. Pract.*
- (79) Jones, K. E.; Patel, N. G.; Levy, M. A.; Storeygard, A.; Balk, D.; Gittleman, J. L.; Daszak, P. Global Trends in Emerging Infectious Diseases. *Nature* **2008**. <https://doi.org/10.1038/nature06536>.
- (80) Rao, T. S.; Kora, A. J.; Chandramohan, P.; Panigrahi, B. S.; Narasimhan, S. V. Biofouling and Microbial Corrosion Problem in the Thermo-Fluid Heat Exchanger and Cooling Water System of a Nuclear Test Reactor. *Biofouling* **2009**. <https://doi.org/10.1080/08927010903016543>.
- (81) Brooks, J. D.; Flint, S. H. Biofilms in the Food Industry: Problems and Potential Solutions. *Int. J. Food Sci. Technol.* **2008**, *43* (12), 2163–2176. <https://doi.org/https://doi.org/10.1111/j.1365-2621.2008.01839.x>.
- (82) Khatoun, Z.; McTiernan, C. D.; Suuronen, E. J.; Mah, T.-F.; Alarcon, E. I. Bacterial Biofilm Formation on Implantable Devices and Approaches to Its Treatment and Prevention. *Heliyon* **2018**, *4* (12), e01067. <https://doi.org/https://doi.org/10.1016/j.heliyon.2018.e01067>.
- (83) Rao, T. S. Chapter 6 - Biofouling in Industrial Water Systems; Amjad, Z., Demadis, K. D. B. T.-M. S. and D., Eds.; Elsevier: Amsterdam, 2015; pp 123–140. <https://doi.org/https://doi.org/10.1016/B978-0-444-63228-9.00006-1>.
- (84) Brown, J. M.; Mistry, J. B.; Cherian, J. J.; Elmallah, R. K.; Chughtai, M.; Harwin, S. F.; Mont, M. A. Femoral Component Revision of Total Hip Arthroplasty. *Orthopedics* **2016**, *39* (6), e1129–e1139. <https://doi.org/10.3928/01477447-20160819-06>.
- (85) Okike, K.; Bhattacharyya, T. Trends in the Management of Open Fractures. A Critical Analysis. *J. Bone Joint Surg. Am.* **2006**, *88* (12), 2739–2748. <https://doi.org/10.2106/JBJS.F.00146>.
- (86) Nathan, C.; Cars, O. Antibiotic Resistance — Problems, Progress, and Prospects. *N. Engl. J. Med.* **2014**. <https://doi.org/10.1056/nejmp1408040>.
- (87) Martens, E.; Demain, A. L. The Antibiotic Resistance Crisis, with a Focus on the United States. *Journal of Antibiotics*. 2017. <https://doi.org/10.1038/ja.2017.30>.
- (88) Høiby, N.; Bjarnsholt, T.; Givskov, M.; Molin, S.; Ciofu, O. Antibiotic Resistance of Bacterial Biofilms. *International Journal of Antimicrobial Agents*. 2010. <https://doi.org/10.1016/j.ijantimicag.2009.12.011>.
- (89) Fux, C. A.; Stoodley, P.; Hall-Stoodley, L.; Costerton, J. W. Bacterial Biofilms: A Diagnostic and Therapeutic Challenge. *Expert Review of Anti-Infective Therapy*. 2003.

- <https://doi.org/10.1586/14787210.1.4.667>.
- (90) Lagier, J. C.; Edouard, S.; Pagnier, I.; Mediannikov, O.; Drancourt, M.; Raoult, D. Current and Past Strategies for Bacterial Culture in Clinical Microbiology. *Clin. Microbiol. Rev.* **2015**. <https://doi.org/10.1128/CMR.00110-14>.
- (91) Váradi, L.; Luo, J. L.; Hibbs, D. E.; Perry, J. D.; Anderson, R. J.; Orenga, S.; Groundwater, P. W. Methods for the Detection and Identification of Pathogenic Bacteria: Past, Present, and Future. *Chemical Society Reviews*. 2017. <https://doi.org/10.1039/c6cs00693k>.
- (92) Al-Awadhi, H.; Dashti, N.; Khanafer, M.; Al-Mailem, D.; Ali, N.; Radwan, S. Bias Problems in Culture-Independent Analysis of Environmental Bacterial Communities: A Representative Study on Hydrocarbonoclastic Bacteria. *Springerplus* **2013**. <https://doi.org/10.1186/2193-1801-2-369>.
- (93) Belgrader, P.; Bennett, W.; Hadley, D.; Richards, J.; Stratton, P.; Mariella, R.; Milanovich, F. PCR Detection of Bacteria in Seven Minutes. *Science*. 1999. <https://doi.org/10.1126/science.284.5413.449>.
- (94) Järvinen, A. K.; Laakso, S.; Piiparinen, P.; Aittakorpi, A.; Lindfors, M.; Huopaniemi, L.; Piiparinen, H.; Mäki, M. Rapid Identification of Bacterial Pathogens Using a PCR- and Microarray-Based Assay. *BMC Microbiol.* **2009**. <https://doi.org/10.1186/1471-2180-9-161>.
- (95) Law, J. W. F.; Mutalib, N. S. A.; Chan, K. G.; Lee, L. H. Rapid Methods for the Detection of Foodborne Bacterial Pathogens: Principles, Applications, Advantages and Limitations. *Front. Microbiol.* **2014**. <https://doi.org/10.3389/fmicb.2014.00770>.
- (96) Li, D.; Fang, Y.; Zhang, X. Bacterial Detection and Elimination Using a Dual-Functional Porphyrin-Based Porous Organic Polymer with Peroxidase-Like and High Near-Infrared-Light-Enhanced Antibacterial Activity. *ACS Appl. Mater. Interfaces* **2020**. <https://doi.org/10.1021/acsami.9b20102>.
- (97) Li, M.; Liu, X.; Tan, L.; Cui, Z.; Yang, X.; Li, Z.; Zheng, Y.; Yeung, K. W. K.; Chu, P. K.; Wu, S. Noninvasive Rapid Bacteria-Killing and Acceleration of Wound Healing through Photothermal/Photodynamic/Copper Ion Synergistic Action of a Hybrid Hydrogel. *Biomater. Sci.* **2018**. <https://doi.org/10.1039/c8bm00499d>.
- (98) Fattahi, N.; Nieves-Otero, P. A.; Masigol, M.; Van Der Vlies, A. J.; Jensen, R. S.; Hansen, R. R.; Platt, T. G. Photodegradable Hydrogels for Rapid Screening, Isolation, and Genetic Characterization of Bacteria with Rare Phenotypes. *Biomacromolecules* **2020**. <https://doi.org/10.1021/acs.biomac.0c00543>.
- (99) Spychalska, K.; Zajac, D.; Baluta, S.; Halicka, K.; Cabaj, J. Functional Polymers Structures for (Bio)Sensing Application-a Review. *Polymers*. 2020. <https://doi.org/10.3390/POLYM12051154>.
- (100) Woller, E. K.; Walter, E. D.; Morgan, J. R.; Singel, D. J.; Cloninger, M. J. Altering the Strength of Lectin Binding Interactions and Controlling the Amount of Lectin Clustering Using Mannose/Hydroxyl-Functionalized Dendrimers. *J. Am. Chem. Soc.* **2003**. <https://doi.org/10.1021/ja0352496>.
- (101) Pan, Y.; Bai, H.; Ma, C.; Deng, Y.; Qin, W.; Qian, X. Brush Polymer Modified and Lectin Immobilized Core-Shell Microparticle for Highly Efficient Glycoprotein/Glycopeptide Enrichment. *Talanta* **2013**. <https://doi.org/10.1016/j.talanta.2013.06.031>.
- (102) Liener, Irvin E., Nathan Sharon, I. J. G. *The Lectins - Properties, Functions, and Applications in Biology and Medicine*; 1979.

- (103) Bundle, D. R.; Young, N. M. Carbohydrate-Protein Interactions in Antibodies and Lectins. *Curr. Opin. Struct. Biol.* **1992**. [https://doi.org/10.1016/0959-440X\(92\)90199-H](https://doi.org/10.1016/0959-440X(92)90199-H).
- (104) Wang, Y.; Ye, Z.; Ying, Y. New Trends in Impedimetric Biosensors for the Detection of Foodborne Pathogenic Bacteria. *Sensors*. 2012. <https://doi.org/10.3390/s120303449>.
- (105) Zeng, X.; Andrade, C. A. S.; Oliveira, M. D. L.; Sun, X. L. Carbohydrate-Protein Interactions and Their Biosensing Applications. *Analytical and Bioanalytical Chemistry*. 2012. <https://doi.org/10.1007/s00216-011-5594-y>.
- (106) Seiler, B. T.; Cartwright, M.; Dinis, A. L. M.; Duffy, S.; Lombardo, P.; Cartwright, D.; Super, E. H.; Lanzaro, J.; Dugas, K.; Super, M.; et al. Broad-Spectrum Capture of Clinical Pathogens Using Engineered Fc-Mannose-Binding Lectin Enhanced by Antibiotic Treatment [Version 1; Peer Review: 2 Approved]. *F1000Research* **2019**. <https://doi.org/10.12688/f1000research.17447.1>.
- (107) Bundy, J. L.; Fenselau, C. Lectin and Carbohydrate Affinity Capture Surfaces for Mass Spectrometric Analysis of Microorganisms. *Anal. Chem.* **2001**. <https://doi.org/10.1021/ac0011639>.
- (108) Safina, G. Application of Surface Plasmon Resonance for the Detection of Carbohydrates, Glycoconjugates, and Measurement of the Carbohydrate-Specific Interactions: A Comparison with Conventional Analytical Techniques. A Critical Review. *Analytica Chimica Acta*. 2012. <https://doi.org/10.1016/j.aca.2011.11.016>.
- (109) Drury, J. L.; Mooney, D. J. Hydrogels for Tissue Engineering: Scaffold Design Variables and Applications. *Biomaterials*. 2003. [https://doi.org/10.1016/S0142-9612\(03\)00340-5](https://doi.org/10.1016/S0142-9612(03)00340-5).
- (110) Sadat Ebrahimi, M. M.; Dohm, N.; Müller, M.; Jansen, B.; Schönherr, H. Self-Reporting Hydrogels Rapidly Differentiate among Enterohemorrhagic Escherichia Coli (EHEC) and Non-Virulent Escherichia Coli (K12). *Eur. Polym. J.* **2016**. <https://doi.org/10.1016/j.eurpolymj.2016.06.010>.
- (111) Bodenberger, N.; Kubiczek, D.; Halbgebauer, D.; Rimola, V.; Wiese, S.; Mayer, D.; Rodriguez Alfonso, A. A.; Ständker, L.; Stenger, S.; Rosenau, F. Lectin-Functionalized Composite Hydrogels for “Capture-and-Killing” of Carbapenem-Resistant Pseudomonas Aeruginosa. *Biomacromolecules* **2018**. <https://doi.org/10.1021/acs.biomac.8b00089>.
- (112) Zhang, Y.; Zhang, J.; Chen, M.; Gong, H.; Thamphiwatana, S.; Eckmann, L.; Gao, W.; Zhang, L. A Bioadhesive Nanoparticle-Hydrogel Hybrid System for Localized Antimicrobial Drug Delivery. *ACS Appl. Mater. Interfaces* **2016**. <https://doi.org/10.1021/acsami.6b04858>.
- (113) Hoare, T. R.; Kohane, D. S. Hydrogels in Drug Delivery: Progress and Challenges. *Polymer*. 2008. <https://doi.org/10.1016/j.polymer.2008.01.027>.
- (114) Zhu, J.; Marchant, R. E. Design Properties of Hydrogel Tissue-Engineering Scaffolds. *Expert Review of Medical Devices*. 2011. <https://doi.org/10.1586/erd.11.27>.
- (115) Nicodemus, G. D.; Bryant, S. J. Cell Encapsulation in Biodegradable Hydrogels for Tissue Engineering Applications. *Tissue Engineering - Part B: Reviews*. 2008. <https://doi.org/10.1089/ten.teb.2007.0332>.
- (116) Wang, H.; Zhou, S.; Guo, L.; Wang, Y.; Feng, L. Intelligent Hybrid Hydrogels for Rapid in Situ Detection and Photothermal Therapy of Bacterial Infection. *ACS Appl. Mater. Interfaces* **2020**. <https://doi.org/10.1021/acsami.0c12355>.
- (117) Raman, R.; Hua, T.; Gwynne, D.; Collins, J.; Tamang, S.; Zhou, J.; Esfandiary, T.; Soares, V.; Pajovic, S.; Hayward, A.; et al. Light-Degradable Hydrogels as Dynamic Triggers for Gastrointestinal Applications. *Sci. Adv.* **2020**. <https://doi.org/10.1126/sciadv.aay0065>.

- (118) Bertrand, O.; Gohy, J. F. Photo-Responsive Polymers: Synthesis and Applications. *Polymer Chemistry*. 2017. <https://doi.org/10.1039/c6py01082b>.
- (119) Flemming, H.-C.; Schaule, G.; Griebe, T.; Schmitt, J.; Tamachkiarowa, A. Biofouling—the Achilles Heel of Membrane Processes. *Desalination* **1997**, *113* (2), 215–225. [https://doi.org/https://doi.org/10.1016/S0011-9164\(97\)00132-X](https://doi.org/https://doi.org/10.1016/S0011-9164(97)00132-X).
- (120) Krzeminski, P.; Leverette, L.; Malamis, S.; Katsou, E. Membrane Bioreactors – A Review on Recent Developments in Energy Reduction, Fouling Control, Novel Configurations, LCA and Market Prospects. *J. Memb. Sci.* **2017**, *527*, 207–227. <https://doi.org/https://doi.org/10.1016/j.memsci.2016.12.010>.
- (121) Asatekin, A.; Menniti, A.; Kang, S.; Elimelech, M.; Morgenroth, E.; Mayes, A. Antifouling Nanofiltration Membranes for Membrane Bioreactors from Self-Assembling Graft Copolymers. *J. Memb. Sci.* **2006**, *285*, 81–89. <https://doi.org/10.1016/j.memsci.2006.07.042>.
- (122) Zodrow, K.; Brunet, L.; Mahendra, S.; Li, D.; Zhang, A.; Li, Q.; Alvarez, P. J. J. Polysulfone Ultrafiltration Membranes Impregnated with Silver Nanoparticles Show Improved Biofouling Resistance and Virus Removal. *Water Res.* **2009**, *43* (3), 715–723. <https://doi.org/https://doi.org/10.1016/j.watres.2008.11.014>.
- (123) Mauter, M. S.; Wang, Y.; Okemgbo, K. C.; Osuji, C. O.; Giannelis, E. P.; Elimelech, M. Antifouling Ultrafiltration Membranes via Post-Fabrication Grafting of Biocidal Nanomaterials. *ACS Appl. Mater. Interfaces* **2011**, *3* (8), 2861–2868. <https://doi.org/10.1021/am200522v>.
- (124) He, M.; Gao, K.; Zhou, L.; Jiao, Z.; Wu, M.; Cao, J.; You, X.; Cai, Z.; Su, Y.; Jiang, Z. Zwitterionic Materials for Antifouling Membrane Surface Construction. *Acta Biomater.* **2016**, *40*, 142–152. <https://doi.org/https://doi.org/10.1016/j.actbio.2016.03.038>.
- (125) Wang, H.; Christiansen, D. E.; Mehraeen, S.; Cheng, G. Winning the Fight against Biofilms: The First Six-Month Study Showing No Biofilm Formation on Zwitterionic Polyurethanes. *Chem. Sci.* **2020**. <https://doi.org/10.1039/c9sc06155j>.
- (126) Luo, J.; Lv, P.; Zhang, J.; Fane, A. G.; McDougald, D.; Rice, S. A. Succession of Biofilm Communities Responsible for Biofouling of Membrane Bioreactors (MBRs). *PLoS One* **2017**. <https://doi.org/10.1371/journal.pone.0179855>.
- (127) Lim, S. Y.; Kim, S.; Yeon, K. M.; Sang, B. I.; Chun, J.; Lee, C. H. Correlation between Microbial Community Structure and Biofouling in a Laboratory Scale Membrane Bioreactor with Synthetic Wastewater. *Desalination* **2012**. <https://doi.org/10.1016/j.desal.2011.09.030>.
- (128) Meng, F.; Liao, B.; Liang, S.; Yang, F.; Zhang, H.; Song, L. Morphological Visualization, Componential Characterization and Microbiological Identification of Membrane Fouling in Membrane Bioreactors (MBRs). *Journal of Membrane Science*. 2010. <https://doi.org/10.1016/j.memsci.2010.06.006>.
- (129) Cheng, L.; Zhang, S.; MacLennan, G. T.; Williamson, S. R.; Davidson, D. D.; Wang, M.; Jones, T. D.; Lopez-Beltran, A.; Montironi, R. Laser-Assisted Microdissection in Translational Research: Theory, Technical Considerations, and Future Applications. *Applied Immunohistochemistry and Molecular Morphology*. 2013. <https://doi.org/10.1097/PAI.0b013e31824d0519>.
- (130) Nguyen, T.; Roddick, F. A.; Fan, L. Biofouling of Water Treatment Membranes: A Review of the Underlying Causes, Monitoring Techniques and Control Measures. *Membranes*. 2012. <https://doi.org/10.3390/membranes2040804>.

- (131) Liou, G. Y.; Storz, P. *Reactive Oxygen Species in Cancer*; 2010; Vol. 44. <https://doi.org/10.3109/10715761003667554>.
- (132) Pelicano, H.; Carney, D.; Huang, P. ROS Stress in Cancer Cells and Therapeutic Implications. *Drug Resist. Updat.* **2004**, 7 (2), 97–110. <https://doi.org/10.1016/j.drug.2004.01.004>.
- (133) Chen, Q.; Vazquez, E. J.; Moghaddas, S.; Hoppel, C. L.; Lesnefsky, E. J. Production of Reactive Oxygen Species by Mitochondria: Central Role of Complex III. *J. Biol. Chem.* **2003**, 278 (38), 36027–36031. <https://doi.org/10.1074/jbc.M304854200>.
- (134) Halliwell, B.; Clement, M. V.; Long, L. H. Hydrogen Peroxide in the Human Body. *FEBS Lett.* **2000**, 486 (1), 10–13. [https://doi.org/S0014-5793\(00\)02197-9](https://doi.org/S0014-5793(00)02197-9) [pii].
- (135) Valko, M.; Leibfritz, D.; Moncol, J.; Cronin, M. T.; Mazur, M.; Telser, J. Free Radicals and Antioxidants in Normal Physiological Functions and Human Disease. *Int. J. Biochem. Cell Biol.* **2007**, 39 (1), 44–84. [https://doi.org/S1357-2725\(06\)00219-6](https://doi.org/S1357-2725(06)00219-6) [pii].
- (136) Xu, Q.; He, C.; Xiao, C.; Chen, X.; Napoli, A.; Valentini, M.; Tirelli, N.; Müller, M.; Hubbell, J. A.; Sies, H. Hydrogen Peroxide as a Central Redox Signaling Molecule in Physiological Oxidative Stress: Oxidative Eustress. *Nat. Mater.* **2016**, 16 (5), 183–189. <https://doi.org/10.1016/j.redox.2016.12.035>.
- (137) Napoli, A.; Tirelli, N.; Kilcher, G.; Hubbell, A. New Synthetic Methodologies for Amphiphilic Multiblock Copolymers of Ethylene Glycol and Propylene Sulfide. *Macromolecules* **2001**, 34 (26), 8913–8917. <https://doi.org/10.1021/ma0108057>.
- (138) Sobotta, F. H.; Hausig, F.; Harz, D. O.; Hoepfener, S.; Schubert, U. S.; Brendel, J. C. Oxidation-Responsive Micelles by a One-Pot Polymerization-Induced Self-Assembly Approach. *Polym. Chem.* **2018**, 9 (13), 1593–1602. <https://doi.org/10.1039/C7PY01859B>.
- (139) Velluto, D.; Thomas, S. N.; Simeoni, E.; Swartz, M. A.; Hubbell, J. A. PEG-b-PPS-b-PEI Micelles and PEG-b-PPS/PEG-b-PPS-b-PEI Mixed Micelles as Non-Viral Vectors for Plasmid DNA: Tumor Immunotoxicity in B16F10 Melanoma. *Biomaterials*. 2011, pp 9839–9847. <https://doi.org/10.1016/j.biomaterials.2011.08.079>.
- (140) Broaders, K. E.; Grandhe, S.; Frechet, J. M. A Biocompatible Oxidation-Triggered Carrier Polymer with Potential in Therapeutics. *J. Am. Chem. Soc.* **2011**, 133 (4), 756–758. <https://doi.org/10.1021/ja110468v> [doi].
- (141) de, G. L.; Joshi-Barr, S.; Nguyen, T.; Mahmoud, E.; Schopf, E.; Fomina, N.; Almutairi, A. Biocompatible Polymeric Nanoparticles Degrade and Release Cargo in Response to Biologically Relevant Levels of Hydrogen Peroxide. *J. Am. Chem. Soc.* **2012**, 134 (38), 15758–15764. <https://doi.org/10.1021/ja303372u>.
- (142) Wilson, D. S.; Dalmasso, G.; Wang, L.; Sitaraman, S. V.; Merlin, D.; Murthy, N. Orally Delivered Thioketal Nanoparticles Loaded with TNF- α -SiRNA Target Inflammation and Inhibit Gene Expression in the Intestines. *Nat. Mater.* **2010**, 9, 923.
- (143) Mahmoud, E. A.; Sankaranarayanan, J.; Morachis, J. M.; Kim, G.; Almutairi, A. Inflammation Responsive Logic Gate Nanoparticles for the Delivery of Proteins. *Bioconjug. Chem.* **2011**, 22 (7), 1416–1421. <https://doi.org/10.1021/bc200141h> [doi].
- (144) Stadtman, E. R.; Moskovitz, J.; Levine, R. L. Oxidation of Methionine Residues of Proteins: Biological Consequences. *Antioxid. Redox Signal.* **2003**, 5 (5), 577–582. <https://doi.org/10.1089/152308603770310239>.
- (145) Napoli, A.; Valentini, M.; Tirelli, N.; Müller, M.; Hubbell, J. A. Oxidation-Responsive Polymeric Vesicles. *Nat. Mater.* **2004**, 3 (3), 183–189. <https://doi.org/10.1038/nmat1081>.
- (146) Cerritelli, S.; O'Neil, C. P.; Velluto, D.; Fontana, A.; Adrian, M.; Dubochet, J.; Hubbell, J.

- A. Aggregation Behavior of Poly(Ethylene Glycol-*B*l-Propylene Sulfide) Di- and Triblock Copolymers in Aqueous Solution. *Langmuir* **2009**, *25* (19), 11328–11335. <https://doi.org/10.1021/la900649m>.
- (147) Cerritelli, S.; Velluto, D.; Hubbell, J. A. PEG-SS-PPS: Reduction-Sensitive Disulfide Block Copolymer Vesicles for Intracellular Drug Delivery. *Biomacromolecules* **2007**, *8* (6), 1966–1972. <https://doi.org/10.1021/bm070085x>.
- (148) Velluto, D.; Demurtas, D.; Hubbell, J. A. PEG-*b*-PPS Diblock Copolymer Aggregates for Hydrophobic Drug Solubilization and Release: Cyclosporin A as an Example. *Mol. Pharm.* **2008**, *5* (4), 632–642. <https://doi.org/10.1021/mp7001297>.
- (149) O’Neil, C. P.; Suzuki, T.; Demurtas, D.; Finka, A.; Hubbell, J. A. A Novel Method for the Encapsulation of Biomolecules into Polymersomes via Direct Hydration. *Langmuir* **2009**, *25* (16), 9025–9029. <https://doi.org/10.1021/la900779t>.
- (150) Yoo, J.; Sanoj Rejinold, N.; Lee, D.; Jon, S.; Kim, Y.-C. Protease-Activatable Cell-Penetrating Peptide Possessing ROS-Triggered Phase Transition for Enhanced Cancer Therapy. *Journal of Controlled Release*. 2017, pp 89–101. <https://doi.org/10.1016/j.jconrel.2017.08.026>.
- (151) Rodriguez, A. R.; Kramer, J. R.; Deming, T. J. Enzyme-Triggered Cargo Release from Methionine Sulfoxide Containing Copolypeptide Vesicles. *Biomacromolecules* **2013**, *14* (10), 3610–3614. <https://doi.org/10.1021/bm400971p>.
- (152) Ma, N.; Li, Y.; Ren, H.; Xu, H.; Li, Z.; Zhang, X. Selenium-Containing Block Copolymers and Their Oxidation-Responsive Aggregates. *Polym. Chem.* **2010**, *1* (10), 1609–1614. <https://doi.org/10.1039/C0PY00144A>.
- (153) Han, P.; Ma, N.; Ren, H.; Xu, H.; Li, Z.; Wang, Z.; Zhang, X. Oxidation-Responsive Micelles Based on a Selenium-Containing Polymeric Superamphiphile. *Langmuir* **2010**, *26* (18), 14414–14418. <https://doi.org/10.1021/la102837a> [doi].
- (154) Sies, H. Hydrogen Peroxide as a Central Redox Signaling Molecule in Physiological Oxidative Stress: Oxidative Eustress. *Redox Biology*. 2017, pp 613–620. <https://doi.org/10.1016/j.redox.2016.12.035>.
- (155) Gupta, M. K.; Meyer, T. A.; Nelson, C. E.; Duvall, C. L. Poly(PS-*b*-DMA) Micelles for Reactive Oxygen Species Triggered Drug Release. *Journal of Controlled Release*. 2012, pp 591–598. <https://doi.org/10.1016/j.jconrel.2012.07.042>.
- (156) Perrier, S.; Takolpuckdee, P.; Mars, C. A. Reversible Addition–Fragmentation Chain Transfer Polymerization: End Group Modification for Functionalized Polymers and Chain Transfer Agent Recovery. *Macromolecules* **2005**, *38* (6), 2033–2036. <https://doi.org/10.1021/ma047611m>.
- (157) Coutinho, P. J. G.; Castanheira, E. M. S.; Céu Rei, M.; Real Oliveira, M. E. C. Nile Red and DCM Fluorescence Anisotropy Studies in C12E7/DPPC Mixed Systems. *J. Phys. Chem. B* **2002**, *106* (49), 12841–12846. <https://doi.org/10.1021/jp026479u>.
- (158) Kresse, G.; Furthmüller, J. Efficient Iterative Schemes for Ab Initio Total-Energy Calculations Using a Plane-Wave Basis Set. *Phys. Rev. B. Condens. Matter* **1996**, *54* (16), 11169.
- (159) Perdew, J. P.; Burke, K.; Ernzerhof, M. Generalized Gradient Approximation Made Simple; Louisiana State University, Baton Rouge, LA (United States): United States.
- (160) Blöchl, P. E. Projector Augmented-Wave Method. *Phys. Rev. B* **1994**, *50* (24), 17953–17979. <https://doi.org/10.1103/PhysRevB.50.17953>.
- (161) Yu, M.; Trinkle, D. Accurate and Efficient Algorithm for Bader Charge Integration. *J.*

- Chem. Phys.* **2011**, *134* (6), 64111–64118. <https://doi.org/10.1063/1.3553716>.
- (162) Chu, J.-W.; Trout, B. L. On the Mechanisms of Oxidation of Organic Sulfides by H₂O₂ in Aqueous Solutions. *J. Am. Chem. Soc.* **2004**, *126* (3), 900–908. <https://doi.org/10.1021/ja036762m>.
- (163) Junglee, S.; Urban, L.; Sallanon, H.; Lopez-Lauri, F. Optimized Assay for Hydrogen Peroxide Determination in Plant Tissue Using Potassium Iodide. *Am. J. Anal. Chem.* **2014**, *5* (11), 730–736. <https://doi.org/10.4236/ajac.2014.511081>.
- (164) Srinivasan, C.; Kuthalingam, P.; Arumugam, N. Substituent and Steric Effects in the Oxidation of Alkyl Aryl Sulfides by Peroxydisulfate. *Can. J. Chem.* **1978**, *56* (24), 3043–3046. <https://doi.org/10.1139/v78-497>.
- (165) Mohr, N.; Barz, M.; Forst, R.; Zentel, R. A Deeper Insight into the Postpolymerization Modification of Polypenta Fluorophenyl Methacrylates to Poly(N-(2-Hydroxypropyl) Methacrylamide). *Macromol. Rapid Commun.* **2014**, *35* (17), 1522–1527. <https://doi.org/10.1002/marc.201400249>.
- (166) Li, Y.; Duong, H. T. T.; Jones, M. W.; Basuki, J. S.; Hu, J.; Boyer, C.; Davis, T. P. Selective Postmodification of Copolymer Backbones Bearing Different Activated Esters with Disparate Reactivities. *ACS Macro Lett.* **2013**, *2* (10), 912–917. <https://doi.org/10.1021/mz4004375>.
- (167) Chen, H.; Kim, S.; Li, L.; Wang, S.; Park, K.; Cheng, J. X. Release of Hydrophobic Molecules from Polymer Micelles into Cell Membranes Revealed by Förster Resonance Energy Transfer Imaging. *Proc. Natl. Acad. Sci. U. S. A.* **2008**, *105* (18), 6596–6601. <https://doi.org/10.1073/pnas.0707046105>.
- (168) Kobayashi, Y.; Nishikawa, M.; Hyoudou, K.; Yamashita, F.; Hashida, M. Hydrogen Peroxide-Mediated Nuclear Factor KB Activation in Both Liver and Tumor Cells during Initial Stages of Hepatic Metastasis. *Cancer Sci.* **2008**, *99* (8), 1546–1552. <https://doi.org/10.1111/j.1349-7006.2008.00856.x>.
- (169) Huang, R. P.; Peng, A.; Hossain, M. Z.; Fan, Y.; Jagdale, A.; Boynton, A. L. Tumor Promotion by Hydrogen Peroxide in Rat Liver Epithelial Cells. *Carcinogenesis* **1999**, *20* (3), 485–492. <https://doi.org/10.1093/carcin/20.3.485>.
- (170) Djordjevic, J.; Djordjevic, A.; Adzic, M.; Niciforovic, A.; Radojicic, M. B. Chronic Stress Differentially Affects Antioxidant Enzymes and Modifies the Acute Stress Response in Liver of Wistar Rats. *Physiol. Res.* **2010**, *59* (5), 729–736.
- (171) Sakurai, T.; He, G.; Matsuzawa, A.; Yu, G. Y.; Maeda, S.; Hardiman, G.; Karin, M. Hepatocyte Necrosis Induced by Oxidative Stress and IL-1 α Release Mediate Carcinogen-Induced Compensatory Proliferation and Liver Tumorigenesis. *Cancer Cell* **2008**, *14* (2), 156–165. <https://doi.org/10.1016/j.ccr.2008.06.016>.
- (172) Liang, K.; Chung, J. E.; Gao, S. J.; Yongvongsoontorn, N.; Kurisawa, M. Highly Augmented Drug Loading and Stability of Micellar Nanocomplexes Composed of Doxorubicin and Poly(Ethylene Glycol)–Green Tea Catechin Conjugate for Cancer Therapy. *Adv. Mater.* **2018**, *30* (14), 1–8. <https://doi.org/10.1002/adma.201706963>.
- (173) Kan, J.; Guo, W.; Huang, C.; Bao, G.; Zhu, Y.; Zhu, Y. Z. S-Propargyl-Cysteine, a Novel Water-Soluble Modulator of Endogenous Hydrogen Sulfide, Promotes Angiogenesis through Activation of Signal Transducer and Activator of Transcription 3. *Antioxidants Redox Signal.* **2014**, *20* (15), 2303–2316. <https://doi.org/10.1089/ars.2013.5449>.
- (174) Chen, J. J. Y.; Van Der Vlies, A. J.; Hasegawa, U. Hydrogen Sulfide-Releasing Micelles for Promoting Angiogenesis. *Polym. Chem.* **2020**. <https://doi.org/10.1039/d0py00495b>.

- (175) Materazzi, S.; Zagli, G.; Nassini, R.; Bartolini, I.; Romagnoli, S.; Chelazzi, C.; Benemei, S.; Coratti, A.; De Gaudio, A. R.; Patacchini, R. Vasodilator Activity of Hydrogen Sulfide (H₂S) in Human Mesenteric Arteries. *Microvasc. Res.* **2017**, *109*, 38–44. <https://doi.org/10.1016/j.mvr.2016.11.001>.
- (176) Sen, N.; Paul, B. D.; Gadalla, M. M.; Mustafa, A. K.; Sen, T.; Xu, R.; Kim, S.; Snyder, S. H. Hydrogen Sulfide-Linked Sulfhydration of NF-KappaB Mediates Its Antiapoptotic Actions. *Mol. Cell* **2012**, *45* (1), 13–25. <https://doi.org/10.1016/j.molcel.2011.10.021> [doi].
- (177) Gemici, B.; Wallace, J. L. Anti-Inflammatory and Cytoprotective Properties of Hydrogen Sulfide. In *Methods in Enzymology*; 2015. <https://doi.org/10.1016/bs.mie.2014.11.034>.
- (178) Wu, Y. C.; Wang, X. J.; Yu, L.; Chan, F. K.; Cheng, A. S.; Yu, J.; Sung, J. J.; Wu, W. K.; Cho, C. H. Hydrogen Sulfide Lowers Proliferation and Induces Protective Autophagy in Colon Epithelial Cells. *PLoS One* **2012**, *7* (5). <https://doi.org/10.1371/journal.pone.0037572> [doi].
- (179) Sakuma, S.; Minamino, S.; Takase, M.; Ishiyama, Y.; Hosokura, H.; Kohda, T.; Ikeda, Y.; Fujimoto, Y. Hydrogen Sulfide Donor GYY4137 Suppresses Proliferation of Human Colorectal Cancer Caco-2 Cells by Inducing Both Cell Cycle Arrest and Cell Death. *Heliyon* **2019**, *5* (8), e02244. <https://doi.org/10.1016/j.heliyon.2019.e02244>.
- (180) Bhattacharyya, S.; Saha, S.; Giri, K.; Lanza, I. R.; Nair, K. S.; Jennings, N. B.; Rodriguez-Aguayo, C.; Lopez-Berestein, G.; Basal, E.; Weaver, A. L.; et al. Cystathionine Beta-Synthase (CBS) Contributes to Advanced Ovarian Cancer Progression and Drug Resistance. *PLoS One* **2013**, *8* (11). <https://doi.org/10.1371/journal.pone.0079167>.
- (181) Pei, Y.; Wu, B.; Cao, Q.; Wu, L.; Yang, G. Hydrogen Sulfide Mediates the Anti-Survival Effect of Sulforaphane on Human Prostate Cancer Cells. *Toxicol. Appl. Pharmacol.* **2011**, *257* (3), 420–428. <https://doi.org/10.1016/j.taap.2011.09.026>.
- (182) Cai, W. J.; Wang, M. J.; Ju, L. H.; Wang, C.; Zhu, Y. C. Hydrogen Sulfide Induces Human Colon Cancer Cell Proliferation: Role of Akt, ERK and P21. *Cell Biol. Int.* **2010**, *34* (6), 565–573. <https://doi.org/10.1042/CBI20090368> [doi].
- (183) Jurkowska, H.; Placha, W.; Nagahara, N.; Wrobel, M. The Expression and Activity of Cystathionine-Gamma-Lyase and 3-Mercaptopyruvate Sulfurtransferase in Human Neoplastic Cell Lines. *Amino Acids* **2011**, *41* (1), 151–158. <https://doi.org/10.1007/s00726-010-0606-3>.
- (184) Szabo, C.; Coletta, C.; Chao, C.; Modis, K.; Szczesny, B.; Papapetropoulos, A.; Hellmich, M. R. Tumor-Derived Hydrogen Sulfide, Produced by Cystathionine-Beta-Synthase, Stimulates Bioenergetics, Cell Proliferation, and Angiogenesis in Colon Cancer. *Proc. Natl. Acad. Sci. U. S. A.* **2013**, *110* (30), 12474–12480. <https://doi.org/10.1073/pnas.1306241110> [doi].
- (185) Szabo, C.; Hellmich, M. R. Endogenously Produced Hydrogen Sulfide Supports Tumor Cell Growth and Proliferation. *Cell Cycle* **2013**, *12* (18), 2915–2917. <https://doi.org/10.4161/cc.26064> [doi].
- (186) Lee, Z. W.; Teo, X. Y.; Tay, E. Y.; Tan, C. H.; Hagen, T.; Moore, P. K.; Deng, L. W. Utilizing Hydrogen Sulfide as a Novel Anti-Cancer Agent by Targeting Cancer Glycolysis and PH Imbalance. *Br. J. Pharmacol.* **2014**, *171* (18), 4322–4337. <https://doi.org/10.1111/bph.12773> [doi].
- (187) Feng, W.; Teo, X. Y.; Novera, W.; Ramanujulu, P. M.; Liang, D.; Huang, D.; Moore, P. K.; Deng, L. W.; Dymock, B. W. Discovery of New H₂S Releasing Phosphordithioates

- and 2,3-Dihydro-2-Phenyl-2-Sulfanylenebenzo[d][1,3,2]Oxazaphospholes with Improved Antiproliferative Activity. *J. Med. Chem.* **2015**, *58* (16), 6456–6480. <https://doi.org/10.1021/acs.jmedchem.5b00848>.
- (188) Lee, Z. W.; Zhou, J.; Chen, C. S.; Zhao, Y.; Tan, C. H.; Li, L.; Moore, P. K.; Deng, L. W. The Slow-Releasing Hydrogen Sulfide Donor, GYY4137, Exhibits Novel Anti-Cancer Effects in Vitro and in Vivo. *PLoS One* **2011**, *6* (6). <https://doi.org/10.1371/journal.pone.0021077> [doi].
- (189) Chattopadhyay, M.; Kodela, R.; Nath, N.; Dastagirzada, Y. M.; Velazquez-Martinez, C. A.; Boring, D.; Kashfi, K. Hydrogen Sulfide-Releasing NSAIDs Inhibit the Growth of Human Cancer Cells: A General Property and Evidence of a Tissue Type-Independent Effect. *Biochem. Pharmacol.* **2012**, *83* (6), 715–723. <https://doi.org/10.1016/j.bcp.2011.12.018> [doi].
- (190) Dong, Q.; Yang, B.; Han, J. G.; Zhang, M. M.; Liu, W.; Zhang, X.; Yu, H. L.; Liu, Z. G.; Zhang, S. H.; Li, T.; et al. A Novel Hydrogen Sulfide-Releasing Donor, HA-ADT, Suppresses the Growth of Human Breast Cancer Cells through Inhibiting the PI3K/AKT/MTOR and Ras/Raf/MEK/ERK Signaling Pathways. *Cancer Lett.* **2019**. <https://doi.org/10.1016/j.canlet.2019.04.031>.
- (191) Devarie-Baez, N. O.; Bagdon, P. E.; Peng, B.; Zhao, Y.; Park, C. M.; Xian, M. Light-Induced Hydrogen Sulfide Release from “Caged” Gem-Dithiols. *Org. Lett.* **2013**, *15* (11), 2786–2789. <https://doi.org/10.1021/ol401118k>.
- (192) Hasegawa, U.; Van Der Vlies, A. J. Design and Synthesis of Polymeric Hydrogen Sulfide Donors. *Bioconjug. Chem.* **2014**, *25* (7), 1290–1300. <https://doi.org/10.1021/bc500150s>.
- (193) Takatani-Nakase, T.; Katayama, M.; Matsui, C.; Hanaoka, K.; van der Vlies, A. J.; Takahashi, K.; Nakase, I.; Hasegawa, U. Hydrogen Sulfide Donor Micelles Protect Cardiomyocytes from Ischemic Cell Death. *Mol. Biosyst.* **2017**, *13* (9), 1705–1709. <https://doi.org/10.1039/c7mb00191f> [doi].
- (194) Hasegawa, U.; van der Vlies, A. J. Design and Synthesis of Polymeric Hydrogen Sulfide Donors. *Bioconjug. Chem.* **2014**, *25* (7), 1290–1301. <https://doi.org/10.1021/bc500150s> [doi].
- (195) Chong, Y. K.; Moad, G.; Rizzardo, E.; Thang, S. H. Thiocarbonylthio End Group Removal from RAFT-Synthesized Polymers by Radical-Induced Reduction. *Macromolecules* **2007**, *40* (13), 4446–4456. <https://doi.org/10.1021/ma062919u>.
- (196) Coutinho, P. J. G.; Castanheira, E. M. S.; Céu Rei, M.; Real Oliveira, M. E. C. Nile Red and DCM Fluorescence Anisotropy Studies in C12E7/DPPC Mixed Systems. *J. Phys. Chem. B* **2002**, *106* (49), 12841–12847. <https://doi.org/10.1021/jp026479u>.
- (197) Liu, C.; Pan, J.; Li, S.; Zhao, Y.; Wu, L. Y.; Berkman, C. E.; Whorton, A. R.; Xian, M. Capture and Visualization of Hydrogen Sulfide by a Fluorescent Probe. *Angew. Chemie Int. Ed.* **2011**, *50* (44), 10327–10329. <https://doi.org/10.1002/anie.201104305>.
- (198) Zhou, M.; Qian, Y.; Zhu, Y.; Matson, J. Elastase-Triggered H₂S Delivery from Polymer Hydrogels. *Chem. Commun.* **2020**, *56* (7), 1085–1088. <https://doi.org/10.1039/C9CC08752D>.
- (199) Rios, E. C.; Soriano, F. G.; Olah, G.; Gero, D.; Szczesny, B.; Szabo, C. Hydrogen Sulfide Modulates Chromatin Remodeling and Inflammatory Mediator Production in Response to Endotoxin, but Does Not Play a Role in the Development of Endotoxin Tolerance. *J. Inflamm. (Lond)*. **2016**, *13*. <https://doi.org/10.1186/s12950-016-0119-2> [doi].
- (200) Marutani, E.; Yamada, M.; Ida, T.; Tokuda, K.; Ikeda, K.; Kai, S.; Shirozu, K.;

- Hayashida, K.; Kosugi, S.; Hanaoka, K.; et al. Thiosulfate Mediates Cytoprotective Effects of Hydrogen Sulfide against Neuronal Ischemia. *J. Am. Heart Assoc.* **2015**, *4* (11), 1–10. <https://doi.org/10.1161/JAHA.115.002125>.
- (201) Zelzer, M.; Todd, S. J.; Hirst, A. R.; McDonald, T. O.; Ulijn, R. V. Enzyme Responsive Materials: Design Strategies and Future Developments. *Biomaterials Science*. 2013. <https://doi.org/10.1039/c2bm00041e>.
- (202) Ulijn, R. V. Enzyme-Responsive Materials: A New Class of Smart Biomaterials. *J. Mater. Chem.* **2006**. <https://doi.org/10.1039/b601776m>.
- (203) Zheng, Y.; Yu, B.; Ji, K.; Pan, Z.; Chittavong, V.; Wang, B. Esterase-Sensitive Prodrugs with Tunable Release Rates and Direct Generation of Hydrogen Sulfide. *Angew. Chem. Int. Ed. Engl.* **2016**, *55* (14), 4514–4518. <https://doi.org/10.1002/anie.201511244>.
- (204) Nomura, H.; Fujimoto, N.; Seiki, M.; Mai, M.; Okada, Y. Enhanced Production of Matrix Metalloproteinases and Activation of Matrix Metalloproteinase 2 (Gelatinase A) in Human Gastric Carcinomas. *Int. J. cancer* **1996**, *69* (1), 9–16. [https://doi.org/10.1002/\(SICI\)1097-0215\(19960220\)69:1<9::AID-IJC3>3.0.CO;2-8](https://doi.org/10.1002/(SICI)1097-0215(19960220)69:1<9::AID-IJC3>3.0.CO;2-8).
- (205) Garbett, E. A.; Reed, M. W.; Brown, N. J. Proteolysis in Human Breast and Colorectal Cancer. *Br. J. Cancer* **1999**, *81* (2), 287–293. <https://doi.org/10.1038/sj.bjc.6690689>.
- (206) Murnane, M. J.; Cai, J.; Shuja, S.; McAneny, D.; Klepeis, V.; Willett, J. B. Active MMP-2 Effectively Identifies the Presence of Colorectal Cancer. *Int. J. cancer* **2009**, *125* (12), 2893–2902. <https://doi.org/10.1002/ijc.24682>.
- (207) De Vicente, J. C.; Fresno, M. F.; Villalain, L.; Vega, J. A.; Hernández Vallejo, G. Expression and Clinical Significance of Matrix Metalloproteinase-2 and Matrix Metalloproteinase-9 in Oral Squamous Cell Carcinoma. *Oral Oncol.* **2005**, *41* (3), 283–293. <https://doi.org/10.1016/j.oraloncology.2004.08.013>.
- (208) Torng, P.-L.; Mao, T.-L.; Chan, W.-Y.; Huang, S.-C.; Lin, C.-T. Prognostic Significance of Stromal Metalloproteinase-2 in Ovarian Adenocarcinoma and Its Relation to Carcinoma Progression. *Gynecol. Oncol.* **2004**, *92* (2), 559–567. <https://doi.org/10.1016/j.ygyno.2003.11.011>.
- (209) Kessenbrock, K.; Plaks, V.; Werb, Z. Matrix Metalloproteinases: Regulators of the Tumor. *Cell* **2010**, *141* (1), 52–67. <https://doi.org/10.1038/jid.2014.371>.
- (210) Patterson, J.; Hubbell, J. A. Enhanced Proteolytic Degradation of Molecularly Engineered PEG Hydrogels in Response to MMP-1 and MMP-2. *Biomaterials* **2010**, *31* (30), 7836–7845. <https://doi.org/10.1016/j.biomaterials.2010.06.061>.
- (211) Lutolf, M. P.; Lauer-Fields, J.; Schmoekel, H. G.; Metters, A. T.; Weber, F. E.; Fields, G. B.; Hubbell, J. A. Synthetic Matrix Metalloproteinase-Sensitive Hydrogels for the Conduction of Tissue Regeneration: Engineering Cell-Invasion Characteristics. *Proc Natl Acad Sci USA* **2003**, *100* (9), 5413. <https://doi.org/10.1073/pnas.0737381100>.
- (212) Zhu, L.; Perche, F.; Wang, T.; Torchilin, V. P. Matrix Metalloproteinase 2-Sensitive Multifunctional Polymeric Micelles for Tumor-Specific Co-Delivery of siRNA and Hydrophobic Drugs. *Biomaterials* **2014**, *35* (13), 4213–4222. <https://doi.org/10.1016/j.biomaterials.2014.01.060>.
- (213) Yao, Q.; Liu, Y.; Kou, L.; Tu, Y.; Tang, X.; Zhu, L. Tumor-Targeted Drug Delivery and Sensitization by MMP2-Responsive Polymeric Micelles. *Nanomedicine Nanotechnology, Biol. Med.* **2019**, *19*, 71–80. <https://doi.org/10.1016/j.nano.2019.03.012>.
- (214) Guo, F.; Wu, J.; Wu, W.; Huang, D.; Yan, Q.; Yang, Q.; Gao, Y.; Yang, G. PEGylated Self-Assembled Enzyme-Responsive Nanoparticles for Effective Targeted Therapy

- against Lung Tumors. *J. Nanobiotechnology* **2018**, *16* (1), 1–13.
<https://doi.org/10.1186/s12951-018-0384-8>.
- (215) Hasegawa, U.; Van Der Vlies, A. J. Polymeric Micelles for Hydrogen Sulfide Delivery. *Medchemcomm* **2015**, *6* (2), 273–276. <https://doi.org/10.1039/c4md00373j>.
- (216) Lutolf, M. P.; Lauer-Fields, J. L.; Schmoekel, H. G.; Metters, A. T.; Weber, F. E.; Fields, G. B.; Hubbell, J. A. Synthetic Matrix Metalloproteinase-Sensitive Hydrogels for the Conduction of Tissue Regeneration: Engineering Cell-Invasion Characteristics. *Proc. Natl. Acad. Sci. U. S. A.* **2003**, *100* (9), 5413–5418.
<https://doi.org/10.1073/pnas.0737381100>.
- (217) Lauer-Fields, J. L.; Tuzinski, K. A.; Shimokawa, K.; Nagase, H.; Fields, G. B. Hydrolysis of Triple-Helical Collagen Peptide Models by Matrix Metalloproteinases. *J. Biol. Chem.* **2000**, *275* (18), 13282–13291. <https://doi.org/10.1074/jbc.275.18.13282> [pii].
- (218) Yao, Q.; Kou, L.; Tu, Y.; Zhu, L. MMP-Responsive ‘Smart’ Drug Delivery and Tumor Targeting. *Trends Pharmacol. Sci.* **2018**, *39* (8), 766–781.
<https://doi.org/10.1016/j.tips.2018.06.003>.
- (219) Eckhard, U.; Huesgen, P. F.; Schilling, O.; Bellac, C. L.; Butler, G. S.; Cox, J. H.; Dufour, A.; Goebeler, V.; Kappelhoff, R.; auf dem Keller, U.; et al. Active Site Specificity Profiling Datasets of Matrix Metalloproteinases (MMPs) 1, 2, 3, 7, 8, 9, 12, 13 and 14. *Data Br.* **2016**, *7*, 299–310. <https://doi.org/10.1016/j.dib.2016.02.036>.
- (220) Mohr, N.; Barz, M.; Forst, R.; Zentel, R. A Deeper Insight into the Postpolymerization Modification of Polypenta Fluorophenyl Methacrylates to Poly(N-(2-Hydroxypropyl) Methacrylamide). *Macromol. Rapid Commun.* **2014**, *35* (17), 1522–1528.
<https://doi.org/10.1002/marc.201400249>.
- (221) Eckhard, U.; Huesgen, P. F.; Schilling, O.; Bellac, C. L.; Butler, G. S.; Cox, J. H.; Dufour, A.; Goebeler, V.; Kappelhoff, R.; auf dem Keller, U.; et al. Active Site Specificity Profiling of the Matrix Metalloproteinase Family: Proteomic Identification of 4300 Cleavage Sites by Nine MMPs Explored with Structural and Synthetic Peptide Cleavage Analyses. *Matrix Biol.* **2016**, *49* (2016), 37–60.
<https://doi.org/10.1016/j.matbio.2015.09.003>.
- (222) Donlan, R. M. Biofilms: Microbial Life on Surfaces. *Emerg. Infect. Dis.* **2002**, *8* (9), 881–890. <https://doi.org/10.3201/eid0809.020063>.
- (223) Costerton, J. W. Introduction to Biofilm. *Int. J. Antimicrob. Agents* **1999**, *11* (3), 217–221. [https://doi.org/10.1016/S0924-8579\(99\)00018-7](https://doi.org/10.1016/S0924-8579(99)00018-7).
- (224) Donlan, R. M.; Costerton, J. W. Biofilms: Survival Mechanisms of Clinically Relevant Microorganisms. *Clin. Microbiol. Rev.* **2002**, *15* (2), 167–193.
<https://doi.org/10.1128/cmr.15.2.167-193.2002>.
- (225) Chang, C.-Y. Surface Sensing for Biofilm Formation in *Pseudomonas Aeruginosa*. *Frontiers in Microbiology*. 2018, p 2671.
- (226) Gupta, P.; Sarkar, S.; Das, B.; Bhattacharjee, S.; Tribedi, P. Biofilm, Pathogenesis and Prevention—a Journey to Break the Wall: A Review. *Arch. Microbiol.* **2016**, *198* (1), 1–15. <https://doi.org/10.1007/s00203-015-1148-6>.
- (227) Bjarnsholt, T. The Role of Bacterial Biofilms in Chronic Infections. *APMIS* **2013**, *121* (s136), 1–58. <https://doi.org/10.1111/apm.12099>.
- (228) Simões, M.; Simões, L. C.; Vieira, M. J. A Review of Current and Emergent Biofilm Control Strategies. *LWT - Food Sci. Technol.* **2010**, *43* (4), 573–583.
<https://doi.org/10.1016/j.lwt.2009.12.008>.

- (229) Bannister, J.; Sievers, M.; Bush, F.; Bloecher, N. Biofouling in Marine Aquaculture: A Review of Recent Research and Developments. *Biofouling* **2019**, *35* (6), 631–648. <https://doi.org/10.1080/08927014.2019.1640214>.
- (230) Schultz, M. P. Effects of Coating Roughness and Biofouling on Ship Resistance and Powering. *Biofouling* **2007**, *23* (5), 331–341. <https://doi.org/10.1080/08927010701461974>.
- (231) Schultz, M. P.; Bendick, J. A.; Holm, E. R.; Hertel, W. M. Economic Impact of Biofouling on a Naval Surface Ship. *Biofouling* **2011**, *27* (1), 87–98. <https://doi.org/10.1080/08927014.2010.542809>.
- (232) Deng, L.; Guo, W.; Ngo, H. H.; Zhang, H.; Wang, J.; Li, J.; Xia, S.; Wu, Y. Biofouling and Control Approaches in Membrane Bioreactors. *Bioresour. Technol.* **2016**, *221*, 656–665. <https://doi.org/10.1016/j.biortech.2016.09.105>.
- (233) Yeon, K.-M.; Lee, J.; Kim, J. Magnetic Enzyme Carrier for Effective Biofouling Control in the Membrane Bioreactor Based on Enzymatic Quorum Quenching. *Environ. Sci. Technol.* **2009**, *43*, 7403–7409. <https://doi.org/10.1021/es901323k>.
- (234) Yeon, K.-M.; Cheong, W.-S.; Oh, H.-S.; Lee, W.-N.; Hwang, B.-K.; Lee, C.-H.; Beyenal, H.; Lewandowski, Z. Quorum Sensing: A New Biofouling Control Paradigm in a Membrane Bioreactor for Advanced Wastewater Treatment. *Environ. Sci. Technol.* **2009**, *43* (2), 380–385. <https://doi.org/10.1021/es8019275>.
- (235) Bzdrenga, J.; Daudé, D.; Rémy, B.; Jacquet, P.; Plener, L.; Elias, M.; Chabrière, E. Biotechnological Applications of Quorum Quenching Enzymes. *Chem. Biol. Interact.* **2017**, *267*, 104–115. <https://doi.org/10.1016/j.cbi.2016.05.028>.
- (236) Matar, G. K.; Bagchi, S.; Zhang, K.; Oerther, D. B.; Saikaly, P. E. Membrane Biofilm Communities in Full-Scale Membrane Bioreactors Are Not Randomly Assembled and Consist of a Core Microbiome. *Water Res.* **2017**. <https://doi.org/10.1016/j.watres.2017.06.052>.
- (237) Piasecka, A.; Souffreau, C.; Vandepitte, K.; Vanysacker, L.; Bilad, R. M.; de Bie, T.; Hellemans, B.; de Meester, L.; Yan, X.; Declerck, P.; et al. Analysis of the Microbial Community Structure in a Membrane Bioreactor during Initial Stages of Filtration. *Biofouling* **2012**. <https://doi.org/10.1080/08927014.2012.662640>.
- (238) Vanysacker, L.; Boerjan, B.; Declerck, P.; Vankelecom, I. F. J. Biofouling Ecology as a Means to Better Understand Membrane Biofouling. *Applied Microbiology and Biotechnology*. 2014. <https://doi.org/10.1007/s00253-014-5921-2>.
- (239) Herrera-Robledo, M.; Morgan-Sagastume, J. M.; Noyola, A. Biofouling and Pollutant Removal during Long-Term Operation of an Anaerobic Membrane Bioreactor Treating Municipal Wastewater. *Biofouling* **2010**. <https://doi.org/10.1080/08927010903243923>.
- (240) Jun, D.; Kim, Y.; Hafeznezami, S.; Yoo, K.; Hoek, E. M. V.; Kim, J. Biologically Induced Mineralization in Anaerobic Membrane Bioreactors: Assessment of Membrane Scaling Mechanisms in a Long-Term Pilot Study. *J. Memb. Sci.* **2017**. <https://doi.org/10.1016/j.memsci.2017.08.025>.
- (241) Stewart, P. S.; Franklin, M. J. Physiological Heterogeneity in Biofilms. *Nature Reviews Microbiology*. 2008. <https://doi.org/10.1038/nrmicro1838>.
- (242) Pérez-Osorio, A. C.; Williamson, K. S.; Franklin, M. J. Heterogeneous RpoS and RhlR mRNA Levels and 16S rRNA/rdnA (rRNA Gene) Ratios within *Pseudomonas aeruginosa* Biofilms, Sampled by Laser Capture Microdissection. *J. Bacteriol.* **2010**. <https://doi.org/10.1128/JB.01598-09>.

- (243) Podgorny, O. V.; Lazarev, V. N. Laser Microdissection: A Promising Tool for Exploring Microorganisms and Their Interactions with Hosts. *Journal of Microbiological Methods*. 2017. <https://doi.org/10.1016/j.mimet.2016.01.001>.
- (244) Van Der Vlies, A. J.; Barua, N.; Nieves-Otero, P. A.; Platt, T. G.; Hansen, R. R. On Demand Release and Retrieval of Bacteria from Microwell Arrays Using Photodegradable Hydrogel Membranes. *ACS Appl. Bio Mater.* **2019**. <https://doi.org/10.1021/acsabm.8b00592>.
- (245) Barua, N.; Herken, A. M.; Stern, K. R.; Reese, S.; Powers, R. L.; Morrell-Falvey, J. L.; Platt, T. G.; Hansen, R. R. Simultaneous Discovery of Positive and Negative Interactions among Root Microbiome Bacteria Using Microwell Recovery Arrays. *bioRxiv*. 2020. <https://doi.org/10.1101/2020.01.03.894477>.
- (246) Bolyen, E.; Rideout, J. R.; Dillon, M. R.; Bokulich, N. A.; Abnet, C. C.; Al-Ghalith, G. A.; Alexander, H.; Alm, E. J.; Arumugam, M.; Asnicar, F.; et al. Reproducible, Interactive, Scalable and Extensible Microbiome Data Science Using QIIME 2. *Nature Biotechnology*. 2019. <https://doi.org/10.1038/s41587-019-0209-9>.
- (247) Amir, A.; McDonald, D.; Navas-Molina, J. A.; Kopylova, E.; Morton, J. T.; Zech Xu, Z.; Kightley, E. P.; Thompson, L. R.; Hyde, E. R.; Gonzalez, A.; et al. Deblur Rapidly Resolves Single-Nucleotide Community Sequence Patterns. *mSystems* **2017**. <https://doi.org/10.1128/msystems.00191-16>.
- (248) Rastogi, R. P.; Richa; Kumar, A.; Tyagi, M. B.; Sinha, R. P. Molecular Mechanisms of Ultraviolet Radiation-Induced DNA Damage and Repair. *Journal of Nucleic Acids*. 2010. <https://doi.org/10.4061/2010/592980>.
- (249) Kishore, R.; Reef Hardy, W.; Anderson, V. J.; Sanchez, N. A.; Buoncristiani, M. R. Optimization of DNA Extraction from Low-Yield and Degraded Samples Using the BioRobot® EZ1 and BioRobot® M48. *J. Forensic Sci.* **2006**. <https://doi.org/10.1111/j.1556-4029.2006.00204.x>.
- (250) Shaw, K. J.; Thain, L.; Docker, P. T.; Dyer, C. E.; Greenman, J.; Greenway, G. M.; Haswell, S. J. The Use of Carrier RNA to Enhance DNA Extraction from Microfluidic-Based Silica Monoliths. *Anal. Chim. Acta* **2009**. <https://doi.org/10.1016/j.aca.2009.03.038>.
- (251) El Bali, L.; Diman, A.; Bernard, A.; Roosens, N. H. C.; Dekeersmaecker, S. C. J. Comparative Study of Seven Commercial Kits for Human Dna Extraction from Urine Samples Suitable for Dna Biomarker-Based Public Health Studies. *J. Biomol. Tech.* **2014**. <https://doi.org/10.7171/jbt.14-2504-002>.
- (252) GmbH, Q. QIAamp Viral RNA Mini Handbook. **2010**, No. July, 1–44.
- (253) Handbook, Q. May 2010 QIAamp ® DNA Micro Handbook Sample & Assay Technologies QIAGEN Sample and Assay Technologies. *Micro* **2010**, No. May.
- (254) Witzig, R.; Manz, W.; Rosenberger, S.; Krüger, U.; Kraume, M.; Szewzyk, U. Microbiological Aspects of a Bioreactor with Submerged Membranes for Aerobic Treatment of Municipal Wastewater. *Water Res.* **2002**. [https://doi.org/10.1016/S0043-1354\(01\)00221-4](https://doi.org/10.1016/S0043-1354(01)00221-4).
- (255) Nascimento, A. L.; Souza, A. J.; Andrade, P. A. M.; Andreote, F. D.; Coscione, A. R.; Oliveira, F. C.; Regitano, J. B. Sewage Sludge Microbial Structures and Relations to Their Sources, Treatments, and Chemical Attributes. *Front. Microbiol.* **2018**. <https://doi.org/10.3389/fmicb.2018.01462>.
- (256) Qin, H.; Ji, B.; Zhang, S.; Kong, Z. Study on the Bacterial and Archaeal Community Structure and Diversity of Activated Sludge from Three Wastewater Treatment Plants.

- Mar. Pollut. Bull.* **2018**. <https://doi.org/10.1016/j.marpolbul.2018.08.010>.
- (257) Lin, H.; Peng, W.; Zhang, M.; Chen, J.; Hong, H.; Zhang, Y. A Review on Anaerobic Membrane Bioreactors: Applications, Membrane Fouling and Future Perspectives. *Desalination*. 2013. <https://doi.org/10.1016/j.desal.2013.01.019>.
- (258) Noh, J.; Jung, E.; Lee, J.; Hyun, H.; Hong, S.; Lee, D. Engineered Polymeric Micelles for Combinational Oxidation Anticancer Therapy through Concurrent HO-1 Inhibition and ROS Generation. *Biomacromolecules* **2019**, *20* (2), 1109–1117. <https://doi.org/10.1021/acs.biomac.8b01802>.

Appendix A-Supporting information from Chapter 2

Synthesis of *N*-(3-(methylthio)propyl)acetamide (TPAM). 3-(methylthio)propan-1-amine (564 mg, 5.4 mmol) and 948 μL of Et_3N (6.8 mmol, 1.3 eq) were dissolved in 5 mL CH_2Cl_2 and cooled on ice for 30 min. To the cold solution was added dropwise over the course of 5 min 643 μL (6.8 mmol, 1.3 eq) Ac_2O in 5 mL CH_2Cl_2 . After warming to RT and stirring for 24 h ninhydrin stain indicated the presence of unreacted amine and another 95 μL of Ac_2O (1.0 mmol, 0.18 eq) and 139 μL of Et_3N (1.0 mmol, 0.18 eq) was added. After stirring for another 43 h the reaction mixture was evaporated in a stream of air at 30°C. The clear oil was dissolved in 10 mL of 5% NaHCO_3 (aq) and the aqueous solution was extracted with CH_2Cl_2 (3 x 10 mL). After drying over MgSO_4 , the solution was concentrated in a stream of air. The clear oil was dissolved in 10 mL of 1 M HCl (aq) and extracted with CH_2Cl_2 (3 x 10 mL). The clear organic phase was dried over MgSO_4 , concentrated in stream of air and dried under vacuum to yield 576 mg of a viscous oil (3.9 mmol, 72%). ^1H NMR in CDCl_3 (**Figure A.2a**), (ppm): 5.87 (bs, 1H, NH), 3.33 (m, 2H, CH_2NH), 2.52 (t, 2H, CH_2S), 2.08 (s, 3H, SCH_3), 1.97 (s, 3H, CH_3CO), 1.80 (m, 2H, $\text{CH}_2\text{CH}_2\text{CH}_2$).

Synthesis of 1-thiomorpholinoethan-1-one (TMAM). Thiomorpholine (531 mg, 5.2 mmol), 767 μL of Et_3N (5.5 mmol, 1.1 eq) and 9.7 mg of DMAP (0.08 mmol, 0.02 eq) were dissolved in 5 mL of CH_2Cl_2 and put on ice for 30 min. To the cooled solution was added 520 μL of Ac_2O (5.5 mmol, 1.1 eq). After stirring for 43 h the mixture was concentrated in a stream of air. The clear oil was dissolved in 10 mL of 5% NaHCO_3 (aq) and the aqueous solution was extracted with CH_2Cl_2 (3 x 10 mL). After drying over MgSO_4 , the solution was concentrated in a stream of air. The clear oil was dissolved in 10 mL of 1 M HCl (aq) and the solution extracted with CH_2Cl_2 (3 x 10 mL). The clear organic phase was dried over MgSO_4 , concentrated in flow of air and dried under vacuum to yield 443 mg of a clear oil (3.1 mmol, 59%). ^1H NMR in CDCl_3 (**Figure A.2b**, Supporting Information), δ (ppm): 3.86 (m, 2H, CH_2NCH_2), 3.72 (m, 2H, CH_2NCH_2), 2.61 (m, 4H, CH_2SCH_2), 2.09 (s, 3H, CH_3CO).

Synthesis of *N*-(3-(methylthio)benzyl)acetamide (TPhAM). (3-(methylthio)phenyl)methanamine· HCl salt (952 mg, 5.0 mmol) was suspended in 5 mL of CH_2Cl_2 and cooled on ice for 3 min before adding 1.46 mL of Et_3N (10.5 mmol, 2.1 eq). To homogenize the mixture another 5 mL of CH_2Cl_2 was added. After stirring for 5 min at 0°C 520 μL of Ac_2O (5.5 mmol, 1.1 eq) was added making the reaction mixture become clear. After adding 13.3 mg of DMAP (0.11 mmol, 0.02 eq) the mixture was stirred for 23 h. The reaction mixture was evaporated in a stream of air at 30°C. The residue was suspended in 10 mL of 5% NaHCO_3 (aq) and the mixture was extracted with CH_2Cl_2 (3 x 10 mL). After drying over MgSO_4 , the solution was concentrated in a stream of air. The white solid was suspended in 10 mL of 1 M HCl (aq) and the mixture was extracted with CH_2Cl_2 (3 x 10 mL). The clear organic phase was dried over MgSO_4 , concentrated in a flow of air and dried under vacuum to yield 862 mg of a white solid (4.4 mmol, 87%). ^1H NMR in CDCl_3 (**Figure A.2c**, Supporting Information), δ (ppm): 7.21 (m, 4H, $\text{CH}_{\text{aromat}}$), 5.75 (bs, 1H, NH), 4.39 (d, 2H, CH_2NH), 2.47 (s, 3H, CH_3S), 2.01 (s, 3H, CH_3CO).

Synthesis of *N*-(3-(methylsulfinyl)propyl)acetamide (TPAM-SO) (90 mg, 0.6 mmol) was dissolved in 540 μL of water in a glass vial and 68 μL of 9.0 M H_2O_2 (0.6 mmol, 1 eq) was added. The mixture was rotated at RT for 28 h, frozen and lyophilized to yield 99 mg of a white solid. ^1H NMR showed complete disappearance of the signals of TPAM and the appearance of new signals assigned to be those of the sulfoxide as shown by FTIR (**Figure 2.5a** manuscript). ^1H NMR in CDCl_3 (**Figure A.2d**, Supporting Information), δ (ppm): 6.55 (bs, 1H, NH), 3.38 (m, 2H, $\text{CH}_2\text{-NH}$), 2.74 (m, 2H, $\text{CH}_2\text{S(O)}$), 2.57 (s, 3H, S(O)CH_3), 2.05 (m, 2H, $\text{CH}_2\text{CH}_2\text{CH}_2$), 2.02 (s, 3H, CH_3CO). In addition, some sulfone formed as suggested by the signals at 6.40 (bs, NH), 3.07 (m, 2H), 2.91 (s, $\text{S(O}_2\text{)CH}_3$), 1.97 (s, COCH_3). Other signals of the sulfone were not observed due to overlap with the sulfoxide signals.

Synthesis of 1-(1-oxidomorpholino)ethan-1-one (TMAM-SO) (119 mg, 0.8 mmol) was dissolved in 817 μL of water in a glass vial and 91 μL of 9.0 M H_2O_2 (0.8 mmol) was added. The mixture was rotated for 28 h, frozen and lyophilized to yield 119 mg of a white solid. ^1H NMR showed complete disappearance of TMAM and the appearance of new signals assigned to be the sulfoxide as shown by FTIR (**Figure 2.5b**, manuscript). ^1H NMR in CDCl_3 (**Figure A.2e**, Supporting Information), δ (ppm): 4.48 (m, 1H, CH_2NCH_2), 4.13 (m, 1H, CH_2NCH_2), 3.73 (m, 2H, CH_2NCH_2), 2.84 (m, 2H, $\text{CH}_2\text{S(O)CH}_2$), 2.67 (m, 2H, $\text{CH}_2\text{S(O)CH}_2$), 2.13 (s, 3H, COCH_3). In addition, some sulfone had formed as suggested by the signals at 3.94 (m, CH_2), 3.03 (m, CH_2), 2.16 (s, COCH_3). Other signals of the sulfone were not observed due to overlap with the sulfoxide signals.

Synthesis of *N*-(3-(methylsulfinyl)benzyl)acetamide (TPhAM-SO) (23 mg, 0.1 mmol) was dissolved in 180 μL of dioxane in a glass vial and to the clear solution was added 76 μL of 1.75 M H_2O_2 (aq) (0.1 mmol) and the mixture was stirred for 7 d at RT. The reaction mixture was diluted with water and the clear solution was lyophilized to yield 25 mg of a white solid. ^1H NMR showed 90% of TPhAM to be oxidized to the sulfoxide as shown by FTIR (**Figure 2.5c**, manuscript). ^1H NMR in CDCl_3 (**Figure A.2f**, Supporting Information), δ (ppm): 7.57 (d, 2H, $\text{CH}_{\text{aromat}}$), 7.42 (d, 2H, $\text{CH}_{\text{aromat}}$), 6.25 (bs, 1H, NH), 4.47 (d, 2H, $\text{PhCH}_2\text{S(O)}$), 2.68 (s, 3H, S(O)CH_3), 2.05 (s, 3H, COCH_3).

Synthesis of 5-[(2-aminoethyl)thioureidyl]fluorescein TFA salt (FITC-NH₂·TFA). FITC-NH₂·TFA was synthesized as reported previously with slight modifications [Simirnov et al., J. Am. Chem. Soc. 2013, 135, 2887-2890]. Tert-butyl *N*-(2-aminoethyl)carbamate (50 mg, 0.314 mmol) was dissolved in 50 mL of 0.1 M NaHCO_3 (aq) and 2.5 mL of CH_3CN on ice. To this solution, fluorescein isothiocyanate (100 mg, 0.257 mmol) suspended in 3.5 mL of CH_3CN was added. The reaction mixture was stirred for 1 d in the dark. The clear orange solution was neutralized with 1 M HCl (aq) and evaporated under reduced pressure at 40°C to remove CH_3CN . The orange-brown precipitate was collected by centrifugation, washed with deionized water (2 x 10 mL) and lyophilized. The crude product was dissolved in 25 mL EtOAc and centrifuged to remove an insoluble brown solid. The clear yellow supernatant was evaporated at 40°C under reduced pressure. The solid was dissolved in 2 mL of TFA/water (95/5 v/v%) and stirred at RT for 2 h. The reaction mixture was evaporated under air flow at RT. The residue was

dissolved in 1 mL DMF and added dropwise to 50 mL Et₂O. The precipitate was collected on a glass filter, dissolved in water and lyophilized. ¹H NMR of the product in *d*₆-DMSO was measured to confirm the successful synthesis of FITC-NH₂·TFA.

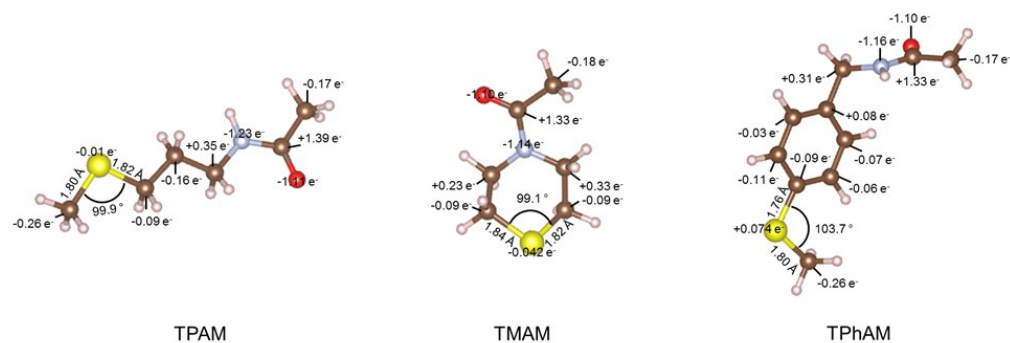


Figure A.1. Molecular structures of TPAM, TMAM, and TPhAM. Color code: brown-C, yellow-S, blue-N, red-O, white-H

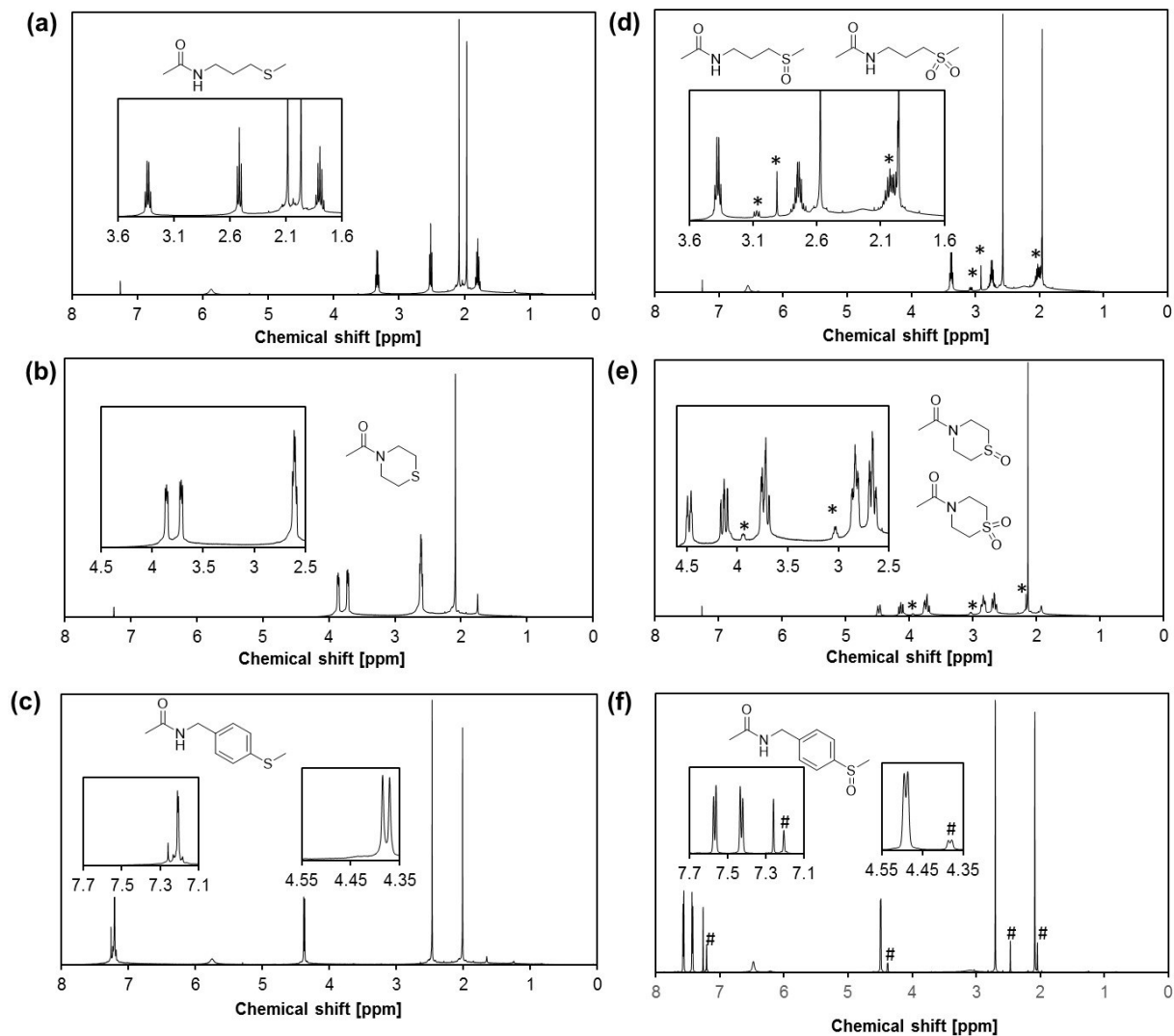


Figure A.2. ^1H NMR spectra of the thioether model compounds before (a-c) and after oxidation with H_2O_2 (d-f). TPAM (a and d), TMAM (b and e) and TPhAM (c and f). Asterisk (*) symbols in (d and e) indicate signals due to the sulfone. Hash (#) symbols in (f) indicate signals from unreacted TPhAM.

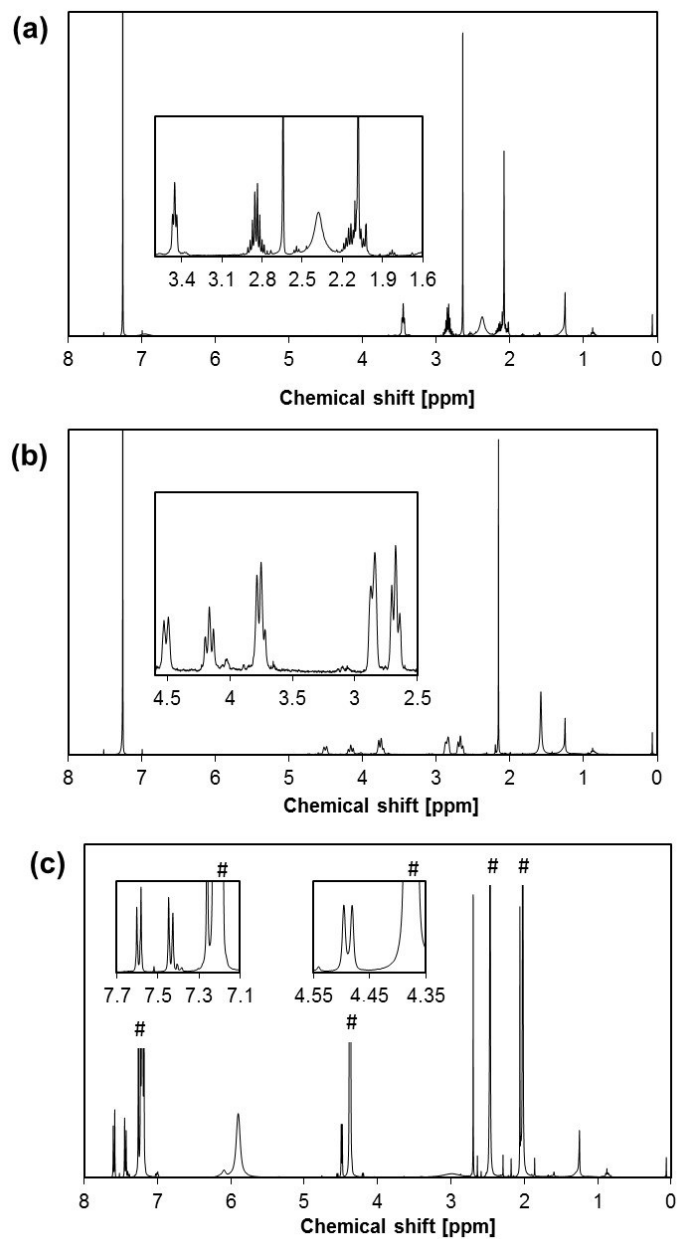


Figure A.3. ^1H NMR spectra of the reaction mixture of the time course experiment. After 48 h the reaction mixtures were lyophilized, extracted with chloroform, concentrated and dried under vacuum at 40°C . ^1H NMR spectra of the samples showed the presence of the sulfoxide of TPAM (a), TMAM (b) and TPhAM (c). In case of TPAM and TMAM the starting thioether signals are not present due to evaporation during lyophilization and drying. In case of TPhAM signals of the starting material have been indicated with hash (#) symbols.

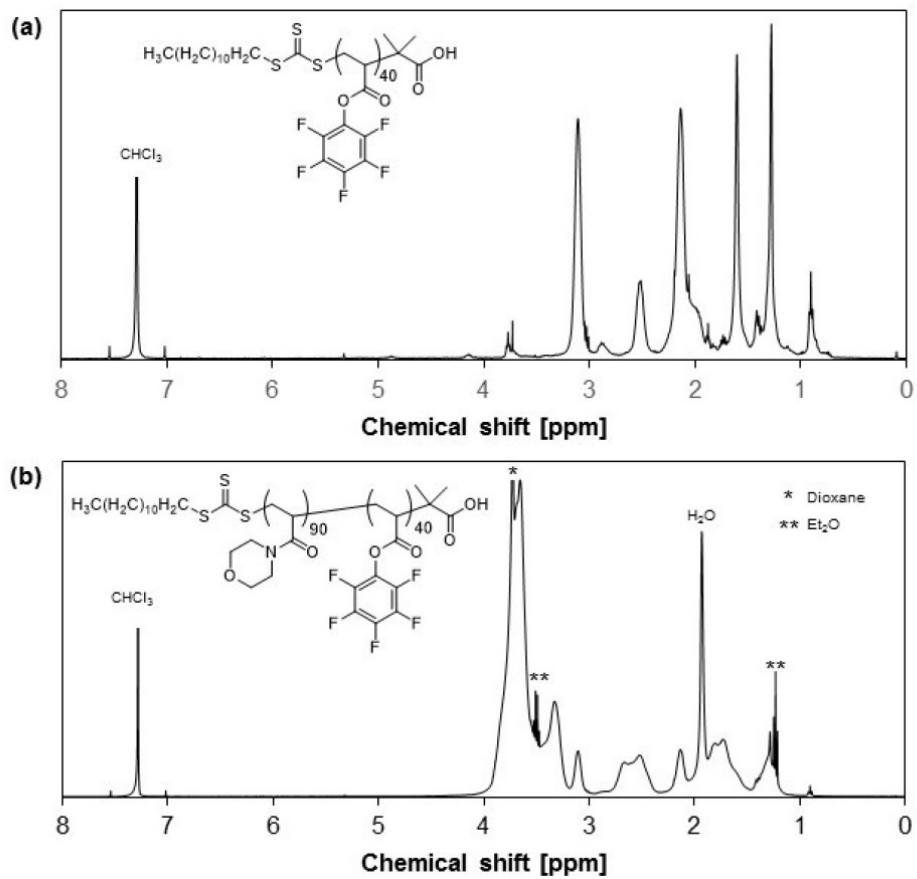


Figure A.4. ^1H NMR spectra of (a) PPFPA40 and (b) PAM-PPFPA40 in CDCl_3

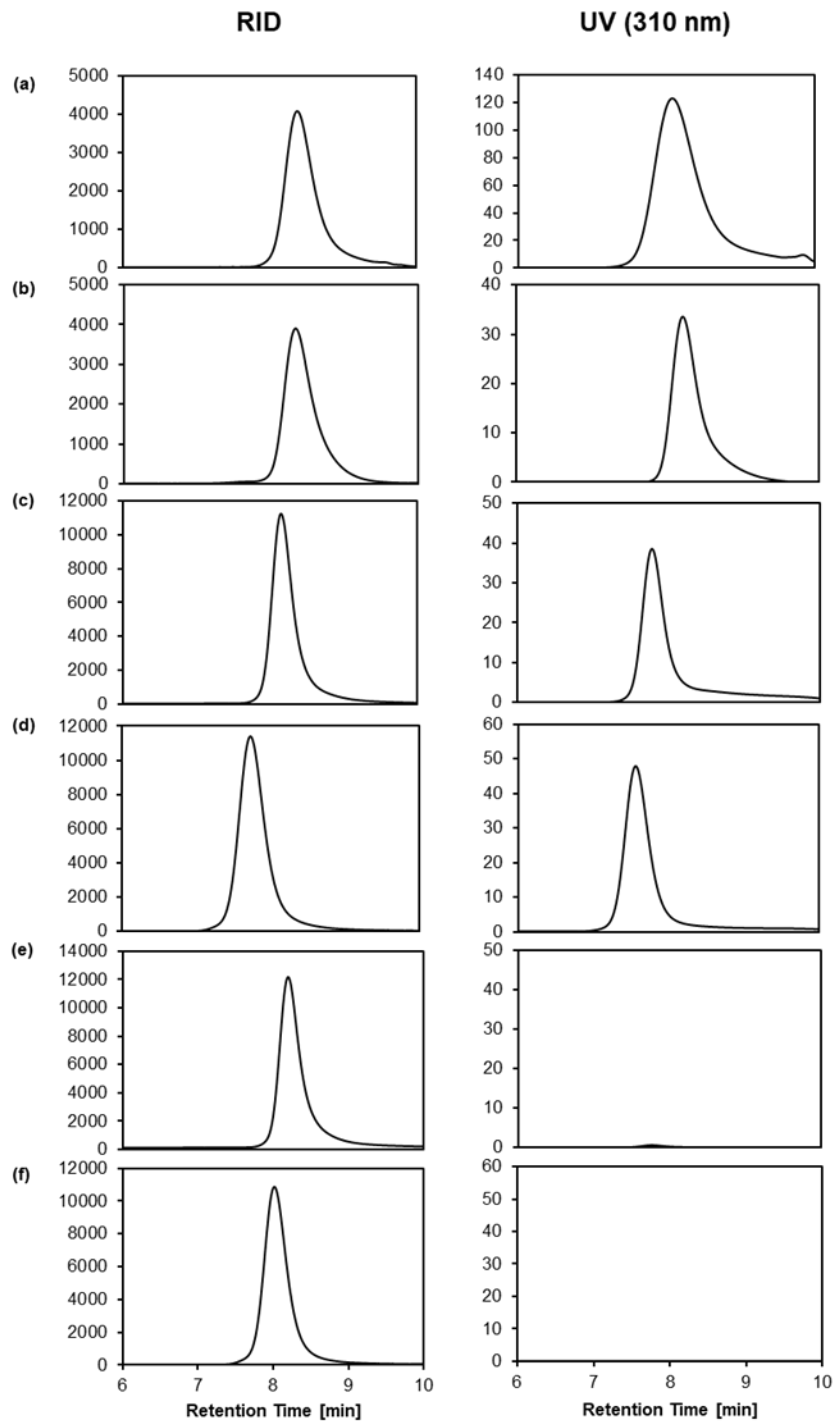


Figure A.5. GPC elution profiles of (a) PPFPA20, (b) PPFPA40, (c) PAM-PPFPA20, (d) PAM-PPFPA40, (e) CTA removed PAM-PPFPA20 and (f) CTA removed PAM-PPFPA40. Left panels: refractive index detector (RID) signal. Right panels: UV absorbance at 310 nm.

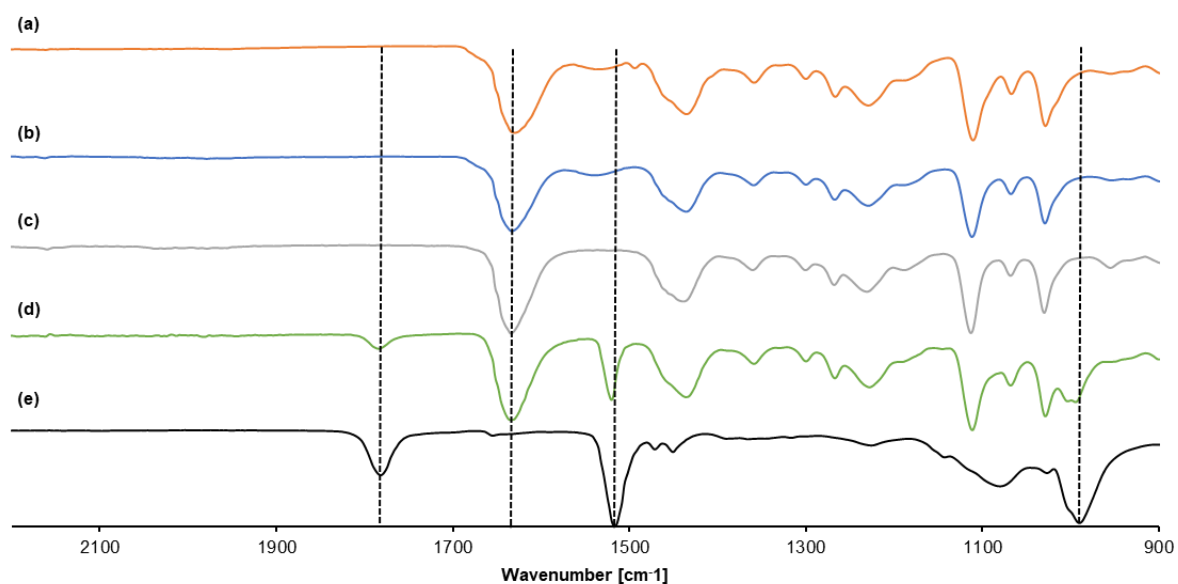


Figure A.6. FT-IR spectra of (a) TPh20, (b) TP20, (c) TM20, (d) CTA removed PAM-PPFPA20, (e) PPFPA20. Signals at 1780 (C=O), 1510 (C=C) and 1000 (C-F) cm^{-1} are due to vibrations of the pentafluorophenyl acrylate groups. The signal at 1620 (C=O) cm^{-1} is due to the amide group of PAM.

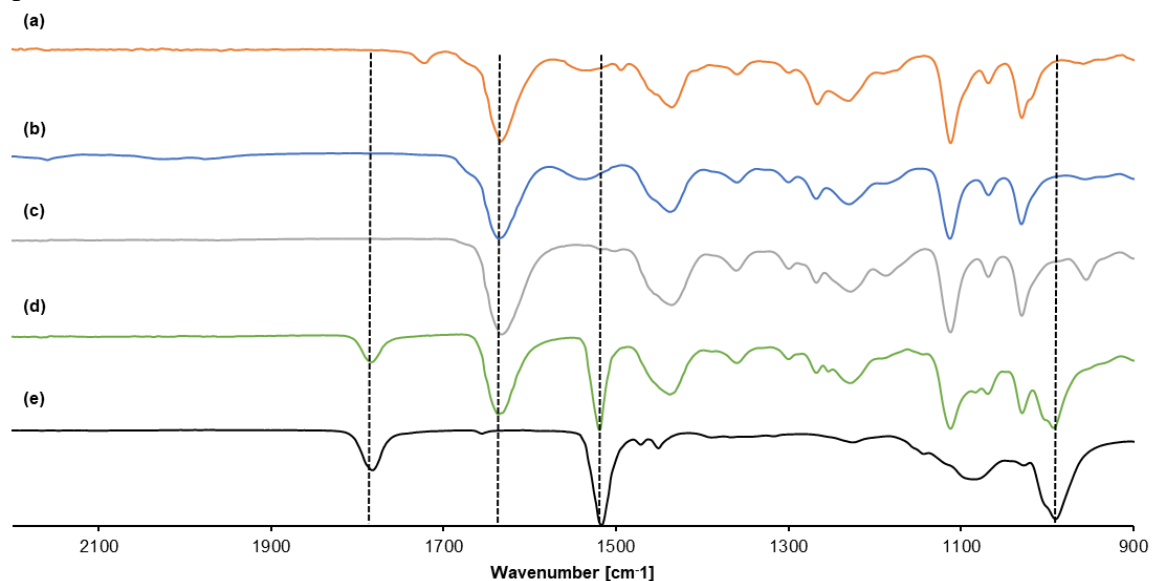


Figure A.7. FT-IR spectra. (a) TPh40, (b) TP40, (c) TM40, (d) CTA removed PAM-PPFPA40 and (e) PPFPA40. Signals at 1780 (C=O), 1510 (C=C) and 1000 (C-F) cm^{-1} are due to vibrations of the pentafluorophenyl acrylate groups. The signal at 1620 (C=O) cm^{-1} is due to the amide group of PAM.

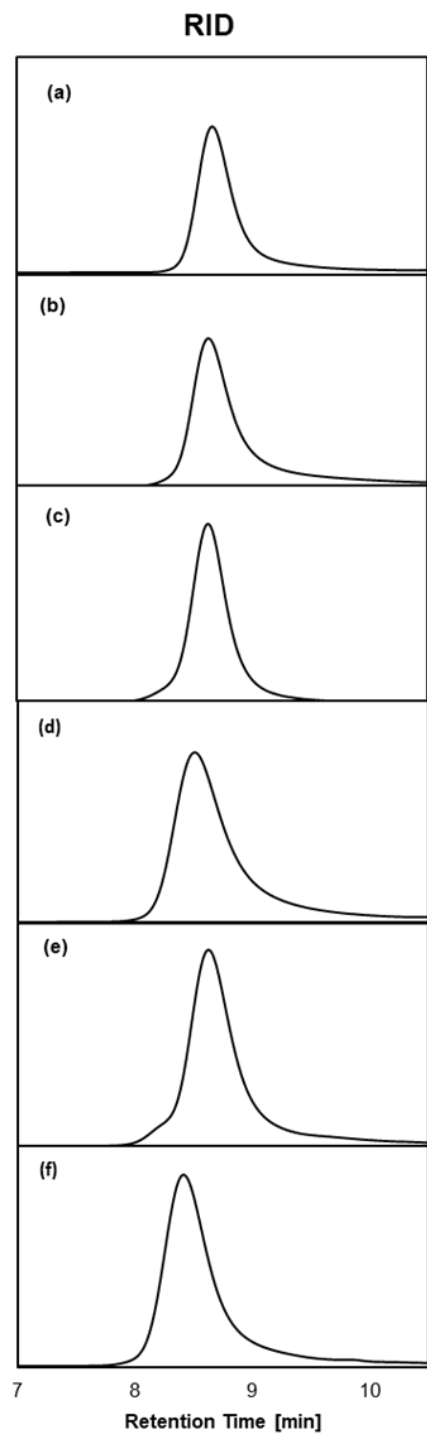


Figure A.8 GPC elution profiles of (a) TP20, (b) TM20, (c) TPh20, (d) TP40, (e) TM40 and (f) TPh40. RID: refractive index detector signal.

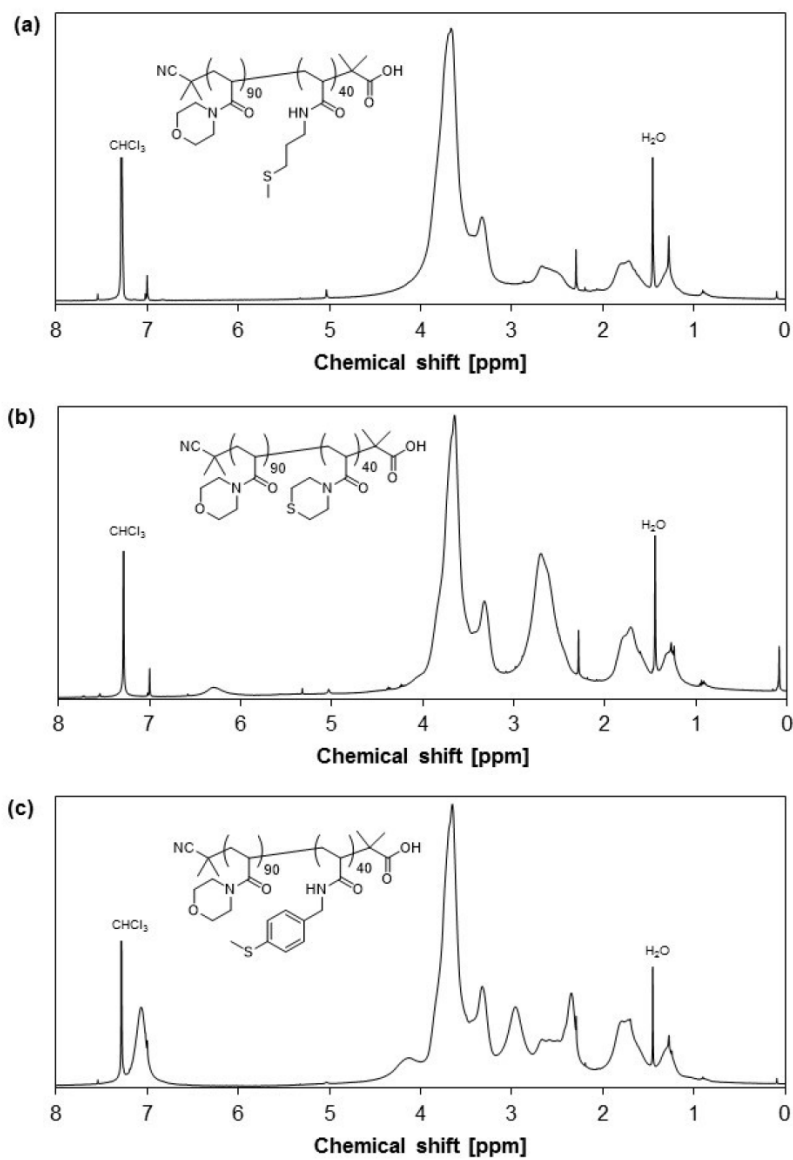


Figure A.9. ¹H NMR spectra of (a)TP40, (b) TM40, and (c)TPh40 in CDCl₃

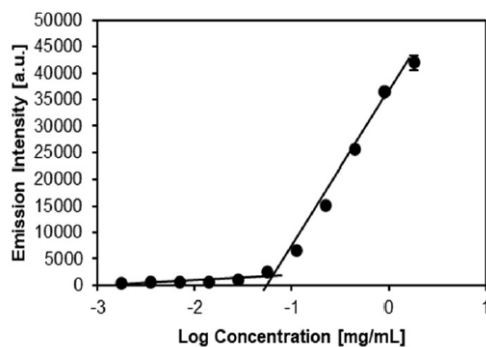


Figure A.10. A typical fluorescence versus polymer concentration plot to determine the critical micelle concentration (CMC) by the Nile red fluorescence assay. The CMC values were calculated from the intersection between the linear fits of the low and high concentration shown here for TPh20 micelles.

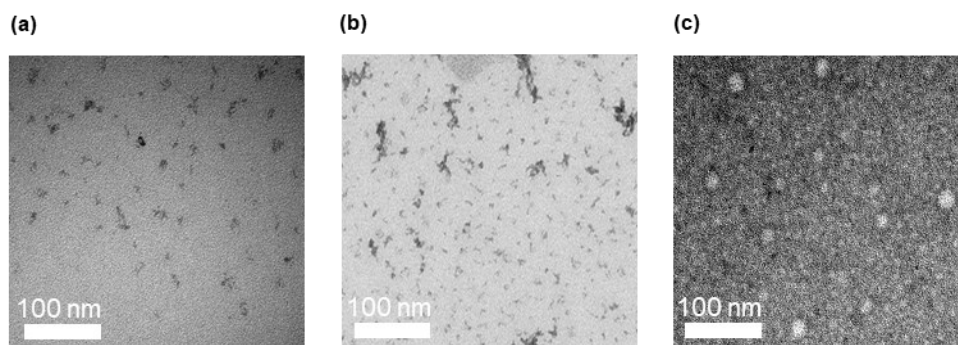


Figure A.11. TEM images of thioether-bearing micelles after treatment with H_2O_2 . The micelles were treated with 100 mM H_2O_2 at 37 °C for 24 h. (a) TP20, (b) TM20, (c) TPh20 micelles.

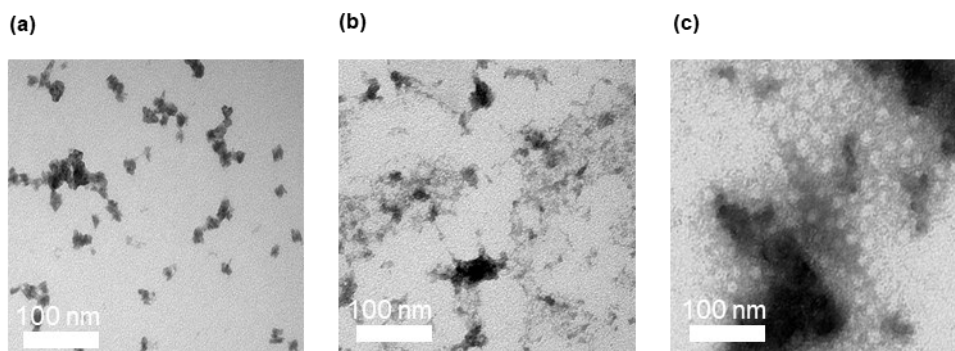


Figure A.12. TEM images of thioether-bearing micelles after treatment with H_2O_2 . The micelles were treated with 100 mM H_2O_2 at 37 °C for 24 h. (a) TP40, (b) TM40, (c) TPh40 micelles.

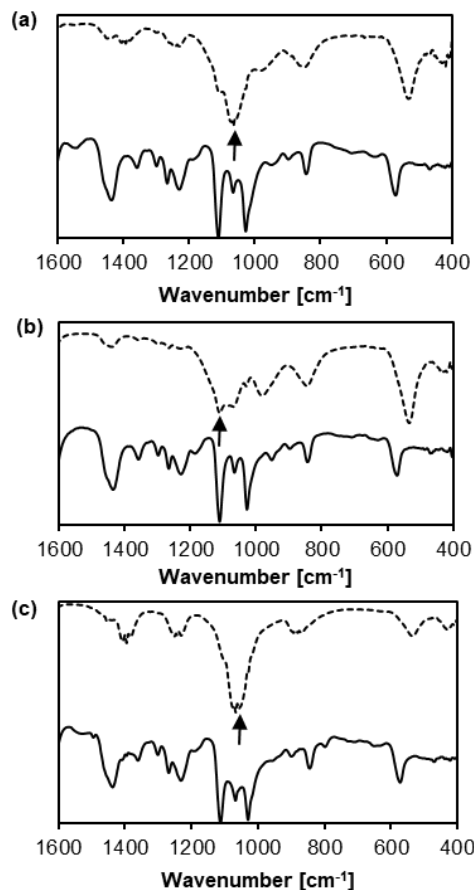


Figure A.13. FT-IR spectra before (solid line) and after (dotted line) treatment with 100 mM H_2O_2 at 37 °C for 24 h (a) TP20, (b) TM20 and (c) TPh20. Arrows indicate the sulfoxide S=O stretching vibration.

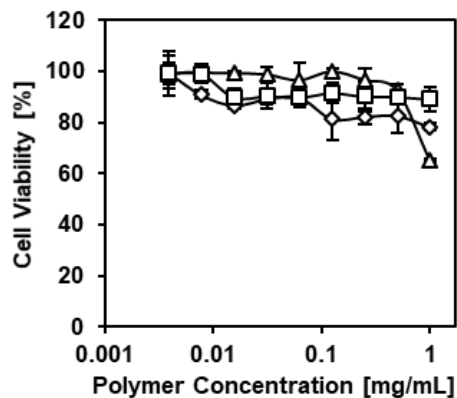


Figure A.14. Cytotoxicity of micelles alone in HepG2 cells. HepG2 cells were cultured in the presence of micelles without Dox for 2 d. Cell viability was measured by MTT assay. TP40 (triangles), TM40 (diamonds), TPh40 (squares).

Appendix B-Supporting information from Chapter 3

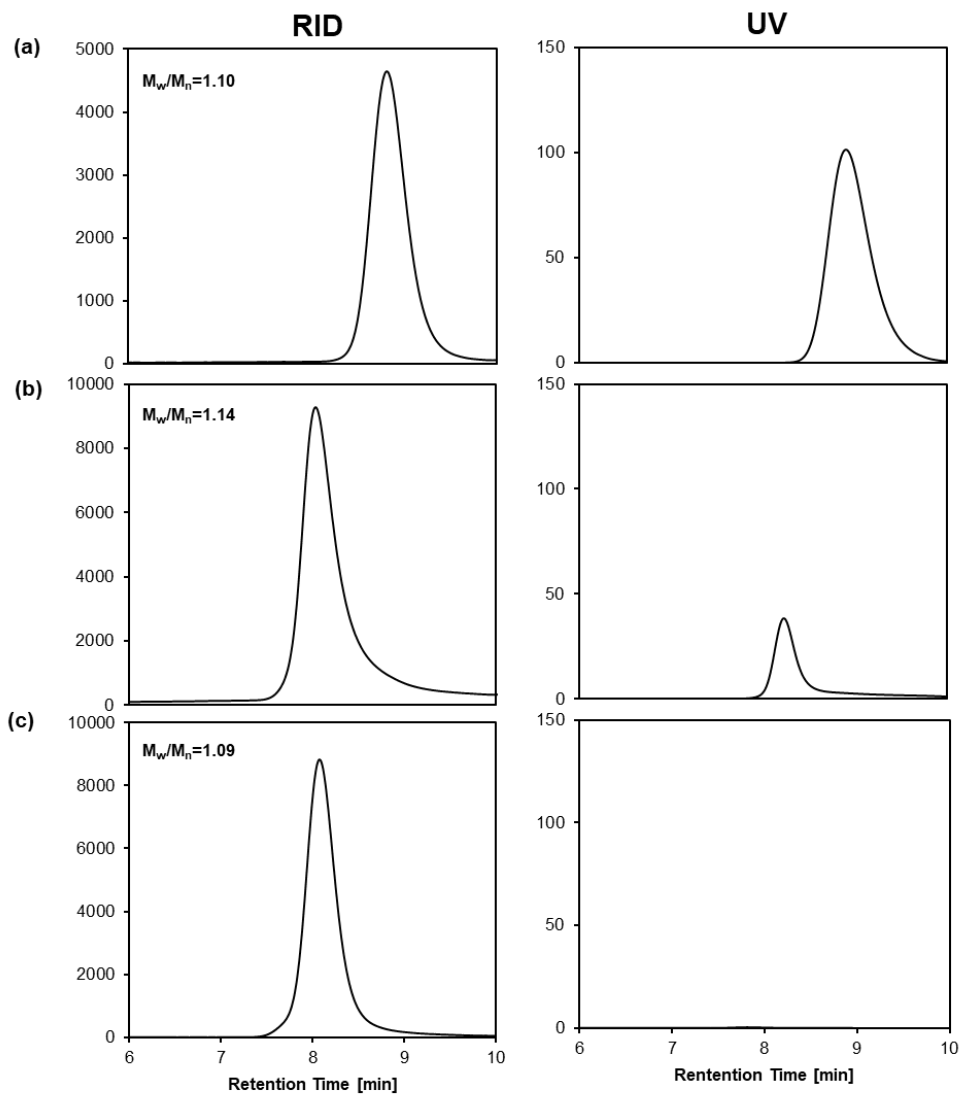


Figure B.1. GPC elution profiles of (a) PPFPA, (b) PAM-PPFPA and (c) CTA removed PAM-PPFPA. Left panels: Refractive index detector (RID) signal. Right panels: UV absorbance at 310 nm

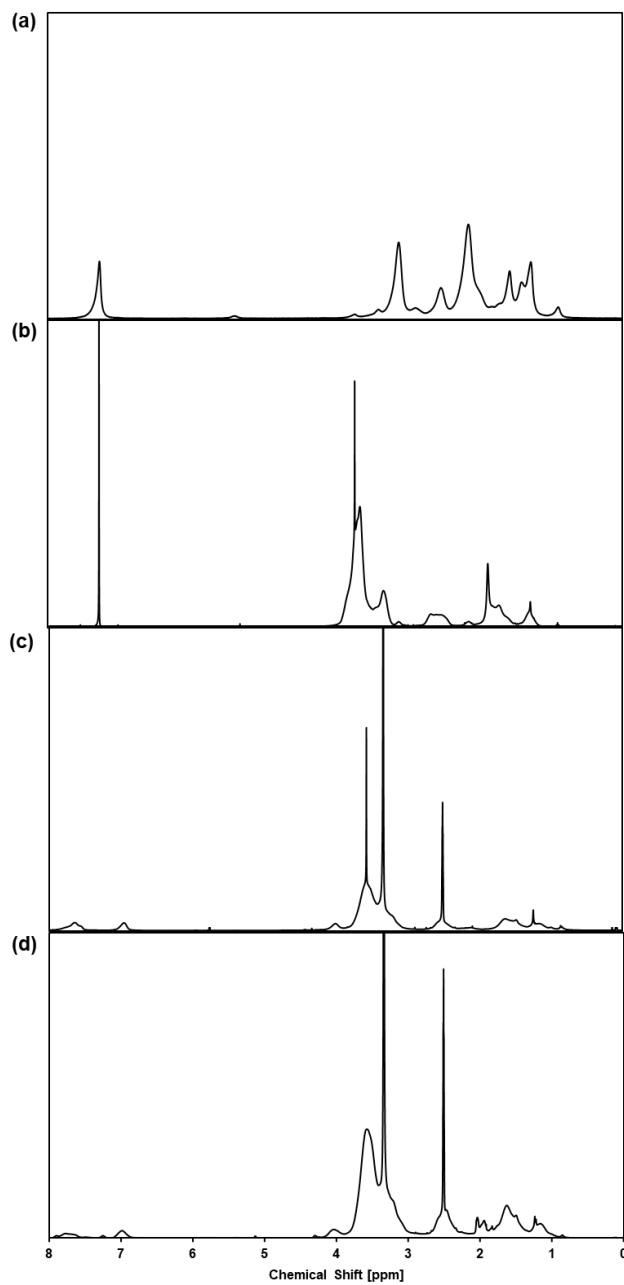


Figure B.2. ¹H NMR spectra of (a) PPFPA and (b) PAM-PPFPA (c)ADTM and (d) ADT-TPM in CDCl₃ or (CD₃)₂SO.

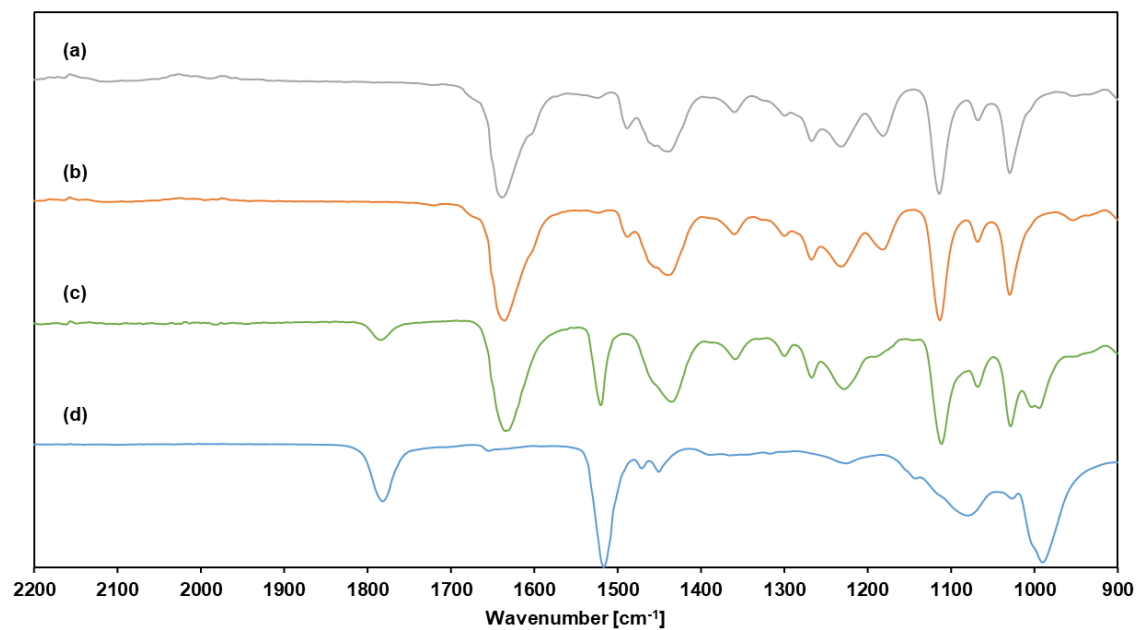


Figure B.3. FT-IR spectra of (a) ADT-TPM, (b) ADTM, (c) CTA removed PAM-PPFPA, and (d) PPFPA

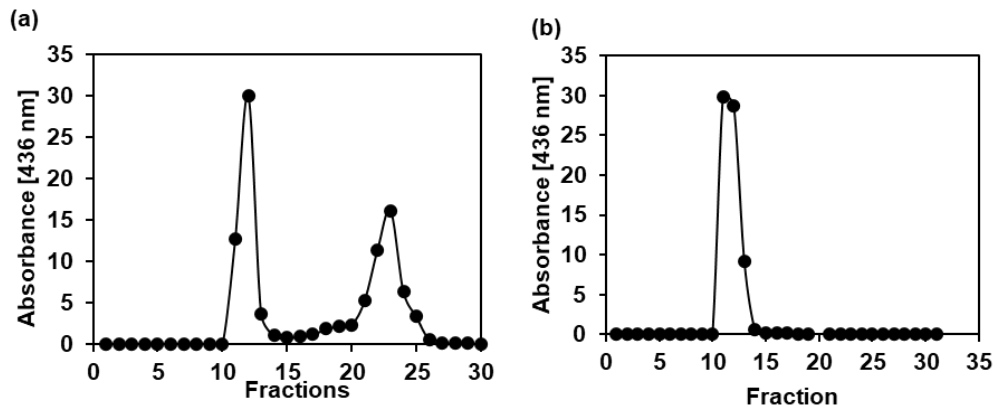


Figure B.4. Absorbance for (a) ADTM and (b) ADT-TPM fractions collected after separation by LH-20 column chromatography. Absorbance was measured at 436 nm by Nanodrop corresponding to absorbance of ADT group. The successfully conjugated polymer is eluted in fractions 11-13 and free ADT group is eluted in fractions 20-25.

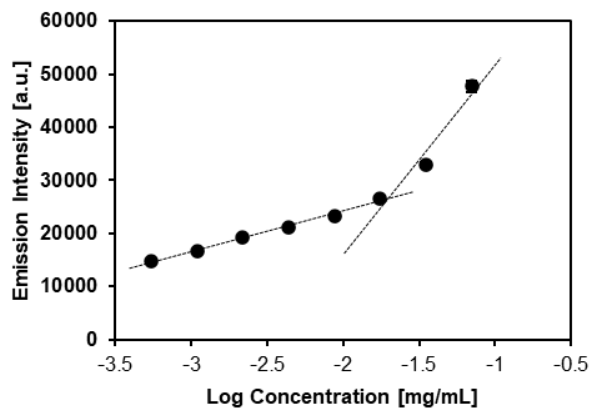


Figure B.5. Example determination of CMC by the Nile red fluorescence assay. The fluorescence emission intensity was recorded at 630 nm ($\lambda_{ex}=530$ nm). $n=3$

Appendix C-Supporting information for Chapter 4

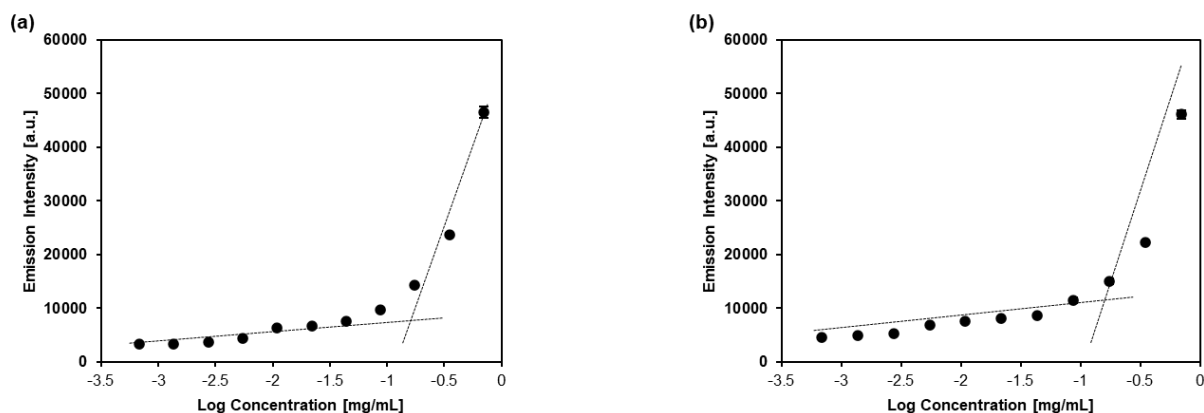


Figure C.1. Determination of CMC of (a) ADT-GPLGL and (b) ADT-GPLL micelles by the Nile red fluorescence assay. The fluorescence emission intensity was recorded at 630 nm ($\lambda_{\text{ex}}=530$ nm). $n=3$

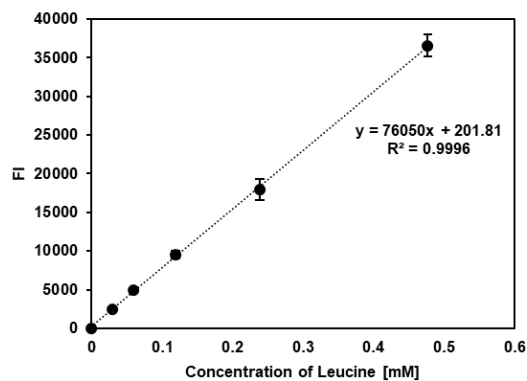


Figure C.2. Standard curve of amino group Leucine in Tricine buffer determined by fluorescamine assay. Fluorescence intensity was measured at $\lambda_{\text{ex}}=390$ nm, $\lambda_{\text{em}}=475$ nm. $n=3$

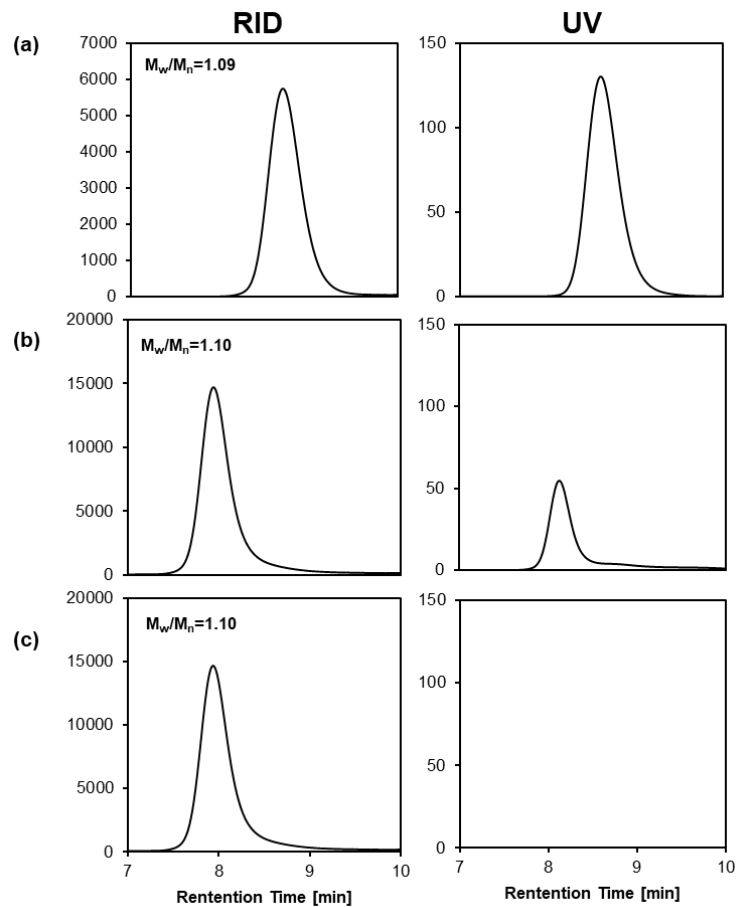


Figure C.3. GPC elution profiles of (a) PPFPA, (b) PAM-PPFPA and (c) CTA removed PAM-PPFPA. Left panels: Refractive index detector (RID) signal. Right panels: UV absorbance at 310 nm

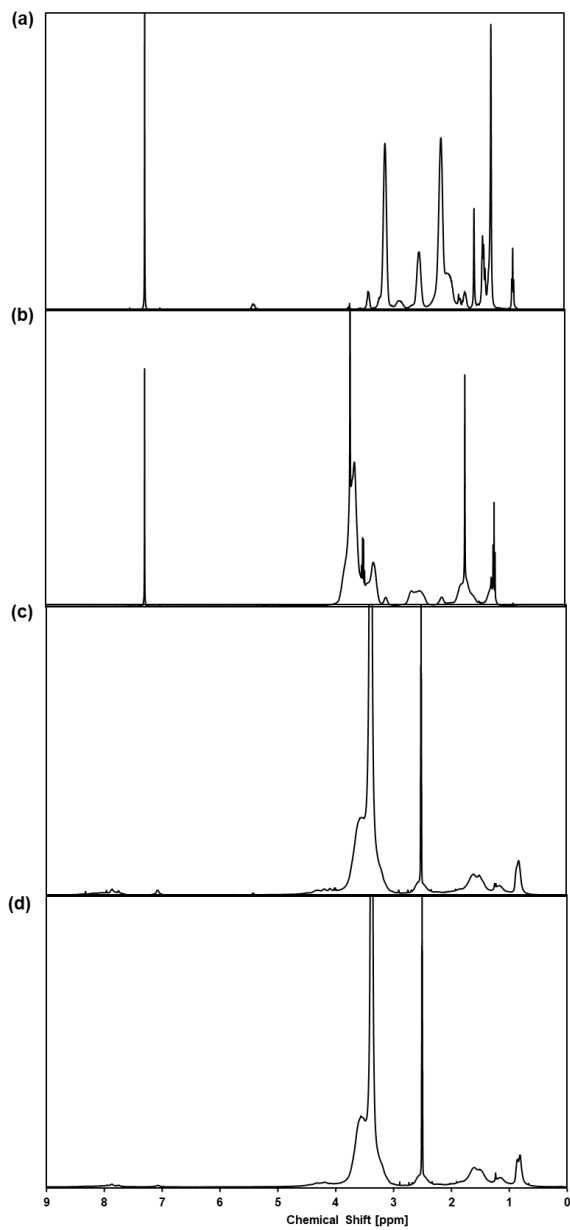


Figure C.4. ¹H NMR spectra of (a) PPFPA and (b) PAM-PPFPA (c)ADT-GPLGL and (d) ADT-GPLL in CDCl₃ or (CD₃)₂SO.

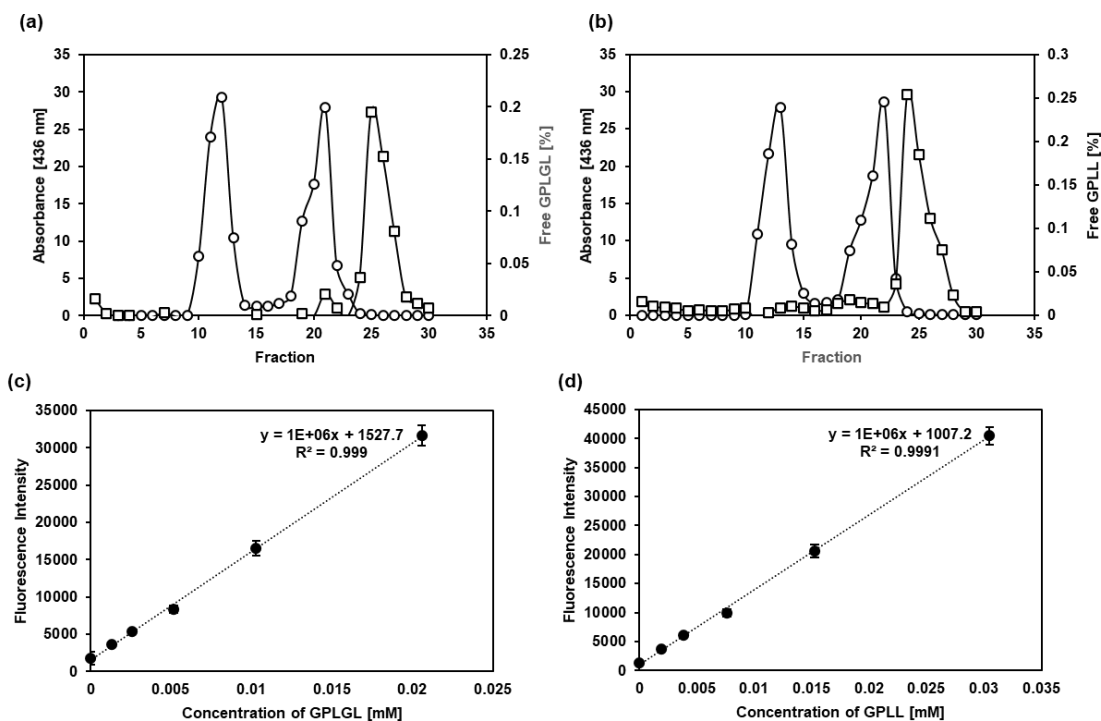


Figure C.5. (a-b) Absorbance (circles) and amount of free peptide (squares) for (a) ADT-GPLGL and (b) ADT-GPLL fractions collected after separation by LH-20 column chromatography. Absorbance was measured at 436 nm by Nanodrop corresponding to absorbance of ADT group. The successfully conjugated polymer is eluted in fractions 10-13 and free ADT group is eluted in fractions 20-24. Amount of free peptide was determined by fluorescamine assay relative to the amount of peptide added to the reaction. Fluorescence intensity was measured at $\lambda_{\text{ex}}=390$ nm, $\lambda_{\text{em}}=475$ nm. $n=3$. (c-d) Standard curve of peptides (c) GPLGL-NH₂ and (d) GPLL-NH₂ determined by fluorescamine assay. Peptide solution in DMF was mixed with fluorometric Tricine buffer followed by the addition of fluorescamine solution in acetone. Fluorescence intensity was measured at $\lambda_{\text{ex}}=390$ nm, $\lambda_{\text{em}}=475$ nm after 15 min of incubation at room temperature. $n=3$

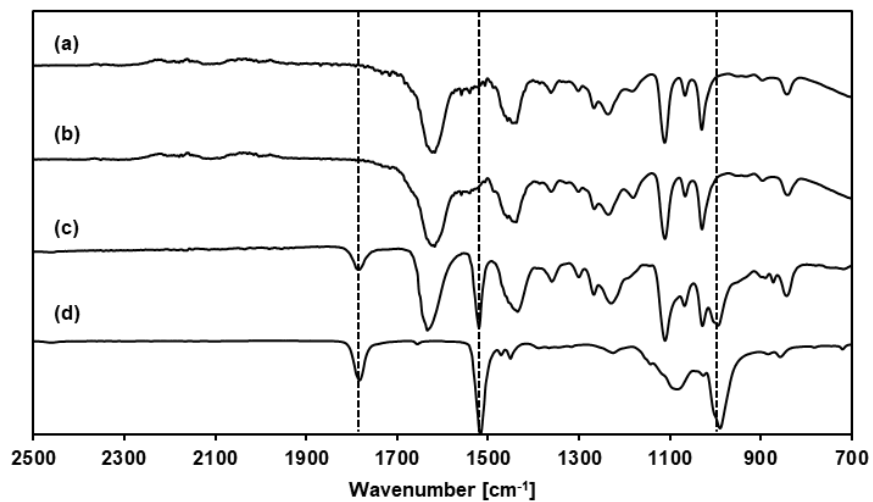


Figure C.6. FT-IR spectra of (a) ADT-GPLL, (b) ADT-GPLGL, (c) CTA removed PAM-PPFPA, and (d) PPFPA

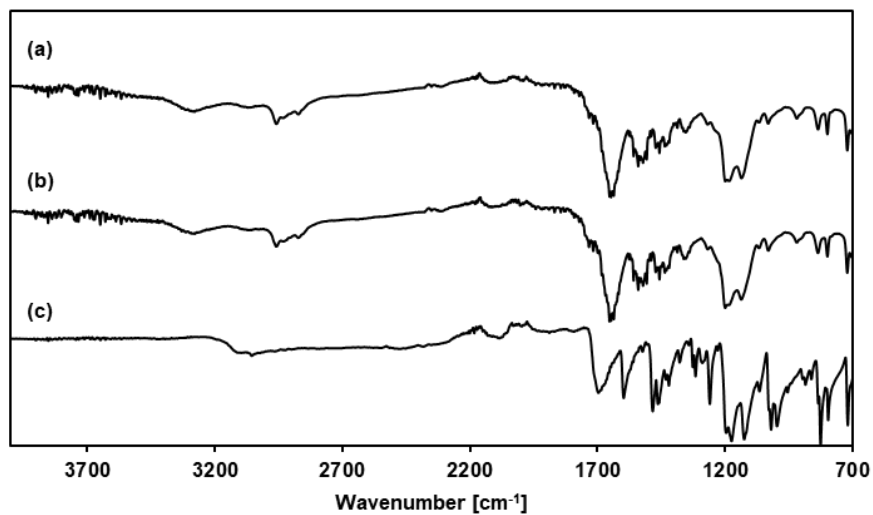


Figure C.7. FT-IR spectra of (a) GPLL-NH₂·TFA, (b) GPLGL-NH₂·TFA and (c) ADT-NH₂·TFA

Appendix D-List of Abbreviation

Name	Abbreviation
1-methyl-2-pyrrolidinone	NMP
2-(dodecylthiocarbonothioylthio)-2-methylpropionic acid	CTA
2,2'-azobis(isobutyronitrile)	AIBN
3-(4,5-dimethylthiazol-2-yl)-2,5-diphenyltetrazolium bromide	MTT
3-mercaptopropyl) trimethoxysilane	MPTS
3-mercaptopyruvate sulfur transferase	3-MST
3-methylthiopropylamide	TPAM
3-methylthiopropylamine	TP
4-(methylthio)benzylamide	TPhAM
4-(methylthio)benzylamine	TPh
4-acryloylmorpholine	AM
4-dimethylamiopyridine	DMAP
Acetic anhydride	Ac ₂ O
Acetonitrile	CH ₃ CN
Aluminum oxide	Al ₂ O ₃
Anethole dithiolethione	ADT
Attenuated total reflection infrared spectroscopy	ATR-IR
Block copolymer polymeric micelles	BCPMs
Calcium hydride	CaH ₂
Carbon monoxide	CO
Carbonyl sulfide	COS
Confocal laser scanning fluorescence microscopy	CLSFM
Copper sulfide	CuS
Critical micelle concentration	CMC
cysthathionine β-synthase	CBE
Cysthathionine γ-lyase	CSE
Deionized water	DI water
Deuterated chloroform	CDCl ₃
Deuterated dimethyl sulfoxide	(CD ₃) ₂ SO
Diallyl trisulfide	DATS
Diethyl ether	Et ₂ O
Diethylamine ethyl acetate	DEAEA
Dimethylformamide	DMF
Doxorubicin	Dox
Dynamic light scattering	DLS
Enhanced Permeability and Retention effect	EPR effect
Enzyme-linked immunosorbent assay	ELISA
Epidermal growth factor	EGF
Ethanol	EtOH
Ethyl acetate	EtOAc
Extracellular matrix	ECM
Extracellular polymeric substances	EPS
Fluorescence intensities	FI

Gardiquimod	GDQ
Gel permeation chromatography	GPC
Hexane	HA
Human neutrophil elastase	HNE
Human umbilical endothelial cells	HUVECs
Hydrochloric acid	HCl
Hydrodynamic diameter	D_h
Hydrogen peroxide	H_2O_2
Hydrogen sulfide	H_2S
Hydroxyl radical	$\cdot OH$
Laser capture microdissection	LCM
Matrix metalloproteinases	MMPs
Matrix metalloproteinase-2	MMP-2
Mesoporous silica	mSiO ₂
Methanol	MeOH
Mononuclear phagocytic system	MPS
morpholin-4-ium 4-methoxyphenyl(morpholino) phosphinodithioate	GY4137
<i>N</i> -acetyl-L-cysteine	NAC
Near-infrared light	NIR light
Nitrogen oxide	NO
Number average molecular weight	M_n
Paclitaxel	PTX
Pearson's Correlation Coefficient	PCC
PEG-diacrylate	PEGDA
Pentaerythritol tetra (mercaptoethyl) polyoxyethylene	$((CH_2)_2-SH)_4$
Pentafluorophenyl acrylate	PFPA
Phosphate-buffered saline	PBS]
Phosphor pentoxide	P ₄ O ₁₀
poly(<i>N</i> -acryloyl morpholine)	PAM
poly(pentafluorophenyl acrylate)	PPFPA
Poly(propylene sulfide)	PPS
Polydispersity index	PDI
Polyethersulfone	PES
Polyethylene glycol	PEG
Polymer surface dissection method	PSD method
Polymerase chain reaction	PCR
Polymeric micelles	PMs
Polyvinylidene difluoride	PVDF
Potassium hydroxide	KOH
Proton NMR	¹ H NMR
Reactive oxygen species	ROS
Reticuloendothelial system	RES
Reversible addition fragmentation chain transfer polymerization	RAFT polymerization
<i>S</i> -aroylthiooximes	SATOs
Singlet oxygen	¹ O ₂
Sodium bicarbonate	NaHCO ₃

Sodium dodecyl sulfate	SDS
Sodium hydrosulfide	NaHS
Sodium sulfide	Na ₂ S
Superoxide anion radical	O ₂ ^{·-}
Tetrahydrofuran	THF
Thiomorpholine amide	TMAM
Thiomorpholine	TM
Toluene	TL
Transmission electron microscopy	TEM
Triethylamine	TEA
Trifluoroacetic acid	TFA
Tumor microenvironment	TME
Ultraviolet light	UV light
Weight average molecular weight	<i>M_w</i>
<i>Wheat Germ Agglutinin</i>	WGA